THE BELL SYSTEM

# Technical Journal

DEVOTED TO THE SCIENTIFIC AND ENGINEERING ASPECTS OF ELECTRICAL COMMUNICATION

VOLUME XLVI DECEMBER 1967 NUMBER 10

The Dynamics of High-Field Propagating Domains in Bulk Semiconductors K. KUROKAWA 2235

A Millimeter Wave, Two-Pole, Circular-Electric Mode, Channel-Dropping Filter Structure R. D. STANDLEY 2261

Sheet Resistivity Measurements on Rectangular Surfaces—General Solution for Four Point Probe Conversion Factors M. A. LOGAN 2277

Scaling Laws for Large Shields in Quasi-Stationary Magnetic Fields G. KRONACHER 2323

Optimal Routing in Connecting Networks Over Finite Time Intervals V. E. BENEŠ 2341

Restoration of Photographs Blurred by Image Motion D. SLEPIAN 2353

Cathode Activity Measurement: A Modification of the Dip Test D. W. MAURER 2363

The CPC: A Medium Current Density, High Reliability Cathode D. W. MAURER AND C. M. PLEASS 2375

Contraction Maps and Equivalent Linearization J. M. HOLTZMAN 2405

Power Density Spectrum of the Sum of Two Correlated Intermodulation Noise Contributors in FM Systems T. G. CROSS 2437

Phase Progression in Conical Waveguides E. R. NAGELBERG 2453

Mode Conversion in Lens Guides with Imperfect Lenses D. GLOGE 2467

Contributors to This Issue 2485

COPYRIGHT © 1967 AMERICAN TELEPHONE AND TELEGRAPH COMPANY

# THE BELL SYSTEM TECHNICAL JOURNAL


## ADVISORY BOARD

P. A. GORMAN, *President, Western Electric Company*

J. B. FISK, *President, Bell Telephone Laboratories*

A. S. ALSTON, *Executive Vice President, American Telephone and Telegraph Company*

## EDITORIAL COMMITTEE

W. E. DANIELSON, *Chairman*

F. T. ANDREWS, JR.
E. E. DAVID
C. W. HOOVER, JR.
A. E. JOEL
D. H. LOONEY
E. C. READ
E. D. REED
M. TANENBAUM
Q. W. WIEST
C. R. WILLIAMSON

## EDITORIAL STAFF

G. E. SCHINDLER, JR., *Editor*

E. F. SCHWEITZER, *Assistant Editor*

H. M. PURVIANCE, *Production and Illustrations*

F. J. SCHWETJE, *Circulation*



THE BELL SYSTEM TECHNICAL JOURNAL is published ten times a year by the American Telephone and Telegraph Company, B. S. Gilmer, President, C. E. Wampler, Vice President and Secretary, J. J. Scanlon, Vice President and Treasurer. Checks for subscriptions should be made payable to American Telephone and Telegraph Company and should be addressed to the Treasury Department, Room 2312C, 195 Broadway, New York, N. Y. 10007. Subscriptions $5.00 per year; single copies $1.25 each. Foreign postage $1.08 per year; 18 cents per copy. Printed in U.S.A.

THE BELL SYSTEM
TECHNICAL JOURNAL

VOLUME XLVI | DECEMBER 1967 | NUMBER 10

# The Dynamics of High-Field Propagating Domains in Bulk Semiconductors

By K. KUROKAWA

(Manuscript received June 23, 1967)

*This paper discusses the dynamics of high-field propagating domains in bulk semiconductors such as gallium arsenide. First, the origin of a high-field domain and its nucleation mechanism are discussed. Next, important properties of a steady-state high-field domain are briefly reviewed. Then, the "unequal" areas rule is derived to explain transient domain behavior. Domain buildup or decay speeds are discussed in detail, and conditions are presented under which two or more domains can exist simultaneously. Finally, the above discussions are applied to explain the high-field domain behavior in pulse circuits, variable frequency oscillators, waveform generators, and domain bypassing schemes. Numerical examples are also given to illustrate how fast these operations can be performed.*

## I. INTRODUCTION

In the past several years, it was found that several bulk semiconductors showed voltage-controlled differential negative resistance over a certain range of applied electric field. The cause of this negative resistance is vastly different from one material to another. For example, it is attributable to field dependent trapping effect in gold-doped germanium, to phonon-electron interaction in CdS and to inter-valley scattering mechanism in GaAs, InP, CdTe and ZnSe. Regardless of the origin, however, the voltage-controlled differential negative resistance effect nucleates a high field domain in the bulk.[1] Once it is nucleated, the domain travels toward the anode with al-

most constant velocity; e.g., $10^7$ cm/sec for GaAs and $10^5$ cm/sec for CdS.[2] As the domain is absorbed into the anode, another domain is nucleated in the bulk and the whole process repeats again.

Although the detailed mechanism of the negative resistance is still a subject of intense discussion, the high-field domain itself appears to have a great significance in future electronics. The objective of this paper is to clarify the dynamics of high-field propagating domains in bulk semiconductors. Since the high field domain in GaAs is presently best understood, we shall mostly concentrate on it. However, similar discussions must be possible for the high field domains in other materials as well.

## II. DOMAIN NUCLEATION

The inter-valley scattering effect in GaAs is explained as follows.[3, 4] When electrons are accelerated to a certain drift velocity by an applied electric field inside the bulk, they acquire enough energy to jump into a different valley of the conduction band where the mobility is low compared to the original valley and their drift velocity is reduced. As the applied field increases, more and more electrons come into the low mobility state and on the average the electron drift velocity $v(E)$ decreases. Thus, the material exhibits the differential negative resistance effect as shown in Fig. 1 between $E_p$ and $E_v$. If the field is increased further, the material shows positive resistance again since most of the electrons are now in the low mobility state and the transition effect fades away. Suppose that we attach two electrodes at the ends of the bulk and slowly increase the voltage between them until the inside field reaches some point in the negative resistance range. The field can stay there indefinitely if no disturbance is applied. How-

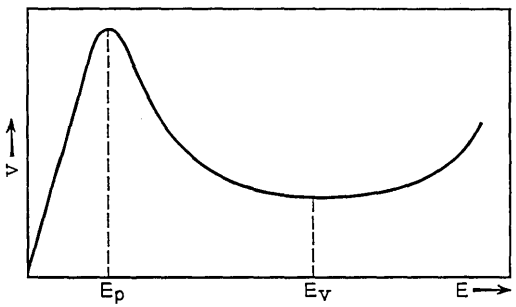


Fig. 1 — Electron velocity vs field inside GaAs.

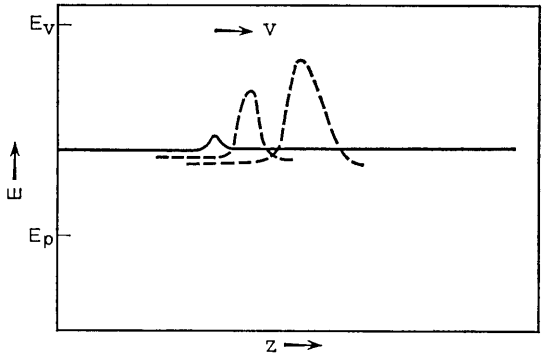


Fig. 2 — Nucleation of a high-field domain.

ever, suppose a small spatial disturbance is given to the field due to noise or due to other transient effect as shown by the solid line in Fig. 2. Then, the electrons in the disturbed region become slower than elsewhere. Hence, the electron density at the trailing edge of the disturbance increases while the leading edge is depleted. This increases the field in the region further and since the area under the field curve should be equal to the applied voltage, the field outside the region decreases slightly. Therefore, taking into account the motion of electrons as a whole toward the anode, the field distribution should look like one of the dotted lines in Fig. 2 sometime after the initial disturbance is applied. When the disturbance is fully grown it is called a high-field domain since the field there is higher than elsewhere. On the other hand, suppose that the opposite type of disturbance is initially given to the field as shown by the solid line in Fig. 3. Then, a similar reasoning to the above leads to a conclusion that the disturbance grows with time into a low field domain as illustrated by the dotted lines in Fig. 3. These two disturbances are equally likely to take place. However, if we raise the field from zero to the value just slightly above the threshold field, $E_p$ in Fig. 1, the first type of disturbance grows but the second one does not since the disturbed portion in the latter is mostly in the positive resistance range. Therefore, under ordinary circumstances, the first one is expected to dominate. If the applied voltage is instantaneously increased to a large value and then gradually reduced, the second type will dominate.

Now since we saw that a small disturbance grew, let us consider how fast it grows initially. To do so, we have to investigate two equa-

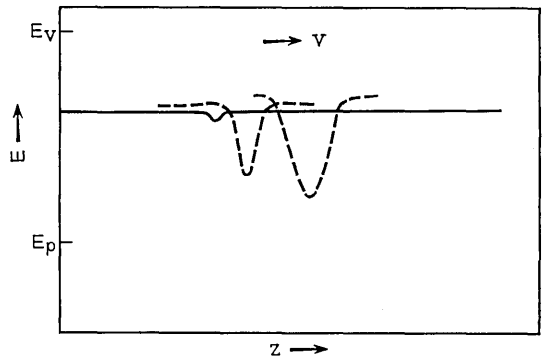


Fig. 3 — Nucleation of a low-field domain.

tions governing the phenomenon. The first one is a one-dimensional Poisson's equation

$$\frac{\partial E}{\partial z} = \frac{e}{\epsilon}(n - n_o), \tag{1}$$

where $-e$ is the electron charge, $n$ the electron density, and $n_o$ the donor density. The second equation is

$$J = env(E) - eD\frac{\partial n}{\partial z} + \epsilon\frac{\partial E}{\partial t}, \tag{2}$$

where $J$ is the total current density, $D$ the diffusion constant and $\epsilon$ the delectric constant of the material. The total current consists of the conduction, diffusion and displacement currents. The positive direction for $J$ and $E$ is taken to be from the anode to cathode and that for $v(E)$ from the cathode to anode. Suppose some disturbance is given inside the bulk and assume that the effect on the electron density has not yet reached $z_1$ and $z_2$, where $z_1$ is on the left and $z_2$ on the right-hand side of the disturbance. Then, from (1) we have

$$\frac{\partial E(z_1)}{\partial z} = \frac{\partial E(z_2)}{\partial z}.$$

Furthermore, $J = J(z_1) = J(z_2)$ gives

$$\epsilon\frac{\partial}{\partial t}\{E(z_1) - E(z_2)\} = en\{v(E(z_2)) - v(E(z_1))\}.$$

The initial condition is $E(z_1) - E(z_2) = 0$, hence $E(z_1)$ has to stay

equal to $E(z_2)$. Let $E_o$ be the field at $z_1$. Then,

$$E_o = E(z_1) = E(z_2).$$

In terms of $E_o$, the current through the device is given by

$$J = en_o v(E_o) + \epsilon \frac{\partial E_o}{\partial t}. \tag{3}$$

Substituting (1) and (3) into (2), we have

$$\frac{\partial}{\partial t}(E - E_o) = \frac{en_o}{\epsilon}\{v(E_o) - v(E)\} + D\frac{\partial^2 E}{\partial z^2} - v(E)\frac{\partial E}{\partial z}.$$

Integrating with respect to $z$ from $z_1$ to $z_2$, we obtain

$$\frac{d}{dt}\int_{z_1}^{z_2}(E - E_o)\,dz = \int_{z_1}^{z_2}\frac{en_o}{\epsilon}\{v(E_o) - v(E)\}\,dz. \tag{4}$$

This equation holds even when the disturbance is large. However, when it is small, using the relation

$$v(E) \cong v(E_o) + \frac{dv}{dE}(E - E_o) \tag{5}$$

(4) becomes

$$\frac{d}{dt}\int_{z_1}^{z_2}(E - E_o)\,dz = -\left(\frac{en_o}{\epsilon}\frac{dv}{dE}\right)\int_{z_1}^{z_2}(E - E_o)\,dz. \tag{6}$$

Since $e$ is positive and $dv/dE$ is negative in the negative resistance range, the size of the disturbance

$$\left|\int_{z_1}^{z_2}(E - E_o)\,dz\right|$$

increases with time. The time constant is given by

$$\tau = \left(\frac{en_o}{\epsilon}\frac{dv}{dE}\right)^{-1}. \tag{7}$$

The negative value means the growth instead of decay.

## III. STEADY STATE DOMAIN[5]†

Next, let us consider the domain in the steady state. When a domain travels with a constant speed without changing its shape, we call it

† This section closely follows Ref. 5. However, it is included here for completeness and continuity of discussion.

in the steady state. Let $v_d$ be the velocity of the domain. Then, both $n$ and $E$ must be functions of a single variable $\xi = z - v_d t$ in the steady state. Therefore, we have

$$\frac{\partial E}{\partial z} = \frac{dE}{d\xi}, \qquad \frac{\partial E}{\partial t} = -v_d \frac{dE}{d\xi}, \qquad \frac{\partial n}{\partial z} = \frac{\partial n}{\partial \xi}.$$

Equation (1) becomes

$$\frac{dE}{d\xi} = \frac{e}{\epsilon}(n - n_o). \tag{8}$$

This shows that $n = n_o$ whenever $dE/d\xi = 0$ and vice versa. As a result, $n$ and $E$ should look like Fig. 4(a) and (b), respectively. Note that the maximum field is located at the neutral position. On the other hand, (2) becomes

$$D\frac{dn}{d\xi} = n(v - v_d) - n_o(v_o - v_d), \tag{9}$$

where $v_o$ is the electron velocity outside the domain and use is made of $J = en_o v_o$. Eliminating $\xi$ from (8) and (9), we have

$$D\frac{dn}{dE} = \frac{n(v - v_d) - n_o(v_o - v_d)}{\frac{e}{\epsilon}(n - n_o)}$$

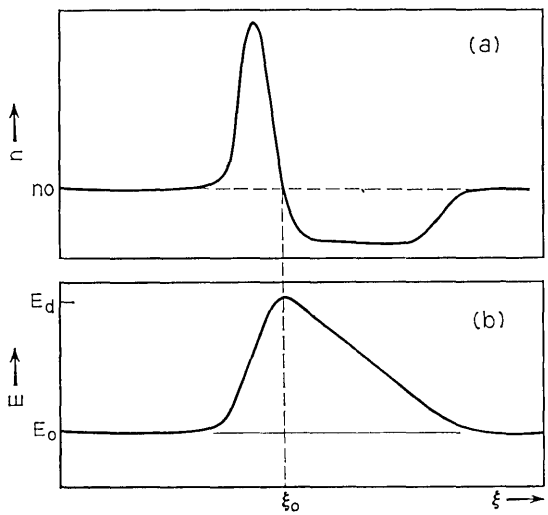


Fig. 4 — Steady-state high-field domain.

which is equivalent to

$$\frac{n - n_o}{nn_o}\frac{dn}{dE} = \frac{\epsilon}{en_oD}\left[v - v_d - \frac{n_o}{n}(v_o - v_d)\right]. \tag{10}$$

Integrating (10) with respect to $E$ and remembering that $n = n_o$ when $E = E_o$, where $E_o$ is the field outside the domain, we get

$$\frac{n}{n_o} - \ln\frac{n}{n_o} - 1 = \frac{\epsilon}{en_oD}\int_{E_o}^{E}\left[v - v_d - \frac{n_o}{n}(v_o - v_d)\right]dE.$$

The integration on the right-hand side can be carried out over the leading or trailing edge of the domain. However, when the upper limit is set equal to the peak field $E_d$ of the domain, the integral should vanish in both cases since $n = n_o$ at the peak point. However, this is impossible unless $v_o = v_d$, since the integral of $(v - v_d)$ is the same while the integral of the remaining term is different in the two cases because $n < n_o$ over the leading edge and $n > n_o$ over the trailing edge. It follows from this that the velocity of the steady-state domain is equal to the electron velocity outside the domain. Furthermore, since

$$\int_{E_o}^{E_d}(v - v_d)\,dE = \int_{E_o}^{E_d}(v - v_o)\,dE = 0$$

for a given $v_o$, $E_d$ can be determined by equating two shaded areas in Fig. 5. Thus, the relation $v_o$ vs $E_d$ should look like the broken line in Fig. 5. As the domain becomes larger, $E_d$ increases from $E_p$ and $v_o$ decreases from the peak velocity $v_p$. However, $E_d$ cannot exceed $E_{dm}$, the field corresponding to the intersection between the broken line and the solid line. This is because the equal areas rule cannot be satisfied beyond this point. When $E_d$ reaches $E_{dm}$, the outside field becomes $E_{om}$ and the velocity $v_{om}$.

The relation between $n$ and $E$ for a domain can be determined from

$$\frac{n}{n_o} - \ln\frac{n}{n_o} - 1 = \frac{\epsilon}{en_oD}\int_{E_o}^{E}(v - v_o)\,dE. \tag{11}$$

With this known $n$ vs $E$, the shape of the domain can be calculated using the integral of (8), i.e.,

$$\xi = \xi_o + \frac{\epsilon}{e}\int_{E_d}^{E}\frac{dE}{n - n_o},$$

where $\xi_o$ indicates the position of $E_d$.

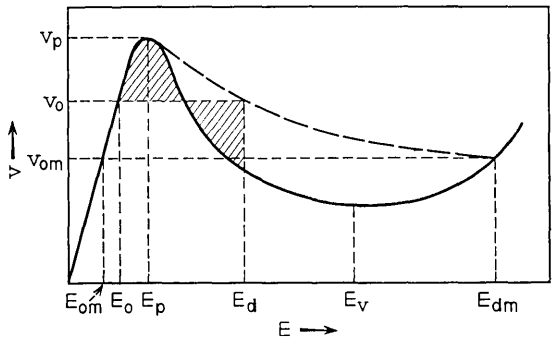


Fig. 5 — The broken line shows the domain velocity vs peak field.

If the diffusion constant is small, the right-hand side of (11) becomes large; hence, $n \gg n_o$ over most part of the trailing edge and $n \cong 0$ over most part of the leading edge. As a result, the trailing edge becomes considerably shorter than the leading edge.

The integral defined by

$$V_{ex} = \int_{\text{domain}} (E - E_o)\, d\xi$$

is called the domain excess voltage.[6] This amount of voltage is necessary to support the domain in addition to the voltage drop in the bulk given by $E_o l$, where $l$ is the sample length. $V_{ex}$ is a function of $E_o$. When $E_o$ is close to $E_p$, $E_d$ is also close to $E_p$, the domain is small and $V_{ex}$ is small. As $E_o$ decreases, $E_d$ increases as we saw in Fig. 5 and $V_{ex}$ increases. The highest field in the domain is limited by $E_{dm}$. However, $V_{ex}$ can increase without limit by increasing the domain width. For $E_o$ below $E_{om}$, there is no steady-state domain. As a result, $V_{ex}$ as a function of $E_o$ should look like the solid line in Fig. 6. The detailed shape changes with $n_o$. In general, for a given $E_o$, $V_{ex}$ decreases with increasing doping.

Now, suppose we apply voltage $V$ to a device with length $l$. Let us draw a straight line through $(o, V)$ and $(V/l, o)$ in Fig. 6, as shown by the broken line and let $P$ be the intersection with the $V_{ex}$ curve. Since $V - V_{ex}$ is exactly equal to $E_o l$ for $P$, the terminal voltage becomes $V$ if a domain determined by $P$ exists in the device. Suppose somehow $V_{ex}$ becomes higher than the value given by $P$. Then, for the steady state, $E_o l$ becomes smaller but not enough to compensate

the increase in $V_{ex}$; hence, $V_{ex}$ has to decrease. Similarly, when $V_{ex}$ decreases, it has to return to $P$ to satisfy the terminal voltage condition. Consequently, $P$ represents the stable operating point. Thus, Fig. 6 can conveniently be utilized to determine $V_{ex}$ and $E_o$ of the steady-state domain. Note that if the applied voltage is high, $V_{ex}$ is correspondingly high and $E_o$ becomes almost equal to $E_{om}$. Then, the current density $en_ov(E_o)$ becomes almost constant regardless of a small variation in the applied voltage. Such a domain is called a saturated domain.

When $V/l$ is slightly smaller than $E_p$ but $V$ is large, there exists two intersections between the solid and broken lines in Fig. 6. In this case, the field in the absence of a domain is smaller than $E_p$ and no domain will be nucleated. However, if a domain exists, it can continue to travel without collapsing. Of these two intersections, only the one which corresponds to the smaller $E_o$ represents the stable operating points. For the other intersection, if $V_{ex}$ increases slightly, $E_ol$ decreases more than enough to compensate the increase in $V_{ex}$; hence, $V_{ex}$ has to increase further until the stable operating point is reached. Similarly, if $V_{ex}$ initially decreases, the domain will disappear. Suppose that the broken line is momentarily raised up to launch a domain by applying additional voltage to the terminal. As the additional voltage decreases, the intersection moves down and reaches the stable operating point without ambiguity. $E_pl$ is called the threshold voltage since it is necessary to launch a domain.

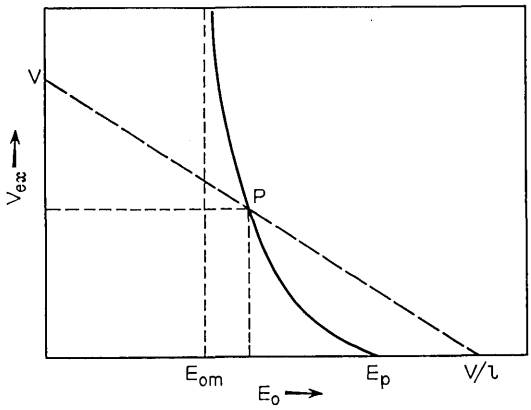


Fig. 6 — Domain excess voltage vs the outside field.

## IV. TRANSIENT BEHAVIOR OF DOMAINS

Now, suppose that we apply a certain voltage higher than $E_p l$ to a device increasing from zero value. Since the field reaches the threshold value $E_p$ first near the cathode because of high resistive layer or inhomogeneity generally existing there, a disturbance grows into a high-field domain near the cathode and travels toward the anode. As the disturbance grows, the cathode current decreases until it reaches $J \times S = en_o v(E_o)S$, where $E_o$ is determined from Fig. 6 and $S$ is the cross-sectional area of the device. This current is maintained until the high-field domain reaches the anode. As the domain disappears into the anode, the field $E$ in the device and hence the current increases to keep the terminal voltage constant. When the field near the cathode reaches the threshold value again, another disturbance grows into a high field domain and the whole process repeats. As a result, the cathode current like that in Fig. 7 is obtained. The height of the peak current is determined by $en_o v(E_p)S$ plus the displacement current due to the rapid change in $E$. The displacement current initially increases as $V_{ex}$ increases. However, the peak current tends to saturate with further increasing $V_{ex}$. Also note that for a given $V_{ex}$ the longer sample gives less displacement current. Similar displacement current exists during the decrease of the current and it may show up as the overshoot of decreasing current.

To get a high-field domain, some initial disturbance in the field distribution is necessary. This may well be due to noise, if the field is increased very slowly. However, in most cases the following process is considered to dominate. Suppose there is a region where the donor density is slightly lower than elsewhere. For each value of the field strength well outside the region, there is a corresponding steady state

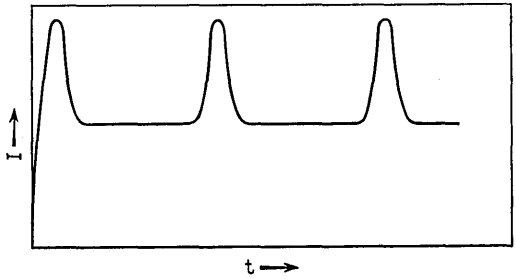


Fig. 7 — Cathode current of bulk semiconductor oscillator.

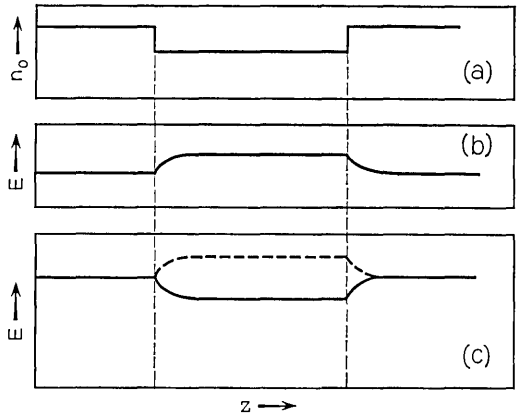


Fig. 8 — Origin of small disturbance in the field distribution.

field distribution. Except for some deviations near the ends of the region, the inside field $E_i$ should be related to the outside field $E_o$ through

$$n_{oi}v(E_i) = n_{oo}v(E_o),$$

where $n_{oi}$ is the donor density in the region and $n_{oo}$ outside the region.* Therefore, the field should look like the solid lines in Fig. 8(b) or (c) depending on whether it is in the positive or negative resistance range, respectively. However, if we change the outside field quickly, from the positive to negative range, since the displacement current has to be approximately equal everywhere and since the inside change is smaller than the outside, the inside field will overshoot the steady-state value as shown by the broken line in Fig. 8(c). As a result, a definite discrepancy from the steady-state value takes place which grows into a high-field domain. In practice, there may be a number

* In this case, corresponding to (4), we have

$$\frac{d}{dt}\int_{z_1}^{z_2} (E - E_o)\, dz = \int_{z_1}^{z_2} \frac{e}{\epsilon} \{n_{oo}v(E_o) - n_o v(E)\}\, dz,$$

which is equivalent to

$$\frac{d}{dt}\int_{z_1}^{z_2} (E - E_s)\, dz = \int_{z_1}^{z_2} \frac{en_o}{\epsilon} \{v(E_s) - v(E)\}\, dz,$$

where $E_s$ indicates the steady-state field. Since this is identical to (4) except that $E_0$ is replaced by $E_s$, no major modification is required in our discussion of growth rate if $V_{cx}$ is redefined by the integral on the left-hand side.

of such nucleating sites. However, only one domain will be fully grown since two steady-state domains cannot exist at a time as we shall discuss shortly.

So far, we have studied the case where the terminal voltage is kept constant. Next, let us consider the case with a constant current source. When we gradually increase the current from zero, except in the vicinity of the cathode, the electron velocity in the device follows the $v(E)$ vs $E$ curve in Fig. 1 until it reaches $v(E_p)$. If we increase the current further and if the sample does not burn out, $E$ probably jumps to a high value where $v(E)$ is equal to $v(E_p)$ and then follows the $v(E)$ vs $E$ curve as before. If we decrease the current, the electron velocity follows the curve until it reaches $v(E_v)$ and then $E$ jumps to a low value where $v(E) = v(E_v)$. There is hysteresis. However, during this process, the field is almost everywhere in the positive resistance range and the device is stable. Now, suppose somehow a high-field domain is already present. If the source happens to supply the same current as the steady-state domain requires, it will continue to travel. However, if the supply current is slightly different, say, larger than the domain current, the electron density increases at the trailing edge and decreases at the leading edge of the domain. As a result, $V_{ex}$ increases. However, the larger the $V_{ex}$ is the smaller the steady-state current becomes. Therefore, no steady state can be achieved. A similar argument holds for the case where the supply current is smaller than the domain current. In this case, $V_{ex}$ decreases to zero. To consider the same problem from a different angle, let us draw a line representing the constant current condition in Fig. 6. It becomes a vertical line. The possible intersection with the $V_{ex}$ curve gives an instable operating point which we discussed before. Thus, with a constant current source, a high-field domain is instable. The reason why two steady-state domains cannot exist simultaneously in a device can be seen in a similar manner. If one of them requires a larger current than the other, $V_{ex}$ of the second one increases. As a result, the first one quickly disappears and all the excess voltage is absorbed by the second one requiring less current. We shall have more to say about this later.

Next, let us consider the situation where no high-field domain exists but the field is in the negative resistance range over a certain length of the device. Suppose a small disturbance exists inside the region. In this case $E_o$ is fixed but (6) still shows that the initial disturbance grows with time with the time constant given by (7). As a result, the terminal voltage should fluctuate considerably.

In many cases, it is desirable to estimate how quickly domains

can grow or decay. The starting point is (4). If the diffusion constant is small, the trailing edge is considerably shorter than the leading edge; hence, the primary contribution to the integral comes from the leading edge. Since $n \cong 0$ over the leading edge, we have

$$\int_{z_1}^{z_2} \frac{n_o e}{\epsilon} \{v(E_o) - v(E)\}\, dz \cong \int_{E_o}^{E_d} \{v(E_o) - v(E)\}\, dE,$$

where use is made of (1). Substituting the above results into (4) we obtain

$$\frac{dV_{ex}}{dt} \cong \int_{E_o}^{E_d} \{v(E_o) - v(E)\}\, dE. \tag{12}$$

For the steady state, $dV_{ex}/dt = 0$ and (12) reduces to the equal areas rule discussed before. It is now obvious that if we draw a figure similar to Fig. 5 and if the lower-right shaded area is larger or smaller than the upper shaded area, the domain grows or decays, respectively. As the difference becomes larger, the rate of change of the domain size increases. It is also obvious why a domain is instable under a constant current condition. Since $E_o$ is fixed if $E_d$ increases slightly from the steady-state value, $V_{ex}$ increases and hence $E_d$ further increases and no steady state is reached.

When $E_d - E_o$ is small, using (5), (12) becomes

$$\frac{dV_{ex}}{dt} = \int_{E_o}^{E_d} \left(-\frac{dv}{dE}\right)(E - E_o)\, dE = \left(-\frac{dv}{dE}\right)\tfrac{1}{2}(E_d - E_o)^2. \tag{13}$$

However, if we assume that the leading edge $w$ is depleted, by integrating (1) twice, we have

$$\tfrac{1}{2}(E_d - E_o)^2 = \frac{1}{2}\left(\frac{n_o w}{\epsilon} e\right)^2 = \frac{n_o e}{\epsilon}\left(\frac{1}{2}\frac{n_o e}{\epsilon} w^2\right) \cong \frac{n_o e}{\epsilon} V_{ex}. \tag{14}$$

Substituting (14) into (13), we obtain

$$\frac{dV_{ex}}{dt} \cong \left(-\frac{dv}{dE}\right)\frac{n_o e}{\epsilon} V_{ex}$$

which gives the same answer as (6). Therefore, provided that $E_d$ is calculated from $V_{ex}$ through (14), the simple formula (12) is also applicable for small disturbances whose electron density distribution is quite different from the one assumed in the derivation.

Now suppose that there are two regions in a device where the donor density is slightly lower than elsewhere. If the terminal voltage is increased to a certain value to bring the field into the negative resistance range, the field disturbances at these two regions start to grow exponentially and at the same time the field $E_o$ outside the disturbances

decreases to compensate the increase of the field in the disturbances. After a while the disturbances become large enough so that we can call them domains. The domain from the larger nucleation site of the two is larger than the other but both continue to grow until $E_o$ reaches a point where the right-hand side of (12) becomes zero for the smaller domain. Then, the smaller domain stops growing and starts to decay because the larger one continues its growth. As a result, the smaller domain will finally disappear and the one from the larger nucleation site remains. However, suppose that the difference in size between the nucleation sites is small. Then, when the smaller domain stops growing, the right-hand side of (12) for the larger one is also small; hence, some time elapses before the larger one absorbs the excess voltage from the smaller one. If the larger domain is on the anode side of the smaller one, it may reach the anode before the absorption is completed. If this happens, the smaller domain starts to grow again as the larger one disappears into the anode. As a result, if there are several nucleation sites of comparable size in a device, one period is not completed until the largest remaining domain becomes smaller than the initial disturbance the largest nucleation site can give.

Summarizing the above discussion, we list some of the important properties of a domain as follows:

(*i*) A high-field domain is nucleated when the field reaches the negative resistance range from the lower side of the $v$ vs $E$ characteristic.

(*ii*) With a constant voltage source, the domain reaches a steady state. However, with a constant current source, no steady-state domain is realized.

(*iii*) The steady-state domain velocity is equal to the electron drift velocity outside the domain.

(*iv*) For a given terminal voltage, the domain excess voltage and the outside field can be determined from Fig. 6.

(*v*) The transient behavior of a domain can be approximately determined by (12).

In the above discussion, the diffusion constant was assumed to be independent of the field. However, many theoretical studies indicate that it is a function of $E$. In that case, the equal areas rule no longer holds and the domain velocity may not be equal to the electron velocity.* Furthermore, an inhomogeneity in the material may create

* If $D\partial n/\partial z$ is replaced by $\partial/\partial z\ (Dn)$ in (2), (4) follows even when $D$ is a function of $E$. Therefore, (12) is considered to be a valid approximation as long as the magnitude of $D$ is small.

an extremely high but localized field within the bulk which ionizes deep donors or even generates hole-electron pairs. Then, the effective $n_o$ becomes larger and $V_{ex}$ lower. However, the following discussions will not be affected.

## V. PULSE CIRCUITS

Let us consider the $I$-$V$ characteristic of a device with the possible presence of a domain. Since for each $I$, the terminal voltage is equal to $V_{ex}$ plus the voltage drop in the device, it should look like Fig. 9. There is hysteresis, but otherwise the curve is very similar to the $I$-$V$ characteristic of a tunnel diode. Therefore, many pulse circuits developed in connection with tunnel diodes are also applicable with the present devices; e.g., relaxation oscillator, monostable circuit and pulse inverter. The main difference is that once a domain is launched, it determines the device current rather than the external circuits and after a while the domain disappears at the anode.

## VI. VARIABLE FREQUENCY OSCILLATOR[7]

Suppose the device has the form of a trapezoid as shown in Fig. 10. If the taper is gradual, high-field domains are expected to have similar properties to one in a uniform device. Therefore, assuming that the relation between the domain excess voltage and the field immediately outside the domain is given by Fig. 6, let us consider how to obtain the outside field as a function of the domain position. First assume

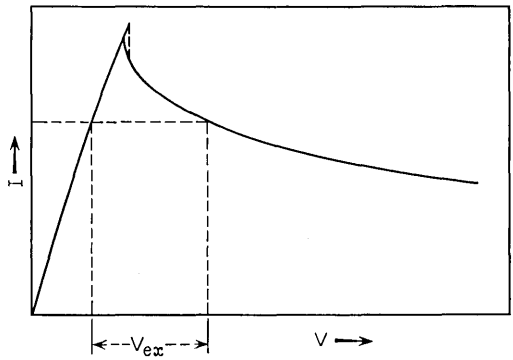


Fig. 9 — $I$-$V$ characteristic of a uniform device.

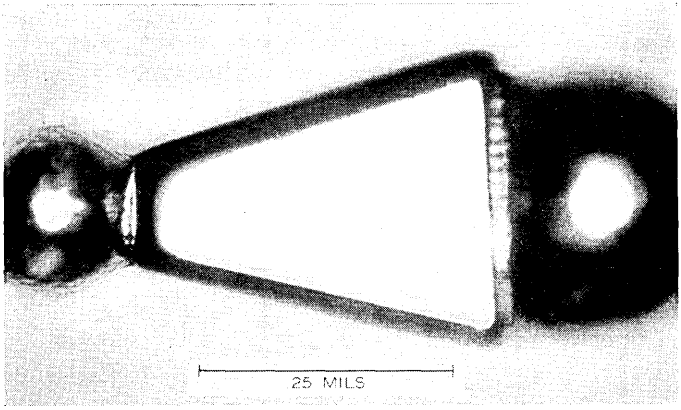


Fig. 10 — An example of trapezoidal oscillators.

that the outside field is $E_o$ when the domain is located at $z = \xi$. The conduction current is given by $env(E_o)S(\xi)$. Neglecting the diffusion and displacement currents outside the domain, the field at arbitrary $z$ except the domain location can be determined from Fig. 1, utilizing

$$I = env(E_o)S(\xi) = env(E)S(z).$$

Once the field is determined as a function of $z$, the area under it plus $V_{ex}(E_o)$ gives the terminal voltage. Keeping this in mind, draw a family of field curves with the terminal current as a parameter as shown in Fig. 11. The highest field curve needed corresponds to $I = env(E_p)S(0)$ and is called the threshold line and the area under it the threshold voltage $V_{th}$. Calculate the area under each curve and add $V_{ex}$ for each point on the $E - z$ plane to obtain the terminal voltage $V$. From this, we obtain a family of constant terminal voltage contours as shown in Fig. 12. Note that a straight line $E = E_{om}$ corresponds to $V = \infty$. Also note that there is no contour crossing the vertical axis above a certain value $E_c$ which is determined as follows. On the $V_{ex}$ vs $E_o$ plane draw a curve representing the area between the threshold line and various field curves as a function of the field at the cathode. This curve intersects the $E$ axis as well as the $V_{ex}$ curve at $E_p$. The other intersection with $V_{ex}$, if any, gives $E_c$ as shown in Fig. 13. Suppose we apply a certain terminal voltage slightly larger than $V_{th}$ and a domain starts to form at the cathode. Then, the field inside the device drops. But if it is higher than $E_c$ at the cathode, the decrease of the area exceeds the corresponding $V_{ex}$; hence, the domain

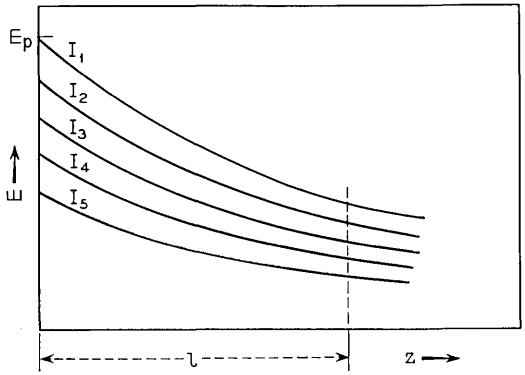


Fig. 11 — Field curves in a tapered device.

further grows until it becomes $E_c$. If the device length is sufficiently short, $E_c$ may not exist depending on the shape of $V_{ex}$ vs $E_o$.

As the domain travels toward the anode, the field immediately outside the domain follows one of the constant voltage contours in Fig. 12. When the contour intersects the threshold line, the field at the cathode reaches the threshold value $E_p$ and a new domain starts to nucleate. Since the new domain in the narrow region grows according to the unequal areas rule given by (12), the old one in the wider region quickly decays and a new period begins. However, the cathode current does not decrease as quickly as in a uniform device since the old domain tends to keep the cathode field up as it decays. Some contours passing through the vicinity of $E_c$ may turn back before they cross the threshold line. In such a case, at the turning point, the terminal

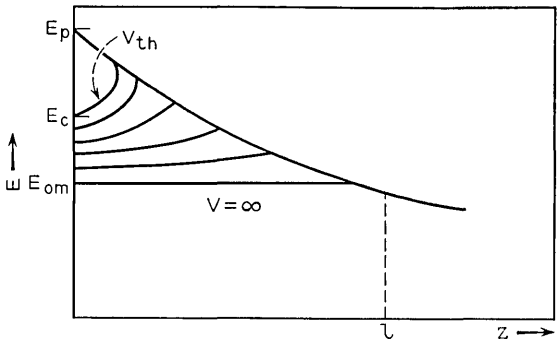


Fig. 12 — Constant terminal voltage contours.

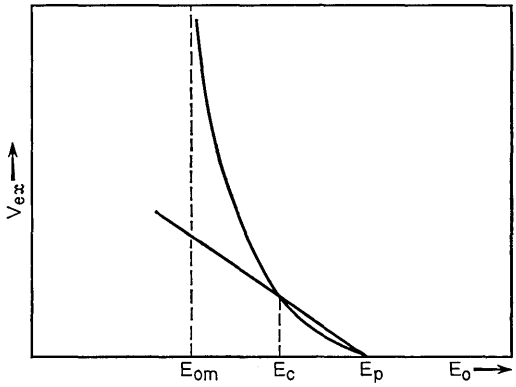


Fig. 13 — Explanation for the method to obtain $E_c$.

voltage becomes insufficient to support the domain due to the voltage drop in the bulk. The domain quickly decays and the field rises to the threshold line to start a new period as before. Note that the maximum current at the end of a period is approximately $env(E_p)S(0)$ regardless of the terminal voltage. In general, as the terminal voltage increases, the turning point or the intersection is further away from the cathode and the domain velocity becomes slower. As a result, the period gets longer. This effect gives a voltage-controlled variable frequency oscillation as shown in Fig. 14. If the straight line $E = E_{om}$ intersects the threshold line within the device, no matter how large terminal voltage is (of course within a certain limit), the domain cannot reach the anode. On the other hand, if the intersection is outside the device, the domain can reach the anode generating a pulse similar to the one shown in Fig. 7 at the end of a period.

## VII. CURRENT WAVEFORM GENERATORS[8]

For a saturated domain, the velocity is constant and the current density at the domain is constant. If the cross-sectional area of the device varies with the distance from the cathode, the cathode current also varies as the domain moves along the sample since it is proportional to the current density times the area. Provided that the variation of the cross section is gradual, the current waveform should become an exact replica of the shape of the device excluding the pulse corresponding to the domain disappearance at the anode. In order to start the domain at or near the cathode, the field there should

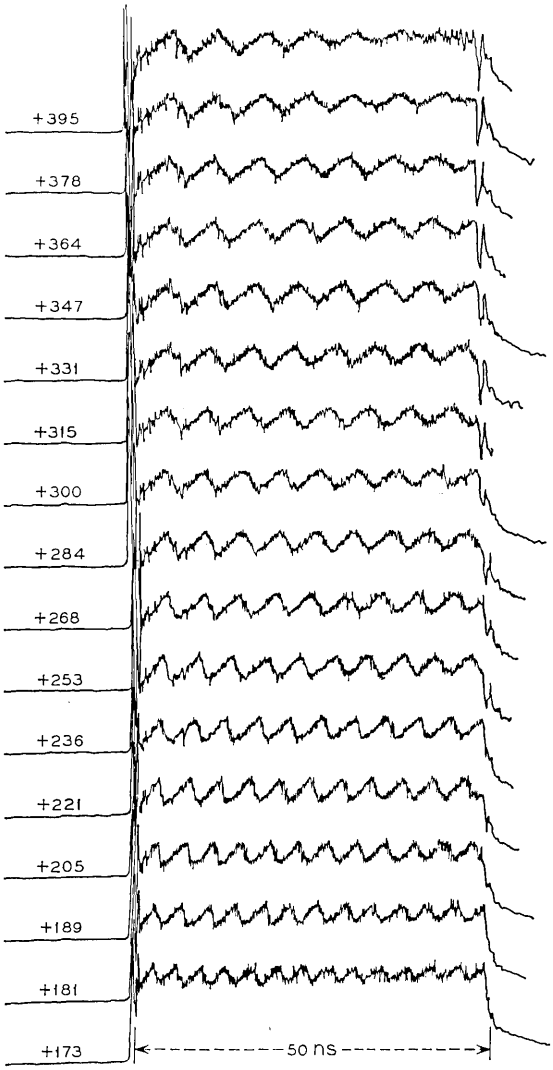


Fig. 14 — Variable frequency oscillation of a trapezoidal oscillator. The supply voltages are indicated on the left-hand side.

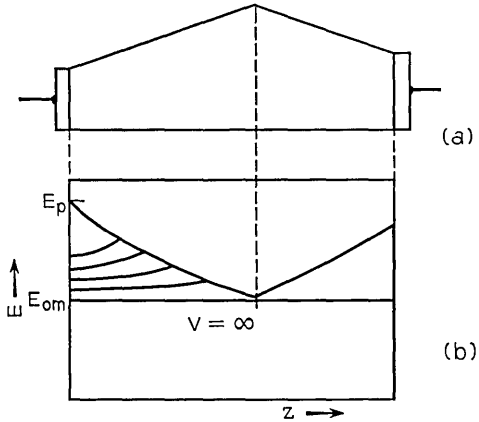


Fig. 15 — Explanation for the sudden change in frequency observed in certain nonuniform devices.

reach $E_p$ before it does elsewhere. This limits the smallest cross-sectional area we can make. In some cases because of the high resistivity layer at the cathode, this minimum can be about 80 percent of the cathode cross section. In order to let the domain arrive at the anode, the threshold field line should never be lower than $E_{om}$ anywhere in the device. This limits the largest cross-sectional area we can make. However, letting the threshold line cross the $E_{om}$ limit, the pulse due to the domain disappearance at the anode can be eliminated. In some waveform generators, the frequency of oscillation suddenly increases as we decrease the terminal voltage. For instance, the constant terminal voltage contours for the device shown in Fig. 15(a) should look like Fig. 15(b). Therefore, if the terminal voltage is reduced slightly, the domain travels only halfway through and the frequency rises approximately one octave as shown in Fig. 16.

## VIII. DOMAIN BYPASSING[9]

So far, we have considered the shaping of an active bulk region. However, a similar effect can be obtained by changing the doping density. In addition to this, there is an interesting method of getting similar or more versatile functions by means of bypass circuits. To explain the principle, let us consider the simplest case illustrated in Fig. 17. There are two additional ohmic contacts attached to the active bulk region. Let $D_1$ be the part between the cathode and the first

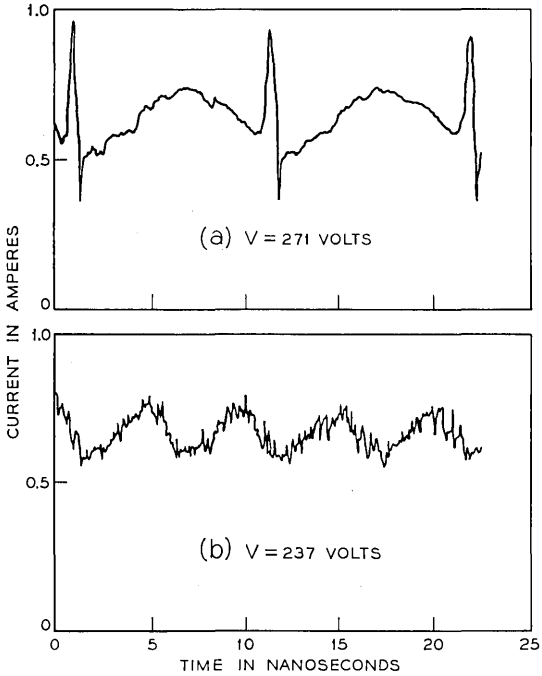


Fig. 16 — Current waveforms observed with a device illustrated in Fig. 15.

contact, $D_2$ between two contacts, and $D_3$ the remainder. Let $d$ indicate the length of $D_2$ and $h$ the device thickness. If a saturated domain is in $D_1$, the cathode current is given by $en_ov(E_{om})S$. When the domain moves into $D_2$, the current becomes approximately $en_ov(E_{om})S + (V_{ex}+E_{om}d)/R$, where $R$ is the resistance of the interconnection between the additional contacts. Finally, when the domain gets into $D_3$, the current returns to $en_ov(E_{om})S$ again. Therefore, the cathode current should look like Fig. 18(a). In addition to regular pulses,

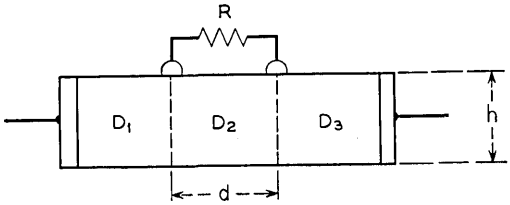


Fig. 17 — Domain bypassing scheme.

there are broad pulses corresponding to $(V_{ex}+E_{om}d)/R$. Now, suppose the interconnection is open circuited, then the additional pulses disappear as shown in Fig. 18(b). Thus, we get a means of controlling the waveform from the outside. The height of the additional pulses, however, cannot be made higher than the regular pulses. If we try to get higher pulses by decreasing $R$, the field at the cathode reaches the threshold value making a new domain nucleate there and the old one in $D_2$ disappear. The sharpness of the pulse edge is limited probably due to the spreading resistance of the contacts. As the thickness $h$ of the bulk gets thinner, the definition is expected to improve.

There are many variations of the above scheme. By providing several contacts and interconnecting them through appropriate networks, various waveforms can be realized. Alternatively, contacting a relatively large electrode through a high resistive layer on one side of the active region and shaping the electrode, again produces various waveforms. Another interesting possible application is a photosenser. Suppose $R$ is photosensitive. Then, the height of the additional pulses varies with illumination. If many such photoelements are lined up along a relatively long device, the domain provides automatic scanning action. A solid-state videcon might be a possibility, if a two-dimensional array of photoelements is made by placing many such devices side by side and the domain in each device is triggered by the pulse in the adjacent device.

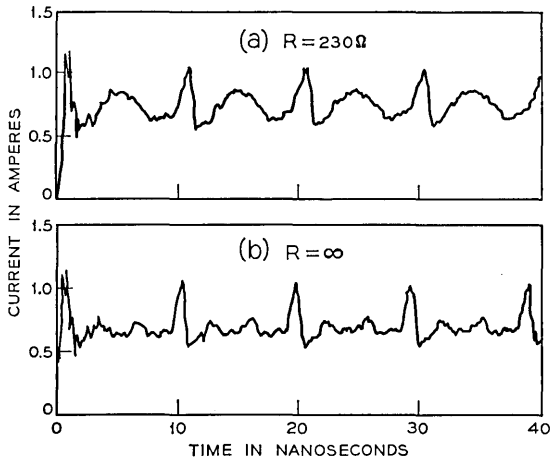


Fig. 18 — Waveforms observed with a device illustrated in Fig. 17.

## IX. NUMERICAL EXAMPLES

The domain velocity for GaAs is approximately $10^7$ cm/sec. If the device length is 1 mm, 100 $\mu$, or 10 $\mu$, the oscillation frequency is about 100 MHz, 1 GHz, or 10 GHz, respectively. The terminal voltage necessary to launch a domain in a uniform device is $E_p l$. Since $E_p$ is approximately 3000 V/cm, 300 volts are required for 100 MHz samples, 30 volts for 1 GHz samples, and 3 volts for 10 GHz samples. The current is given by $env(E)S$. If $S = 0.3 \times 0.3$ mm$^2$ and $n_o = 5 \times 10^{14}$/cm$^3$

$$I = env(E)S = 1.6 \times 10^{-19} \times 5 \times 10^{20} \times 10^5 \times 0.9 \times 10^{-7} = 0.7\text{A}.$$

The peak current is about twice this value.

The domain thickness is a function of doping as well as $V_{ex}$. For simplicity, let us assume that the diffusion constant is small and hence the thickness is approximately given by $w$. Then, as we calculated in (14),

$$w = \sqrt{\frac{2V_{ex}\epsilon}{en_o}}.$$

For $V_{ex} = 50$ volts and $n_o = 5 \times 10^{14}$/cm$^3$, since $\epsilon \cong 12.5 \times 8.85 \times 10^{-12}$ $F/m$ for GaAs

$$w = \sqrt{\frac{2 \times 50 \times 12.5 \times 8.85 \times 10^{-12}}{1.6 \times 10^{-19} \times 5 \times 10^{20}}} = 12 \times 10^{-6}\text{m}$$

or $w = 12$ $\mu$. For larger $n_o$, $w$ becomes smaller.

The time constant of the initial growth of disturbances depends on the value of $|dv/dE|$. There are many theories and experiments suggesting various values ranging from 300 to 10,000 cm$^2$/secV. This fact alone may well indicate how little we know about GaAs. For the moment, let us assume 3000 cm$^2$/secV. Then,

$$|\tau| = \left| \frac{\epsilon}{en_o \dfrac{dv}{dE}} \right| = \frac{12.5 \times 8.85 \times 10^{-12}}{1.6 \times 10^{-19} \times 5 \times 10^{20} \times 0.3} \cong 4.5\text{ps}.$$

This is the time for a small disturbance to become about 2.7 times the original size. If this rate continues, the size becomes 1000 times within 32 ps and more than 100,000 times within 50 ps. In comparison, the time for a domain to disappear after its leading edge reaches the anode is of the order of $w/v$. For a domain 12 $\mu$ long, it is of the order of 120 ps.

If there is a region extending out a length $b$ where the doping is reduced $\alpha$ percent, the initial size of the disturbance can be shown from Fig. 8 to be about $2E_p b\alpha \times 0.01$. For 10 percent inhomogeneity and $b = 5\ \mu$, we have

$$2 \times 300{,}000 \times 5 \times 10^{-6} \times 0.1 = 30 \times 10^{-2} \text{ volts.}$$

The corresponding $(E_d - E_o)$ calculated through (14) is given by

$$(E_d - E_o) = \sqrt{\frac{2n_o e}{\epsilon} V_{ex}} = 6.5 \times 10^3 \text{ V/cm}$$

when $n_o = 5 \times 10^{14}/\text{cm}^3$. This is large and we have to use (12) for the growth rate calculation. For simplicity, let us consider the fastest possible growth. From the area consideration, Fig. 5 shows that the fastest growth takes place when $E_o$ is fixed at $E_p$. Then, the integral in (12) can be roughly approximated by $(E_d - E_p)\ \{v(E_p) - v(E_v)\}$ provided that there is a broad and flat valley region. Since $E_o = E_p$,

$$E_d - E_p \cong \sqrt{\frac{2n_o e}{\epsilon} V_{ex}}\ .$$

Thus, (12) becomes

$$\frac{dV_{ex}}{dt} \cong \sqrt{\frac{2n_o e}{\epsilon} V_{ex}}\{v(E_p) - v(E_v)\}.$$

The solution is given by

$$V_{ex} = \frac{n_o e}{2\epsilon}\{v(E_p) - v(E_v)\}^2 (t + c)^2,$$

where $c$ is a constant determined by the initial value of $V_{ex}$. If $V_{ex}$ is small at $t = 0$, $c$ can be neglected. For GaAs, $v(E_p) - v(E_v) \cong 10^7$ cm/sec and if $n_o = 5 \times 10^{14}/cm^3$ the above expression gives

$$V_{ex} = 3.6 \times 10^{21}(t + c)^2.$$

Since $V_{ex} \cong 0.3$ volts at $t = 0$, $c$ is approximately 9 ps. $V_{ex}$ becomes approximately 36 volts when $t + c = 100$ ps or $t = 91$ ps. If the terminal voltage increases slower than the above rate, $E_o$ decreases and the growth of $V_{ex}$ closely follows the terminal voltage. On the other hand if the terminal voltage increases faster, then $E_o$ has to increase to accommodate the balance of the voltage since the growth rate of $V_{ex}$ is no longer able to follow the applied voltage.

Finally, suppose that a steady-state domain exists and the terminal voltage is suddenly decreased so that $E_o$ is decreased by $\beta$ percent.

In this case, the right-hand side of (12) is approximated by

$$-0.01\beta E_o \frac{dv(E_o)}{dE} \times (E_d - E_o) \cong -0.01\beta E_o \frac{dv(E_o)}{dE} \sqrt{\frac{2n_o e}{\epsilon} V_{ex}} .$$

For $V_{ex} = 50$ V, $n_o = 5 \times 10^{14}/\text{cm}^3$, $dv(E_o)/dE \cong 6000$ cm$^2$/V, $\beta =$ 10 percent and $E_o = 1500$ V/cm, we have

$$\frac{dV_{ex}}{dt} = -0.1 \times 150{,}000 \times 0.6$$

$$\times \sqrt{\frac{2 \times 5 \times 10^{20} \times 1.6 \times 10^{-19}}{12.5 \times 8.85 \times 10^{-12}}} 50 \cong -7.6 \times 10^{10} \text{ V/sec.}$$

## X. ACKNOWLEDGMENTS

Most of the explanations are the outcome of the discussion with M. Shoji. The patience with which he discussed these matters with the author is highly appreciated. The author wishes to thank M. R. Barber for many fruitful discussions as well as for constructive suggestions and comments on the manuscript. Acknowledgments are also due to R. S. Engelbrecht and M. Uenohara for their support to this work.

## REFERENCES

1. Ridley, B. K., Specific Negative Resistance in Solids, Proc. Phys. Soc., *82,* 1963, pp. 954–966.
2. Haydl, W. H. and Quate, C. F., High Field Domain in Cadmium Sulfide, Phys. Letters, *20,* No. 5, March 15, 1966, pp. 463–464.
3. Hilsum, C., Transferred Electron Amplifiers and Oscillators, Proc. IRE, *50,* No. 2, February, 1962, pp. 185–189.
4. McCumber, D. E. and Chynoweth, A. G., Theory of Negative Conductance Amplification and of Gunn Instabilities in "Two-Valley" Semiconductors, IEEE Trans. Electron Devices, *ED-13,* No. 1, January, 1966, pp. 4–21.
5. Butcher, P. N., Fawcett, W., and Hilsum, C., A Simple Analysis of Stable Domain Propagation in the Gunn Effect, Brit. J. Appl. Phys., *17,* 1966, pp. 841–850.
6. Copeland, J. A., Stable Space-Charge Layers in Two-Valley Semiconductors, J. Appl. Phys., *37,* No. 8, August, 1966. pp. 3602–3609.
7. Shoji, M., A Voltage Tunable Gunn-Effect Oscillator, Proc. IEEE, *55,* No. 1, January, 1967, pp. 130–131.
8. Shoji, M., Bulk Semiconductor High-Speed Current Waveform Generator, Proc. IEEE, Corres., *55,* No. 5, May, 1967, pp. 720–721.
9. Shoji, M., Controlled Bulk-Semiconductor Current Pulse Generator, Proc. IEEE, Corres., *55,* No. 5, May, 1967, pp. 710–711.

# A Millimeter Wave, Two-Pole, Circular-Electric Mode, Channel-Dropping Filter Structure

By R. D. STANDLEY

(Manuscript received May 19, 1967)

*Interest in circular-electric mode channel-dropping filters has been stimulated by recent advances in the repeater art. This paper presents the theory and establishes design procedures for filters having two-pole maximally flat response functions. The basic structure uses mode-conversion resonators, i.e., the resonating mode is the $TE_{02}$ circular electric mode, for three of the resonators. The rejection filter portion of the structure is conventional in that two resonators separated by an odd multiple of $\pi/2$ radians realize the desired characteristic. The branching filter is novel in that a rectangular waveguide is wrapped around a mode-conversion resonator and coupled to the $TE_{02}$ resonating mode via a multiplicity of apertures. The rectangular guide is then resonated to permit realization of the two-pole branching filter. The theory developed is an extension of Marcatili's original work on mode-conversion resonators. The mode-conversion resonator parameters are related to the elements of a lumped constant prototype network thus extending the utility of mode-conversion resonators.*

*Experimental results are presented on several filter models. The agreement between theory and experiment is generally good. Four filters were developed for use in an all solid-state repeater experiment with successful results.*

## I. INTRODUCTION

The $TE_{01}$ circular-electric mode in round waveguide has received considerable attention due to its low-loss characteristic. The problem of multiplexing in communication systems using this mode was first approached by Marcatili.[1] His scheme used low-loss, $TE_{02}$ circular-

electric mode resonators* to realize channel-dropping filters having single-pole, maximally flat responses. Interest in channel-dropping filters with multiple-pole responses was stimulated by recent advances in the repeater art. An all solid-state repeater having a 51.7 GHz carrier and operating at a bit rate of 306 megabits per second has been constructed.[2] The repeater performance is such that a 15-mile repeater spacing could be achieved using propagation in the $TE_{01}$ circular-electric mode in two-inch i.d. round guide. Since high bit rates imply increased bandwidth, multiple-pole filters are required to maximize usable channel capacity.

A design procedure has been developed for diplexers having a two-pole, maximally flat amplitude response. Section II describes the structure. Section III presents some preliminary considerations involving arrays of such structures. Section IV outlines the design procedure. Experimental results are presented in Section V.

The major theoretical contribution of this work lies in relating the parameters of the structure to the elements of a low-pass prototype network. This extension of Marcatili's work makes it possible to utilize mode-conversion resonators in multiple-pole filter structures. The analysis is summarized in Appendix A.

The novelty in the physical structure lies primarily in the realization of the branching filter. (See Fig. 1.) A mode conversion resonator

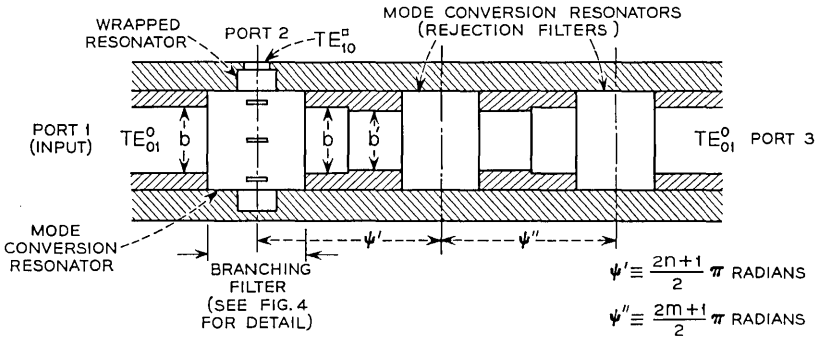


Fig. 1 — Cross section view of two pole diplexer structure.

is coupled to a wrapped rectangular waveguide to permit realization of a two-pole system. The rejection resonator portion of the structure is conventional in that two resonators separated by an odd multiple of $\pi/2$ radians is utilized to realize the two-pole characteristic.

* Throughout this paper, the $TE_{02}$ mode resonators will be referred to as mode conversion resonators.

## II. TWO-POLE FILTER STRUCTURE AND PROTOTYPE EQUIVALENT CIRCUIT

Fig. 1 shows the physical structure and identifies the resonant elements. The input and output guides are above cutoff for the $TE_{01}$ mode and just below cutoff for the $TE_{02}$ mode. The large guide sections are just above cutoff for the $TE_{02}$ mode. The rectangular waveguide output is coupled to the mode-conversion resonator nearest the input port via a wrapped rectangular waveguide.

A qualitative description of the behavior of the structure is obtained as follows. First, consider an individual rejection resonator. A signal incident in the $TE_{01}$ mode is coupled to the $TE_{02}$ mode via a symmetrical diameter discontinuity. Since the input and output guides are below cutoff for the $TE_{02}$ mode, the power in that mode is trapped in the large diameter region. Marcatili's analysis of the structure shows that at resonance the transverse mid-plane of the resonator is effectively a short circuit.[1] The center frequency and bandwidth are dependent on the length of the resonator and the ratio of the input guide to resonator guide diameters. The details of the relationship are given by Marcatili.[1] Now, in the structure of Fig. 1, the mid-planes of adjacent mode-conversion resonators are electrically separated by odd multiples of $\pi/2$ radians. Hence, at resonance, the rejection resonator pair presents an open circuit at the mid-plane of the input mode-conversion resonator. All of the incident $TE_{01}$ mode power appears at the rectangular waveguide output when the various coupling coefficients are properly chosen.

Further insight into the electrical behavior of the structure is obtained by considering the prototype network shown in Fig. 2. The prototype network consists of complementary admittances connected in shunt. The elements of the network have been chosen to yield a two-pole, maximally flat insertion loss response between ports 1 and 2 while maintaining a constant input admittance as a function of fre-

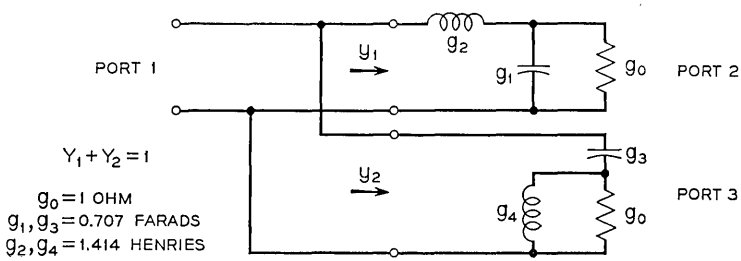


Fig. 2—Prototype network for a two-pole diplexer.

quency.[4, 5] Total power transfer occurs at zero frequency, and half-power transfer occurs at an input angular frequency of one radian per second. The prototype network is converted to a network having total power transfer at some frequency $\omega_0$ through use of the angular frequency mapping function

$$\omega' = Q_L\left(\frac{\omega}{\omega_0} - \frac{\omega_0}{\omega}\right), \tag{1}$$

where

$\omega'$ = angular frequency of the prototype network
$\omega$ = angular frequency of the desired network
$Q_L = \omega_0/(\omega_1 - \omega_2)$
$\omega_1$, $\omega_2$ = half power angular frequencies of the desired network.

The relationship between the prototype network parameters and the parameters of the structure shown in Fig. 1 are discussed in detail in Appendix A. For the purpose of obtaining a qualitative understanding of electrical behavior it is sufficient to state that the performance of the microwave structure will be identical to that of the frequency mapped prototype network subject only to the approximations involved in relating their respective parameters.

## III. PRELIMINARY CONSIDERATIONS

The general problem is to develop an array of channel-dropping filters. The use of mode-conversion resonators results in several fundamental performance limitations as described below.

First, consider the case where the input guides to all filters in the array have the same diameter. Since the input guide must be below cutoff for the $TE_{02}$ mode at the highest significant frequency, the diameter, $b$, of the input guide is restricted to

$$b < 7.016\lambda_u/\pi, \tag{2}$$

where $\lambda_u$ is the free-space wavelength at the highest significant frequency, $f_u$. At the same time, the $TE_{01}$ mode at the lowest significant frequency in the overall system must be passed requiring that

$$b > 3.832\lambda_L/\pi, \tag{3}$$

where $\lambda_L$ is the free-space wavelength at the lowest significant fre-

quency, $f_L$. Combining (2) and (3) gives

$$\Delta f < 0.8309 f_L \ , \tag{4}$$

where $\Delta f$ is the bandwidth of the filter array.

The next case to be considered is that in which successive filters have varying input guide diameters. This arrangement would permit maximization of the intrinsic $Q$'s of each of the resonators. (A short taper is required to interconnect the filters.)

Now assume that the lowest frequency channel is to be dropped first. For the first channel-dropping filter in the array to operate properly, it must be terminated in a matched impedance throughout its passband. Hence, the smallest diameter guide in the system must be above cutoff to the $TE_{01}$-mode at the lowest significant frequency to be dropped. This argument leads to the same restrictions on the overall bandwidth of the array as given by (4).

If the highest frequency channel is the first to be dropped, then the argument leading to (2) and (3) again applies resulting in the bandwidth restriction (4).

In the case of varying input guide diameters, there are other limitations on the array performance which *are* dependent on the order in which the channels are dropped. If the highest frequency channel is the first to be dropped, then the diameter discontinuities produce a small residual return loss at out-of-band frequencies over and above that produced by a conventional resonator. This is true of each successive filter in the array. The effect can become cummulative for certain filter-to-filter spacings. If the lowest frequency channel is the first to be dropped, then the discontinuities cause conversion of power from the incident $TE_{01}$-mode to the $TE_{02}$-mode which can now propagate. In addition, the bandwidth of the array is further restricted by the possibility of $TE_{03q}$ resonances in the mode-conversion resonators. This occurs when the input and output guides to a given resonator are just below cutoff for the $TE_{03}$-mode and the large diameter region is just above the $TE_{03}$-mode cutoff. The diameter discontinuity again produces mode conversion with the $TE_{03}$-mode power trapped in the resonator. The ratio of the $TE_{03}$ to $TE_{02}$-mode cutoff frequencies is

$$\frac{f_{c03}}{f_{c02}} = 1.45.$$

Hence, this problem occurs in the vicinity of 1.45 times the resonant frequency of the first filter in the array.

A more detailed analysis to select the optimum dropping order is beyond the scope of this paper. In the following, it is assumed that the above restrictions have been observed prior to establishing the design for a given filter in the array.

## IV. DESIGN PROCEDURE

The necessary design equations are derived in Appendix A. It is possible to begin with those results and design the three mode-conversion resonators as described by Marcatili. However, a sufficiently accurate and more rapid approach is to use the data obtained by C. N. Tanga[6] shown here as Fig. 3.* Equations (6), (19), and (20)

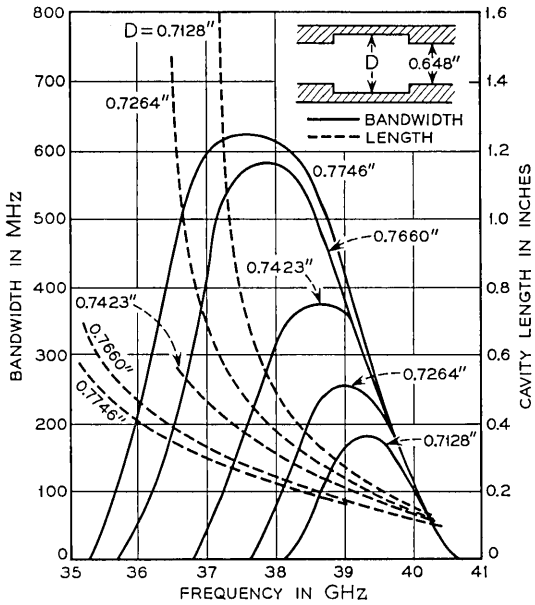


Fig. 3 — Design chart for $TE_{01}^0$ – $TE_{02}^0$ mode conversion resonators (from ref. 6).

are used to compute the required external $Q$'s of the resonators. The data shown in Fig. 3 are used to obtain a design scaled to a lower frequency. Frequency scaling techniques are applied to convert the design to the frequency of interest.

That portion of the structure of Fig. 1 consisting of the first mode-

* While the range of the parameter $D$ is somewhat restricted, the data is believed sufficient for most practical applications.

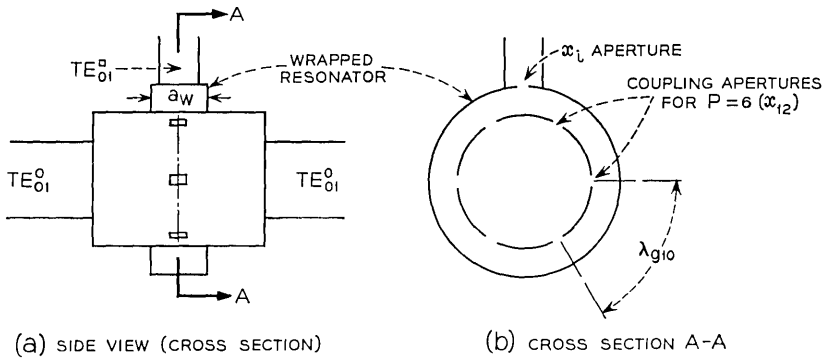


Fig. 4—Physical structure of branching filter.

conversion resonator and the wrapped resonator is defined as the branching filter. See Fig. 4. The wrapped resonator of the branching filter is designed using equations (5) and (11). The additional requirement that the coupling apertures are to be separated by one guide wavelength in the wrapped structure at resonance must also be observed. This is controlled primarily by the width, $a_w$, of the wrapped resonator and the diameter of branching-filter mode-conversion resonator established earlier. The thickness of the wall in which the coupling apertures are placed is also significant.

The coupling aperture dimensions are determined by (18) and (16). Finally, the magnitude of the normalized coupling reactance required at the output of the wrapped resonator, $(X_i/R_1)$, is determined from (10).

The lengths of the guide sections separating the mode-conversion resonators is determined so as to provide an odd multiple of 90 electrical degrees separation between resonators. The calculations required are similar to those given by Marcatili for single-pole filters.[1] Experimental work has shown that a minimum separation of 7 $\pi/2$ radians is required to avoid fringing field interaction.

Note that the two rejection resonators are not identical in that their respective input-to-output guide diameter ratio must be different. (See Appendix A.2). Three methods of realizing this result are possible:

($i$) The resonator diameters can be made the same in which case either a small step or taper is required in the diameters of the connecting lines. The small step case is indicated in Fig. 1 in exaggerated form. In practice, the difference between the diameters $b$ and $b'$ is only a few tenths of a percent.

(*ii*) The input guide diameters can be made the same in which case the resonator diameters are different.

(*iii*) Both input guide diameters and resonator diameters can be different for the two.

## V. EXPERIMENTAL RESULTS

The procedures outlined above were used to develop several channel-dropping filters. All of the filters had the physical form of Fig. 1 with six coupling apertures in the branching filter. The data of Fig. 3 was used to compute the required dimensions of all mode conversion resonators. In developing the filters, the first step was to construct the branching and rejection filters separately. The measured characteristics of the individual parts were then compared with theory through use of the transfer coefficients of Appendix B. The first model developed showed good correlation for the separate parts. However, the complete filter characteristic was found to have less than the theoretical bandwidth. Subsequent measurements indicated that the separation between branching and rejection filters ($\psi'$ of Fig. 1) was too small. This produced interaction between resonators which we believe produced the bandwidth discrepancy. It was found experimentally that a minimum separation of 7 $\pi/2$ radians was required to inhibit this interaction.

Figs. 5 and 6 show the characteristics of two other filter models. The theoretical and measured 3 dB bandwidths were, respectively, 1388 and 1210 mHz for the filter of Fig. 5 and 1130 and 1144 mHz for the filter of Fig. 6.

The filter in Fig. 5 had resonator separations of

$$\psi' = 7\pi/2$$

$$\psi'' = 5\pi/2.$$

Some interaction effects were noted between the rejection resonators. The separation $\psi''$ was increased to 7 $\pi/2$ for the filter of Fig. 6. Note that the out-of-band return loss was much improved for the latter arrangement.

The insertion loss of all filters tested was of the order of 0.5 dB at mid-band.

The finite return loss observed at the circular waveguide input port is believed to be due primarily to dimensional tolerance problems. For example, the data of Fig. 3 indicates that a mode conversion resonator having an input guide diameter of 0.493 inches and a cavity diameter of 0.579 inches should have a 400 mHz bandwidth when resonant at

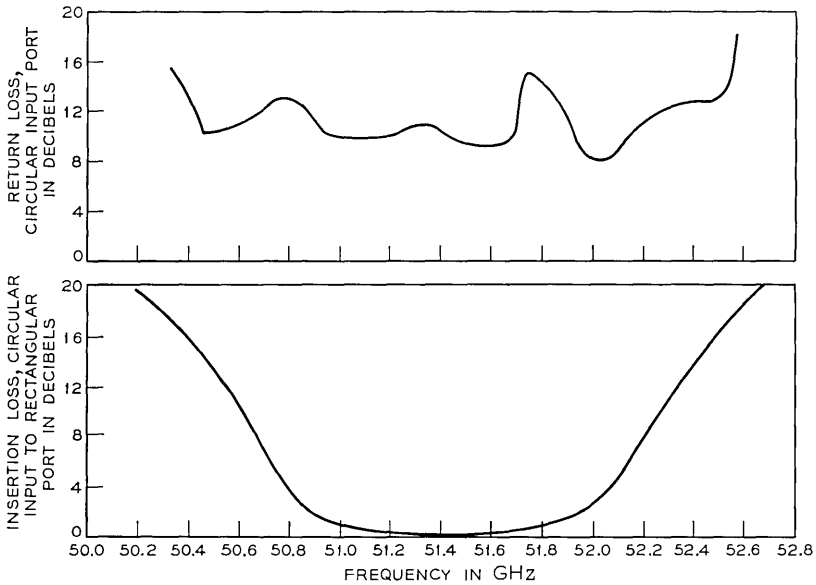


Fig. 5—Frequency response of experimental dropping filter ($\psi' = 7\pi/2$, $\psi'' = 5\pi/2$).

51.7 GHz. A one mil decrease in the input guide diameter would result in a 419 mHz bandwidth at 51.7 GHz. This rapid variation of electrical characteristics with dimensions makes precision machining absolutely necessary.

Another critical parameter was the width of the wrapped resonator. The height of the wrapped resonator for the filters described was 0.074 inch. This resulted in a variation of resonant frequency of the wrapped resonator of about 300 mHz per mil change in the resonator width. Hence, extreme care was required in machining the branching filter to obtain the desired resonant frequency.

Four filters with characteristics very nearly identical to those shown in Fig. 6 were successfully incorporated into the circuitry of the solid-state repeater described in the Introduction.[2]

## VI. CONCLUSIONS

Marcatili's original work has been extended to permit realization of two-pole channel-dropping filters using low-loss mode-conversion resonators. The theory developed relates the mode-conversion resonator parameters to those of a lumped constant prototype network. This

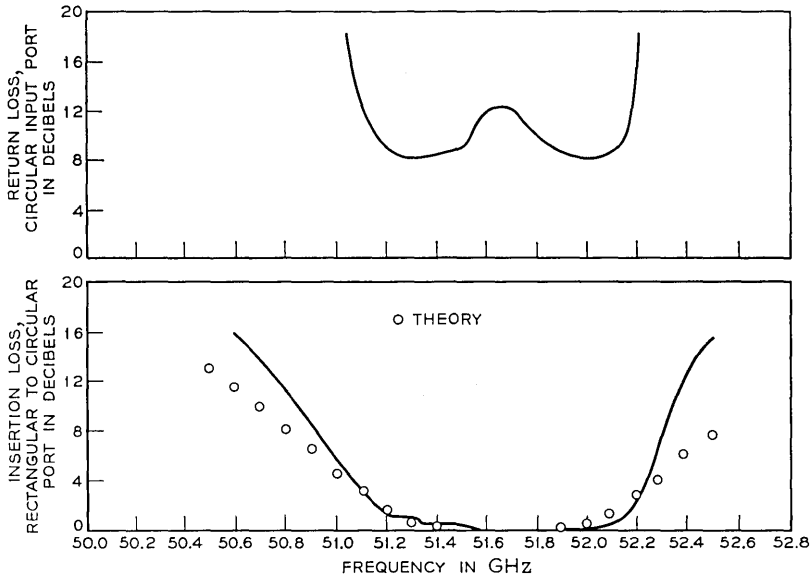


Fig. 6—Frequency response of experimental dropping filter ($\psi' = \psi'' = 7\pi/2$).

step leads to a straightforward design procedure which permits rapid determination of structural dimensions. The method can be readily applied to multiple-pole structures once the exact form of the additional resonators required in the branching filter has been determined. The latter might take the form of additional wrapped resonators or additional resonators in the rectangular waveguide output.

The design procedure evolved has been shown to yield filters whose characteristics compare well with theory. Dimensional tolerances have been shown to be extremely important.

## VII. ACKNOWLEDGMENTS

The author wishes to thank E. A. J. Marcatili for many stimulating discussions during the course of this work. The author also would like to thank his colleagues for their valuable comments.

## APPENDIX A

### *Derivation of the Design Equations*

### A.1 *Branching Filter*

The branching filter consists of a $TE_{01} - TE_{02}$ mode-conversion resonator coupled to a wrapped rectangular waveguide resonator. The

physical parameters of the latter are to be related to that portion of the network of Fig. 2 consisting of the elements $g_0$, $g_1$, and $g_2$. The parameters of interest are the external $Q$'s, $Q_e$, of the two resonators and the coefficient of coupling between them, $k_{12}$. Using the notation of Chapter 8, Ref. 4, there is obtained

$$Q_{ew} = g_0 g_1 \omega_1' Q_L = \frac{\omega_1' Q_L}{\sqrt{2}} \tag{5}$$

$$Q_{em} = g_2 g_0 \omega_1' Q_L = \sqrt{2}\, \omega_1' Q_L \tag{6}$$

$$k_{12} = \frac{1}{\omega_1' Q_L \sqrt{g_1 g_2}} = \frac{1}{\omega_1' Q_L}, \tag{7}$$

where $\omega_1'$ is the bandpass edge angular frequency of the prototype network, and $Q_L$ is the desired loaded $Q$ of the diplexer. The subscripts $w$ and $m$ refer to the wrapped resonator and the mode-conversion resonator, respectively.

The next step is to derive the expressions for the external $Q$'s and coupling coefficient in terms of the physical parameters of the structure.

An analysis of Marcatili's results shows that

$$Q_{em} = \overline{Q_L}, \tag{8}$$

where $\bar{Q}_L$ is given by Marcatili's Equation (70).[1]

The external $Q$ of the wrapped resonator, $Q_{ew}$ is obtained from the defining equation

$$Q_{ew} = \frac{\dfrac{\omega_0}{2} \dfrac{\partial X_1}{\partial \omega}\Big|_{\omega_0}}{R_c}, \tag{9}$$

where

$\omega_0$ = angular resonant frequency,
$X_1$ = resonator reactance function, and
$R_c$ = coupled resistance.

The structure of Fig. 4(b) is used to evaluate $X_1$ and $R_c$. The resulting expressions when substituted in (9) yield

$$Q_{ew} = \frac{Z_{10}\theta_0(\lambda g_{10}/\lambda)^2}{4(X_i^2/R_1)}, \tag{10}$$

where

$Z_{10}$ = characteristic impedance of the wrapped guide,
$\lambda g_{10}$ = guide wavelength of the wrapped guide at resonance,

$X_i$ = reactance of the input iris,
$R_1$ = characteristic impedance of the input guide, and
$\theta_0$ = length of the wrapped structure in radians at resonance.

In general, $\theta_0 = \pi p$ where $p$ is the number of coupling apertures. For loose coupling

$$Q_{ew} = \frac{2\pi p(\lambda g_{10}/\lambda)^2}{c^2}, \tag{11}$$

where

$$c^2 = 8(X_i^2/R_1 Z_{10}) \tag{12}$$

is the power coupling coefficient between guides.

The coupling coefficient $k_{12}$ is given in terms of the resonator parameters by

$$k_{12} = \frac{X_{12}}{\sqrt{x_1 x_2}}, \tag{13}$$

where

$X_{12}$ = coupling reactance,

$x_1 = \frac{\omega_0}{2}\frac{dX_1}{d\omega}\bigg|_{\omega_0}$ = slope parameter of the first resonator, and

$x_2 = \frac{\omega_0}{2}\frac{dX_2}{d\omega}\bigg|_{\omega_0}$ = slope parameter of the second resonator.

To evaluate $k_{12}$, requires calculation of $X_{12}$ as it is related to the physical structure. The slope parameters are known from the external $Q$ calculations. For loose coupling, $X_{12}$ is related to the power coupling coefficient between the $TE_{02}$ waveguide and the $TE_{10}$ wrapped waveguide, $|\Gamma_{12}|^2$, by,

$$|\Gamma_{12}|^2 \cong \frac{X_{12}^2}{2Z_{02}Z_{10}}, \tag{14}$$

where $Z_{02}$ is the characteristic impedance of the $TE_{02}$ waveguide.

If the coupling apertures are assumed sufficiently small so that the electromagnetic field is essentially constant over the aperture, then Bethe's small hole coupling theory can be applied to yield

$$|\Gamma_{12}|^2 = \frac{18p^2k^2G}{abR^4}\frac{\lambda_{g02}}{\lambda_{g10}}M^2, \tag{15}$$

where

$a$ = wrapped guide width,
$b$ = wrapped guide height,
$p$ = number of apertures,
$k$ = 7.016,
$G$ = 0.07075,
$R$ = radius of $TE_{02}$ guide,
$\lambda_{g02}$ = $TE_{02}$ guide wavelength,
$\lambda_{g10}$ = wrapped guide wavelength, and
$M$ = magnetic polarizability of the aperture.

The above assumes the apertures to be $\lambda_{g10}$ apart in the wrapped structure. The magnetic polarizability of the aperture is determined from

$$M = \frac{M_0}{1 - (\lambda_{ca}/\lambda)^2} 10^{-[(2.73tA/\lambda_{ca})\sqrt{1-(\lambda_{ca}/\lambda)^2}]}, \tag{16}$$

where

$M_0$ = static polarizability of the aperture,
$\lambda_{ca}$ = cutoff wavelength of the dominant aperture mode,
$t$ = aperture thickness, and
$A$ = empirical constant.

Equation (16) permits use of Bethe's small hole theory for large apertures.[4] Ref. 4 contains an excellent collection of data on $M_0$ for various types of apertures.

The above analysis when rearranged yields

$$k_{12} = \sqrt{\frac{2Z_{02}Z_{10}}{x_1x_2}} \mid \Gamma_{12} \mid = \frac{1}{\omega_1' Q_L \sqrt{g_1g_2}} \tag{17}$$

from which

$$M = \frac{R^2}{6pkG^{\frac{1}{2}}\omega_1' Q_L} \sqrt{\left(\frac{ab}{g_1g_2}\right)\left(\frac{\lambda_{g10}}{\lambda_{g02}}\right)\left(\frac{x_1}{Z_{10}}\right)\left(\frac{x_2}{Z_{02}}\right)}. \tag{18}$$

The latter then represents the relationship between the required aperture dimensions and the characteristics of the filter.

*A.2 Rejection Filters*

From Ref. 4, it is found that the loaded $Q$'s of the rejection filters

must be

$$Q_{L1} = \sqrt{2}\, Q_L \tag{19}$$

$$Q_{L2} = 2\sqrt{2}\, Q_L\,, \tag{20}$$

where $Q_{L1}$ applies to the rejection filter nearest the branching filter. The loaded $Q$'s of the rejection filters in terms of the physical parameters are given by Marcatili's Equation (139).[1]

## APPENDIX B

### *Transfer Functions and Reflection Coefficients*

The transfer coefficients and reflection coefficients, of the individual diplexer networks are of interest since the experimental development of a diplexer usually requires adjustments on the separate networks. Figs. 7 and 8 show the individual networks with the ports of interest identified. The analysis is straightforward yielding the following results:

$$S_{ab} = \frac{2\sqrt{2}}{D} \tag{21}$$

$$S_{bb} = \frac{(1 - 2g_1g_2\omega'^2) + j\omega'(g_1 - 2g_2)}{D} \tag{22}$$

$$S_{aa} = S_{cc} = \frac{1 + jg_1\omega'}{D} \tag{23}$$

$$S_{ac} = \frac{2(1 - g_1g_2\omega'^2) + jg_2\omega'}{D} \tag{24}$$

$$S_{bc} = \frac{2}{D}\,,$$

where

$$D = (3 - 2g_1g_2\omega'^2) + j(g_1 + 2g_2)\omega' \tag{25}$$

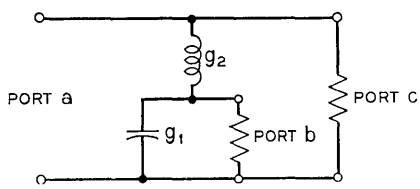


Fig. 7—Branching filter prototype.

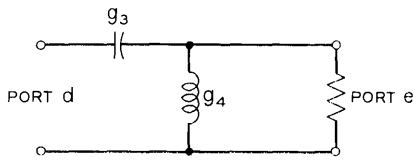


Fig. 8 — Rejection filter prototype.

and

$$S_{de} = -\frac{2g_3g_4\omega'^2}{(1 - 2g_3g_4\omega'^2) + j(g_3 + g_4)\omega'}. \tag{26}$$

The above expressions were used in Section IV to compare theory and experiment with an assumed frequency mapping function

$$\omega' = \omega_1' Q_L\left(\frac{\omega}{\omega_0} - \frac{\omega_0}{\omega}\right). \tag{27}$$

Note that (27) represents a narrow bandwidth approximation to the actual waveguide resonator frequency variation. The accuracy of the result will probably be sufficient for filter bandwidths up to a few percent. It should also be noted that Marcatili obtained good correlation between theory and experiment using the approximate mapping function

$$\omega' = 2Q_L\left(\frac{f - f_0}{f_0}\right)$$

for filters having bandwidths of the order of one percent.[1] The latter mapping function has been shown to yield good results in the frequency range where

$$\frac{|2(f - f_0)|}{f_0} \ll \left(\frac{\lambda_0}{\lambda_{g02}}\right)^2,$$

where $\lambda_0$ is the free space wavelength at frequency $f_0$.

REFERENCES

1. Marcatili, E. A. J., Mode Conversion Filters, B.S.T.J., *40,* January, 1961, pp. 149–184.
2. Hubbard, W. M., et al., A Solid-State Regenerative Repeater for Guided Millimeter-Wave Communication Systems, B.S.T.J., *46,* November, 1967, pp. 1977–2018.
3. Marcatili, E. A. J., A Channel-Dropping Filter in the Millimeter Region Using Circular Electric Modes, IRE Trans., *MTT-9,* March 1961, pp. 176–182.

4. Matthaei, G. L., et al., *Design of Microwave Filters, Impedance Matching Networks, and Coupling Structures,* McGraw-Hill Book Co., Inc., New York, 1964.
5. Matthaei, G. L., et al., Novel Microwave Filter Design Techniques, Contact DA 36-039-AMC-00084(E), Final Report, Chapter 10, Stanford Research Institute, Menlo Park, California, December, 1964.
6. Tanga, C. N., unpublished work.

# Sheet Resistivity Measurements on Rectangular Surfaces–General Solution for Four Point Probe Conversion Factors

By M. A. LOGAN

(Manuscript received July 20, 1967)

*Voltage-current ratios, measured using probes on the surface of a homogeneous conducting sheet, are converted to resistance per square by "conversion factors". For rectangles, a closed form solution for these factors is obtained by using the complex Jacobian sine-amplitude function*

$$x + iy = \mathrm{sn}\,[(u + iv), k]$$

*as a transformation.*

*After transformation, an insulated edge rectangle becomes a semi-infinite sheet. Two conjugate current point images establish the boundary condition. A double-sided rectangle becomes an infinite sheet directly, needing no images.*

*New tables have been prepared for a pattern of probe center locations uniformly distributed over the surface. The probe chosen for these tables is a common arrangement having four equally spaced points on a line parallel to the longer edge of the rectangle.*

## I. INTRODUCTION

Sheet resistivity measurements, made with probes on a bounded surface, are converted to resistance per square by "conversion factors". These factors are a function of the geometry and relative dimensions of the parts. For rectangular slices, tables of such factors[1, 2] are available for the special case of four equally spaced points symmetrically placed on a center line. These tables were computed by use of convergent infinite series, derived for insulated edge and double-sided sheets.

A general closed form solution has been developed for rectangles with arbitrary point locations. The method is applicable to any other

surface shape which, through a conformal transformation, can be converted into a semi-infinite plane. For a rectangle, the transformation is the complex Jacobian sine-amplitude function.

New tables have been computed for four equally-spaced probe points in a line, but with the probe center at points distributed in a uniform pattern over the rectangular surface. With these tables and interpolation, determination of the sheet resistivity now can be made anywhere on the rectangular surface, for either insulated-edge or double-sided conduction. Of course, a new factor can be computed directly for any point not tabulated, rather than calculated by interpolation. (The new tables begin on page 2292.)

The purpose of using the transformation is to change the boundary of the actual slice to the $X$-axis of a semi-infinite plane, and the points to equivalent locations in this semi-infinite sheet. Only two mirror images are added when the slice has insulated edges; none when double sided. This compares to the double infinity of images needed for the former tables, even with the maximum possible symmetry assumed.

## II. METHOD

A sketch of a rectangular slice having dimensions of $a$ and $d$ with four arbitrarily located points is shown in Fig. 1. Without loss of generality, this rectangle can be placed in a coordinate system with the lower edge on the abscissa and the origin at the center of that edge. With this choice and a linear normalization of dimensions to be described later, the ($w$-plane) rectangle is transformed into a ($z$-plane) semi-infinite sheet* of the same sheet resistivity by the complex sine-amplitude function,

$$x + iy = \mathrm{sn}\,[(u + iv), k]. \tag{1}$$

After transformation, the rectangle occupies the entire upper semi-infinite plane. The second part of Fig. 1 shows the locations of the four transformed points. The perimeter of the rectangle becomes the entire $X$-axis.

In order that the desirable logarithmic potential of a current source in an infinite sheet[1] shall apply, it is necessary to complete the lower half of the infinite plane with an attached conducting sheet of the same sheet resistivity.

* Ref. 3, page 57, Example 3.

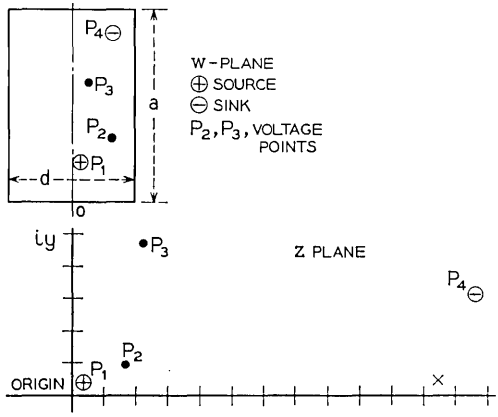


Fig. 1 — Complex sine-amplitude transformation of a rectangle.

### 2.1 *Case 1: Insulated Edges*

The first case described will be that of a transformed insulated edge rectangle. The needed lower sheet may be connected, provided that mirror current images for each real source or sink are included to maintain the boundary condition. Fig. 2 shows the complete point array. An outline for the computations to determine the conversion factor will be given later.

### 2.2 *Case 2: Double-Sided Conduction*

The second case will be that of a double-sided or folded sheet. An extra operation to the rectangle is performed before applying the same transformation as used above. First cut three edges of the double-sided rectangle, unfold and arrange in the coordinate system shown in Fig. 3. This places the upper surface exactly as the insulated edge sheet had been placed in Fig. 1, but the unfolded connected under surface extends the new single sheet into the like area below the abscissa. Now when the sine-amplitude transformation is applied to this entire surface, the rectangle in the upper half of the $w$-plane fills completely the upper semi-infinite $z$-plane, as for the single-sided sheet, and the lower rectangle now fills the lower semi-infinite plane. At the same time, this reconnects the two surfaces along the $X$-axis, eliminating the temporary effect of the cut. The four points again have been transformed exactly as in the lower half of Fig. 1. However, as there now is no boundary condition to fulfill, no images are necessary.

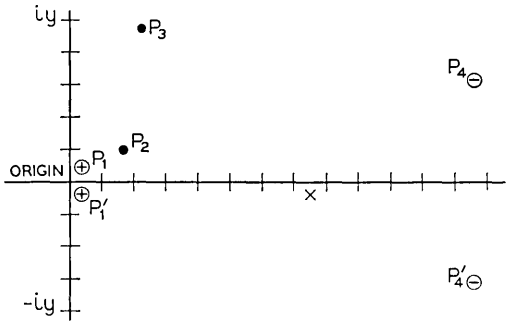


Fig. 2 — Mirror images added with lower sheet to maintain insulated boundary condition.

Thus, the formula will be even simpler than for the insulated edge case.

It is clear that this method can be applied to any surface which can be transformed into a semi-infinite plane. For example, in Ref. 2, this was done with a circle as a step in the proof that a double-sided circular slice behaved exactly as if it were an infinite sheet. This simple result does not apply to a double-sided rectangle because of the singularities of the sn-function.

## III. LOGARITHMIC POTENTIAL

As mentioned earlier, the method used for derivation of the conversion factors is based on use of a conformal transformation leading

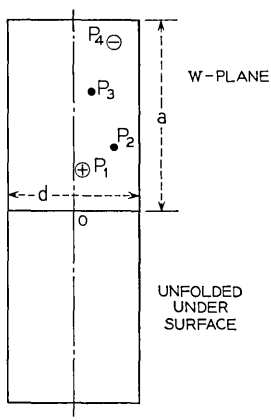


Fig. 3 — Cut and unfolded double sided conduction sheet.

to an infinite sheet. In an infinite sheet, a current source gives rise to the simple logarithmic potential

$$\varphi - \varphi_0 = -\frac{I\rho_s}{2\pi} \ln r, \tag{2}$$

where $\varphi$ is the potential, $I$ the current, $\rho_s$ the sheet resistivity, and $r$ the distance from the current source. For a sink, the sign is reversed. A sketch of a surface with a current source $P_1$ is drawn in Fig. 4. Two points, $P_2$ and $P_3$, have been shown, representing the "voltage points" of a four-point probe. A resistivity measuring set determines their voltage difference. The voltage difference is

$$\varphi_2 - \varphi_3 = V = \frac{I\rho_s}{2\pi} \ln \frac{r_{13}}{r_{12}}. \tag{3}$$

There is a similar expression for each current source or sink. The simple addition, one for each current source or sink is the solution when summing the effects of any number of points. This is because superposition applies.

## IV. CONVERSION FACTOR

The potential difference between the two voltage points ($P_2$ and $P_3$) due to all real and image current source points is:

$$V_+ = \frac{I\rho_s}{2\pi}\left(\ln \frac{r_{13}}{r_{12}} + \ln \frac{r'_{13}}{r'_{12}} + \cdots\right), \tag{4}$$

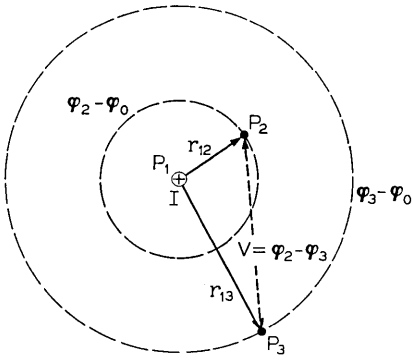


Fig. 4 — Logarithmic potential difference.

where each radius marked by a prime is the distance from an image point to a voltage point.

Likewise for all sinks:

$$V_- = \frac{I\rho_s}{2\pi}\left(\ln\frac{r_{24}}{r_{34}} + \ln\frac{r'_{24}}{r'_{34}} + \cdots\right). \tag{5}$$

4.1 *Case 1: Insulated Edges*

For a rectangle with insulated edges, there are two real current points 1, 4 and two mirror image current points 1′, 4′. Adding the two equations above:

$$V = \frac{I\rho_s}{2\pi}\ln\left[\left(\frac{r_{13}}{r_{12}}\right)\left(\frac{r'_{13}}{r'_{12}}\right)\left(\frac{r_{24}}{r_{34}}\right)\left(\frac{r'_{24}}{r'_{34}}\right)\right]. \tag{6}$$

Rearranging

$$\rho_s = \left(\frac{V}{I}\right) \times \text{C.F.}, \tag{7}$$

where

$$\text{C.F.} = \frac{2\pi}{\ln\left[\left(\frac{r_{13}}{r_{12}}\right)\left(\frac{r'_{13}}{r'_{12}}\right)\left(\frac{r_{24}}{r_{34}}\right)\left(\frac{r'_{24}}{r'_{34}}\right)\right]}. \tag{8}$$

4.2 *Case 2. Double-Sided Sheet*

For a double-sided sheet, there are no images. Clearly the conversion factor can be written directly from (8) above simply by omission of the prime terms:

$$\text{C.F.} = \frac{2\pi}{\ln\left[\left(\frac{r_{13}}{r_{12}}\right)\left(\frac{r_{24}}{r_{34}}\right)\right]} \tag{9}$$

## V. JACOBIAN ELLIPTIC FUNCTION, sn $w$

A description for each of the steps needed for a determination of a conversion factor for a rectangular surface, with arbitrary point locations, has been given. Involved is the use of the complex sine-amplitude function, sn $w$. The next two sections with Appendices A, B, and C, will briefly present all needed material for determination of this function.

The more general but possibly more familiar Schwarz-Christoffel transformation relates a semi-infinite plane and any polygon. The relation is an integral expression between points in the $w$ and $z$ planes. Equation (10) is the form for a rectangle[3] shown in Fig. 1. In this form

it may be considered as one of a transform pair, whose inverse is the equivalent sine-amplitude function, sn $w$. The pair

$$w = \int_0^z \frac{dz}{\sqrt{(1 - z^2)(1 - k^2z^2)}} \tag{10}$$

$$z = \mathrm{sn}\,(w, k). \tag{11}$$

The Schwarz-Christoffel transformation is a directly written expression which serves to identify the sine-amplitude function (11) as a solution for the present problem.

Equation (11) is more convenient for computations to determine where a transformed point from a rectangle in the $w$-plane appears in the $z$-plane. This is the complex sine-amplitude function, which is related to elliptic functions. Ref. 7 has charts of this function.

Tables are in Ref. 8. However, these are double entry tables since the value of an elliptic function depends not only on the argument, but also on the modulus $k$. Interpolation between tabulated values is laborious and subject to error. Fortunately, the functions are representated by rapidly converging series.

## VI. ELLIPTIC FUNCTION PARAMETERS

There are five elliptic function parameters $k$, $k'$, $K$, $K'$, $K'/K$ and two auxiliary nomes $q$ and $q_1$[9], only one of which is independent. For the coordinate choice of Fig. 5, the relation which can be identified through similarity of the rectangles is

$$\frac{K'}{K} \equiv 2\left(\frac{a}{d}\right). \tag{12}$$

Starting with this, Appendix A defines the nomes and compiles a list of rapidly converging series for the other parameters.

Appendix B tabulates the real sn, cn, and dn functions, using the very rapidly converging Theta series.[5] Finally, Appendix C defines the complex sine-amplitude function (11), (38) in terms of the real functions of Appendix B.[6]

## VII. COMPUTATION—GENERAL CASE

A summary of the steps for the general case of arbitrary point locations follows:

*Step 1:* Determine the elliptic function parameters using (20) through (26) starting with the side length ratio $a/d$ of the rectangle.

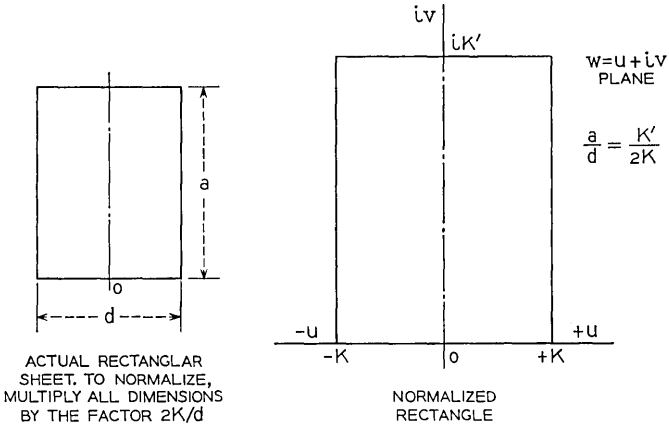


Fig. 5 — The initial linear transformation.

*Step 2:* Transform the points in the rectangle to their place in a normalized rectangle, such as Fig. 5, by linear multiplication of all dimensions with $(2K/d)$.

*Step 3:* Compute the real elliptic functions of (31) through (36) for each probe point.

*Step 4:* Transform each of the normalized probe point locations with the complex sine-amplitude function, (38). When the rectangle has insulated edges, add complex conjugate mirror image current points, as in Fig. 2.

*Step 5:* Determine the distances from each current point to the voltage points.

*Step 6:* Substitute in (8) when edges are insulated, or (9) when the slice is two-sided for the conversion factor.

## VIII. COMPUTATION—FOUR EQUALLY SPACED PROBE POINTS

New tables have been computed for a commonly used four-point in-line probe, having equal point spacings. Fig. 6 shows the probe on the rectangle. The dimensions necessary to determine a particular conversion factor, are defined in the figure as $a$, $b$, $c$, $d$, $s$, and $t$. The letters $a$ and $d$ represent the sides of the rectangle, and $s$ the point spacing. The slice thickness $t$ is needed for double-sided conduction. With double-sided conduction $(d + t)$ and $(a + t)$ are used for $d$ and $a$, respectively. There are two new dimensions, $b$ and $c$. These relate the center of the probe to the center of the rectangle.

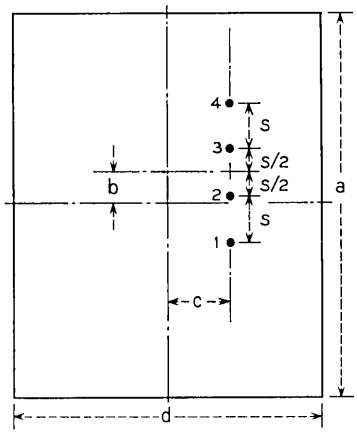


Fig. 6 — General arrangement for the four point probe on a rectangular sheet.

A FORTRAN computer program has been written by S. G. Student, Jr. The computer program and the tables use a dimensionless notation, involving only ratios of these lengths. The notation is shown in Fig. 7 where thirty probe point centers chosen for the tables have been plotted. The number of the center of the probe point location is the

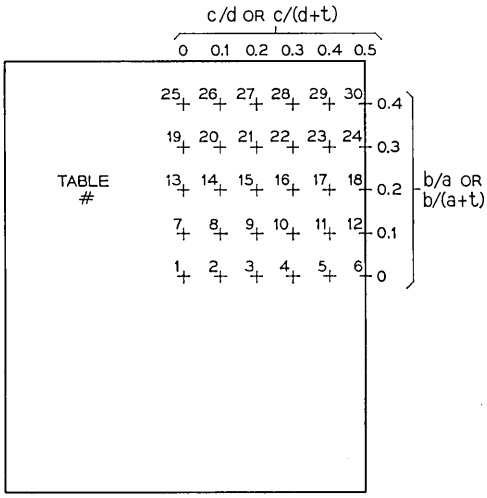


Fig. 7 — Plot of the 30 locations selected for the probe center—dimensionless notation.

same as that of the corresponding table. Hence this figure also serves as an index for the tables.

The probe center locations have been located at the intersections of $b/a = 0, 0.1, 0.2, 0.3$, and $0.4$ with $c/d = 0, 0.1, 0.2, 0.3, 0.4$, and $0.5$. There is a restriction for relative point spacing $d/s$ to keep the four points on the sheet. An expression for this restriction is

$$\frac{a}{2} \geqq b + \frac{3s}{2}$$

which may be rearranged to be

$$\left(\frac{d}{s}\right) \geqq \frac{3}{(a/d)[1 - 2(b/a)]} \tag{13}$$

The tables are for probe center points shown only in one quarter. Because of symmetry, these tables apply to all quarters. That is, $b$ can be either above or below the horizontal center line and $c$ can be either right or left of the vertical center line.

The four-point locations before normalization are

$$\begin{aligned} P_1 &= c + i\left(\frac{a}{2} + b - \frac{3s}{2}\right) \\ P_2 &= c + i\left(\frac{a}{2} + b - \frac{s}{2}\right) \\ P_3 &= c + i\left(\frac{a}{2} + b + \frac{s}{2}\right) \\ P_4 &= c + i\left(\frac{a}{2} + b + \frac{3s}{2}\right). \end{aligned} \tag{14}$$

For a given $a/d$, the elliptic parameters are computed for Step 1. The rectangular coordinates of the above four points are normalized by multiplication by $(2K/d)$. The four normalized points then are

$$\left.\begin{matrix} u_1 + iv_1 \\ u_2 + iv_2 \\ u_3 + iv_3 \\ u_4 + iv_4 \end{matrix}\right\} \quad \begin{matrix} 0 \leqq u \leqq K \\ \\ 0 \leqq v \leqq K'. \end{matrix} \tag{15}$$

This completes Step 2. For Step 3, compute the real elliptic functions, and with Step 4, determine the four real point locations in the semi-

infinite upper half plane.

$$\begin{aligned} x_1 + iy_1 &= \mathrm{sn}\,([u_1 + iv_1], k) \\ x_2 + iy_2 &= \mathrm{sn}\,([u_2 + iv_2], k) \\ x_3 + iy_3 &= \mathrm{sn}\,([u_3 + iv_3], k) \\ x_4 + iy_4 &= \mathrm{sn}\,([u_4 + iv_4], k). \end{aligned} \tag{16}$$

The mirror images are the conjugates of the first and last lines:

$$\begin{aligned} &x_1 - iy_1 \\ &x_4 - iy_4\ . \end{aligned} \tag{17}$$

Then for Step 5 the distance equations are

$$\begin{aligned} r_{12} &= (|\,x_2 - x_1\,|^2 + |\,y_2 - y_1\,|^2)^{\frac{1}{2}} \\ r_{13} &= (|\,x_3 - x_1\,|^2 + |\,y_3 - y_1\,|^2)^{\frac{1}{2}} \\ r_{24} &= (|\,x_4 - x_2\,|^2 + |\,y_4 - y_2\,|^2)^{\frac{1}{2}} \\ r_{34} &= (|\,x_4 - x_3\,|^2 + |\,y_4 - y_3\,|^2)^{\frac{1}{2}}. \end{aligned} \tag{18}$$

If the sheet is insulated then the image distances are

$$\begin{aligned} r'_{12} &= (|\,x_2 - x_1\,|^2 + |\,y_2 + y_1\,|^2)^{\frac{1}{2}} \\ r'_{13} &= (|\,x_3 - x_1\,|^2 + |\,y_3 + y_1\,|^2)^{\frac{1}{2}} \\ r'_{24} &= (|\,x_4 - x_2\,|^2 + |\,y_4 + y_2\,|^2)^{\frac{1}{2}} \\ r'_{34} &= (|\,x_4 - x_3\,|^2 + |\,y_4 + y_3\,|^2)^{\frac{1}{2}}. \end{aligned} \tag{19}$$

Finally, for Step 6, substitute these values in (8) and (9) for the conversion factors.

## IX. EDGE EFFECT

The solution for two-sided conduction does not include two effects which actually are present. First, the equivalent flattened surface defined by using $(d+t)$ and $(a+t)$ for the outside dimensions includes, at the four corners, small square pieces of size $t$ by $t$, which actually are not present. Second, under every edge there is a region of increased conductivity because the diffused impurity entered through two surfaces. This extra diffusion causes the equivalent skin thickness both to be increased and to be lower in bulk resistivity under the edge.

Thus, there exists "frames" of lower resistivity surrounding the surface being tested. It is believed the coefficients may be in error and too low when points are close to an edge of a two-sided slice. This effect has neither been evaluated nor included in the tables.

## X. VERIFICATION

As described above, Table I has previously been determined from infinite series obtained by use of image arrays.* There are some discrepancies in the fourth and fifth significant figures. A few of the earlier factors have been recalculated using the series method. For each case the error was in the prior table.

From Tables I, VII, XIII, XIX, and XXV, some limiting double sided cases may be determined by appropriate changes of the dimensionless parameters. For instance, consider an insulated edge surface with the points on the vertical bisector. Now fold the sheet on this line, placing the right side say, underneath. Note that because of the original symmetry, at every point where the edges now come together, the potentials before connection were identical. Therefore, when connected to form a two-sided sheet, no change in current occurs, and the V/I ratio at the four points is unaltered. Thus, the double-sided sheet with the points on one edge made by folding, has the same numerical conversion factors as the original single sheet with the points in the center when the appropriate $(a/d)$ and $(d/s)$ parameters are identified.

| Two examples: | $b/a$ | $c/d$ | $d/s$ | $a/d$ | C.F. |
|---|---|---|---|---|---|
| Single Sheet | 0 | 0 | 3 | 1 | 2.4562 |
| Double-Sided Sheet | 0 | 0.5 | 1.5 | 2 | 2.4562 |
| Single Sheet | 0 | 0 | 3 | 2 | 2.7000 |
| Double-Sided Sheet | 0 | 0.5 | 1.5 | 4 | 2.7000 |

The same type of identification can be made for other values of $b/a$.

Some limiting insulated edge checks also can be made from Tables I, VII, XIII, XIX, and XXV, through appropriate changes to the dimensionless parameters but this time halving the conversion factor. These new sheets are made by cutting the original sheet along the vertical bisector. Because of vertical symmetry, no current crossed this line before the cut and therefore the field pattern is unaffected after the cut. As before $(a/d)$ and $(d/s)$ are doubled and halved, respectively. However, now all the current flows in half the area. This

* The tables begin on page 2292.

causes all potential differences to be doubled. As the sheet resistivity has not been affected, the conversion factor therefore is just half.

| Two examples: | $b/a$ | $c/d$ | $d/s$ | $a/d$ | C.F. |
|---|---|---|---|---|---|
| Single Sheet | 0 | 0 | 5 | 1 | 3.5098 ÷ 2 |
| Single Sheet | 0 | 0.5 | 2.5 | 2 | = 1.7549 |
| Single Sheet | 0.2 | 0 | 3 | 2 | 2.6647 ÷ 2 |
| Single Sheet | 0.2 | 0.5 | 1.5 | 4 | = 1.3323 |

For an intermediate probe center location, a chart of the complex sine-amplitude function for $(a/d) = 1.2173$, included with Ref. 7, can be read to about three-figure accuracy. Several conversion factors not given in these tables were verified this way.

Finally, when the two current points are on the top and bottom edges of a slice, the double-sided conversion factor is twice that for the insulated edge sheet. This is because exactly half the current flows across the back when double sided.

## APPENDIX A

### *Elliptical Function Parameters*

The elliptic function parameters are related to the rectangle through the identity

$$\frac{K'}{K} \equiv 2\left(\frac{a}{d}\right). \tag{20}$$

This relation uniquely determines the other elliptic function coefficients. It is convenient to define the nomes:

$$q = \exp\left(-\pi \frac{K'}{K}\right) \tag{21}$$

$$q_1 = \exp\left(-\pi \frac{K}{K'}\right). \tag{22}$$

Then the modulus:

$$k = 4\sqrt{q}\left[\frac{1 + q^2 + q^6 + q^{12} + \cdots q^{n(n+1)} + \cdots}{1 + 2(q + q^4 + q^9 + \cdots q^{n^2} + \cdots)}\right]^2. \tag{23}$$

The complementary modulus:

$$\begin{aligned} k' &= \sqrt{1 - k^2} \\ &= \left[\frac{1 - 2q + 2q^4 - 2q^9 + \cdots 2(-1)^n q^{n^2} + \cdots}{1 + 2(q + q^4 + \cdots q^{n^2} + \cdots)}\right]^2. \end{aligned} \tag{24}$$

The complete elliptic integral:

$$K = \int_0^1 \frac{dt}{\sqrt{(1-t^2)(1-k^2t^2)}} \tag{25}$$

$$= \frac{\pi}{2}[1 + 2q + 2q^4 + 2q^9 + \cdots 2q^{n^2} + \cdots]^2.$$

The complementary complete elliptic integral is

$$K' = \int_0^1 \frac{dt}{\sqrt{(1-t^2)(1-k'^2t^2)}}$$

$$= \frac{\pi}{2}[1 + 2q_1 + 2q_1^4 + \cdots 2q_1^{n^2} + \cdots]^2$$

$$= -\frac{\pi K}{\ln q_1} = 2K\left(\frac{a}{d}\right) \tag{26}$$

so that $K'$ is the same function of the complementary modulus $k'$ as $K$ is of $k$.

## APPENDIX B

### *Real Elliptic Functions*

The elliptic functions can be expressed in terms of certain auxiliary functions called the Theta functions (Ref. 5, p. 471). The following definitions and notations are chosen:

$$\theta_0(u/2K, q) = 1 + 2\sum_{n=1}^{\infty}(-1)^n q^{n^2} \cos 2n\frac{\pi u}{2K} \tag{27}$$

$$\theta_1(u/2K, q) = 2q^{\frac{1}{4}}\sum_{n=0}^{\infty}(-1)^n q^{n(n+1)} \sin(2n+1)\frac{\pi u}{2K} \tag{28}$$

$$\theta_2(u/2K, q) = 2q^{\frac{1}{4}}\sum_{n=0}^{\infty} q^{n(n+1)} \cos(2n+1)\frac{\pi u}{2K} \tag{29}$$

$$\theta_3(u/2K, q) = 1 + 2\sum_{n=1}^{\infty} q^{n^2} \cos 2n\frac{\pi u}{2K}. \tag{30}$$

Then

$$\mathrm{sn}\,(u, k) = \frac{1}{\sqrt{k}}\frac{\theta_1(u/2K, q)}{\theta_0(u/2K, q)} \tag{31}$$

$$\begin{aligned} \mathrm{cn}\,(u, k) &= \sqrt{\frac{k'}{k}}\,\frac{\theta_2(u/2K, q)}{\theta_0(u/2K, q)} \\ &= \sqrt{1 - \mathrm{sn}^2\,(u, k)} \end{aligned} \tag{32}$$

$$\begin{aligned} \mathrm{dn}\,(u, k) &= \sqrt{k'}\,\frac{\theta_3(u/2K, q)}{\theta_0(u/2K, q)} \\ &= \sqrt{1 - k^2\,\mathrm{sn}^2\,(u, k)}. \end{aligned} \tag{33}$$

For a complex variable a second set for $v$ will be needed, obtained by permuting the values of $q$ and $q_1$, $k$ and $k'$, and $K$ and $K'$, in (27) through (30).

$$\mathrm{sn}\,(v, k') = \frac{1}{\sqrt{k'}}\,\frac{\theta_1(v/2K', q_1)}{\theta_0(v/2K', q_1)} \tag{34}$$

$$\begin{aligned} \mathrm{cn}\,(v, k') &= \sqrt{\frac{k}{k'}}\,\frac{\theta_2(v/2K', q_1)}{\theta_0(v/2K', q_1)} \\ &= \sqrt{1 - \mathrm{sn}^2\,(v, k')} \end{aligned} \tag{35}$$

$$\begin{aligned} \mathrm{dn}\,(v, k') &= \sqrt{k}\,\frac{\theta_3(v/2K', q_1)}{\theta_0(v/2K', q_1)} \\ &= \sqrt{1 - (k'\,\mathrm{sn}\,(v, k'))^2}. \end{aligned} \tag{36}$$

APPENDIX C

*Complex Sine-Amplitude Elliptic Functions*

For brevity we put[6]

$$\begin{aligned} s &= \mathrm{sn}\,(u, k) & s_1 &= \mathrm{sn}\,(v, k') \\ c &= \mathrm{cn}\,(u, k) & c_1 &= \mathrm{cn}\,(v, k') \\ d &= \mathrm{dn}\,(u, k) & d_1 &= \mathrm{dn}\,(v, k'). \end{aligned} \tag{37}$$

Note that the complementary modulus $k'$, etc., go with the suffix 1. Then

$$\begin{aligned} x + iy &= \mathrm{sn}\,[(u + iv), k] \\ &= \frac{s\,d_1 + ic\,ds_1\,c_1}{c_1^2 + k^2 s^2 s_1^2}. \end{aligned} \tag{38}$$

A substitution, to avoid a negative sign in the denominator, has been made in (38) from page 20 of Ref. 8.

(References are listed on page 2322.)

## Table I—Four Point Probe Conversion Factors for Rectangles

Insulated Edge Sheet

$c/d = 0. \quad b/a = 0$

| $d/S$ | $a/d = 1.000$ | $a/d = 1.200$ | $a/d = 1.500$ | $a/d = 2.000$ | $a/d = 4.000$ |
|---|---|---|---|---|---|
| 1.00 | | | | | 0.9994 |
| 1.25 | | | | | 1.2468 |
| 1.50 | | | | 1.4787 | 1.4893 |
| 1.75 | | | | 1.7197 | 1.7239 |
| 2.00 | | | 1.8978 | 1.9454 | 1.9475 |
| 2.50 | | 2.2244 | 2.3342 | 2.3532 | 2.3541 |
| 3.00 | 2.4562 | 2.6298 | 2.6897 | 2.7000 | 2.7005 |
| 4.00 | 3.1134 | 3.1927 | 3.2197 | 3.2244 | 3.2246 |
| 5.00 | 3.5098 | 3.5563 | 3.5721 | 3.5749 | 3.5750 |
| 7.50 | 4.0089 | 4.0282 | 4.0347 | 4.0358 | 4.0358 |
| 10.00 | 4.2208 | 4.2314 | 4.2350 | 4.2356 | 4.2356 |
| 15.00 | 4.3878 | 4.3925 | 4.3940 | 4.3943 | 4.3943 |
| 20.00 | 4.4498 | 4.4534 | 4.4533 | 4.4534 | 4.4534 |
| 40.00 | 4.5114 | 4.5120 | 4.5123 | 4.5123 | 4.5123 |
| $\infty$ | 4.5324 | 4.5324 | 4.5324 | 4.5324 | 4.5324 |

Double Sided Sheet

$c/(d+t) = 0. \quad b/(a+t) = 0$

| $\frac{d+t}{S}$ | $\frac{a+t}{d+t} = 1.000$ | $\frac{a+t}{d+t} = 1.200$ | $\frac{a+t}{d+t} = 1.500$ | $\frac{a+t}{d+t} = 2.000$ | $\frac{a+t}{d+t} = 4.000$ |
|---|---|---|---|---|---|
| 1.00 | | | | | 1.9497 |
| 1.25 | | | | | 2.3549 |
| 1.50 | | | | 2.9575 | 2.7010 |
| 1.75 | | | | 3.1508 | 2.9887 |
| 2.00 | | | 3.7956 | 3.3381 | 3.2248 |
| 2.50 | | 4.4488 | 3.8987 | 3.6409 | 3.5751 |
| 3.00 | 4.9123 | 4.3701 | 4.0231 | 3.8545 | 3.8109 |
| 4.00 | 4.6477 | 4.3823 | 4.2023 | 4.1123 | 4.0888 |
| 5.00 | 4.5791 | 4.4183 | 4.3068 | 4.2505 | 4.2357 |
| 7.50 | 4.5415 | 4.4735 | 4.4254 | 4.4008 | 4.3943 |
| 10.00 | 4.5353 | 4.4976 | 4.4708 | 4.4571 | 4.4534 |
| 15.00 | 4.5329 | 4.5164 | 4.5045 | 4.4985 | 4.4969 |
| 20.00 | 4.5325 | 4.5233 | 4.5166 | 4.5132 | 4.5123 |
| 40.00 | 4.5324 | 4.5301 | 4.5284 | 4.5276 | 4.5273 |
| $\infty$ | 4.5324 | 4.5324 | 4.5324 | 4.5324 | 4.5324 |

## Table II—Four Point Probe Conversion Factors for Rectangles

Insulated Edge Sheet

$c/d = 0.100 \quad b/a = 0$

| $d/S$ | $a/d = 1.000$ | $a/d = 1.200$ | $a/d = 1.500$ | $a/d = 2.000$ | $a/d = 4.000$ |
|---|---|---|---|---|---|
| 1.00 | | | | | 0.9970 |
| 1.25 | | | | | 1.2407 |
| 1.50 | | | | 1.4566 | 1.4779 |
| 1.75 | | | | 1.6935 | 1.7062 |
| 2.00 | | | 1.8529 | 1.9143 | 1.9233 |
| 2.50 | | 2.1637 | 3.2801 | 2.3124 | 2.3182 |
| 3.00 | 2.3911 | 2.5601 | 2.6306 | 2.6525 | 2.6568 |
| 4.00 | 3.0388 | 3.1222 | 3.1600 | 3.1732 | 3.1761 |
| 5.00 | 3.4414 | 3.4938 | 3.5186 | 3.5278 | 3.5298 |
| 7.50 | 3.9638 | 3.9876 | 3.9995 | 4.0041 | 4.0051 |
| 10.00 | 4.1913 | 4.2050 | 4.2119 | 4.2146 | 4.2153 |
| 15.00 | 4.3731 | 4.3793 | 4.3825 | 4.3838 | 4.3841 |
| 20.00 | 4.4411 | 4.4447 | 4.4465 | 4.4472 | 4.4474 |
| 40.00 | 4.5091 | 4.5100 | 4.5105 | 4.5107 | 4.5107 |
| ∞ | 4.5324 | 4.5324 | 4.5324 | 4.5324 | 4.5324 |

Double Sided Sheet

$c/(d+t) = 0.100 \quad b/(a+t) = 0$

| $\frac{d+t}{S}$ | $\frac{a+t}{d+t} = 1.000$ | $\frac{a+t}{d+t} = 1.200$ | $\frac{a+t}{d+t} = 1.500$ | $\frac{a+t}{d+t} = 2.000$ | $\frac{a+t}{d+t} = 4.000$ |
|---|---|---|---|---|---|
| 1.00 | | | | | 1.9493 |
| 1.25 | | | | | 2.3548 |
| 1.50 | | | | 2.9132 | 2.7009 |
| 1.75 | | | | 3.1216 | 2.9887 |
| 2.00 | | | 3.7058 | 3.3173 | 3.2247 |
| 2.50 | | 4.3275 | 3.8442 | 3.6286 | 3.5751 |
| 3.00 | 4.7822 | 4.2873 | 3.9864 | 3.8463 | 3.8109 |
| 4.00 | 4.5750 | 4.3364 | 4.1823 | 4.1079 | 4.0888 |
| 5.00 | 4.5327 | 4.3891 | 4.2942 | 4.2477 | 4.2357 |
| 7.50 | 4.5209 | 4.4606 | 4.4198 | 4.3996 | 4.3943 |
| 10.00 | 4.5237 | 4.4903 | 4.4677 | 4.4564 | 4.4534 |
| 15.00 | 4.5278 | 4.5132 | 4.5032 | 4.4982 | 4.4969 |
| 20.00 | 4.5296 | 4.5215 | 4.5158 | 4.5130 | 4.5123 |
| 40.00 | 4.5316 | 5.5296 | 4.5282 | 4.5275 | 4.5273 |
| ∞ | 4.5324 | 4.5324 | 4.5324 | 4.5324 | 4.5324 |

## Table III—Four Point Probe Conversion Factors for Rectangles

Insulated Edge Sheet

$c/d = 0.200 \qquad b/a = 0$

| $d/S$ | $a/d = 1.000$ | $a/d = 1.200$ | $a/d = 1.500$ | $a/d = 2.000$ | $a/d = 4.000$ |
|---|---|---|---|---|---|
| 1.00 | | | | | 0.9905 |
| 1.25 | | | | | 1.2243 |
| 1.50 | | | | 1.3971 | 1.4466 |
| 1.75 | | | | 1.6229 | 1.6565 |
| 2.00 | | | 1.7297 | 1.8285 | 1.8539 |
| 2.50 | | 1.9913 | 2.1294 | 2.1947 | 2.2119 |
| 3.00 | 2.1964 | 2.3604 | 2.4601 | 2.5096 | 2.5227 |
| 4.00 | 2.8111 | 2.9100 | 2.9757 | 3.0090 | 3.0179 |
| 5.00 | 3.2254 | 3.2962 | 3.3444 | 3.3689 | 3.3754 |
| 7.50 | 3.8117 | 3.8496 | 3.8758 | 3.8891 | 3.8926 |
| 10.00 | 4.0882 | 4.1116 | 4.1277 | 4.1359 | 4.1381 |
| 15.00 | 4.3202 | 4.3314 | 4.3392 | 4.3431 | 4.3441 |
| 20.00 | 4.4098 | 4.4163 | 4.4208 | 4.4231 | 4.4237 |
| 40.00 | 4.5009 | 4.5026 | 4.5037 | 4.5043 | 4.5045 |
| $\infty$ | 4.5324 | 4.5324 | 4.5324 | 4.5324 | 4.5324 |

Double Sided Sheet

$c/(d + t) = 0.200 \qquad b/(a + t) = 0$

| $\frac{d+t}{S}$ | $\frac{a+t}{d+t} = 1.000$ | $\frac{a+t}{d+t} = 1.200$ | $\frac{a+t}{d+t} = 1.500$ | $\frac{a+t}{d+t} = 2.000$ | $\frac{a+t}{d+t} = 4.000$ |
|---|---|---|---|---|---|
| 1.00 | | | | | 1.9482 |
| 1.25 | | | | | 2.3544 |
| 1.50 | | | | 2.7943 | 2.7007 |
| 1.75 | | | | 3.0440 | 2.9885 |
| 2.00 | | | 3.4595 | 3.2622 | 3.2246 |
| 2.50 | | 3.9827 | 3.6963 | 3.5963 | 3.5750 |
| 3.00 | 4.3928 | 4.0532 | 3.8872 | 3.8248 | 3.8109 |
| 4.00 | 4.3589 | 4.2077 | 4.1282 | 4.0962 | 4.0888 |
| 5.00 | 4.3951 | 4.3075 | 4.2600 | 4.2403 | 4.2356 |
| 7.50 | 4.4601 | 4.4247 | 4.4048 | 4.3964 | 4.3943 |
| 10.00 | 4.4895 | 4.4702 | 4.4593 | 4.4546 | 4.4534 |
| 15.00 | 4.5126 | 4.5042 | 4.4994 | 4.4974 | 4.4969 |
| 20.00 | 4.5211 | 4.5164 | 4.5138 | 4.5126 | 4.5123 |
| 40.00 | 4.5295 | 4.5284 | 4.5277 | 4.5274 | 4.5273 |
| $\infty$ | 4.5324 | 4.5324 | 4.5324 | 4.5324 | 4.5324 |

## Table IV—Four Point Probe Conversion Factors for Rectangles

Insulated Edge Sheet

$c/d = 0.300$ $b/a = 0$

| $d/S$ | $a/d = 1.000$ | $a/d = 1.200$ | $a/d = 1.500$ | $a/d = 2.000$ | $a/d = 4.000$ |
|---|---|---|---|---|---|
| 1.00 | | | | | 0.9823 |
| 1.25 | | | | | 1.2027 |
| 1.50 | | | | 1.3201 | 1.4040 |
| 1.75 | | | | 1.5299 | 1.5868 |
| 2.00 | | | 1.5640 | 1.7110 | 1.7534 |
| 2.50 | | 1.7446 | 1.9197 | 2.0193 | 2.0470 |
| 3.00 | 1.8930 | 2.0691 | 2.2046 | 2.2797 | 2.3002 |
| 4.00 | 2.4394 | 2.5629 | 2.6564 | 2.7067 | 2.7203 |
| 5.00 | 2.8395 | 2.9345 | 3.0053 | 3.0428 | 3.0528 |
| 7.50 | 3.4871 | 3.5438 | 3.5852 | 3.6067 | 3.6124 |
| 10.00 | 3.8453 | 3.8825 | 3.9094 | 3.9233 | 3.9270 |
| 15.00 | 4.1837 | 4.2027 | 4.2163 | 4.2234 | 4.2252 |
| 20.00 | 4.3258 | 4.3371 | 4.3452 | 4.3494 | 4.3505 |
| 40.00 | 4.4779 | 4.4809 | 4.4830 | 4.4841 | 4.4844 |
| $\infty$ | 4.5324 | 4.5324 | 4.5324 | 4.5324 | 4.5324 |

Double Sided Sheet

$c/(d+t) = 0.300$ $b/(a+t) = 0$

| $\frac{d+t}{S}$ | $\frac{a+t}{d+t} = 1.000$ | $\frac{a+t}{d+t} = 1.200$ | $\frac{a+t}{d+t} = 1.500$ | $\frac{a+t}{d+t} = 2.000$ | $\frac{a+t}{d+t} = 4.000$ |
|---|---|---|---|---|---|
| 1.00 | | | | | 1.9469 |
| 1.25 | | | | | 2.3538 |
| 1.50 | | | | 2.6402 | 2.7004 |
| 1.75 | | | | 2.9453 | 2 9883 |
| 2.00 | | | 3.1281 | 3.1929 | 3.2245 |
| 2.50 | | 3.4892 | 3.5019 | 3.5558 | 3.5749 |
| 3.00 | 3.7860 | 3.7237 | 3.7579 | 3.7979 | 3.8108 |
| 4.00 | 4.0283 | 4.0290 | 4.0583 | 4.0817 | 4.0887 |
| 5.00 | 4.1864 | 4.1949 | 4.2160 | 4.2312 | 4.2356 |
| 7.50 | 4.3685 | 4.3753 | 4.3855 | 4.3924 | 4.3943 |
| 10.00 | 4.4382 | 4.4426 | 4.4485 | 4.4523 | 4.4534 |
| 15.00 | 4.4899 | 4.4920 | 4.4946 | 4.4964 | 4.4969 |
| 20.00 | 4.5083 | 4.5096 | 4.5111 | 4.5120 | 4.5123 |
| 40.00 | 4.5263 | 4.5266 | 4.5270 | 4.5273 | 4.5273 |
| $\infty$ | 4.5324 | 4.5324 | 4.5324 | 4.5324 | 4.5324 |

## Table V—Four Point Probe Conversion Factors for Rectangles

Insulated Edge Sheet

$c/d = 0.400 \qquad b/a = 0$

| $d/S$ | $a/d = 1.000$ | $a/d = 1.200$ | $a/d = 1.500$ | $a/d = 2.000$ | $a/d = 4.000$ |
|---|---|---|---|---|---|
| 1.00 | | | | | 0.9754 |
| 1.25 | | | | | 1.1841 |
| 1.50 | | | | 1.2542 | 1.3657 |
| 1.75 | | | | 1.4485 | 1.5217 |
| 2.00 | | | 1.4153 | 1.6026 | 1.6552 |
| 2.50 | | 1.5066 | 1.7206 | 1.8386 | 1.8708 |
| 3.00 | 1.5715 | 1.7774 | 1.9336 | 2.0171 | 2.0395 |
| 4.00 | 2.0054 | 2.1399 | 2.2375 | 2.2882 | 2.3016 |
| 5.00 | 2.3020 | 2.3998 | 2.4695 | 2.5052 | 2.5146 |
| 7.50 | 2.8301 | 2.8871 | 2.9269 | 2.9471 | 2.9524 |
| 10.00 | 3.2128 | 3.2521 | 3.2793 | 3.2930 | 3.2966 |
| 15.00 | 3.7128 | 3.7353 | 3.7508 | 3.7586 | 3.7607 |
| 20.00 | 3.9938 | 4.0082 | 4.0181 | 4.0231 | 4.0244 |
| 40.00 | 4.3709 | 3.3752 | 4.3781 | 4.3796 | 4.3800 |
| $\infty$ | 4.5324 | 4.5324 | 4.5324 | 4.5324 | 4.5324 |

Double Sided Sheet

$c/(d + t) = 0.400 \qquad b/(a + t) = 0$

| $\frac{d+t}{S}$ | $\frac{a+t}{d+t} = 1.000$ | $\frac{a+t}{d+t} = 1.200$ | $\frac{a+t}{d+t} = 1.500$ | $\frac{a+t}{d+t} = 2.000$ | $\frac{a+t}{d+t} = 4.000$ |
|---|---|---|---|---|---|
| 1.00 | | | | | 1.9458 |
| 1.25 | | | | | 2.3534 |
| 1.50 | | | | 2.5085 | 2.7001 |
| 1.75 | | | | 2.8631 | 2.9882 |
| 2.00 | | | 2.8307 | 3.1356 | 3.2244 |
| 2.50 | | 3.0133 | 3.3337 | 3.5225 | 3.5749 |
| 3.00 | 3.1430 | 3.4163 | 3.6475 | 3.7759 | 3.8108 |
| 4.00 | 3.6924 | 3.8660 | 3.9990 | 4.0698 | 4.0887 |
| 5.00 | 3.9774 | 4.0930 | 4.1788 | 4.2237 | 4.2356 |
| 7.50 | 4.2778 | 4.3309 | 4.3693 | 4.3891 | 4.3943 |
| 10.00 | 4.3876 | 4.4177 | 4.4394 | 4.4505 | 4.4534 |
| 15 00 | 4.4675 | 4.4810 | 4.4906 | 4.4956 | 4.4969 |
| 20.00 | 4.4958 | 4.5034 | 4.5088 | 4.5116 | 4.5123 |
| 40.00 | 4.5232 | 4.5251 | 4.5264 | 4.5271 | 4.5273 |
| $\infty$ | 4.5324 | 4.5324 | 4.5324 | 4.5324 | 4.5324 |

## Table VI—Four Point Probe Conversion Factors for Rectangles

Insulated Edge Sheet

$c/d = 0.500 \qquad b/a = 0$

| $d/S$ | $a/d = 1.000$ | $a/d = 1.200$ | $a/d = 1.500$ | $a/d = 2.000$ | $a/d = 4.000$ |
|---|---|---|---|---|---|
| 1.00 | | | | | 0.9727 |
| 1.25 | | | | | 1.1766 |
| 1.50 | | | | 1.2281 | 1.3500 |
| 1.75 | | | | 1.4155 | 1.4941 |
| 2.00 | | | 1.3539 | 1.5567 | 1.6122 |
| 2.50 | | 1.4025 | 1.6333 | 1.7549 | 1.7874 |
| 3.00 | 1.4201 | 1.6434 | 1.8019 | 1.8837 | 1.9054 |
| 4.00 | 1.7716 | 1.8994 | 1.9878 | 2.0326 | 2.0444 |
| 5.00 | 1.9429 | 2.0256 | 2.0821 | 2.1104 | 2.1178 |
| 7.50 | 2.1192 | 2.1564 | 2.1814 | 2.1939 | 2.1972 |
| 10.00 | 2.1828 | 2.2038 | 2.2179 | 2.2249 | 2.2267 |
| 15.00 | 2.2289 | 2.2382 | 2.2445 | 2.2476 | 2.2484 |
| 20.00 | 2.2452 | 2.2504 | 2.2540 | 2.2557 | 2.2562 |
| 40.00 | 2.2609 | 2.2622 | 2.2631 | 2.2635 | 2.2637 |
| $\infty$ | 2.2662 | 2.2662 | 2.2662 | 2.2662 | 2.2662 |

Double Sided Sheet

$c/(d+t) = 0.500 \qquad b/(a+t) = 0$

| $\frac{d+t}{S}$ | $\frac{a+t}{d+t} = 1.000$ | $\frac{a+t}{d+t} = 1.200$ | $\frac{a+t}{d+t} = 1.500$ | $\frac{a+t}{d+t} = 2.000$ | $\frac{a+t}{d+t} = 4.000$ |
|---|---|---|---|---|---|
| 1.00 | | | | | 1.9454 |
| 1.25 | | | | | 2.3532 |
| 1.50 | | | | 2.4562 | 2.7000 |
| 1.75 | | | | 2.8311 | 2.9881 |
| 2.00 | | | 2.7078 | 3.1134 | 3.2244 |
| 2.50 | | 2.8050 | 3.2666 | 3.5098 | 3.5749 |
| 3.00 | 2.8403 | 3.2868 | 3.6038 | 3.7674 | 3.8108 |
| 4.00 | 3.5432 | 3.7987 | 3.9757 | 4.0652 | 4.0887 |
| 5.00 | 3.8859 | 4.0511 | 4.1641 | 4.2208 | 4.2356 |
| 7.50 | 4.2385 | 4.3127 | 4.3629 | 4.3878 | 4.3943 |
| 10.00 | 4.3657 | 4.4076 | 4.4358 | 4.4498 | 4.4534 |
| 15.00 | 4.4578 | 4.4765 | 4.4890 | 4.4952 | 4.4968 |
| 20 00 | 4.4903 | 4.5009 | 4.5079 | 4.5114 | 4.5123 |
| 40.00 | 4.5218 | 4.5245 | 4.5262 | 4.5271 | 4.5273 |
| $\infty$ | 4.5324 | 4.5324 | 4.5324 | 4.5324 | 4.5324 |

## Table VII—Four Point Probe Conversion Factors for Rectangles

Insulated Edge Sheet

$c/d = 0.$ $b/a = 0.100$

| $d/S$ | $a/d = 1.000$ | $a/d = 1.200$ | $a/d = 1.500$ | $a/d = 2.000$ | $a/d = 4.000$ |
|---|---|---|---|---|---|
| 1.00 | | | | | 0.9993 |
| 1.25 | | | | | 1.2467 |
| 1.50 | | | | | 1.4893 |
| 1.75 | | | | | 1.7239 |
| 2.00 | | | | 1.9341 | 1.9475 |
| 2.50 | | | 2.2859 | 2.3487 | 2.3541 |
| 3.00 | | | 2.6639 | 2.6976 | 2.7005 |
| 4.00 | 3.0068 | 3.1482 | 3.2082 | 3.2233 | 3.2246 |
| 5 00 | 3.4487 | 3.5305 | 3.5654 | 3.5742 | 3.5750 |
| 7.50 | 3.9840 | 4.0176 | 4.0319 | 4.0355 | 4.0358 |
| 10.00 | 4.2072 | 4.2256 | 4.2335 | 4.2355 | 4.2356 |
| 15.00 | 4.3818 | 4.3899 | 4.3934 | 4.3942 | 4.3943 |
| 20.00 | 4.4464 | 4.4510 | 4.4529 | 4.4534 | 4.4534 |
| 40.00 | 4.5106 | 4.5117 | 4.5122 | 4.5123 | 4.5123 |
| ∞ | 4.5324 | 4.5324 | 4.5324 | 4.5324 | 4.5324 |

Double Sided Sheet

$c/(d + t) = 0.$ $b/(a + t) = 0.100$

| $\frac{d+t}{S}$ | $\frac{a+t}{d+t} = 1.000$ | $\frac{a+t}{d+t} = 1.200$ | $\frac{a+t}{d+t} = 1.500$ | $\frac{a+t}{d+t} = 2.000$ | $\frac{a+t}{d+t} = 4.000$ |
|---|---|---|---|---|---|
| 1.00 | | | | | 1.9609 |
| 1.25 | | | | | 2.3594 |
| 1.50 | | | | | 2.7034 |
| 1.75 | | | | | 2.9903 |
| 2.00 | | | | 3.4342 | 3.2259 |
| 2.50 | | | 4.0306 | 3.6978 | 3.5757 |
| 3.00 | | | 4.1124 | 3.8925 | 3.8113 |
| 4.00 | 4.7200 | 4.4504 | 4.2513 | 4.1330 | 4.0890 |
| 5.00 | 4.6254 | 4.4616 | 4.3378 | 4.2635 | 4.2358 |
| 7.50 | 4.5621 | 4.4926 | 4.4390 | 4.4065 | 4.3944 |
| 10.00 | 4.5468 | 4.5083 | 4.4784 | 4.4603 | 4.4535 |
| 15.00 | 4.5381 | 4.5211 | 4.5079 | 4 4999 | 4.4969 |
| 20.00 | 4.5354 | 4.5259 | 4.5185 | 4.5140 | 4.5123 |
| 40.00 | 4.5331 | 4.5307 | 4.5289 | 4.5277 | 4.5273 |
| ∞ | 4.5324 | 4.5324 | 4.5324 | 4.5324 | 4.5324 |

## Table VIII—Four Point Probe Conversion Factors for Rectangles

Insulated Edge Sheet

$c/d = 0.100$ $b/a = 0.100$

| $d/S$ | $a/d = 1.000$ | $a/d = 1.200$ | $a/d = 1.500$ | $a/d = 2.000$ | $a/d = 4.000$ |
|---|---|---|---|---|---|
| 1.00 | | | | | 0.9964 |
| 1.25 | | | | | 1.2405 |
| 1.50 | | | | | 1.4778 |
| 1.75 | | | | | 1.7061 |
| 2.00 | | | | 1.8996 | 1.9232 |
| 2.50 | | | 2.2323 | 2.3047 | 2.3181 |
| 3.00 | | | 2.6030 | 2.6473 | 2.6568 |
| 4.00 | 2.9402 | 3.0792 | 3.1459 | 3.1701 | 3.1760 |
| 5.00 | 3.3844 | 3.4678 | 3.5095 | 3.5256 | 3.5298 |
| 7.50 | 3.9400 | 3.9762 | 3.9952 | 4.0030 | 4.0051 |
| 10.00 | 4.1780 | 4.1985 | 4.2094 | 4.2140 | 4.2153 |
| 15.00 | 4.3672 | 4.3764 | 4.3814 | 4.3835 | 4.3741 |
| 20.00 | 4.4378 | 4.4430 | 4.4458 | 4.4471 | 4.4474 |
| 40.00 | 4.5083 | 4.5096 | 4.5103 | 4.5106 | 4.5107 |
| ∞ | 4.5324 | 4.5324 | 4.5324 | 4.5324 | 4.5324 |

Double Sided Sheet

$c/(d + t) = 0.100$ $b/(a + t) = 0.100$

| $\frac{d+t}{S}$ | $\frac{a+t}{d+t} = 1.000$ | $\frac{a+t}{d+t} = 1.200$ | $\frac{a+t}{d+t} = 1.500$ | $\frac{a+t}{d+t} = 2.000$ | $\frac{a+t}{d+t} = 4.000$ |
|---|---|---|---|---|---|
| 1.00 | | | | | 1.9584 |
| 1.25 | | | | | 2.3584 |
| 1.50 | | | | | 2.7029 |
| 1.75 | | | | | 2.9899 |
| 2.00 | | | | 3.4003 | 3.2256 |
| 2.50 | | | 3.9670 | 3.6766 | 3.5756 |
| 3.00 | | | 4.0671 | 3.8780 | 3.8112 |
| 4.00 | 4.6529 | 4.4024 | 4.2253 | 4.1250 | 4.0890 |
| 5.00 | 4.5813 | 4.4302 | 4.3211 | 4.2584 | 4.2358 |
| 7.50 | 4.5420 | 4.4784 | 4.4315 | 4.4043 | 4.3944 |
| 10.00 | 4.5354 | 4.5003 | 4.4742 | 4.4590 | 4.4535 |
| 15.00 | 4.5330 | 4.5175 | 4.5060 | 4.4993 | 4.4969 |
| 20.00 | 4.5325 | 4.5239 | 4.5175 | 4.5137 | 4.5123 |
| 40.00 | 4.5324 | 4.5302 | 4.5286 | 4.5277 | 4.5273 |
| ∞ | 4.5324 | 4.5324 | 4.5324 | 4.5324 | 4.5324 |

## Table IX—Four Point Probe Conversion Factors for Rectangles

Insulated Edge Sheet

$c/d = 0.200$ $b/a = 0.100$

| $d/S$ | $a/d = 1.000$ | $a/d = 1.200$ | $a/d = 1.500$ | $a/d = 2.000$ | $a/d = 4.000$ |
|---|---|---|---|---|---|
| 1.00 | | | | | 0.9885 |
| 1.25 | | | | | 1.2235 |
| 1.50 | | | | | 1.4461 |
| 1.75 | | | | | 1.6562 |
| 2.00 | | | | 1.8043 | 1.8537 |
| 2.50 | | | 2.0797 | 2.1788 | 2.2117 |
| 3.00 | | | 2.4261 | 2.4976 | 2.5226 |
| 4.00 | 2.7315 | 2.8679 | 2.9541 | 3.0010 | 3.0178 |
| 5.00 | 3.1765 | 3.2675 | 3.3288 | 3.3630 | 3.3753 |
| 7.50 | 3.7885 | 3.8348 | 3.8674 | 3.8859 | 3.8926 |
| 10.00 | 4.0744 | 4.1026 | 4.1226 | 4.1340 | 4.1381 |
| 15.00 | 4.3138 | 4.3271 | 4.3367 | 4.3422 | 4.3441 |
| 20.00 | 4.4061 | 4.4138 | 4.4193 | 4.4225 | 4.4236 |
| 40.00 | 4.4999 | 4.5019 | 4.5033 | 4.5042 | 4.5045 |
| $\infty$ | 4.5324 | 4.5324 | 4.5324 | 4.5324 | 4.5324 |

Double Sided Sheet

$c/(d+t) = 0.200$ $b/(a+t) = 0.100$

| $\frac{d+t}{S}$ | $\frac{a+t}{d+t} = 1.000$ | $\frac{a+t}{d+t} = 1.200$ | $\frac{a+t}{d+t} = 1.500$ | $\frac{a+t}{d+t} = 2.000$ | $\frac{a+t}{d+t} = 4.000$ |
|---|---|---|---|---|---|
| 1.00 | | | | | 1.9518 |
| 1.25 | | | | | 2.3558 |
| 1.50 | | | | | 2.7014 |
| 1.75 | | | | | 2.9890 |
| 2.00 | | | | 3.3059 | 3.2250 |
| 2.50 | | | 3.7832 | 3.6188 | 3.5752 |
| 3.00 | | | 3.9378 | 3.8389 | 3.8110 |
| 4.00 | 4.4425 | 4.2593 | 4.1522 | 4.1035 | 4.0888 |
| 5.00 | 4.4431 | 4.3373 | 4.2743 | 4.2448 | 4.2357 |
| 7.50 | 4.4790 | 4.4366 | 4.4107 | 4.3983 | 4.3943 |
| 10.00 | 4.4997 | 4.4767 | 4.4625 | 4.4556 | 4.4534 |
| 15.00 | 4.5170 | 4.5070 | 4.5008 | 4.4978 | 4.4969 |
| 20.00 | 4.5236 | 4.5180 | 4.5145 | 4.5129 | 4.5123 |
| 40.00 | 4.5301 | 4.5287 | 4.5279 | 4.5275 | 4.5273 |
| $\infty$ | 4.5324 | 4.5324 | 4.5324 | 4.5324 | 4.5324 |

## Table X—Four Point Probe Conversion Factors for Rectangles

Insulated Edge Sheet

$c/d = 0.300$ $b/a = 0.100$

| $d/S$ | $a/d = 1.000$ | $a/d = 1.200$ | $a/d = 1.500$ | $a/d = 2.000$ | $a/d = 4.000$ |
|---|---|---|---|---|---|
| 1.00 | | | | | 0.9786 |
| 1.25 | | | | | 1.2012 |
| 1.50 | | | | | 1.4031 |
| 1.75 | | | | | 1.5863 |
| 2.00 | | | | 1.6736 | 1.7530 |
| 2.50 | | | 1.8593 | 1.9946 | 2.0467 |
| 3.00 | | | 2.1594 | 2.2613 | 2.3000 |
| 4.00 | 2.3720 | 2.5147 | 2.6260 | 2.6945 | 2.7201 |
| 5.00 | 2.7913 | 2.8983 | 2.9825 | 3.0337 | 3.0527 |
| 7.50 | 3.4592 | 3.5226 | 3.5720 | 3.6016 | 3.6124 |
| 10.00 | 3.8270 | 3.8687 | 3.9008 | 3.9200 | 3.9270 |
| 15.00 | 4.1744 | 4.1957 | 4.2120 | 4.2217 | 4.2252 |
| 20.00 | 4.3203 | 4.3329 | 4.3426 | 4.3484 | 4.3505 |
| 40.00 | 4.4764 | 4.4798 | 4.4824 | 4.4839 | 4.4844 |
| $\infty$ | 4.5324 | 4.5324 | 4.5324 | 4.5324 | 4.5324 |

Double Sided Sheet

$c/(d+t) = 0.300$ $b/(a+t) = 0.100$

| $\frac{d+t}{S}$ | $\frac{a+t}{d+t} = 1.000$ | $\frac{a+t}{d+t} = 1.200$ | $\frac{a+t}{d+t} = 1.500$ | $\frac{a+t}{d+t} = 2.000$ | $\frac{a+t}{d+t} = 4.000$ |
|---|---|---|---|---|---|
| 1.00 | | | | | 1.9435 |
| 1.25 | | | | | 2.3525 |
| 1.50 | | | | | 2.6996 |
| 1.75 | | | | | 2.9878 |
| 2.00 | | | | 3.1760 | 3.2242 |
| 2.50 | | | 3.5083 | 3.5422 | 3.5747 |
| 3.00 | | | 3.7510 | 3.7879 | 3.8107 |
| 4.00 | 4.0782 | 4.0364 | 4.0499 | 4.0759 | 4.0887 |
| 5.00 | 4.2066 | 4.1950 | 4.2096 | 4.2274 | 4.2356 |
| 7.50 | 4.3730 | 4.3736 | 4.3823 | 4.3907 | 4.3943 |
| 10.00 | 4.4400 | 4.4413 | 4.4466 | 4.4514 | 4.4534 |
| 15.00 | 4.4904 | 4.4913 | 4.4938 | 4.4959 | 4.4968 |
| 20.00 | 4.5086 | 4.5092 | 4.5106 | 4.5118 | 4.5123 |
| 40.00 | 4.5264 | 4.5265 | 4.5269 | 4.5272 | 4.5273 |
| $\infty$ | 4.5324 | 4.5324 | 4.5324 | 4.5324 | 4.5324 |

## Table XI—Four Point Probe Conversion Factors for Rectangles

Insulated Edge Sheet

$c/d = 0.400$ $b/a = 0.100$

| $d/S$ | $a/d = 1.000$ | $a/d = 1.200$ | $a/d = 1.500$ | $a/d = 2.000$ | $a/d = 4.000$ |
|---|---|---|---|---|---|
| 1.00 | | | | | 0.9703 |
| 1.25 | | | | | 1.1820 |
| 1.50 | | | | | 1.3646 |
| 1.75 | | | | | 1.5209 |
| 2.00 | | | | 1.5537 | 1.6547 |
| 2.50 | | | 1.6423 | 1.8091 | 1.8705 |
| 3.00 | | | 1.8792 | 1.9966 | 2.0393 |
| 4.00 | 1.9280 | 2.0841 | 2.2048 | 2.2759 | 2.3015 |
| 5.00 | 2.2469 | 2.3605 | 2.4465 | 2.4966 | 2.5145 |
| 7.50 | 2.7986 | 2.8648 | 2.9140 | 2.9423 | 2.9523 |
| 10.00 | 3.1911 | 3.2368 | 3.2705 | 3.2898 | 3.2966 |
| 15.00 | 3.7005 | 3.7267 | 3.7458 | 3.7568 | 3.7606 |
| 20.00 | 3.9858 | 4.0027 | 4.0150 | 4.0219 | 4.0244 |
| 40.00 | 4.3686 | 4.3736 | 4.3772 | 4.3792 | 4.3800 |
| $\infty$ | 4.5324 | 4.5324 | 4.5324 | 4.5324 | 4.5324 |

Double Sided Sheet

$c/(d + t) = 0.400$ $b/(a + t) = 0.100$

| $\frac{d+t}{S}$ | $\frac{a+t}{d+t} = 1.000$ | $\frac{a+t}{d+t} = 1.200$ | $\frac{a+t}{d+t} = 1.500$ | $\frac{a+t}{d+t} = 2.000$ | $\frac{a+t}{d+t} = 4.000$ |
|---|---|---|---|---|---|
| 1.00 | | | | | 1.9367 |
| 1.25 | | | | | 2.3498 |
| 1.50 | | | | | 2.6982 |
| 1.75 | | | | | 2.9869 |
| 2.00 | | | | 3.0566 | 3.2235 |
| 2.50 | | | 3.2235 | 3.4755 | 3.5744 |
| 3.00 | | | 3.5696 | 3.7444 | 3.8104 |
| 4.00 | 3.6212 | 3.7988 | 3.9552 | 4.0526 | 4.0885 |
| 5.00 | 3.9241 | 4.0485 | 4.1508 | 4.2129 | 4.2355 |
| 7.50 | 4.2518 | 4.3106 | 4.3569 | 4.3843 | 4.3943 |
| 10.00 | 4.3726 | 4.4063 | 4.4324 | 4.4478 | 4.4534 |
| 15.00 | 4.4607 | 4.4759 | 4.4875 | 4.4944 | 4.4968 |
| 20.00 | 4.4919 | 4.5005 | 4.5071 | 4.5109 | 4.5123 |
| 40.00 | 4.5222 | 4.5244 | 4.5260 | 4.5270 | 4.5273 |
| $\infty$ | 4.5324 | 4.5324 | 4.5324 | 4.5324 | 4.5324 |

## Table XII—Four Point Probe Conversion Factors for Rectangles

Insulated Edge Sheet

$c/d = 0.500$ $b/a = 0.100$

| $d/S$ | $a/d = 1.000$ | $a/d = 1.200$ | $a/d = 1.500$ | $a/d = 2.000$ | $a/d = 4.000$ |
|---|---|---|---|---|---|
| 1.00 | | | | | 0.9670 |
| 1.25 | | | | | 1.1744 |
| 1.50 | | | | | 1.3488 |
| 1.75 | | | | | 1.4933 |
| 2.00 | | | | 1.5034 | 1.6116 |
| 2.50 | | | 1.5453 | 1.7243 | 1.7871 |
| 3.00 | | | 1.7453 | 1.8636 | 1.9052 |
| 4.00 | 1.6839 | 1.8439 | 1.9578 | 2.0218 | 2.0442 |
| 5.00 | 1.8899 | 1.9912 | 2.0633 | 2.1036 | 2.1177 |
| 7.50 | 2.0966 | 2.1415 | 2.1733 | 2.1909 | 2.1971 |
| 10.00 | 2.1702 | 2.1955 | 2.2133 | 2.2232 | 2.2267 |
| 15.00 | 2.2233 | 2.2346 | 2.2425 | 2.2469 | 2.2484 |
| 20.00 | 2.2420 | 2.2484 | 2.2528 | 2.2553 | 2.2561 |
| 40.00 | 2.2601 | 2.2617 | 2.2628 | 2.2634 | 2.2637 |
| $\infty$ | 2.2662 | 2.2662 | 2.2662 | 2.2662 | 2.2662 |

Double Sided Sheet

$c/(d + t) = 0.500$ $b/(a + t) = 0.100$

| $\frac{d+t}{S}$ | $\frac{a+t}{d+t} = 1.000$ | $\frac{a+t}{d+t} = 1.200$ | $\frac{a+t}{d+t} = 1.500$ | $\frac{a+t}{d+t} = 2.000$ | $\frac{a+t}{d+t} = 4.000$ |
|---|---|---|---|---|---|
| 1.00 | | | | | 1.9341 |
| 1.25 | | | | | 2.3487 |
| 1.50 | | | | | 2.6976 |
| 1.75 | | | | | 2.9866 |
| 2.00 | | | | 3.0068 | 3.2233 |
| 2.50 | | | 3.0906 | 3.4487 | 3.5742 |
| 3.00 | | | 3.4906 | 3.7271 | 3.8103 |
| 4.00 | 3.3679 | 3.6877 | 3.9157 | 4.0435 | 4.0885 |
| 5.00 | 3.7797 | 3.9824 | 4.1266 | 4.2072 | 4.2355 |
| 7.50 | 4.1931 | 4.2830 | 4.3465 | 4.3818 | 4.3942 |
| 10.00 | 4.3405 | 3.3910 | 4.4266 | 4.4464 | 4.4534 |
| 15.00 | 4.4467 | 4.4692 | 4.4850 | 4.4938 | 4.4968 |
| 20.00 | 4.4841 | 4.4967 | 4.5056 | 4.5106 | 4.5123 |
| 40.00 | 4.5203 | 4.5234 | 4.5257 | 4.5269 | 4.5273 |
| $\infty$ | 4.5324 | 4.5324 | 4.5324 | 4.5324 | 4.5324 |

## Table XIII—Four Point Probe Conversion Factors for Rectangles

Insulated Edge Sheet

$c/d = 0.$ $b/a = 0.200$

| $d/S$ | $a/d = 1.000$ | $a/d = 1.200$ | $a/d = 1.500$ | $a/d = 2.000$ | $a/d = 4.000$ |
|---|---|---|---|---|---|
| 1.00 | | | | | |
| 1.25 | | | | | 1.2451 |
| 1.50 | | | | | 1.4889 |
| 1.75 | | | | | 1.7237 |
| 2.00 | | | | | 1.9475 |
| 2.50 | | | | 2.2874 | 2.3541 |
| 3.00 | | | | 2.6647 | 2.7005 |
| 4.00 | | | 3.1175 | 3.2086 | 3.2246 |
| 5.00 | 3.1345 | 3.3772 | 3.5128 | 3.5656 | 3.5750 |
| 7.50 | 3.8589 | 3.9553 | 4.0103 | 4.0320 | 4.0358 |
| 10.00 | 4.1388 | 4.1915 | 4.2216 | 4.2335 | 4.2356 |
| 15.00 | 4.3520 | 4.3750 | 4.3882 | 4.3934 | 4.3943 |
| 20.00 | 4.4297 | 4.4426 | 4.4500 | 4.4529 | 4.4534 |
| 40.00 | 4.5064 | 4.5096 | 4.5114 | 4.5122 | 4.5123 |
| $\infty$ | 4.5324 | 4.5324 | 4.5324 | 4.5324 | 4.5324 |

Double Sided Sheet

$c/(d+t) = 0.$ $b/(a+t) = 0.200$

| $\frac{d+t}{S}$ | $\frac{a+t}{d+t} = 1.000$ | $\frac{a+t}{d+t} = 1.200$ | $\frac{a+t}{d+t} = 1.500$ | $\frac{a+t}{d+t} = 2.000$ | $\frac{a+t}{d+t} = 4.000$ |
|---|---|---|---|---|---|
| 1.00 | | | | | |
| 1.25 | | | | | 2.4187 |
| 1.50 | | | | | 2.7359 |
| 1.75 | | | | | 3.0111 |
| 2.00 | | | | | 3.2405 |
| 2.50 | | | | 3.9559 | 3.5843 |
| 3.00 | | | | 4.0662 | 3.8170 |
| 4.00 | | | 4.4278 | 4.2278 | 4.0921 |
| 5.00 | 4.7608 | 4.5990 | 4.4499 | 4.3234 | 4.2377 |
| 7.50 | 4.6225 | 4.5536 | 4.4885 | 4.4329 | 4.3952 |
| 10.00 | 4.5809 | 4.5426 | 4.5062 | 4.4750 | 4.4539 |
| 15.00 | 4.5532 | 4.5364 | 4.5202 | 4.5064 | 4.4971 |
| 20.00 | 4.5440 | 4.5345 | 4.5255 | 4.5177 | 4.5124 |
| 40.00 | 4.5352 | 4.5329 | 4.5306 | 4.5287 | 4.5274 |
| $\infty$ | 4.5324 | 4.5324 | 4.5324 | 4.5324 | 4.5324 |

## Table XIV—Four Point Probe Conversion Factors for Rectangles

Insulated Edge Sheet

$c/d = 0.100$ $b/a = 0.200$

| $d/S$ | $a/d = 1.000$ | $a/d = 1.200$ | $a/d = 1.500$ | $a/d = 2.000$ | $a/d = 4.000$ |
|---|---|---|---|---|---|
| 1.00 | | | | | |
| 1.25 | | | | | 1.2362 |
| 1.50 | | | | | 1.4756 |
| 1.75 | | | | | 1.7047 |
| 2.00 | | | | | 1.9222 |
| 2.50 | | | | 2.2374 | 2.3174 |
| 3.00 | | | | 2.6069 | 2.6562 |
| 4.00 | | | 3.0539 | 3.1484 | 3.1757 |
| 5.00 | 3.0884 | 3.3212 | 3.4534 | 3.5113 | 3.5295 |
| 7.50 | 3.8212 | 3.9148 | 3.9704 | 3.9962 | 4.0050 |
| 10.00 | 4.1126 | 4.1642 | 4.1953 | 4.2100 | 4.2152 |
| 15.00 | 4.3385 | 4.3612 | 4.3750 | 4.3816 | 4.3840 |
| 20.00 | 4.4217 | 4.4345 | 4.4422 | 4.4460 | 4.4474 |
| 40.00 | 4.5043 | 4.5075 | 4.5094 | 4.5104 | 4.5107 |
| $\infty$ | 4.5324 | 4.5324 | 4.5324 | 4.5324 | 4.5324 |

Double Sided Sheet

$c/(d+t) = 0.100$ $b/(a+t) = 0.200$

| $\frac{d+t}{S}$ | $\frac{a+t}{d+t} = 1.000$ | $\frac{a+t}{d+t} = 1.200$ | $\frac{a+t}{d+t} = 1.500$ | $\frac{a+t}{d+t} = 2.000$ | $\frac{a+t}{d+t} = 4.000$ |
|---|---|---|---|---|---|
| 1.00 | | | | | |
| 1.25 | | | | | 2.4074 |
| 1.50 | | | | | 2.7294 |
| 1.75 | | | | | 3.0068 |
| 2.00 | | | | | 3.2375 |
| 2.50 | | | | 3.9067 | 3.5825 |
| 3.00 | | | | 4.0296 | 3.8158 |
| 4.00 | | | 4.3898 | 4.2062 | 4.0915 |
| 5.00 | 4.7307 | 4.5683 | 4.4239 | 4.3093 | 4.2373 |
| 7.50 | 4.6071 | 4.5384 | 4.4762 | 4.4265 | 4.3951 |
| 10.00 | 4.5718 | 4.5337 | 4.4992 | 4.4714 | 4.4538 |
| 15.00 | 4.5491 | 4.5323 | 4.5171 | 4.5048 | 4.4970 |
| 20.00 | 4.5416 | 4.5322 | 4.5237 | 4.5168 | 4.5124 |
| 40.00 | 4.5346 | 4.5323 | 4.5302 | 4.5284 | 4.5274 |
| $\infty$ | 4.5324 | 4.5324 | 4.5324 | 4.5324 | 4.5324 |

## Table XV—Four Point Probe Conversion Factors for Rectangles

Insulated Edge Sheet

$c/d = 0.200 \quad b/a = 0.200$

| $d/S$ | $a/d = 1.000$ | $a/d = 1.200$ | $a/d = 1.500$ | $a/d = 2.000$ | $a/d = 4.000$ |
|---|---|---|---|---|---|
| 1.00 | | | | | |
| 1.25 | | | | | 1.2121 |
| 1.50 | | | | | 1.4396 |
| 1.75 | | | | | 1.6517 |
| 2.00 | | | | | 1.8503 |
| 2.50 | | | | 2.0931 | 2.2094 |
| 3.00 | | | | 2.4367 | 2.5209 |
| 4.00 | | | 2.8538 | 2.9614 | 3.0166 |
| 5.00 | 2.9283 | 3.1329 | 3.2598 | 3.3342 | 3.3745 |
| 7.50 | 3.6832 | 3.7711 | 3.8316 | 3.8704 | 3.8921 |
| 10.00 | 4.0140 | 4.0647 | 4.1007 | 4.1244 | 4.1378 |
| 15.00 | 4.2861 | 4.3094 | 4.3263 | 4.3376 | 4.3440 |
| 20.00 | 4.3903 | 4.4036 | 4.4133 | 4.4198 | 4.4236 |
| 40.00 | 4.4959 | 4.4993 | 4.5018 | 4.5035 | 4.5044 |
| $\infty$ | 4.5324 | 4.5324 | 4.5324 | 4.5324 | 4.5324 |

Double Sided Sheet

$c/(d+t) = 0.200 \quad b/(a+t) = 0.200$

| $\frac{d+t}{S}$ | $\frac{a+t}{d+t} = 1.000$ | $\frac{a+t}{d+t} = 1.200$ | $\frac{a+t}{d+t} = 1.500$ | $\frac{a+t}{d+t} = 2.000$ | $\frac{a+t}{d+t} = 4.000$ |
|---|---|---|---|---|---|
| 1.00 | | | | | |
| 1.25 | | | | | 2.3768 |
| 1.50 | | | | | 2.7121 |
| 1.75 | | | | | 2.9957 |
| 2.00 | | | | | 3.2296 |
| 2.50 | | | | 3.7584 | 3.5779 |
| 3.00 | | | | 3.9223 | 3.8128 |
| 4.00 | | | 4.2683 | 4.1442 | 4.0898 |
| 5.00 | 4.6181 | 4.4612 | 4.3420 | 4.2693 | 4.2363 |
| 7.50 | 4.5493 | 4.4861 | 4.4382 | 4.4086 | 4.3946 |
| 10.00 | 4.5377 | 4.5034 | 4.4774 | 4.4613 | 4.4536 |
| 15.00 | 4.5334 | 4.5186 | 4.5073 | 4.5003 | 4.4969 |
| 20.00 | 4.5327 | 4.5244 | 4.5182 | 4.5142 | 4.5123 |
| 40.00 | 4.5324 | 4.5303 | 4.5288 | 4.5278 | 4.5273 |
| $\infty$ | 4.5324 | 4.5324 | 4.5324 | 4.5324 | 4.5324 |

## Table XVI—Four Point Probe Conversion Factors for Rectangles

Insulated Edge Sheet

$c/d = 0.300$ $b/a = 0.200$

| $d/S$ | $a/d = 1.000$ | $a/d = 1.200$ | $a/d = 1.500$ | $a/d = 2.000$ | $a/d = 4.000$ |
|---|---|---|---|---|---|
| 1.00 | | | | | |
| 1.25 | | | | | 1.1809 |
| 1.50 | | | | | 1.3916 |
| 1.75 | | | | | 1.5786 |
| 2.00 | | | | | 1.7473 |
| 2.50 | | | | 1.8795 | 2.0430 |
| 3.00 | | | | 2.1753 | 2.2973 |
| 4.00 | | | 2.5060 | 2.6369 | 2.7183 |
| 5.00 | 2.5907 | 2.7616 | 2.8926 | 2.9907 | 3.0514 |
| 7.50 | 3.3551 | 3.4443 | 3.5196 | 3.5768 | 3.6116 |
| 10.00 | 3.7602 | 3.8176 | 3.8668 | 3.9040 | 3.9265 |
| 15.00 | 4.1405 | 4.1697 | 4.1947 | 4.2136 | 4.2250 |
| 20.00 | 4.3001 | 4.3175 | 4.3324 | 4.3436 | 4.3503 |
| 40.00 | 4.4711 | 4.4757 | 4.4796 | 4.4826 | 4.4844 |
| $\infty$ | 4.5324 | 4.5324 | 4.5324 | 4.5324 | 4.5324 |

Double Sided Sheet

$c/(d + t) = 0.300$ $b/(a + t) = 0.200$

| $\frac{d+t}{S}$ | $\frac{a+t}{d+t} = 1.000$ | $\frac{a+t}{d+t} = 1.200$ | $\frac{a+t}{d+t} = 1.500$ | $\frac{a+t}{d+t} = 2.000$ | $\frac{a+t}{d+t} = 4.000$ |
|---|---|---|---|---|---|
| 1.00 | | | | | |
| 1.25 | | | | | 2.3364 |
| 1.50 | | | | | 2.6901 |
| 1.75 | | | | | 2.9816 |
| 2.00 | | | | | 3.2197 |
| 2.50 | | | | 3.5218 | 3.5721 |
| 3.00 | | | | 3.7603 | 3.8089 |
| 4.00 | | | 4.0533 | 4.0551 | 4.0877 |
| 5.00 | 4.3434 | 4.2388 | 4.2024 | 4.2130 | 4.2350 |
| 7.50 | 4.4122 | 4.3821 | 4.3757 | 4.3838 | 4.3940 |
| 10.00 | 4.4580 | 4.4441 | 4.4422 | 4.4474 | 4.4533 |
| 15.00 | 4.4972 | 4.4920 | 4.4917 | 4.4942 | 4.4968 |
| 20.00 | 4.5122 | 4.5094 | 4.5094 | 4.5108 | 4.5123 |
| 40.00 | 4.5272 | 4.5266 | 4.5266 | 4.5270 | 4.5273 |
| $\infty$ | 4.5324 | 4.5324 | 4.5324 | 4.5324 | 4.5324 |

## Table XVII—Four Point Probe Conversion Factors for Rectangles

Insulated Edge Sheet

$c/d = 0.400$ $b/a = 0.200$

| $d/S$ | $a/d = 1.000$ | $a/d = 1.200$ | $a/d = 1.500$ | $a/d = 2.000$ | $a/d = 4.000$ |
|---|---|---|---|---|---|
| 1.00 | | | | | |
| 1.25 | | | | | 1.1542 |
| 1.50 | | | | | 1.3494 |
| 1.75 | | | | | 1.5111 |
| 2.00 | | | | | 1.6477 |
| 2.50 | | | | 1.6645 | 1.8662 |
| 3.00 | | | | 1.8960 | 2.0363 |
| 4.00 | | | 2.0700 | 2.2156 | 2.2997 |
| 5.00 | 2.0458 | 2.2102 | 2.3514 | 2.4543 | 2.5133 |
| 7.50 | 2.6821 | 2.7787 | 2.8602 | 2.9185 | 2.9516 |
| 10.00 | 3.1105 | 3.1777 | 3.2338 | 3.2736 | 3.2961 |
| 15.00 | 3.6540 | 3.6929 | 3.7250 | 3.7476 | 3.7604 |
| 20.00 | 3.9559 | 3.9810 | 4.0016 | 4.0161 | 4.0242 |
| 40.00 | 4.3597 | 4.3671 | 4.3732 | 4.3775 | 4.3799 |
| $\infty$ | 4.5324 | 4.5324 | 4.5324 | 4.5324 | 4.5324 |

Double Sided Sheet

$c/(d + t) = 0.400$ $b/(a + t) = 0.200$

| $\frac{d+t}{S}$ | $\frac{a+t}{d+t} = 1.000$ | $\frac{a+t}{d+t} = 1.200$ | $\frac{a+t}{d+t} = 1.500$ | $\frac{a+t}{d+t} = 2.000$ | $\frac{a+t}{d+t} = 4.000$ |
|---|---|---|---|---|---|
| 1.00 | | | | | |
| 1.25 | | | | | 2.3014 |
| 1.50 | | | | | 2.6718 |
| 1.75 | | | | | 2.9701 |
| 2.00 | | | | | 3.2117 |
| 2.50 | | | | 3.2608 | 3.5674 |
| 3.00 | | | | 3.5961 | 3.8058 |
| 4.00 | | | 3.7889 | 3.9704 | 4.0860 |
| 5.00 | 3.7970 | 3.9021 | 4.0414 | 4.1606 | 4.2339 |
| 7.50 | 4.1715 | 4.2390 | 4.3073 | 4.3613 | 4.3936 |
| 10.00 | 4.3241 | 4.3650 | 4.4044 | 4.4349 | 4.4530 |
| 15.00 | 4.4382 | 4.4572 | 4.4750 | 4.4886 | 4.4967 |
| 20.00 | 4.4791 | 4.4900 | 4.5000 | 4.5077 | 4.5122 |
| 40.00 | 4.5190 | 4.5217 | 4.5242 | 4.5262 | 4.5273 |
| $\infty$ | 4.5324 | 4.5324 | 4.5324 | 4.5324 | 4.5324 |

## Table XVIII—Four Point Probe Conversion Factors for Rectangles

Insulated Edge Sheet

$c/d = 0.500$ $b/a = 0.200$

| $d/S$ | $a/d = 1.000$ | $a/d = 1.200$ | $a/d = 1.500$ | $a/d = 2.000$ | $a/d = 4.000$ |
|---|---|---|---|---|---|
| 1.00 | | | | | |
| 1.25 | | | | | 1.1437 |
| 1.50 | | | | | 1.3323 |
| 1.75 | | | | | 1.4828 |
| 2.00 | | | | | 1.6043 |
| 2.50 | | | | 1.5672 | 1.7828 |
| 3.00 | | | | 1.7614 | 1.9023 |
| 4.00 | | | 1.8259 | 1.9673 | 2.0427 |
| 5.00 | 1.6678 | 1.8474 | 1.9815 | 2.0694 | 2.1168 |
| 7.50 | 2.0041 | 2.0801 | 2.1378 | 2.1760 | 2.1967 |
| 10.00 | 2.1191 | 2.1613 | 2.1935 | 2.2149 | 2.2265 |
| 15.00 | 2.2009 | 2.2195 | 2.2337 | 2.2432 | 2.2483 |
| 20.00 | 2.2294 | 2.2399 | 2.2479 | 2.2532 | 2.2561 |
| 40.00 | 2.2570 | 2.2596 | 2.2616 | 2.2629 | 2.2636 |
| ∞ | 2.2662 | 2.2662 | 2.2662 | 2.2662 | 2.2662 |

Double Sided Sheet

$c/(d + t) = 0.500$ $b/(a + t) = 0.200$

| $\frac{d+t}{S}$ | $\frac{a+t}{d+t} = 1.000$ | $\frac{a+t}{d+t} = 1.200$ | $\frac{a+t}{d+t} = 1.500$ | $\frac{a+t}{d+t} = 2.000$ | $\frac{a+t}{d+t} = 4.000$ |
|---|---|---|---|---|---|
| 1.00 | | | | | |
| 1.25 | | | | | 2.2874 |
| 1.50 | | | | | 2.6647 |
| 1.75 | | | | | 2.9656 |
| 2.00 | | | | | 3.2086 |
| 2.50 | | | | 3.1345 | 3.5656 |
| 3.00 | | | | 3.5229 | 3.8046 |
| 4.00 | | | 3.6519 | 3.9345 | 4.0854 |
| 5.00 | 3.3357 | 3.6948 | 3.9629 | 4.1388 | 4.2335 |
| 7.50 | 4.0083 | 4.1601 | 4.2756 | 4.3520 | 4.3934 |
| 10.00 | 4.2382 | 4.3227 | 4.3870 | 4.4297 | 4.4529 |
| 15.00 | 4.4017 | 4.4390 | 4.4675 | 4.4864 | 4.4966 |
| 20.00 | 4.4589 | 4.4798 | 4.4958 | 4.5064 | 4.5122 |
| 40.00 | 4.5140 | 4.5192 | 4.5232 | 4.5259 | 4.5273 |
| ∞ | 4.5324 | 4.5324 | 4.5324 | 4.5324 | 4.5324 |

## Table XIX—Four Point Probe Conversion Factors for Rectangles

Insulated Edge Sheet

$c/d = 0.$ $b/a = 0.300$

| $d/S$ | $a/d = 1.000$ | $a/d = 1.200$ | $a/d = 1.500$ | $a/d = 2.000$ | $a/d = 4.000$ |
|---|---|---|---|---|---|
| 1.00 | | | | | |
| 1.25 | | | | | |
| 1.50 | | | | | |
| 1.75 | | | | | |
| 2.00 | | | | | 1.9342 |
| 2.50 | | | | | 2.3488 |
| 3.00 | | | | | 2.6976 |
| 4.00 | | | | 3.0207 | 3.2233 |
| 5.00 | | | 3.1364 | 3.4573 | 3.5742 |
| 7.50 | 3.3137 | 3.6363 | 3.8599 | 3.9877 | 4.0355 |
| 10.00 | 3.8480 | 4.0185 | 4.1394 | 4.2092 | 4.2355 |
| 15.00 | 4.2264 | 4.2998 | 4.3523 | 4.3828 | 4.3942 |
| 20.00 | 4.3597 | 4.4006 | 4.4299 | 4.4470 | 4.4534 |
| 40.00 | 4.4890 | 4.4992 | 4.5065 | 4.5107 | 4.5123 |
| ∞ | 4.5324 | 4.5324 | 4.5324 | 4.5324 | 4.5324 |

Double Sided Sheet

$c/(d+t) = 0.$ $b/(a+t) = 0.300$

| $\frac{d+t}{S}$ | $\frac{a+t}{d+t} = 1.000$ | $\frac{a+t}{d+t} = 1.200$ | $\frac{a+t}{d+t} = 1.500$ | $\frac{a+t}{d+t} = 2.000$ | $\frac{a+t}{d+t} = 4.000$ |
|---|---|---|---|---|---|
| 1.00 | | | | | |
| 1.25 | | | | | |
| 1.50 | | | | | |
| 1.75 | | | | | |
| 2.00 | | | | | 3.4160 |
| 2.50 | | | | | 3.6878 |
| 3.00 | | | | | 3.8860 |
| 4.00 | | | | 4.5183 | 4.1295 |
| 5.00 | | | 4.6857 | 4.5081 | 4.2613 |
| 7.50 | 4.7125 | 4.6570 | 4.5933 | 4.5144 | 4.4056 |
| 10.00 | 4.6317 | 4.6009 | 4.5651 | 4.5208 | 4.4597 |
| 15.00 | 4.5759 | 4.5623 | 4.5464 | 4.5267 | 4.4996 |
| 20.00 | 4.5567 | 4.5491 | 4.5402 | 4.5291 | 4.5139 |
| 40.00 | 4.5384 | 4.5365 | 4.5343 | 4.5315 | 4.5277 |
| ∞ | 4.5324 | 4.5324 | 4.5324 | 4.5324 | 4.5324 |

## Table XX—Four Point Probe Conversion Factors for Rectangles

Insulated Edge Sheet

$c/d = 0.100$ $b/a = 0.300$

| $d/S$ | $a/d = 1.000$ | $a/d = 1.200$ | $a/d = 1.500$ | $a/d = 2.000$ | $a/d = 4.000$ |
|---|---|---|---|---|---|
| 1.00 | | | | | |
| 1.25 | | | | | |
| 1.50 | | | | | |
| 1.75 | | | | | |
| 2.00 | | | | | 1.9007 |
| 2.50 | | | | | 2.3055 |
| 3.00 | | | | | 2.6478 |
| 4.00 | | | | 2.9618 | 3.1705 |
| 5.00 | | | 3.0931 | 3.3997 | 3.5259 |
| 7.50 | 3.2943 | 3.6086 | 3.8240 | 3.9476 | 4.0031 |
| 10.00 | 3.8317 | 3.9977 | 4.1143 | 4.1825 | 4.2141 |
| 15.00 | 4.2170 | 4.2885 | 4.3393 | 4.3693 | 4.3835 |
| 20.00 | 4.3539 | 4.3938 | 4.4222 | 4.4390 | 4.4471 |
| 40.00 | 4.4875 | 4.4973 | 4.5044 | 4.5086 | 4.5106 |
| $\infty$ | 4.5324 | 4.5324 | 4.5324 | 4.5324 | 4.5324 |

Double Sided Sheet

$c/(d+t) = 0.100$ $b/(a+t) = 0.300$

| $\frac{d+t}{S}$ | $\frac{a+t}{d+t} = 1.000$ | $\frac{a+t}{d+t} = 1.200$ | $\frac{a+t}{d+t} = 1.500$ | $\frac{a+t}{d+t} = 2.000$ | $\frac{a+t}{d+t} = 4.000$ |
|---|---|---|---|---|---|
| 1.00 | | | | | |
| 1.25 | | | | | |
| 1.50 | | | | | |
| 1.75 | | | | | |
| 2.00 | | | | | 3.3858 |
| 2.50 | | | | | 3.6685 |
| 3.00 | | | | | 3.8728 |
| 4.00 | | | | 4.4810 | 4.1222 |
| 5.00 | | | 4.6662 | 4.4813 | 4.2566 |
| 7.50 | 4.7137 | 4.6520 | 4.5820 | 4.5013 | 4.4035 |
| 10.00 | 4.6317 | 4.5974 | 4.5582 | 4.5131 | 4.4586 |
| 15.00 | 4.5757 | 4.5605 | 4.5432 | 4.5233 | 4.4991 |
| 20.00 | 4.5566 | 4.5481 | 4.5383 | 4.5271 | 4.5136 |
| 40.00 | 4.5384 | 4.5363 | 4.5338 | 4.5310 | 4.5276 |
| $\infty$ | 4.5324 | 4.5324 | 4.5324 | 4.5324 | 4.5324 |

## Table XXI—Four Point Probe Conversion Factors for Rectangles

Insulated Edge Sheet

$c/d = 0.200$ $b/a = 0.300$

| $d/S$ | $a/d = 1.000$ | $a/d = 1.200$ | $a/d = 1.500$ | $a/d = 2.000$ | $a/d = 4.000$ |
|---|---|---|---|---|---|
| 1.00 | | | | | |
| 1.25 | | | | | |
| 1.50 | | | | | |
| 1.75 | | | | | |
| 2.00 | | | | | 1.8077 |
| 2.50 | | | | | 2.1812 |
| 3.00 | | | | | 2.4995 |
| 4.00 | | | | 2.7720 | 3.0022 |
| 5.00 | | | 2.9396 | 3.2080 | 3.3639 |
| 7.50 | 3.2150 | 3.4999 | 3.6905 | 3.8065 | 3.8864 |
| 10.00 | 3.7634 | 3.9138 | 4.0187 | 4.0857 | 4.1343 |
| 15.00 | 4.1766 | 4.2418 | 4.2884 | 4.3192 | 4.3423 |
| 20.00 | 4.3289 | 4.3654 | 4.3917 | 4.4093 | 4.4226 |
| 40.00 | 4.4806 | 4.4897 | 4.4963 | 4.5007 | 4.5042 |
| ∞ | 4.5324 | 4.5324 | 4.5324 | 4.5324 | 4.5324 |

Double Sided Sheet

$c/(d + t) = 0.200$ $b/(a + t) = 0.300$

| $\frac{d+t}{S}$ | $\frac{a+t}{d+t} = 1.000$ | $\frac{a+t}{d+t} = 1.200$ | $\frac{a+t}{d+t} = 1.500$ | $\frac{a+t}{d+t} = 2.000$ | $\frac{a+t}{d+t} = 4.000$ |
|---|---|---|---|---|---|
| 1.00 | | | | | |
| 1.25 | | | | | |
| 1.50 | | | | | |
| 1.75 | | | | | |
| 2.00 | | | | | 3.3004 |
| 2.50 | | | | | 3.6157 |
| 3.00 | | | | | 3.8369 |
| 4.00 | | | | 4.3519 | 4.1024 |
| 5.00 | | | 4.5820 | 4.3905 | 4.2441 |
| 7.50 | 4.7042 | 4.6211 | 4.5352 | 4.4576 | 4.3980 |
| 10.00 | 4.6230 | 4.5771 | 4.5301 | 4.4879 | 4.4555 |
| 15.00 | 4.5707 | 4.5506 | 4.5301 | 4.5119 | 4.4978 |
| 20.00 | 4.5535 | 4.5423 | 4.5309 | 4.5207 | 4.5128 |
| 40.00 | 4.5376 | 4.5348 | 4.5319 | 4.5294 | 4.5275 |
| ∞ | 4.5324 | 4.5324 | 4.5324 | 4.5324 | 4.5324 |

## Table XXII—Four Point Probe Conversion Factors for Rectangles

Insulated Edge Sheet

$c/d = 0.300$ $b/a = 0.300$

| $d/S$ | $a/d = 1.000$ | $a/d = 1.200$ | $a/d = 1.500$ | $a/d = 2.000$ | $a/d = 4.000$ |
|---|---|---|---|---|---|
| 1.00 | | | | | |
| 1.25 | | | | | |
| 1.50 | | | | | |
| 1.75 | | | | | |
| 2.00 | | | | | 1.6792 |
| 2.50 | | | | | 1.9984 |
| 3.00 | | | | | 2.2641 |
| 4.00 | | | | 2.4283 | 2.6964 |
| 5.00 | | | 2.6075 | 2.8365 | 3.0351 |
| 7.50 | 2.9833 | 3.2084 | 3.3665 | 3.4872 | 3.6024 |
| 10.00 | 3.5491 | 3.6726 | 3.7679 | 3.8456 | 3.9205 |
| 15.00 | 4.0408 | 4.0979 | 4.1446 | 4.1840 | 4.2220 |
| 20.00 | 4.2420 | 4.2751 | 4.3026 | 4.3260 | 4.3485 |
| 40.00 | 4.4560 | 4.4645 | 4.4718 | 4.4779 | 4.4839 |
| ∞ | 4.5324 | 4.5324 | 4.5324 | 4.5324 | 4.5324 |

Double Sided Sheet

$c/(d+t) = 0.300$ $b/(a+t) = 0.300$

| $\frac{d+t}{S}$ | $\frac{a+t}{d+t} = 1.000$ | $\frac{a+t}{d+t} = 1.200$ | $\frac{a+t}{d+t} = 1.500$ | $\frac{a+t}{d+t} = 2.000$ | $\frac{a+t}{d+t} = 4.000$ |
|---|---|---|---|---|---|
| 1.00 | | | | | |
| 1.25 | | | | | |
| 1.50 | | | | | |
| 1.75 | | | | | |
| 2.00 | | | | | 3.1805 |
| 2.50 | | | | | 3.5449 |
| 3.00 | | | | | 3.7897 |
| 4.00 | | | | 4.0884 | 4.0769 |
| 5.00 | | | 4.3423 | 4.2144 | 4.2280 |
| 7.50 | 4.6078 | 4.4946 | 4.4119 | 4.3770 | 4.3909 |
| 10.00 | 4.5564 | 4.4985 | 4.4579 | 4.4423 | 4.4515 |
| 15.00 | 4.5371 | 4.5133 | 4.4972 | 4.4915 | 4.4960 |
| 20.00 | 4.5339 | 4.5209 | 4.5122 | 4.5092 | 4.5118 |
| 40.00 | 4.5325 | 4.5293 | 4.5272 | 4.5265 | 4.5272 |
| ∞ | 4.5324 | 4.5324 | 4.5324 | 4.5324 | 4.5324 |

## Table XXIII—Four Point Probe Conversion Factors for Rectangles

Insulated Edge Sheet

$c/d = 0.400$ $b/a = 0.300$

| $d/S$ | $a/d = 1.000$ | $a/d = 1.200$ | $a/d = 1.500$ | $a/d = 2.000$ | $a/d = 4.000$ |
|---|---|---|---|---|---|
| 1.00 | | | | | |
| 1.25 | | | | | |
| 1.50 | | | | | |
| 1.75 | | | | | |
| 2.00 | | | | | 1.5604 |
| 2.50 | | | | | 1.8134 |
| 3.00 | | | | | 1.9996 |
| 4.00 | | | | 1.9827 | 2.2778 |
| 5.00 | | | 2.0607 | 2.2895 | 2.4979 |
| 7.50 | 2.3738 | 2.5410 | 2.6924 | 2.8250 | 2.9430 |
| 10.00 | 2.8994 | 3.0123 | 3.1180 | 3.2096 | 3.2903 |
| 15.00 | 3.5308 | 3.5969 | 3.6585 | 3.7112 | 3.7570 |
| 20.00 | 3.8758 | 3.9189 | 3.9588 | 3.9928 | 4.0221 |
| 40.00 | 4.3356 | 4.3486 | 4.3606 | 4.3706 | 4.3793 |
| $\infty$ | 4.5324 | 4.5324 | 4.5324 | 4.5324 | 4.5324 |

Double Sided Sheet

$c/(d+t) = 0.400$ $b/(a+t) = 0.300$

| $\frac{d+t}{S}$ | $\frac{a+t}{d+t} = 1.000$ | $\frac{a+t}{d+t} = 1.200$ | $\frac{a+t}{d+t} = 1.500$ | $\frac{a+t}{d+t} = 2.000$ | $\frac{a+t}{d+t} = 4.000$ |
|---|---|---|---|---|---|
| 1.00 | | | | | |
| 1.25 | | | | | |
| 1.50 | | | | | |
| 1.75 | | | | | |
| 2.00 | | | | | 3.0681 |
| 2.50 | | | | | 3.4825 |
| 3.00 | | | | | 3.7491 |
| 4.00 | | | | 3.6999 | 4.0553 |
| 5.00 | | | 3.8172 | 3.9776 | 4.2145 |
| 7.50 | 4.1431 | 4.1234 | 4.1814 | 4.2771 | 4.3851 |
| 10.00 | 4.2733 | 4.2859 | 4.3298 | 4.3871 | 4.4482 |
| 15.00 | 4.4063 | 4.4183 | 4.4409 | 4.4673 | 4.4946 |
| 20.00 | 4.4595 | 4.4674 | 4.4806 | 4.4956 | 4.5110 |
| 40.00 | 4.5137 | 4.5159 | 4.5194 | 4.5231 | 4.5270 |
| $\infty$ | 4.5324 | 4.5324 | 4.5324 | 4.5324 | 4.5324 |

## Table XXIV—Four Point Probe Conversion Factors for Rectangles

Insulated Edge Sheet

$c/d = 0.500$ $b/a = 0.300$

| $d/S$ | $a/d = 1.000$ | $a/d = 1.200$ | $a/d = 1.500$ | $a/d = 2.000$ | $a/d = 4.000$ |
|---|---|---|---|---|---|
| 1.00 | | | | | |
| 1.25 | | | | | |
| 1.50 | | | | | |
| 1.75 | | | | | |
| 2.00 | | | | | 1.5103 |
| 2.50 | | | | | 1.7287 |
| 3.00 | | | | | 1.8665 |
| 4.00 | | | | 1.7316 | 2.0234 |
| 5.00 | | | 1.6789 | 1.9240 | 2.1046 |
| 7.50 | 1.6878 | 1.8696 | 2.0106 | 2.1132 | 2.1914 |
| 10.00 | 1.9485 | 2.0459 | 2.1230 | 2.1798 | 2.2235 |
| 15.00 | 2.1268 | 2.1689 | 2.2027 | 2.2277 | 2.2470 |
| 20.00 | 2.1880 | 2.2116 | 2.2305 | 1.2445 | 2.2553 |
| 40.00 | 2.2467 | 2.2526 | 2.2573 | 2.2607 | 2.2635 |
| $\infty$ | 2.2662 | 2.2662 | 2.2662 | 2.2662 | 2.2662 |

Double Sided Sheet

$c/(d+t) = 0.500$ $b/(a+t) = 0.300$

| $\frac{d+t}{S}$ | $\frac{a+t}{d+t} = 1.000$ | $\frac{a+t}{d+t} = 1.200$ | $\frac{a+t}{d+t} = 1.500$ | $\frac{a+t}{d+t} = 2.000$ | $\frac{a+t}{d+t} = 4.000$ |
|---|---|---|---|---|---|
| 1.00 | | | | | |
| 1.25 | | | | | |
| 1.50 | | | | | |
| 1.75 | | | | | |
| 2.00 | | | | | 3.0207 |
| 2.50 | | | | | 3.4573 |
| 3.00 | | | | | 3.7330 |
| 4.00 | | | | 3.4632 | 4.0468 |
| 5.00 | | | 3.3578 | 3.8480 | 4.2092 |
| 7.50 | 3.3755 | 3.7392 | 4.0211 | 4.2264 | 4.3828 |
| 10.00 | 3.8970 | 4.0917 | 4.2460 | 4.3597 | 4.4469 |
| 15.00 | 4.2535 | 4.3379 | 4.4054 | 4.4554 | 4.4940 |
| 20.00 | 4.3761 | 4.4232 | 4.4610 | 4.4890 | 4.5107 |
| 40.00 | 4.4934 | 4.5051 | 4.5145 | 4.5214 | 4.5269 |
| $\infty$ | 4.5324 | 4.5324 | 4.5324 | 4.5324 | 4.5324 |

## Table XXV—Four Point Probe Conversion Factors for Rectangles

Insulated Edge Sheet

$c/d = 0.$ $b/a = 0.400$

| $d/S$ | $a/d = 1.000$ | $a/d = 1.200$ | $a/d = 1.500$ | $a/d = 2.000$ | $a/d = 4.000$ |
|---|---|---|---|---|---|
| 1.00 | | | | | |
| 1.25 | | | | | |
| 1.50 | | | | | |
| 1.75 | | | | | |
| 2.00 | | | | | |
| 2.50 | | | | | |
| 3.00 | | | | | |
| 4.00 | | | | | 3.0207 |
| 5.00 | | | | | 3.4573 |
| 7.50 | | | | 3.3139 | 3.9877 |
| 10.00 | | | 3.3588 | 3.8481 | 4.2092 |
| 15.00 | 3.3790 | 3.7411 | 4.0217 | 4.2264 | 4.3828 |
| 20.00 | 3.8996 | 4.0929 | 4.2463 | 4.3597 | 4.4469 |
| 40.00 | 4.3769 | 4.4235 | 4.4611 | 4.4890 | 4.5107 |
| $\infty$ | 4.5324 | 4.5324 | 4.5324 | 4.5324 | 4.5324 |

Double Sided Sheet

$c/(d+t) = 0.$ $b/(a+t) = 0.400$

| $\frac{d+t}{S}$ | $\frac{a+t}{d+t} = 1.000$ | $\frac{a+t}{d+t} = 1.200$ | $\frac{a+t}{d+t} = 1.500$ | $\frac{a+t}{d+t} = 2.000$ | $\frac{a+t}{d+t} = 4.000$ |
|---|---|---|---|---|---|
| 1.00 | | | | | |
| 1.25 | | | | | |
| 1.50 | | | | | |
| 1.75 | | | | | |
| 2.00 | | | | | |
| 2.50 | | | | | |
| 3.00 | | | | | |
| 4.00 | | | | | 4.5179 |
| 5.00 | | | | | 4.5079 |
| 7.50 | | | | 4.6912 | 4.5143 |
| 10.00 | | | 4.6490 | 4.6204 | 4.5207 |
| 15.00 | 4.5981 | 4.5915 | 4.5838 | 4.5711 | 4.5267 |
| 20.00 | 4.5692 | 4.5655 | 4.5612 | 4.5540 | 4.5291 |
| 40.00 | 4.5415 | 4.5406 | 4.5396 | 4.5377 | 4.5315 |
| $\infty$ | 4.5324 | 4.5324 | 4.5324 | 4.5324 | 4.5324 |

## TABLE XXVI—FOUR POINT PROBE CONVERSION FACTORS FOR RECTANGLES

Insulated Edge Sheet

$c/d = 0.100$ $b/a = 0.400$

| $d/S$ | $a/d = 1.000$ | $a/d = 1.200$ | $a/d = 1.500$ | $a/d = 2.000$ | $a/d = 4.000$ |
|---|---|---|---|---|---|
| 1.00 | | | | | |
| 1.25 | | | | | |
| 1.50 | | | | | |
| 1.75 | | | | | |
| 2.00 | | | | | |
| 2.50 | | | | | |
| 3.00 | | | | | |
| 4.00 | | | | | 2.9619 |
| 5.00 | | | | | 3.3997 |
| 7.50 | | | | 3.2950 | 3.9477 |
| 10.00 | | | 3.3505 | 3.8323 | 4.1826 |
| 15.00 | 3.3769 | 3.7375 | 4.0159 | 4.2173 | 4.3693 |
| 20.00 | 3.8979 | 4.0904 | 4.2426 | 4.3541 | 4.4390 |
| 40.00 | 4.3763 | 4.4228 | 4.4600 | 4.4875 | 4.5086 |
| ∞ | 4.5324 | 4.5324 | 4.5324 | 4.5324 | 4.5324 |

Double Sided Sheet

$c/(d + t) = 0.100$ $b/(a + t) = 0.400$

| $\frac{d+t}{S}$ | $\frac{a+t}{d+t} = 1.000$ | $\frac{a+t}{d+t} = 1.200$ | $\frac{a+t}{d+t} = 1.500$ | $\frac{a+t}{d+t} = 2.000$ | $\frac{a+t}{d+t} = 4.000$ |
|---|---|---|---|---|---|
| 1.00 | | | | | |
| 1.25 | | | | | |
| 1.50 | | | | | |
| 1.75 | | | | | |
| 2.00 | | | | | |
| 2.50 | | | | | |
| 3.00 | | | | | |
| 4.00 | | | | | 4.4807 |
| 5.00 | | | | | 4.4812 |
| 7.50 | | | | 4.6949 | 4.5012 |
| 10.00 | | | 4.6576 | 4.6218 | 4.5131 |
| 15.00 | 4.6050 | 4.5972 | 4.5874 | 4.5714 | 4.5232 |
| 20.00 | 4.5731 | 4.5687 | 4.5632 | 4.5542 | 4.5271 |
| 40.00 | 4.5425 | 4.5414 | 4.5401 | 4.5378 | 4.5310 |
| ∞ | 4.5324 | 4.5324 | 4.5324 | 4.5324 | 4.5324 |

## Table XXVII—Four Point Probe Conversion Factors for Rectangles

Insulated Edge Sheet

$c/d = 0.200$ $b/a = 0.400$

| $d/S$ | $a/d = 1.000$ | $a/d = 1.200$ | $a/d = 1.500$ | $a/d = 2.000$ | $a/d = 4.000$ |
|---|---|---|---|---|---|
| 1.00 | | | | | |
| 1.25 | | | | | |
| 1.50 | | | | | |
| 1.75 | | | | | |
| 2.00 | | | | | |
| 2.50 | | | | | |
| 3.00 | | | | | |
| 4.00 | | | | | 2.7720 |
| 5.00 | | | | | 3.2081 |
| 7.50 | | | | 3.2172 | 3.8065 |
| 10.00 | | | 3.3128 | 3.7650 | 4.0857 |
| 15.00 | 3.3662 | 3.7202 | 3.9890 | 4.1775 | 4.3192 |
| 20.00 | 3.8895 | 4.0783 | 4.2250 | 4.3293 | 4.4093 |
| 40.00 | 4.3736 | 4.4191 | 4.4550 | 4.4807 | 4.5008 |
| $\infty$ | 4.5324 | 4.5324 | 4.5324 | 4.5324 | 4.5324 |

Double Sided Sheet

$c/(d+t) = 0.200$ $b/(a+t) = 0.400$

| $\frac{d+t}{S}$ | $\frac{a+t}{d+t} = 1.000$ | $\frac{a+t}{d+t} = 1.200$ | $\frac{a+t}{d+t} = 1.500$ | $\frac{a+t}{d+t} = 2.000$ | $\frac{a+t}{d+t} = 4.000$ |
|---|---|---|---|---|---|
| 1.00 | | | | | |
| 1.25 | | | | | |
| 1.50 | | | | | |
| 1.75 | | | | | |
| 2.00 | | | | | |
| 2.50 | | | | | |
| 3.00 | | | | | |
| 4.00 | | | | | 4.3517 |
| 5.00 | | | | | 4.3904 |
| 7.50 | | | | 4.6922 | 4.4575 |
| 10.00 | | | 4.6800 | 4.6167 | 4.4879 |
| 15.00 | 4.6288 | 4.6151 | 4.5962 | 4.5680 | 4.5119 |
| 20.00 | 4.5863 | 4.5786 | 4.5679 | 4.5520 | 4.5207 |
| 40.00 | 4.5458 | 4.5438 | 4.5412 | 4.5371 | 4.5294 |
| $\infty$ | 4.5324 | 4.5324 | 4.5324 | 4.5324 | 4.5324 |

## Table XXVIII—Four Point Probe Conversion Factors for Rectangles

Insulated Edge Sheet

$c/d = 0.300$ $b/a = 0.400$

| $d/S$ | $a/d = 1.000$ | $a/d = 1.200$ | $a/d = 1.500$ | $a/d = 2.000$ | $a/d = 4.000$ |
|---|---|---|---|---|---|
| 1.00 | | | | | |
| 1.25 | | | | | |
| 1.50 | | | | | |
| 1.75 | | | | | |
| 2.00 | | | | | |
| 2.50 | | | | | |
| 3.00 | | | | | |
| 4.00 | | | | | 2.4284 |
| 5.00 | | | | | 2.8366 |
| 7.50 | | | | 2.9868 | 3.4873 |
| 10.00 | | | 3.1754 | 3.5519 | 3.8456 |
| 15.00 | 3.3173 | 3.6457 | 3.8834 | 4.0423 | 4.1840 |
| 20.00 | 3.8497 | 4.0240 | 4.1538 | 4.2429 | 4.3260 |
| 40.00 | 4.3599 | 4.4019 | 4.4338 | 4.4561 | 4.4780 |
| ∞ | 4.5324 | 4.5324 | 4.5324 | 4.5324 | 4.5324 |

Double Sided Sheet

$c/(d+t) = 0.300$ $b/(a+t) = 0.400$

| $\frac{d+t}{S}$ | $\frac{a+t}{d+t} = 1.000$ | $\frac{a+t}{d+t} = 1.200$ | $\frac{a+t}{d+t} = 1.500$ | $\frac{a+t}{d+t} = 2.000$ | $\frac{a+t}{d+t} = 4.000$ |
|---|---|---|---|---|---|
| 1.00 | | | | | |
| 1.25 | | | | | |
| 1.50 | | | | | |
| 1.75 | | | | | |
| 2.00 | | | | | |
| 2.50 | | | | | |
| 3.00 | | | | | |
| 4.00 | | | | | 4.0885 |
| 5.00 | | | | | 4.2144 |
| 7.50 | | | | 4.6047 | 4.3770 |
| 10.00 | | | 4.6784 | 4.5547 | 4.4423 |
| 15.00 | 4.6732 | 4.6360 | 4.5890 | 4.5364 | 4.4915 |
| 20.00 | 4.6099 | 4.5888 | 4.5625 | 4.5334 | 4.5092 |
| 40.00 | 4.5513 | 4.5460 | 4.5395 | 4.5323 | 4.5265 |
| ∞ | 4.5324 | 4.5324 | 4.5324 | 4.5324 | 4.5324 |

## Table XXIX—Four Point Probe Conversion Factors for Rectangles

Insulated Edge Sheet

$c/d = 0.400$ $b/a = 0.400$

| $d/S$ | $a/d = 1.000$ | $a/d = 1.200$ | $a/d = 1.500$ | $a/d = 2.000$ | $a/d = 4.000$ |
|---|---|---|---|---|---|
| 1.00 | | | | | |
| 1.25 | | | | | |
| 1.50 | | | | | |
| 1.75 | | | | | |
| 2.00 | | | | | |
| 2.50 | | | | | |
| 3.00 | | | | | |
| 4.00 | | | | | 1.9828 |
| 5.00 | | | | | 2.2896 |
| 7.50 | | | | 2.3770 | 2.8250 |
| 10.00 | | | 2.6425 | 2.9019 | 3.2097 |
| 15.00 | 2.9967 | 3.2263 | 3.3934 | 3.5325 | 3.7112 |
| 20.00 | 3.5598 | 3.6860 | 3.7872 | 3.8768 | 3.9928 |
| 40.00 | 4.2459 | 4.2797 | 4.3089 | 4.3358 | 4.3706 |
| $\infty$ | 4.5324 | 4.5324 | 4.5324 | 4.5324 | 4.5324 |

Double Sided Sheet

$c/(d+t) = 0.400$ $b/(a+t) = 0.400$

| $\frac{d+t}{S}$ | $\frac{a+t}{d+t} = 1.000$ | $\frac{a+t}{d+t} = 1.200$ | $\frac{a+t}{d+t} = 1.500$ | $\frac{a+t}{d+t} = 2.000$ | $\frac{a+t}{d+t} = 4.000$ |
|---|---|---|---|---|---|
| 1.00 | | | | | |
| 1.25 | | | | | |
| 1.50 | | | | | |
| 1.75 | | | | | |
| 2.00 | | | | | |
| 2.50 | | | | | |
| 3.00 | | | | | |
| 4.00 | | | | | 3.7000 |
| 5.00 | | | | | 3.9777 |
| 7.50 | | | | 4.1463 | 4.2771 |
| 10.00 | | | 4.3750 | 4.2751 | 4.3871 |
| 15.00 | 4.6073 | 4.5018 | 4.4276 | 4.4071 | 4.4673 |
| 20.00 | 4.5562 | 4.5026 | 4.4671 | 4.4598 | 4.4956 |
| 40.00 | 4.5338 | 4.5219 | 4.5146 | 4.5137 | 4.5232 |
| $\infty$ | 4.5324 | 4.5324 | 4.5324 | 4.5324 | 4.5324 |

## Table XXX —Four Point Probe Conversion Factors for Rectangles

Insulated Edge Sheet

$c/d = 0.500$ $b/a = 0.400$

| $d/S$ | $a/d = 1.000$ | $a/d = 1.200$ | $a/d = 1.500$ | $a/d = 2.000$ | $a/d = 4.000$ |
|---|---|---|---|---|---|
| 1.00 | | | | | |
| 1.25 | | | | | |
| 1.50 | | | | | |
| 1.75 | | | | | |
| 2.00 | | | | | |
| 2.50 | | | | | |
| 3.00 | | | | | |
| 4.00 | | | | | 1.7317 |
| 5.00 | | | | | 1.9240 |
| 7.50 | | | | 1.6895 | 2.1132 |
| 10.00 | | | 1.6914 | 1.9498 | 2.1799 |
| 15.00 | 1.6921 | 1.8751 | 2.0188 | 2.1274 | 2.2277 |
| 20.00 | 1.9518 | 2.0496 | 2.1282 | 2.1884 | 2.2445 |
| 40.00 | 2.1891 | 2.2127 | 2.2319 | 2.2467 | 2.2608 |
| ∞ | 2.2662 | 2.2662 | 2.2662 | 2.2662 | 2.2662 |

Double Sided Sheet

$c/(d + t) = 0.500$ $b/(a + t) = 0.400$

| $\frac{d+t}{S}$ | $\frac{a+t}{d+t} = 1.000$ | $\frac{a+t}{d+t} = 1.200$ | $\frac{a+t}{d+t} = 1.500$ | $\frac{a+t}{d+t} = 2.000$ | $\frac{a+t}{d+t} = 4.000$ |
|---|---|---|---|---|---|
| 1.00 | | | | | |
| 1.25 | | | | | |
| 1.50 | | | | | |
| 1.75 | | | | | |
| 2.00 | | | | | |
| 2.50 | | | | | |
| 3.00 | | | | | |
| 4.00 | | | | | 3.4634 |
| 5.00 | | | | | 3.8481 |
| 7.50 | | | | 3.3790 | 4.2264 |
| 10.00 | | | 3.3829 | 3.8996 | 4.3597 |
| 15.00 | 3.3842 | 3.7502 | 4.0376 | 4.2548 | 4.4554 |
| 20.00 | 3.9035 | 4.0992 | 4.2564 | 4.3767 | 4.4890 |
| 40.00 | 4.3781 | 4.4254 | 4.4639 | 4.4935 | 4.5215 |
| ∞ | 4.5324 | 4.5324 | 4.5324 | 4.5324 | 4.5324 |

REFERENCES

1. Smits, F. M., Measurement of Sheet Resistivities with the Four-Point Probe, B.S.T.J., *37,* May, 1958, pp. 711–718.
2. Logan, M. A., An A-C Bridge for Semi-conductor Resistivity Measurements Using a Four-Point Probe, B.S.T.J., *40,* May, 1961, pp. 885–920.
3. Bowman, F., *Introduction to Elliptic Functions with Applications,* Dover Publications, S922, 1961.
4. Ref. 3 Chapter VI is one of many books.
5. Wilson, E. B., Advanced Calculus Chapter XVIII, Section 177 (Uses a different notation).
6. Ref. 3, IV, *Art. 4.*
7. Henderson, F. M., *Elliptic Functions with Complex Arguments,* University of Michigan Press, 1960.
8. Milne-Thomson, L. M., *Jacobian Elliptic Function Tables,* Dover Publications S194, 1950.
9. Ref. 8, Table on p. 106 with definition on page 13.

# Scaling Laws for Large Shields in Quasi-Stationary Magnetic Fields

By G. KRONACHER

(Manuscript received August 10, 1967)

*The application of the classical scaling laws of electro-magnetic fields to the design of a scaled-down model of, say, a building-sized shield is often difficult, even when using the simplifications permissible with a quasi-stationary magnetic field. The reasons are that (i) the scaled wall thickness often becomes impractically thin and (ii) the required scaling of frequency sometimes reduces the ratio of intrinsic wave-length in air to the enclosure length such that the quasi-stationary field theory no longer applies.*

*In the case of a completely closed shield these limitations can be circumvented by having a model with two distinct geometric scaling factors, one for the wall thickness and one for the overall dimensions. The modified scaling laws governing this type of model are derived.*

## I. INTRODUCTION

Protection of electronic equipment against electromagnetic interference is often achieved by providing a metallic enclosure. Large electronic complexes, such as radar installations and data processing centers may be protected by covering the entire building with a metallic shield. (Some penetrations into this enclosure are usually required for the purpose of air-vents, cable-inlets, access tunnels etc.) The performance of the enclosure is measured by the shielding effectiveness, which is the ratio of the field strength at an exterior location where the field is undisturbed by the shield to the field strength at a point inside the enclosure.

A first approximation of the shielding effectiveness can be obtained analytically.[1] In this case, (*i*) constant permeability is assumed, and (*ii*) the actual shape of the enclosure is replaced by a geometrically simpler shape, such as an infinite cylindrical shell or a spherical shell.

The evaluation of the shielding effectiveness by testing is, for economical reasons, best conducted on scaled down models of the enclosure. The following discussion concerns itself with the constraints on the scaling-factors for distance, time, conductivity, etc., necessary to produce a model either having the same shielding effectiveness as the original, full-scale enclosure or having one of known relation to it. It will be seen that full compliance with the ideal constraints on scaling-factors is rarely possible. However, useful results can be obtained with partial compliance, especially in the case of large enclosures.

## II. IDEAL CONSTRAINTS ON SCALING FACTORS

An ideal, scaled model is a replica of the original configuration with each physical parameter scaled up or down by a fixed ratio. To each point in space and time of the original exists a corresponding point in the model. The ratio of any distance, time, field strength, etc. of the original to its counterpart in the model is called a scaling-factor. If one identifies any parameter or variable of the original with the index "1" and of the model with the index "2" one can write the scaling-factors for distance, time, electric and magnetic field strength, permeability (instantaneous ratio of magnetic flux density to magnetic field strength), dielectric constant, conductivity as $l_2/l_1$, $t_2/t_1$, $E_2/E_1$, $H_2/H_1$, $\mu_2/\mu_1$, $\epsilon_2/\epsilon_1$, $\sigma_2/\sigma_1$. (For instance, $l_1$, represents the distance between two arbitrarily selected points of the original, full-scaled enclosure, whereas, $l_2$ represents the distance between the corresponding points of the model.) Were these scaling-factors selected arbitrarily, the model would not be physically realizable because the electromagnetic field of the model would not satisfy Maxwell's equations. These equations when formulated for the original and for the model contain the constraints required to make the model physically realizable. They also interrelate the scaling-factors for electric and magnetic field strengths. The results* are expressed by (1), (2), and (3)

$$\left(\frac{E_2}{E_1}\right)\cdot\left(\frac{H_1}{H_2}\right) = \left(\frac{l_2}{l_1}\right)\cdot\left(\frac{t_1}{t_2}\right)\cdot\left(\frac{\mu_2}{\mu_1}\right) \tag{1}$$

$$\frac{l_2^2\cdot\sigma_2\cdot\mu_2}{t_2} = \frac{l_1^2\cdot\sigma_1\cdot\mu_1}{t_1} \tag{2}$$

$$\frac{l_2^2\cdot\epsilon_2\cdot\mu_2}{t_2^2} = \frac{l_1^2\cdot\epsilon_1\cdot\mu_1}{t_1^2}. \tag{3}$$

* For the mathematical derivation see either Appendix A or Ref. 2, p. 488.

Introducing the angular frequency, $\omega$, one obtains the following scaling constraints for CW fields:

$$l_2^2\omega_2\sigma_2\mu_2 = l_1^2\omega_1\sigma_1\mu_1 \tag{4}$$

$$l_2^2\omega_2^2\epsilon_2\mu_2 = l_1^2\omega_1^2\epsilon_1\mu_1 \tag{5}$$

## III. INTERPRETATION OF THE MATHEMATICAL RESULTS

First, it should be pointed out that the derivation of (2) and (3) is not based on a field-strength-independent permeability or dielectric constant. Consequently, model tests of ferromagnetic shields of variable permeability will give correct answers, provided the model uses the same steel as the original, is tested at the field strength encountered in the original and satisfies (2) and (3).

Second, the shielding effectiveness, $\eta$, of geometrically similar models changes from model to model only if the expressions (2) and (3) change. In other words, the shielding effectiveness of geometrically similar models is a function of these two dimensionless quantities only, i.e.,

$$\eta = f\left[\left(\frac{l^2\cdot\sigma\cdot\mu}{t}\right), \left(\frac{l^2\cdot\epsilon\cdot\mu}{t^2}\right)\right]. \tag{6}$$

Here, $l$ might be the length of the enclosure, $t$, the pulse duration, etc.

The physical meaning of (4) and (5) becomes clearer if we introduce the skin depth,* $\delta$, of a conductor of constant permeability and the intrinsic wavelength in a pure dielectric, $\lambda_\epsilon$:

$$\delta = \sqrt{\frac{2}{\omega\mu\sigma}} \tag{7}$$

$$\lambda_\epsilon = \frac{2\pi}{\omega\sqrt{\epsilon\mu}}. \tag{8}$$

Substituting these values into (4) and (5) one obtains

$$\frac{l_2}{\delta_2} = \frac{l_1}{\delta_1} \tag{9}$$

$$\frac{l_2}{\lambda_{\epsilon_2}} = \frac{l_1}{\lambda_{\epsilon_1}} \tag{10}$$

* Here $(2\pi\delta)$ is equal to the intrinsic wavelength in metal, $\lambda_\sigma$.

In other words, the skin depth of the shield material as well as the intrinsic wavelength of the surrounding space have to be scaled by the same ratio as the linear dimensions of the model.

It can now be seen that it usually is not feasible to produce a model which satisfies both (2) and (3). For instance, after the scaling factor $(l_2/l_1)$ has been selected, (2) and (3) can be satisfied only if two other parameters, such as conductivity, $\sigma$, and time, $t$, are properly scaled. Unfortunately, the only scaling factor which usually can be suitably controlled is that of time (duration of an applied pulse, period of an applied ac field). Consequently, only one of the scaling requirements, either (2) or (3) can be readily satisfied. Therefore one has to be content with imperfect models which will be discussed next.

## IV. SEVERAL TYPES OF IMPERFECT MODELS

### 4.1 *The Geometrically Perfect Model in a Quasi-Stationary Magnetic Field*

A model shall be considered geometrically perfect if *all* of its dimensions, the overall dimensions such as width, height, and length as well as the thickness of the shield and the size of its openings are scaled by the same factor.

The quasi-stationary magnetic field is a well known simplifying concept which is applicable whenever the linear dimensions of the configuration are small compared to the intrinsic wavelength of the dielectric medium. It is the magnetic field one obtains mathematically if one assumes the time derivatives of the electric displacement, $\partial/\partial t$ $(\epsilon E)$, to be zero.

In this case, as shown in Appendix A, one obtains only one constraint equation for the scaling factors, namely that expressed by either (2), (4), or (9).

In order to obtain an idea of the error caused by this simplification, one may look at a geometrically simple shield, such as a spherical shell, for which analytical solutions are available.[1] According to a graph given in Ref. 1, the magnetic shielding effectiveness at the center of a spherical shell, if calculated on the basis of a quasi-stationary field, is in error by less than 2.6 dB for a wavelength to diameter ratio of 2.8 or higher. The electric shielding effectiveness (electric field outside of the shielded space to that inside) is equal to the magnetic shielding effectiveness at this wave length to diameter ratio and increases rapidly for higher ratios.

Unfortunately, there are two serious shortcomings to this type of model. First, the wall-thickness of the scaled-down enclosure often becomes impractically thin. For instance the original enclosure may have been built with 0.010-inch thick copper. Assuming a geometric scaling factor of 0.1 the model would have to be built of 0.001-inch thick copper. Second, (assuming identical $\sigma$, $\mu$, and $\epsilon$ for model and original) due to the scaling of frequency, as called for by (4), the ratio of the intrinsic wavelength in air to the length of the model becomes proportional to the geometric scaling factor, $(l_2/l_1)$. This is a simple consequence of (4) and (8). Sometimes, this ratio decreases for the model to the point where the quasi-stationary field theory no longer applies.

As shall be shown next, both of these shortcomings can be circumvented in the case of large enclosures without openings by using two geometric scaling-factors, one for the overall dimensions and one for the wall thickness.

### 4.2 *Models with Two Geometric Scaling-Factors, One for the Overall Dimensions and One for the Wall-Thickness of the Enclosure in Quasi-Stationary Magnetic Fields*

In the following, models of large enclosures without openings will be considered. The scaling factor for the overall dimensions is designated as $(L_2/L_1)$ and that for the wall thickness as $(d_2/d_1)$. (The wall thickness does not have to be uniform). Assuming the wall thickness to be very small compared to the overall dimensions of the enclosure, the spaces internal and external to the enclosure of the model remain geometrically similar to those of the original.

With this in mind, it will be shown that the internal and external magnetic fields of this type of model, *individually,* are substantially similar to those of the original if the ratio of shield thickness to skin-depth remains unchanged.

The validity of this statement rests on two simplifying assumptions: namely (*i*) that, the external magnetic field is almost identical to that outside of an enclosure of infinite conductivity (the field component normal to the surface is negligible compared to the tangential one), and (*ii*) that within the shield (see Fig. 1) the rates of change of the tangential magnetic and electric field strength in the direction normal to the surface $(\partial H_z/\partial y)$ and $(\partial E_x/\partial y)$ are much larger than the rate of change of the field strengths normal to the surface in the tangential direction $(\partial H_y/\partial z)$ and $(\partial E_y/\partial x)$; i.e., $\partial H_y/\partial z \ll \partial H_z/\partial y$ and $\partial E_y/\partial x \ll$

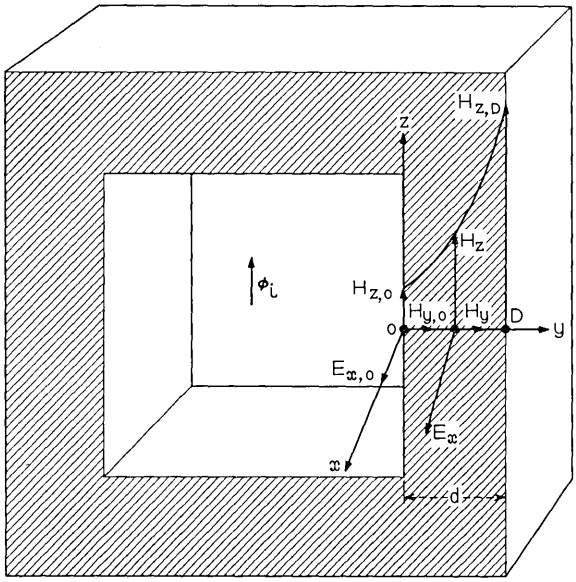


Fig. 1 — Local coordinates of the field in the shield.

$\partial E_x/\partial y$. (The field changes rapidly across the shield but only gradually in the tangential directions.)

From assumption (*ii*) it follows that the tangential magnetic field-strength at some point $D$ on the outside of the shield, $H_{zD}$, is determined by the tangential electric and magnetic field strengths, $H_{z,0}$ and $E_{x,0}$, at the opposing point "0" on the inside surface of the enclosure. Specifically, $H_z$ is governed by the following differential equations:

$$\sigma E_x = \frac{\partial H_z}{\partial y} \tag{11}$$

$$-\frac{\partial}{\partial t}(\mu H_z) = -\frac{\partial E_x}{\partial y} \tag{12}$$

and by the following boundary conditions:

$$\text{At} \quad y = 0: \qquad H_z = H_{z,0}\ ; \qquad E_x = E_{x,0} \tag{13}$$

In the case of a sufficiently large enclosure, the boundary conditions can be simplified. Specifically, Appendix B shows that the effect of $H_{z,0}$ on $H_{z,D}$ can be neglected if the following inequalities are

satisfied:*

$$\frac{\sqrt{2}\cdot 2\cdot(\mu_r)_{\mathrm{av}}\cdot\delta_{\mathrm{av}}}{D} \ll 1; \qquad d > \frac{\delta_{\mathrm{av}}}{\sqrt{2}} \tag{14}$$

$$\frac{2\cdot(\mu_r)_{\mathrm{av}}\cdot\delta_{\mathrm{av}}^2}{d\cdot D} \ll 1; \qquad d < \frac{\delta_{\mathrm{av}}}{\sqrt{2}}. \tag{15}$$

$(\mu_r)_{\mathrm{av}}$ is the average relative permeability of the shield,† and $\delta_{\mathrm{av}}$ is the skin-depth based on $(\mu_r)_{\mathrm{av}}$. The equivalent diameter, $D$, is four times the cross section of the enclosure divided by its circumference, measured in a plane which is normal to the field and which bisects the enclosure. (For simplicity, one may use for $D$ the smallest major dimension of the enclosure.)

If the above inequalities are satisfied the boundary conditions simplify to

$$y = 0: \qquad H_z = 0; \qquad E_x = E_{x,0}\ . \tag{16}$$

Now, let us put the following question: Provided the internal electric and magnetic fields of model and original are similar to each other, under which condition will the external magnetic fields be similar, too? According to assumption (*i*) the only conditions are (*i*) that the distributions of the tangential magnetic field strength at the outside surface of the shield of the model and of the original are similar to each other and (*ii*) that, of course, the applied external fields are similar to each other. With the internal fields being assumed similar to each other, condition (*i*) is satisfied if the field distributions across the shields are similar, too. In consideration of the simplified field equations (11) and (12) this is the case if, (*i*) the general scaling equation (2) is satisfied with respect to the y-coordinate (see Fig. 1), i.e., if

$$\frac{d_2^2\cdot\sigma_2\cdot\mu_2}{t_2} = \frac{d_1^2\cdot\sigma_1\cdot\mu_1}{t_1} \tag{17}‡$$

and (*ii*) if scaling equation (1) is valid for the boundary values $H_{z,0}$ and $E_{x,0}$ (using the shield parameters, $d$ and $\mu_{\mathrm{shield}}$). For the special

* Note, that, for $d > \delta_{\mathrm{av}}/\sqrt{2}$, if inequality (14) is satisfied, inequality (15) will be satisfied too and for $d < \delta_{\mathrm{av}}/\sqrt{2}$, if inequality (15) is satisfied, inequality (14) will be satisfied too.

† If the shield is several skin depths thick, $(\mu_r)_{\mathrm{av}}$ is the permeability near the inside surface of the enclosure.

‡ For field-strength independent $\mu$ the expression $\sqrt{t/\sigma\mu}$ is proportional to the skin-depth, $\delta$, and (17) becomes $d_2/\delta_2 = d_1/\delta_1$.

case of a large enclosure for which inequalities (14) and (15) are valid, it was shown that $H_{z,0}$ may be assumed equal to zero without substantial effect on the external field. However, with $H_{z,0}$ being zero, scaling equation (1) as applied to the boundary values $H_{z,0}$, $E_{x,0}$ is automatically satisfied since the term $(H_1/H_2)$ becomes (0/0). Consequently, internal and external fields of the model and the original are individually similar to each other if (17) and inequalities (14) and (15) are satisfied.

The relation between the shielding effectiveness of model and original is obtained by using (1). Specifically, $(H_{z,D,1})/(H_{z,D,2})$ and $(E_{x,0,1})/(E_{x,0,2})$ are related to each other as follows:

$$\frac{E_{x,0,2}\cdot H_{z,D,1}}{E_{x,0,1}\cdot H_{z,D,2}} = \frac{d_2\cdot t_1\cdot \mu_2}{d_1\cdot t_2\cdot \mu_1}. \tag{18}$$

Applying, again, (1) to the internal air field one obtains

$$\frac{E_{x,0,2}}{E_{x,0,1}}\frac{H_{z,0,1}}{H_{z,0,2}} = \frac{L_2\cdot t_1}{L_1\cdot t_2}. \tag{19}$$

From (18) and (19) one obtains

$$\frac{H_{z,0,2}}{H_{z,0,1}}\cdot\frac{H_{z,D,1}}{H_{z,D,2}} = \frac{d_2\cdot L_1\cdot \mu_2}{d_1\cdot L_2\cdot \mu_1}. \tag{20}$$

Since the ratio $H_{z,D}/H_{z,0}$ is proportional to the shielding effectiveness one obtains the following relation between the shielding effectiveness of model and original:

$$\eta_1 \approx \left(\frac{L_1\cdot d_2\cdot \mu_2}{L_2\cdot d_1\cdot \mu_1}\right)\cdot \eta_2 \ . \tag{21}$$

Note, that (21) is valid only if the similarity requirement for conductors, as expressed by (17), is satisfied, and if the quasi-stationary field theory is applicable (wavelength in air larger than the linear dimensions of the enclosure). If the scaling factor for the overall dimensions $(L_2/L_1)$ is chosen so that the similarity requirement for air is also satisfied [see (3)] it appears that the restriction to quasi-stationary fields can be dropped. Strictly speaking, this is not so. First, at half wavelengths close to or less than the dimensions of the enclosure, the internal field will no longer be approximately uniform, as this was assumed in Appendix B. This assumption was necessary to show that, for large enclosures, the tangential magnetic field component at the inside surface of the shield is of negligible effect on

the magnetic field at the outside surface. However, the higher the frequency the less important becomes the assumption of an approximately uniform magnetic field.

Second, the ratio of magnetic to electric field strength in air along the outside surface of the shield will not satisfy the scaling requirement (1). This latter imperfection, however, will be of minor consequence if the characteristic wave-impedance in the shield is low compared to that of the waves in the external space. In this case, almost complete reflection occurs at the outside wall of the shield, which means that the effect of the tangential electric field strength on the external field is negligible.

All things considered, it is advisable to satisfy for relatively short wavelengths the similarity requirement for air [see (3)].

Appendix C illustrates, with the aid of a numerical example, the above derived scaling laws.

### 4.3 *Shielding Effectiveness of an Enclosure with Uniform Wall*

In Section 4.2 it was shown that the fields internal and external to a model of an enclosure without openings are practically similar to those of the original if the wall of the model is such that the ratio of external tangential magnetic field strength to internal tangential electric field-strength is similar to that of the original. For CW fields, this requirement is satisfied if the inequalities (14) and (15) are satisfied, the shield is uniform along its tangential coordinates (however, it may be nonuniform along the normal coordinate such as in the case of laminated metals) and the permeability and conductivity are constant (field strength independent). Specifically, in the case for which the shield is uniform throughout (including along the normal coordinate), the ratio between tangential magnetic and electric field strength can be given in closed analytical form. According to Appendix D, the external tangential magnetic field strength, $H_{zD}$, is related to the internal tangential electric field strength, $E_{x0}$, (see Fig. 1) as follows:

$$H_{z,D} = \left[\left(\frac{\sigma}{\sqrt{j\omega\mu\sigma}}\right) \sinh\left(\sqrt{j\omega\mu\sigma d^2}\right)\right] E_{x,0} \,. \tag{22}$$

According to the law of induction, $E_{x0}$ is proportional to some representative internal magnetic field strength, $H_i$, to its angular frequency, $\omega$, to a representative linear dimension, $L$, of the shielded space and to its permeability, $\mu_0$ (assuming air). Consequently, one

obtains for $H_{zD}$,

$$H_{z,D} = C\left(\frac{\sigma \cdot \omega \cdot L \cdot \mu_0}{\sqrt{j \cdot \omega\mu\sigma}}\right) \sinh\left(\sqrt{j\omega\mu\sigma d^2}\right) \cdot H_i \tag{23}$$

in which $C$ is a constant independent of the scaling factors. The ratio of $H_{z,D}$ to the internal field strength, $H_i$, is proportional to the shielding effectiveness, $\eta$. Consequently,

$$\eta = K\sqrt{\frac{\omega \cdot \sigma \cdot \mu_0^2}{j \cdot \mu} \cdot L^2} \cdot \sinh\left(\sqrt{j\omega\mu\sigma d^2}\right) \tag{24}$$

in which $K$ is a constant, independent of the scaling factors. It depends only on the geometry of the shielded space, on that of the applied field and on the reference points for external and internal field strengths. $K$ is obtained by measuring $\eta$ on a model of known parameters ($\omega_2$, $L_2$, $\sigma_2$, etc.). Note that, in general, (i.e., if the scaling equation (17) is not satisfied), the scaling factor for $\eta$, i.e., $(\eta_2/\eta_1)$, is frequency dependent. Therefore, the response of the model to a pulsed field is not similar to the response of the original.

For the case that the thickness, $d$, is large compared to the skin depth, $\delta$, one can write (24) in the form

$$\eta \approx \frac{K}{2}\sqrt{\frac{\omega\sigma\mu_0^2}{j\mu} L^2} \exp \sqrt{j\omega\mu\sigma d^2}, \qquad d \gg \delta. \tag{25}$$

For the case in which $d$ is small compared to $\delta$, one can write

$$\eta \approx K(\omega \cdot \mu_0 \sigma \cdot d \cdot L), \qquad d \ll \delta. \tag{26}$$

In the latter case $(\eta_2/\eta_1)$ is frequency independent. Therefore, the model can be used to evaluate the effect of pulsed fields as well as CW fields.

## V. SUMMARY

The shielding effectiveness of the scaled model of a metallic enclosure is identical to that of the original if (*i*) the ratio of the wavelength in air to some specified linear dimension (say, the length of the enclosure) remains unchanged, and (*ii*) the ratio of the skin depth of the shielding material to some specified linear dimension remains unchanged. In the case of nonlinear, ferro-magnetic materials, instead of the second requirement, the expression of length$^2\times$ frequency$\times$conductivity$\times$permeability has to be the same for model and original. Given a certain scaling factor for the length the above

requirements could be met by properly selecting two other scaling factors, say, those for time and conductivity. Usually, however, only the scaling factor for time can be readily controlled. Consequently, one has to be content with imperfect models which, however, will yield good results over given ranges of frequency.

If one is concerned with the magnetic shielding effectiveness only, the first requirement may be waived, provided the intrinsic wavelength in air is large compared to the linear dimensions of the model. For enclosures of building size this applies to frequencies up to several magacycles. Unfortunately, there are two shortcomings to this type of model: (*i*) The shield thickness of the scaled-down model often becomes impractically thin, and (*ii*) due to the necessary scaling of frequency, the ratio of the intrinsic wavelength in air to the length of the model sometimes decreases to the point where the quasi-stationary field-theory becomes invalid. If the enclosure is free of openings one can use a model with one scaling factor for the overall dimensions and another one for the thickness of the shield, provided the scaling factor for time is selected such that the ratio of skin depth to wall thickness remains unchanged. In this case, a simple formula relates the shielding effectiveness of the original to that of the model. If the enclosure is free of openings, of uniform thickness and of a material of constant permeability (nonferromagnetic metal) and if the applied magnetic field varies sinusoidally with time the dependence of the shielding effectiveness on scaling factors can be established analytically. Consequently, no constraints are put on the selection of the scaling factors of the model.

## VI. ACKNOWLEDGMENT

The author appreciates the suggestions and comments supplied by Mr. A. H. Carter of Bell Telephone Laboratories, and Prof. F. A. Russel of Newark College of Engineering.

## APPENDIX A

### *Derivation of the General Scaling Constraints for Electromagnetic Models*

Maxwell's Equations if applied to the original configuration can be written in integral form as follows.

$$\oint_{a_1} \mathbf{E}_1 \cdot \mathrm{d}l_1 = -\frac{\partial}{\partial t_1} \iint_{A_1} \mu_1 \cdot \mathbf{H}_1 \cdot \mathrm{d}s_1 \tag{27}$$

$$\oint_{a_1} \mathbf{H}_1 \cdot \mathbf{d}l_1 = \iint_{A_1} \sigma_1 \cdot \mathbf{E}_1 \cdot \mathbf{d}s_1 + \frac{\partial}{\partial t_1} \iint_{A_1} \epsilon_1 \cdot \mathbf{E}_1 \cdot \mathbf{d}s_1 \tag{28}$$

($a_1$ is a closed path in the original, or model "1". $A_1$ is an area bounded by $a_1$. The symbol $ds_1$ represents a surface element of $A_1$.) Using the corresponding closed path in the model as well as corresponding length, area and time increments and introducing the scaling factors, Maxwell's equations for the model read as follows:

$$\frac{l_2 \cdot E_2}{l_1 \cdot E_1} \oint_{a_1} \mathbf{E}_1 \cdot \mathbf{d}l_1 = -\frac{l_2^2 \cdot t_1 \cdot \mu_2 \cdot H_2}{l_1^2 \cdot t_2 \cdot \mu_1 \cdot H_1} \cdot \frac{\partial}{\partial t_1} \iint_{A_1} \mu_1 \cdot \mathbf{H}_1 \cdot \mathbf{d}s_1 \tag{29}$$

$$\frac{l_2 \cdot H_2}{l_1 \cdot H_1} \oint_{a_1} \mathbf{H}_1 \cdot \mathbf{d}l_1 = \frac{l_2^2 \cdot \sigma_2 E_2}{l_1^2 \cdot \sigma_1 E_1} \iint_{A_1} \sigma_1 \mathbf{E}_1 \cdot \mathbf{d}s_1 + \frac{l_2^2 \cdot t_1 \cdot \epsilon_2 \cdot E_2}{l_1^2 \cdot t_2 \cdot \epsilon_1 \cdot E_1} \frac{\partial}{\partial t_1} \iint_{A_1} \epsilon_1 \cdot \mathbf{E}_1 \cdot \mathbf{d}s_1 \tag{30}$$

From (27) and (29) one obtains

$$\frac{E_2 \cdot H_1}{E_1 \cdot H_2} = \left(\frac{l_2}{l_1}\right)\left(\frac{t_1}{t_2}\right)\left(\frac{\mu_2}{\mu_1}\right). \tag{31}$$

From (28), (30), and (31) one obtains

$$\left(1 - \frac{l_2^2 \cdot t_1 \cdot \sigma_2 \cdot \mu_2}{l_1^2 \cdot t_2 \cdot \sigma_1 \cdot \mu_1}\right) \iint_{A_1} \sigma_1 \cdot \mathbf{E}_1 \cdot \mathbf{d}s_1 + \left(1 - \frac{l_2^2 \cdot t_1^2 \cdot \epsilon_2 \cdot \mu_2}{l_1^2 \cdot t_2^2 \cdot \epsilon_1 \cdot \mu_1}\right) \cdot \frac{\partial}{\partial t_1} \iint_{A_1} \epsilon_1 \cdot \mathbf{E}_1 \cdot \mathbf{d}s_1 = 0. \tag{32}$$

In general, the ratio $(\iint_{A_1} \sigma_1 \cdot \mathbf{E}_1 \cdot \mathbf{d}s_1)/(\partial/\partial t_1 \iint_{A_1} \epsilon_1 \cdot \mathbf{E}_1 \cdot \mathbf{d}s_1)$ is a function of time. It then follows that (32) can be satisfied only if each of its terms in parenthesis is zero, which leads to the following two scaling equations:

$$\frac{l_2^2 \cdot \sigma_2 \cdot \mu_2}{t_2} = \frac{l_1^2 \cdot \sigma_1 \cdot \mu_1}{t_1} \tag{33*}$$

$$\frac{l_2^2 \cdot \epsilon_2 \cdot \mu_2}{t_2^2} = \frac{l_1^2 \cdot \epsilon_1 \cdot \mu_1}{t_1^2}. \tag{34}$$

In the case of a quasi-stationary magnetic field which assumes the term $\partial(\epsilon \mathbf{E})/\partial t$ to be negligible only (33) is needed to satisfy (32).

---

* See Ref. 2, p. 488.

APPENDIX B

*Conditions Under Which the Effect of the Magnetic Field Intensity at the Inside Surface on that at the Outside Surface is Negligible*

Equations (11) and (12) of Section 4.2 can be readily integrated for the special case of constant permeability, $\mu$. The result of this integration with $E$ and $H$ being sinusoidal time functions is

$$H_{z,D} = E_{x,0}\cdot\frac{\sigma}{\sqrt{j\omega\mu\sigma}}\cdot\sinh\left(\frac{\sqrt{2j}\cdot d}{\delta}\right) + H_{z,0}\cdot\cosh\left(\frac{\sqrt{2j}\cdot d}{\delta}\right). \tag{35}$$

For $\sqrt{2}\cdot d > \delta$ the sinh-term is of the same order of magnitude as the cosh-term. Consequently, the effect of $H_{z0}$ on $H_{zD}$ is negligible if

$$\left| E_{x,0}\frac{\sigma}{\sqrt{j\omega\mu\sigma}} \right| \gg | H_{z,0} |; \qquad d > \frac{\delta}{\sqrt{2}}. \tag{36}$$

For $\sqrt{2}\cdot d < \delta$ the sinh-term and the cosh-term shall be approximated by the first terms of their Taylor-series. One obtains

$$H_{z,D} \approx E_{x,0}\frac{\sigma}{\sqrt{j\omega\mu\sigma}}\cdot\sqrt{2\cdot j}\cdot\frac{d}{\delta} + H_{z,0}\cdot 1 \tag{37}$$

In this case, the effect of $H_{z,0}$ on $H_{z,D}$ is negligible if

$$\left| E_{x,0}\frac{\sigma}{\sqrt{j\omega\mu\sigma}}\cdot\sqrt{2j}\,\frac{d}{\delta} \right| \gg H_{z,0}\ ; \qquad d < \frac{\delta}{\sqrt{2}}. \tag{38}$$

If, as in the case of iron, the permeability is variable it appears reasonable to replace in inequalities (36) and (38) the permeability $\mu$ by an average permeability $\mu_{av}$ and the skin depth $\delta$ by an average skin depth, $\delta_{av}$, which is equal to $\sqrt{2/\omega\cdot\mu_{av}\cdot\sigma}$*. The conditions for making the effect of $H_{z0}$ on $H_{zD}$ negligible become then

$$\left| E_{x,0}\frac{\sigma}{\sqrt{j\omega\mu_{av}\cdot\sigma}} \right| \gg | H_{z,0} |; \qquad d > \frac{\delta_{av}}{\sqrt{2}}$$

$$\left| E_{x,0}\frac{\sigma}{\sqrt{j\cdot\omega\cdot\mu_{av}\cdot\sigma}}\cdot\sqrt{2j}\,\frac{d}{\delta_{av}} \right| \gg | H_{z,0} |; \qquad d < \frac{\delta_{av}}{\sqrt{2}}. \tag{39}$$

The order of magnitude of $(E_{x,0}/H_{z,0})$ for an enclosure of regular

* In the case that $\delta_{av}$ is small compared to $d$, as this is usual with iron shields one best uses for $\mu_{av}$ the average permeability of that part of the shield that is within a distance $\delta_{av}$ from its inside-surface. This is based on the thought that if $H_z$ is practically independent of $H_{z0}$ at $y = \delta_{av}/\sqrt{2}$ it will remain so for larger values of, $y$, regardless of the permeabilities at larger values of $y$.

shape can be evaluated. The average magnetic field strength normal to the area $A_0$ (see Fig. 2) which passes through point 0 and is normal to the direction of the internal flux will be called $H_{\text{av},0}$. The average electric field strength tangential to the line of length, $l_0$, which is formed by the intersection of plane $A_0$ and the inside surface of the shield will be called $E_{\text{av},0}$. $H_{\text{av},0}$ and $E_{\text{av},0}$ are interrelated as follows:

$$j \cdot \omega \cdot \mu_0 \cdot A_0 \cdot H_{\text{av},0} = E_{\text{av},0} \cdot l_0 \ . \tag{40}$$

If one assumes that the ratio $H_{z,0}/E_{x,0}$ is of the same order of magnitude as $H_{\text{av},0}/E_{\text{av},0}$ one obtains for the order of magnitude of $E_{x,0}/H_{z,0}$

$$(E_{x,0}/H_{z,0})_{\textit{order of magnitude}} = \frac{j \cdot \omega \cdot \mu_0 \cdot A_0}{l_0}. \tag{41}$$

If one calls $4(A_0/l_0)$ the equivalent diameter $D$, recalls the expression for $\delta$ and introduces the average relative permeability $(\mu_r)_{\text{av}}$ one obtains from expressions (39) and (41)

$$\frac{\sqrt{2} \cdot 2 \cdot (\mu_r)_{\text{av}} \cdot \delta_{\text{av}}}{D} \ll 1; \qquad d > \frac{\delta_{\text{av}}}{\sqrt{2}} \tag{42}$$

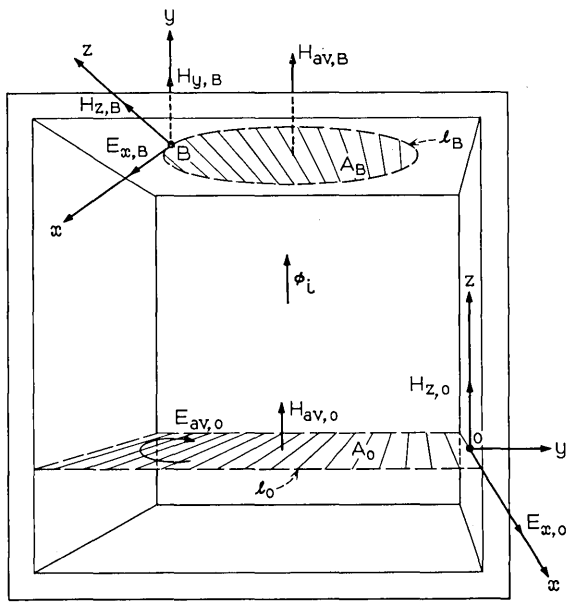


Fig. 2. — Local coordinates at two points of the enclosure.

and

$$\frac{2\cdot(\mu_r)_{\text{av}}\cdot\delta_{\text{av}}^2}{d\cdot D} \ll 1; \qquad d < \frac{\delta_{\text{av}}}{\sqrt{2}}. \tag{43}$$

If one selects as reference point, point $B$ of Fig. (2) one obtains a relationship as given by (40) between the normal internal magnetic field strength and the tangential, internal electric field strength. Since, with respect to area $A_B$, the direction of the magnetic field is predominantly normal the tangential magnetic field component is less than the normal one. Consequently, as before, the effect of the tangential internal magnetic field strength on the external one is negligible if the inequalities (42) and (43) are satisfied with, $D$, being the equivalent diameter of the area $A_B$. [For symmetry reasons the tangential flux-density approaches zero as the center-line is approached. Consequently, its effect is negligible in this area (small $D$) regardless of inequalities (42) and (43).]

## APPENDIX C

### *Numerical Example for the Scaling Laws of a Model of Two Distinct Geometrical Scaling Factors*

The shielding effectiveness of an enclosure to a magnetic field pulse shall be evaluated by testing a scaled down model. The size of the enclosure is 15 m×15 m×15 m. Its material is sheet steel of thickness $d = 0.00317$ m(0.125 inch), of average relative permeability $(\mu_r)_{\text{av}} = 500$ and of conductivity $\sigma = 1 \times 10^7$ mho/m. The peak excursion of the applied magnetic pulse is 10 oersted and its significant frequency content is within a band from $1 \times 10^4$ to $5 \times 10^6$ Hz.* (The corresponding range of the intrinsic wavelength in air is from 30,000 to 60 m.)

Tentatively the scaling factor for the overall dimensions, $L_2/L_1$, is selected as 0.1. Since the minimum intrinsic wavelength in air is only four times the length of the enclosure it is advisable to satisfy (3) (keeping the ratio of intrinsic wavelength to length of the model unchanged). Accordingly, the time scaling factor $(t_2/t_1)$ becomes 0.1. According to (17) the thickness scaling factor $(d_2/d_1)$ becomes $\sqrt{0.1} = 0.316$. The shielding effectiveness of the original, $\eta_1$, according to (21),

* It is assumed that the frequency content of the pulse below $10^4$ cps is so small that it will not cause any damage even though the shielding effectiveness of a large enclosure approaches unity at very low frequencies.

becomes

$$\eta_1 = \left(\frac{1}{0.1}\right) \times 0.316 \cdot \eta_2 \ .$$

Because of the high intensity of the applied pulse the iron-shield will be driven into saturation near its outer surface. Consequently, the model enclosure must be built of the same steel as the original and the peak intensity of the magnetic pulse applied to the model must be equal to that acting on the original.

Finally, one has to test whether the inequalities (14) and (15) are satisfied. Based on a frequency of $1 \times 10^5$ Hz (the lowest significant frequency applied to the model) the average skin-depth is

$$(\delta_{av})_2 = \sqrt{\frac{2}{(2\pi \times 100{,}000) \times (4\pi \times 10^{-7} \times 500) \times (1 \times 10^{7})}}$$
$$= 2.3 \times 10^{-5}\text{m}.$$

With the smallest overall dimension, $D$, being 1.5 m one obtains for the expression of inequality (14)

$$\frac{\sqrt{2} \cdot 2 \times (\mu_r)_{av} \cdot \delta_{av}}{D} = \frac{\sqrt{2} \times 2 \times 500 \times 2.3 \times 10^{-5}}{1.5} = 0.022.$$

One can readily verify that inequality (14) is satisfied for the original as well.

## APPENDIX D

*Integration of the Differential Equations (11) and (12) of the Field in the Shield for Constant $\mu$ and $\sigma$*

For a CW field, (11) and (12) read as follows:

$$\sigma E_x = \frac{dH_z}{dy} \tag{44}$$

$$j\omega\mu H_z = \frac{dE_x}{dy}. \tag{45}$$

Eliminating $E_x$, one obtains

$$j\omega\mu\sigma H_z - \frac{d^2H_z}{dy^2} = 0. \tag{46}$$

The general solution of this equation is

$$H_z = C_1 \exp(+\sqrt{j\omega\mu\sigma}\, y) + C_2 \exp(-\sqrt{j\omega\mu\sigma}\, y). \tag{47}$$

With the boundary conditions given by (16) one obtains,

$$H_{z,D} = \left(\frac{\sigma \cdot E_{x,0}}{\sqrt{j\omega\mu\sigma}}\right) \cdot \sinh\left(\sqrt{j\omega\mu\sigma} \cdot d\right) \tag{48}$$

LIST OF SYMBOLS

$C$ = constant factor.
$d$ = thickness of shield.
$E$ = electric field strength.
$H$ = magnetic field strength
$j$ = $\sqrt{-1}$.
$K$ = proportionality factor.
$l, L$ = distance proportional to the size of the model.
$t$ = time proportional to a specified time interval of the applied electromagnetic field (for instance duration of a pulse).
$\delta$ = skin depth $\sqrt{2/\omega\mu\sigma}$.
$\epsilon$ = dielectric constant.
$\mu$ = permeability (usually of the shield).
$\mu_0$ = permeability of vacuum, ($4\pi \times 10^{-7}$ Henry/m).
$\mu_r$ = relative permeability
$\sigma$ = conductivity.
$\omega$ = angular frequency.
$\lambda_\epsilon$ = intrinsic wavelength in dielectric $2\pi/\omega\sqrt{\epsilon\mu}$.
$\lambda_\sigma$ = intrinsic wavelength in conductor $2\pi\sqrt{2/\omega\mu\sigma}$.
$\eta$ = shielding effectiveness.
$\Phi$ = magnetic flux.
$(L_2/L_1)$ = linear scaling factor of overall shield dimensions.
$(d_2/d_1)$ = scaling factor of shield thickness.
$(l_2/l_1)$ = linear geometric scaling factor if $(L_2/L_1) \equiv (d_2/d_1)$.

REFERENCES

1. Kaden, H., Wirbelströme und Shirmung in der Nachrichtentechnik, Springer-Verlag, 1959.
2. Stratton, J. A., *Electromagnetic Theory,* McGraw-Hill Book Co., Inc., New York, 1941.

# Optimal Routing in Connecting Networks Over Finite Time Intervals

By V. E. BENEŠ

(Manuscript received May 31, 1967)

*A telephone connecting network is given, and with full information at all times about its state, routing policies are sought which minimize the expected number of attempted calls denied service in some finite interval. In this paper, the search is pursued as a mathematical problem in the context of a standard traffic model in terms of optimal control theory and dynamic programming. Certain combinatorial properties of the network, earlier found to be the key to minimizing the loss, also turn out to be relevant here: they lead to policies which differ from optimal policies only in accepting all unblocked call attempts, and provide a "practical" solution of the problem posed. In many cases, the policies found vindicate heuristic policies earlier conjectured to be optimal.*

## I. INTRODUCTION AND SUMMARY

We study the problem of optimally routing calls in a telephone connecting network during a finite time interval $[0, t]$ over which the traffic intensity need not be constant. The present work reports on extensions of earlier results[1] on routing in telephone networks with constant traffic intensity; the principal novelty lies in the fact that whereas previously we minimized the probability of blocking* here we seek to minimize simply the expected total number of call attempts denied service in a given fixed time interval $[0, t]$ on which the traffic intensity may vary.

A traffic model, the same as that used in Ref. 1, is described (Sections II to IV), and the problem is formulated mathematically in the manner of optimal control theory (Section V). The associated Hamilton–Jacobi equation is written and it is noted that this equation has a solution constructible in terms of functions satisfying nonlinear integral

* Defined asymptotically as the stochastic limit, as $t$ becomes large, of the *fraction* of attempted calls blocked or rejected in $[0, t]$.

equations derived from the principle of optimality, (Section VI). An isotony theorem, based on the same combinatorial properties as were used in Ref. 1 to minimize the loss fraction, then exposes the optimal policies to within rejection of unblocked attempted calls. That is, policies are arrived at which differ from optimal policies only in that the latter might reject some unblocked calls at some times (Sections VII and VIII); these policies are the same as those that were arrived at in minimizing the loss.

## II. STATES, EVENTS, AND ASSIGNMENTS

The mathematical model of Ref. 1 will be used. The elements of this model separate naturally into combinatorial ones and probabilistic. The former arise from the structure of the connecting network and from the ways in which calls can be put up in it; the latter represent assumptions about the random traffic the network is to carry. The combinatorial and structural aspects are discussed in this section; terminology and notation for them are introduced. The probabilistic aspects are considered in a later section.

A connecting network $\nu$ is a quadruple $\nu = (G, I, \Omega, S)$, where $G$ is a graph depicting network structure, $I$ is the set of nodes of $G$ which are inlets, $\Omega$ is the set of nodes of $G$ that are outlets, and $S$ is the set of permitted states. Variables $x$, $y$, $z$ at the end of the alphabet denote states, while $u$ and $v$ (respectively) denote a typical inlet and a typical outlet. A state $x$ can be thought of as a set of disjoint chains on $G$, each chain joining $I$ to $\Omega$. Not every such set of chains represents a state: sets with wastefully circuitous chains may be excluded from $S$. It is possible that $I = \Omega$, that $I \cap \Omega = \theta =$ null set, or that some intermediate condition obtain, depending on the "community of interest" aspects of the network $\nu$.

The set $S$ of states is partially ordered by inclusion $\leqq$, where $x \leqq y$ means that state $x$ can be obtained from state $y$ by removing zero or more calls. If $x$ and $y$ satisfy the same assignment of inlets to outlets, i.e., are such that all and only those inlets $u \in I$ are connected in $x$ to outlets $v \in \Omega$ which are connected to the same $v$ in $y$ (though possibly by different routes), then we say that $x$ and $y$ are equivalent, written $x \sim y$.

The set $S$ of states determines another set $\mathcal{E}$ of events, either hangups (terminations of calls), successes (successful call attempts), or blocked or rejected calls (unsuccessful call attempts). The occurrence of an event in a state may lead to a new state obtained by adding or removing

a call in progress, or it may, if it is a blocked call or one that is rejected, lead to no change of state. Not every event can occur in every state: naturally, only those calls can hang up in a state which are in progress in that state, and only those inlet-outlet pairs can ask for a connection between them in a state that are idle in that state. The notation $e$ is used for a (general) event, $h$ for a hangup, and $c$ for an attempted call. If $e$ can occur in $x$ we write $e \varepsilon x$. A call $c \varepsilon x$ is blocked in a state $x$ if there is no $y \varepsilon S$ which covers $x$ in the sense of the partial ordering $\leqq$ and in which $c$ is in progress. For $h \varepsilon x$, $x - h$ is the state obtained from $x$ by performing the hangup $h$.

We denote by $A_x$ the set of states that are immediately above $x$ in the partial ordering $\leqq$, and by $B_x$ the set of those that are immediately below. Thus,

$$A_x = \{\text{states accessible from } x \text{ by adding a call}\}$$

$$B_x = \{\text{states accessible from } x \text{ by a hangup}\}.$$

For an event $e \varepsilon x$, the set $A_{ex}$ is to consist of those states $y \neq x$ to which the network might pass upon the occurrence of $e$ in $x$. Thus, if $e$ is a blocked call, $A_{ex} = \theta$; also

$$\bigcup_{h \varepsilon x} A_{hx} = B_x$$

$$\bigcup_{\substack{c \varepsilon x \\ c \text{ not blocked in } x}} A_{cx} = A_x .$$

The number of calls in progress in state $x$ is denoted by $|x|$ . The number of call attempts $c \varepsilon x$ which are not blocked in $x$ is denoted by $s(x)$, for "successes in $x$." The functions $|\cdot|$ and $s(\cdot)$ defined on $S$ play important roles in the stochastic process to be used for studying routing. In addition, we use

$\beta_x$ = number of idle inlet-outlet pairs blocked in state $x$

$\alpha_x$ = number of idle inlet-outlet pairs in state $x$,

and note that $\alpha = \beta + s$.

It can be seen, further, that the set $S$ of states is not merely partially ordered by $\leqq$, but also forms a semilattice, or a partially ordered system with intersections, with $x \cap y$ defined to be the state consisting of those calls and their respective routes which are common to both $x$ and $y$.

An assignment is a specification of what inlets should be connected to what outlets. The set $A$ of assignments can be represented as the

set of all fixed-point-free correspondences from $I$ to $\Omega$. The set $A$ is partially ordered by inclusion, and there is a natural map $\gamma(\cdot): S \to A$ which takes each state $x \in S$ into the assignment it realizes; the map $\gamma(\cdot)$ is a semilattice homomorphism of $S$ into $A$, since

$$x \geqq y \quad \text{implies} \quad \gamma(x) \geqq \gamma(y),$$
$$\gamma(x \cap y) \leqq \gamma(x) \cap \gamma(y).$$

We denote by $F_x$ the set of calls that are *free* or idle in $x$, i.e.,

$$F_x = \{c: c \text{ is idle in } x\} = \{\gamma(y - x): y \in A_x\},$$

where $y - x$ is the state obtained from $y$ by removing all the calls of $x \leqq y$.

## III. PROBABILISTIC ASSUMPTIONS

A Markov stochastic process $x_t$ taking values on $S$ is used as a mathematical description of an operating connecting network subject to random traffic. Specifically, the Markov process of Ref. 1 will be used, with the modification that the calling-rate per idle inlet-outlet pair can depend on time. This model can be paraphrased in the informal terminology of "rates" by two simple assumptions:

(*i*) The hang-up rate per call in progress is unity.

(*ii*) The calling-rate between an inlet and a distinct outlet, both idle at time $u$, is $\lambda(u) \geqq 0$.

The transition probabilities of $x_t$ will be described after a discussion of system operation and routing.

## IV. ROUTING POLICIES

It will be assumed here, as in Ref. 1, that attempted calls to busy terminals are rejected, and have no effect on the state of the network; similarly, blocked attempts to call an idle terminal are refused, with no change of state. Attempts to place a call are completed instantly with some choice of route, or are rejected, in accordance with some *routing policy*.

A routing policy over $[0, t]$ will be described by a measurable matrix-valued function of time, denoted by $R(u) = (r_{xy}(u))$, $x, y \in S$, $0 \leqq u \leqq t$, having the following properties and interpretation: for each $x \in S$, let $\Pi_x$ be the partition of $A_x$ induced by the relation $\sim$ of "having the same calls up," or satisfying the same assignment of inlets to outlets;

it can be seen that $\Pi_x$ consists of exactly the sets $A_{cx}$ for $c \varepsilon x$, $c$ not blocked in $x$; for each $u \varepsilon [0, t]$, $Y \varepsilon \Pi_x$, $r_{xy}(u)$ for $y \varepsilon Y$ is a possibly improper probability distribution over $Y$, (that is, it may not sum to unity over $Y$),

$$r_{xx}(u) = s(x) - \sum_{y \varepsilon A_x} r_{xy}(u),$$

and $r_{xy}(u) = 0$ in all other cases.

The interpretation of the routing matrix $R(u)$ is to be this: any $Y \varepsilon \Pi_x$ represents all the ways in which a particular call $c$ (free and not blocked in $x$) *could* be completed when the network is in state $x$; for $y \varepsilon Y$, $r_{xy}(u)$ is the chance that if call $c$ is attempted in state $x$ at time $u$, it will be completed by being routed through the network so as to take the system to state $y$. That is, we assume that if $c$ is attempted in $x$ at $u$, then with probability

$$1 - \sum_{y \varepsilon A_{cx}} r_{xy}(u) \tag{1}$$

it is rejected (even though it is not blocked), and with probability $r_{xy}(u)$ it is assigned the route which would change the state $x$ to $y$, for $y \varepsilon A_{cx}$. The possibly improper distribution of probability

$$\{r_{xy}(u), y \varepsilon Y\}$$

indicates how the calling-rate $\lambda(u)$ due to $c$ at time $u$ is to be spread over the possible ways of putting up the call $c$, while the improper part (1) is just the chance that it is rejected outright.

It is to be noted that, as in Ref. 1, routing is carried out with perfect information about the current state of the network. The problem of optimal routing with only partial information is much more difficult (than the problem to be considered here), and it is not taken up.

Alternatively, we may define the convex set $C$ of all (routing) matrices $R = (r_{xy})$ such that $r_{xy} \geqq 0$, $r_{xy} = 0$ unless $y \varepsilon A_x$, and

$$\sum_{y \varepsilon A_{cx}} r_{xy} \leqq 1,$$

for $c \varepsilon x$ not blocked in $x$,

$$r_{xx} = s(x) - \sum_{y \varepsilon A_x} r_{xy},$$

and describe the routing policies as measurable functions on $[0, t]$ taking values in $C$.

A routing policy $R(\cdot)$ with $r_{xy}(u) \equiv 0$ or 1 is called a *fixed* policy.

## V. FORMULATION OF THE PROBLEM

For the purpose of defining a Markov stochastic process it is convenient and customary to collect the probabilistic and operational assumptions made above in a time-dependent matrix $Q(\cdot)$ of *transition rates.* Indeed, each routing policy $R(\cdot)$ determines such a matrix function, and so a process, according to the relationship $Q = Q(R)$ given in detail by

$$q_{xy}(u) = \begin{cases} 1, & y \in B_x \\ \lambda(u) r_{xy}(u), & y \in A_x \\ -|x| - \lambda(u)[s(x) - r_{xx}], & y = x \\ 0, & \text{otherwise.} \end{cases}$$

If the routing policy $R(\cdot)$ is used, the transition probability matrix $P(u, t) = (p_{xy}(u, t))$, with

$$p_{xy}(u, t) = \Pr\{x_t = y \mid x_u = x\},$$

will develop according to the backward Kolmogorov equation

$$P(t, t) \equiv I, \qquad Q = Q(R)$$

$$\frac{\partial}{\partial u} P(u, t) = -Q(u)P(u, t), \qquad 0 \leqq u \leqq t.$$

In particular, if the system starts at 0 with an initial probability distribution given by the column vector $p(0)$, then its distribution $p(u)$ at time $u$ is $[p(0)'P(0, u)]'$, which satisfies the equation $\dot{p}(u) = Q(u)'p(u)$. If the network is in state $x$ at time $u$, the rate at which blocked or rejected calls are being generated is $\lambda(u)[r_{xx}(u) + \beta_x]$. Thus, with $r(u) = r(R(u))$ the vector function $\{r_{xx}(u), x \in S\}$, the total expected number of calls denied service during [0, t] is just

$$D = D(p(0), t) = \int_0^t p(u)'[r(u) + \beta]\lambda(u)\, du. \tag{2}$$

We may, therefore, state our routing problem thus: Minimize $D$ subject to the conditions $p(0)$ given, $\dot{p}(u) = Q(u)'p(u)$, $Q = Q(R)$, $R(u) \in C$, for $u \in [0, t]$.

Let us now view the $|S|$-dimensional probability vector $p = p(u)$ as a "state-variable" whose "motion" is governed by the linear differential equation $\dot{p}(u) = Q(u)'p(u)$. The criterion $D$ is linear in $p(\cdot)$ and the matrix entries of the control $R(\cdot)$ appear as coefficients in

the equation and in the criterion. The problem of minimizing $D$ can be approached and solved by the now classical methods of the theory of optimal control.

## VI. THE HAMILTON-JACOBI EQUATION

Let $p$, $q$ be $|S|$-dimensional vector variables, and introduce the Hamiltonian function

$$H(p, u, q, R) = \lambda(u)p'(\beta + r) + \sum_x p_x\{\sum_{y \varepsilon B_x} q_y + \lambda(u) \sum_{y \varepsilon A_x} r_{xy}q_y - (\lambda(u)r_x + |x|)q_x\}.$$

Let $H^*$ be the minimum of $H$ for $R \varepsilon C$, i.e.,

$$H^*(p, u, q) = \min_{R \varepsilon C} \{\lambda(u)p'Hq + \lambda(u)p'Rq - \sum_x p_x[\lambda(u)r_x + |x|]q_x\},$$

where $H = (h_{xy})$ is the "hangup matrix" such that $h_{xy} = 1$ or $0$ according as $y \varepsilon B_x$ or not. The Hamilton–Jacobi equation associated with the minimization of $D$ above is just

$$\frac{\partial V}{\partial u} + H^*\left(p, u, \frac{\partial V}{\partial p}\right) = 0, \qquad 0 \leqq u \leqq t, \qquad p \geqq 0. \tag{3}$$
$$V(p, t) \equiv 0.$$

It follows from a known theorem[2] of the theory of optimal control that if we can find a continuously differentiable solution $V(p, u)$ of the Hamilton–Jacobi equation (3), then a control policy $R(\cdot) = (r_{xy}(\cdot))$ such that by components

$$R(u) \frac{\partial V}{\partial p}(p, u) = \min_{R \varepsilon C} R \frac{\partial V}{\partial p}(p, u), \qquad 0 \leqq u \leqq t$$

is optimal.

To find a solution of the Hamilton-Jacobi equation (3) let us consider the problem of starting the connecting system at a time $u < t$, and operating it until $t$ so as to minimize the expected number of blocked calls over $(u, t)$. We define, with $t$ fixed, and $u < t$,

$E_x(u)$ = expected number of blocked calls in $(u, t)$ using an optimal policy, starting in state $x$.

To solve the problem we note that two possibilities arise: Either an event occurs in $(u, t)$, or else none does. In the latter case, the system stays in its initial state $x$ throughout $(u, t)$, and no calls are blocked during the interval. In the former case the first event $e$ to occur does so

at some time epoch $\tau \varepsilon (u, t)$ and can lead to one of the states in $A_{ex} \cup \{x\}$. The minimum expected blocking to be suffered in the remaining interval $(\tau, t)$ is just

$$\begin{cases} \min \{1 + E_x(\tau), \min\limits_{y \varepsilon A_{cx}} E_y(\tau)\} & \text{if} \quad e = c \\ E_{x-h}(\tau) & \text{if} \quad e = h. \end{cases}$$

With

$$c_x(u) = | x | + \alpha_x \lambda(u),$$

$$C_x(u) = \int_0^u c_x(v)\, dv,$$

the probability density that the first event to occur does so at $\tau$, and is $e$, equals

$$c_x(\tau) \exp \{-C_x(\tau) + C_x(u)\} \cdot \begin{cases} \dfrac{1}{c_x(\tau)}, & e = h \\ \dfrac{\lambda(\tau)}{c_x(\tau)}, & e = c. \end{cases}$$

Hence, applying the "principle of optimality," we conclude that the vector function $E(u)$, $0 \leqq u \leqq t$, satisfies the equation

$$E_x(u) = \int_u^t \exp \{-C_x(\tau) + C_x(u)\}$$
$$\cdot [\sum_{y \varepsilon B_x} E_y(\tau) + \lambda(\tau) \sum_{c \varepsilon x} \min \{1 + E_x(\tau), \min_{y \varepsilon A_{cx}} E_y(\tau)\}]\, d\tau. \tag{4}$$

We now observe that if $E(\cdot)$ satisfies (4), then the scalar function $V(p, u) = p'E(u)$ satisfies the Hamilton-Jacobi equation. This is of course not surprising since the equation for $E(\cdot)$ was obtained from the optimality principle. To see it we differentiate (4) with respect to $u$, obtaining

$$\begin{aligned} \frac{\partial}{\partial u} E_x(u) &= (| x | + \lambda(u)\alpha_x)E_x(u) - \sum_{y \varepsilon B_x} E_y(u) - \lambda(u)\beta_x \\ &\qquad - \lambda(u) \sum_{c \varepsilon x} \min \{1 + E_x(u), \min_{y \varepsilon A_{cx}} E_y(u)\} \\ &= [| x | + \lambda(u)s(x)]E_x(u) - \sum_{y \varepsilon B_x} E_y(u) - \lambda(u)\beta_x \\ &\qquad - \lambda(u) \sum_{\substack{c \varepsilon x \\ c \text{ not blocked in } x}} \min \{1 + E_x(u), \min_{y \varepsilon A_{cx}} E_y(u)\}. \end{aligned}$$

Now note that

$$\begin{aligned}
&\sum_{\substack{c \varepsilon x \\ c \text{ not blocked in } x}} \min \{1 + E_x(u), \min_{y \varepsilon A_{cx}} E_y(u)\} \\
&= \sum_{\substack{c \varepsilon x \\ c \text{ not blocked in } x}} \min_{R \varepsilon C} \{(1 - \sum_{y \varepsilon A_{cx}} r_{xy})[E_x(u) + 1] + \sum_{y \varepsilon A_{cx}} r_{xy} E_y(u)\} \\
&= \min_{R \varepsilon C} \{ \sum_{\substack{c \varepsilon x \\ c \text{ not blocked in } x}} (1 - \sum_{y \varepsilon A_{cx}} r_{xy})[E_x(u) + 1] + \sum_{y \varepsilon A_{cx}} r_{xy} E_y(u)\} \\
&= \min_{R \varepsilon C} \{[s(x) - \sum_{y \varepsilon A_x} r_{xy}][E_x(u) + 1] + \sum_{y \varepsilon A_x} r_{xy} E_y(u)\} \\
&= \min_{R \varepsilon C} \{r_{xx}[E_x(u) + 1] + \sum_{y \varepsilon A_x} r_{xy} E_y(u)\}.
\end{aligned}$$

Therefore,

$$\begin{aligned}
\frac{\partial}{\partial u} E_x(u) + \min_{R \varepsilon C} \{&-(| x | + \lambda(u)[s(x) - r_{xx}])E_x(u) \\
&+ \sum_{y \varepsilon B_x} E_y(u) + \lambda(u)[\beta_x + r_{xx}] + \sum_{y \varepsilon A_x} r_{xy} E_y(u)\} = 0.
\end{aligned}$$

Now with $V = p'E$ and $\partial V/\partial p = E$, $r = r(R) = \{r_{xx}, x \varepsilon S\}$, $p \geqq 0$,

$$\begin{aligned}
\frac{\partial V}{\partial u} + \min_{R \varepsilon C} \{&\lambda(u)p'(\beta + r) - \sum_x p_x(| x | + \lambda(u)[s(x) - r_{xx}])E_x(u) \\
&+ \sum_x p_x(\sum_{y \varepsilon B_x} + \sum_{y \varepsilon A_x} r_{xy})E_y(u)\} = 0.
\end{aligned}$$

This is the Hamilton–Jacobi equation. It follows that the minimum of $D$ is achieved by a fixed policy, as could be expected on intuitive grounds.

## VII. ISOTONY THEOREM

In Ref. 1 we introduced some combinatorial "monotone" properties of the partial ordering $(S, \leqq)$ of states which (when present) provide an intuitive and straightforward description of the routing choices for accepted calls which minimize the loss probability. These properties are also relevant to minimizing the criterion $D$ of (2).

The properties in question can be paraphrased as follows: the relative merit of states vis à vis blocking is consistent or continuous, i.e., if a state $x$ is "better" than another $y$, then the neighbors of $x$ in $\leqq$ are in the same sense better than the corresponding neighbors of $y$. Specifically, we deal in detail only with the weakest property used in Ref. 1,

and we say that a relation $P$ on $S$ has the *weak monotone property* if $xPy$ implies

(*i*) $|x| = |y|$,
(*ii*) $\exists\, \mu: B_x \leftrightarrow B_y$ and $z \in B_x$ implies $zP\mu z$,
(*iii*) $\exists\, \nu: F_y \to F_x$ and (a) $c \in F_y$, $z \in A_{cy}$ imply $\exists\, w \in A_{(\nu c)x}$ with $wPz$,
(b) $c, c' \in F_y$, $\nu c = \nu c'$ imply $c = c'$.

We now prove the following isotony result:

*Theorem: If $P$ is a relation on $S$ having the weak monotone property, then $xPy$ implies*

$$\frac{\partial V}{\partial p_x} \leqq \frac{\partial V}{\partial p_y}.$$

*Proof:* Define recursively $E_x(0, u) \equiv 0$,

$$\begin{aligned} E_x(1, u) &= \beta_x[C_x(t) - C_x(u)] \exp\{C_x(u) - C_x(t)\} \\ &= \Pr\{\text{first \& only event in } (u, t) \text{ is a blocked call} \mid x_u = x\}, \end{aligned}$$

$$\begin{aligned} E_x(n+1, u) = \int_u^t & \exp\{C_x(u) - C_x(\tau)\} \\ & \cdot [\sum_{y \in B_x} E_y(n, \tau) + \beta_x \lambda(\tau)[E_x(n, \tau) + 1] \\ & + \lambda(\tau) \sum_{\substack{c \in x \\ c \text{ not blocked in } x}} \min\{1 + E_x(n, \tau), \min_{y \in A_{cx}} E_y(n, \tau)\}]\, d\tau. \end{aligned}$$

It follows easily that $E(1, u) \leqq E(u)$, and that $E(n+1, u) \geqq E(n, u)$. Furthermore, standard methods[3] using the inequality

$$|\min_{1 \leqq i \leqq n} y_i - \min_{1 \leqq i \leqq n} (y_i + \epsilon_i)| \leqq \max_{1 \leqq i \leqq n} |\epsilon_i|$$

show that the functions $E_x(n, \cdot)$ converge monotonely as $n \to \infty$ to the unique solution of (3).

If now $xPy$, then $\beta_x \leqq \beta_y$, $c_x(\cdot) \equiv c_y(\cdot)$, and so $E_x(1, u) \leqq E_y(1, u)$. Assume as a hypothesis of induction that $xPy$ implies $E_x(n, u) \leqq E_y(n, u)$, $0 \leqq u \leqq t$. Then with $\mu$ and $\nu$ as in the definition of the weak monotone property

$$E_z(n, u) \leqq E_{\mu z}(n, u) \quad \text{for} \quad z \in B_x$$

$$\begin{aligned} \min\{1 + E_x(n, u), \min_{z \in A_{(\nu c)x}} E_z(n, u)\} \\ \leqq \min\{1 + E_y(n, u), \min_{z \in A_{cy}} E_z(n, u)\} \end{aligned}$$

$$\sum_{z \varepsilon B_y} E_z(n, u) + \beta_y \lambda(u)[E_y(n, u) + 1]$$
$$+ \lambda(u) \sum_{\substack{c \varepsilon y \\ c \text{ not blocked in } y}} \min \{1 + E_y(n, u), \min_{z \varepsilon A_{cy}} E_z(n, u)\}$$
$$\geqq \sum_{z \varepsilon B_x} E_z(n, u) + \beta_x \lambda(u)[E_x(n, u) + 1] + \lambda(u)(\beta_y - \beta_x)[E_y(n, u) + 1]$$
$$- \lambda(u)[E_y(n, u) + 1] \sum_{\substack{c \varepsilon x \\ c \notin \operatorname{rng} \nu \\ c \text{ not blocked in } x}} 1$$
$$+ \lambda(u) \sum_{\substack{c \varepsilon x \\ c \text{ not blocked in } x}} \min \{1 + E_x(n, u), \min_{z \varepsilon A_{cx}} E_z(n, u)\}.$$

It can be seen that with $| X |$ the cardinality of a set $X$,

$$\beta_y - \beta_x \geqq | \{c \varepsilon x : c \notin \operatorname{rng} \nu, c \text{ not blocked in } x\} |,$$

whence $E_x(n+1, u) \leqq E_y(n+1, u)$. Since $\partial V/\partial p = E$ and $E(n, u) \uparrow E(u)$, the theorem follows.

## VIII. THE NATURE OF THE OPTIMAL POLICIES

Where it is applicable, the isotony theorem allows us to infer the optimal routes for accepted calls. Its relevance to the optimal policies for networks for which there is a relation $P$ with the weak monotone property is this: Let $c \varepsilon x$ be a call that is not blocked in state $x$, so that $A_{cx} \neq \theta$, and suppose that there is at least one $y \varepsilon A_{cx}$ such that $yPz$ for every $z \varepsilon A_{cx}$. It follows from the isotony theorem that at any time $u$, such a $y$ is at least as good a way of routing $c$ (if $c$ is attempted at $u$) as any other state of $A_{cx}$. The only action which might conceivably be better in this situation than accepting $c$ and routing it so as to take the system to $y$ is rejecting $c$ altogether. Such a rejection would be optimal if and only if

$$1 + \frac{\partial V}{\partial p_x} \leqq \frac{\partial V}{\partial p_y};$$

for $u$'s close to $t$, clearly, this is false. In these circumstances a policy that routes $c$ in $x$ so as to take the system to $y$ can differ (so far as $x$ and $c$ are concerned) from an optimal policy only in the respect that the latter might reject $c$ in $x$.

In Ref. 1, the notation

$$\sup_P A_{cx}$$

was used for the set

$$\{y : z \varepsilon A_{cx} \text{ implies } yPz\} \cap A_{cx} ,$$

whenever this set was nonempty. The set $\sup_P A_{cx}$ consists precisely of the possible states to which an optimal policy takes the system from state $x$ if it accepts the attempted call $c$.

The preceding observations are summarized in the *Corollary: If $P$ on $S$ has the weak monotone property then there exists an optimal policy $R(\cdot)$ such that $c \varepsilon x$, $y \varepsilon A_{cx} r_{xy}(u) > 0$, $0 < u < t$ imply*

$$y \varepsilon \sup_P A_{cx} .$$

The theory of routing for minimal $D$ constructed here can be developed in greater detail in the fashion of the optimal routing theorems of Section XVIII of Ref. 1; however, the isotony theorem and corollary embody the basic idea, and we shall leave the topic at this stage.

REFERENCES

1. Beneš, V. E., Programming and Control Problems Arising from Optimal Routing in Telephone Networks, B.S.T.J., *45,* November, 1966, pp. 1373–1438.
2. Athans, M. and Falb, P. L., *Optimal Control,* McGraw-Hill Book Co., Inc., New York, 1966, p. 360, Theorem 5–13.
3. Bellman R., *Stability Theory of Differential Equations,* McGraw-Hill Book Co., Inc., New York, 1953, pp. 65–9.

# Restoration of Photographs Blurred by Image Motion

By DAVID SLEPIAN

(Manuscript received May 16, 1967)

*The blurring of photographs by image motion during exposure is studied by means of a simple model. Conditions under which it is possible to recover the unblurred image are determined and some methods of restoration are described.*

## I. INTRODUCTION AND SUMMARY

This paper is concerned with the feasibility of restoring photographs that have been blurred during exposure by relative motion between the camera and the entire scene being photographed.* It is assumed that all objects of the scene are at rest relative to each other. Several simple mathematical models of this situation are investigated.

Section II treats the case of uniform translation between film and image. During exposure an area, $A$, of the image crosses over the margins onto the film. It is shown that unique restoration of the scene from the blurred photograph is, in general, impossible without *a priori* knowledge of certain portions of the undistorted image of area $A$. An algorithm is given for the restoration when this *a priori* knowledge is available, and a filtering technique is described that covers a case of frequent interest,—the photographing of a small object viewed against a uniform background.

The restoration techniques require knowledge of the translation undergone. Section III describes a method of estimating this displacement from the blurred photograph.

In Section IV more general image motions are considered. The case of pure rotation has many features in common with that of pure translation. Estimation of the parameters of the motion, however, appears to be more difficult in this case.

* This work was carried out at the Woods Hole 1966 Summer Study on Restoration of Atmospherically degraded Images held by the National Academy of Sciences.

## II. IMAGE TRANSLATION

We are concerned here with photographs blurred because of a uniform relative motion during exposure between the camera and the object being photographed. For mathematical simplicity, in this section we treat the problem as one-dimensional; the modifications necessary to describe the more accurate two-dimensional model are evident.

Let $g(x)$ denote the illuminance from a scene or object being photographed that would result along a line in the image plane of the camera if there were no relative motion between the camera and the object. We suppose $g(x)$ defined for all values of $x$. The film occupies the interval $|x| \leqq L$. Imagine now that during the exposure time $T$ the image moves with constant velocity $v$ along the image plane in the $x$-direction. The total light energy $\epsilon(x)$ incident on a point $x$ in this plane is

$$\begin{aligned} \epsilon(x) &= c_1 \int_0^T g(x - vt)\, dt \\ &= c_2 \int_{x-a}^{x} g(y)\, dy, \end{aligned} \tag{1}$$

where $a = vT$. In appropriate units, the density of the photograph is then

$$f(x) = r[\epsilon(x)], \qquad |x| \leqq L, \tag{2}$$

where $r(\epsilon)$ is the response curve of the film. Our aim is to recover $g$, or a portion of $g$, from a knowledge of $f(x)$, $|x| \leqq L$. If we assume the film response is monotone and known, knowledge of $f(x)$ is equivalent by (2) to knowledge of $\epsilon(x) = r^{-1}[f(x)]$, $|x| \leqq L$. For our purposes, then, it suffices to assume $\epsilon(x)$ known, or equivalently, to assume that the film response is linear. Accordingly, we henceforth consider recovering the undistorted scene $g(x)$ from the blurred photograph

$$f(x) = \int_{x-a}^{x} g(y)\, dy, \qquad |x| \leqq L, \tag{3}$$

where it is assumed that $a$ is known. (The problem of estimating $a$ is treated in Section III.)

From (3) we obtain at once

$$f'(x) = g(x) - g(x - a)$$

or

$$g(x) = f'(x) + g(x - a), \qquad |x| \leqq L, \tag{4}$$

the basic recovery equation. If $g(x)$ were known for $-L - a \leqq x \leqq -L$, say

$$g(x) = \varphi(x), \qquad -L - a \leqq x \leqq -L, \tag{5}$$

then $g$ could be determined at once from (4) across the entire film interval. One has

$$\begin{aligned}
g(x) &= f'(x) + \varphi(x - a) \qquad -L \leqq x \leqq -L + a \\
g(x) &= f'(x) + g(x - a) \\
&= f'(x) + f'(x - a) + \varphi(x - 2a), \\
&\qquad\qquad -L + a \leqq x \leqq -L + 2a \\
g(x) &= \sum_{j=0}^{k-1} f'(x - ja) + \varphi(x - ka), \\
&\qquad\qquad -L + (k - 1)a \leqq x \leqq -L + ka \\
&\qquad\qquad\qquad k = 1, 2, \cdots, K \\
g(x) &= \sum_{j=0}^{K} f'(x - ja) + \varphi[x - (K + 1)a], \\
&\qquad\qquad -L + Ka \leqq x \leqq L,
\end{aligned} \tag{6}$$

where $K = [2L/a]$ is the largest integer not greater than $2L/a$. Similarly, if $g(x)$ is known on any interval $H$ of length $a$ contained in the interval $I \equiv (-L - a, L)$, (4) can be used to determine $g$ first in the intervals of length $a$ adjacent to $H$ and then successively to determine $g$ throughout $I$. More generally, if $g$ is known on a set $S$ of intervals in $I$ whose translates by various multiples of $a$ form a set containing an interval of length $a$ in $I$, then $g$ can be determined everywhere in $I$ by repeated application of (4). We call such a set $S$ an admissible *a priori* set.

Two quite different cases of restoration are now evident: (*i*) $g$ known beforehand on an admissible *a priori* set; (*ii*) $g$ not so known. In the former case, exact restoration is possible in principle. In the latter case, unique restoration is *not* possible. Indeed, a given blurred photograph $f$ could arise from infinitely many different scenes. For example, if no *a priori* knowledge of $g$ is available, choose $g(x) = \varphi(x)$ for $-L - a \leqq x < -L$ with $\varphi$ arbitrary. Use (6) then to determine $g$ for $-L \leqq x \leqq L$. This scene $g$ will give rise to a blurred photograph differing from $f$ by at most a constant. (By judicious choice of background, and by moving the camera, it is possible to make the devil appear as only a slightly-blurred saint!) Similar considerations show that if

$g$ is not known beforehand on some admissible *a priori* set, its values can be assigned arbitrarily on some set of points in $I$ and determined elsewhere to give a scene that could produce a given blurred photograph. There seems to be little useful that can be said, in general, about restoration of blurred photographs when $g$ is not known on some admissible *a priori* set.

A case of importance in practice where something of value can be said concerns the restoration of a photograph of a small object moving across a uniform background. We suppose the background corresponds to photographic density zero and that the blurred object image is smaller than the photograph. Specifically, assume that it is known *a priori* that the unblurred object image $g(x)$ would be nonzero only in the interval $x_0 \leqq x \leqq x_0 + (p - 1)a$, where $x_0 \geqq -L$, $x_0 + pa \leqq L$. The blurred photograph then would have a density different from zero only for $-L \leqq x_0 \leqq x \leqq x_0 + pa \leqq L$. We define $f$ everywhere by taking

$$f(x) \equiv 0, \qquad x < x_0 , \qquad x > x_0 + pa. \tag{7}$$

We define $g = 0$ for $x < x_0$ and $x > x_0 + (p - 1)a$. In this case, the solution of form (6) becomes simply

$$g(x) = \sum_{j=0}^{p-1} f'(x - ja), \qquad x \leqq x_0 + pa \tag{8}$$

$$g(x) = \sum_{j=1}^{p} f'(x - ja), \qquad x_0 + pa < x \leqq x_0 + (p + 1)a$$

$$\vdots$$

$$g(x) = \sum_{j=n}^{p+n-1} f'(x - ja), \qquad x_0 + (p + n - 1)a < x \leqq x_0 + (p + n)a$$

$$n = 1, 2, \cdots . \tag{9}$$

Because of our assumptions, the sums in (9) must give zero for $n = 1, 2, \cdots$ and $x$ in the indicated ranges. They are in this sense nugatory. Equation (8) gives $g = 0$ for $x < x_0$ because of (7). In the range of interest $x_0 \leqq x \leqq x_0 + pa$, it gives a simple algorithm for obtaining a true picture of the object.

Equation (8) can be instrumented in many ways. The derivative $f'$ of the blurred photo extended by (7) can be obtained as a transparency by optical filtering techniques. The sum (8) then can be found by $p$-tuple exposure of a film with the image of $f'$ being translated by an amount $a$ by a mirror between each exposure.

An alternate restoration method suggested by (8) sheds some light on a filtering technique previously reported in the literature.[1] Let us define for all $x$

$$\hat{g}(x) \equiv \sum_{j=0}^{p-1} f'(x - ja) \tag{10}$$

with $f$ defined everywhere by (7).

For $x \leqq x_0 + pa$, $\hat{g}$ will coincide with $g$, but for $x > x_0 + pa$ it gives values different from $g$. From the Fourier representation

$$f(x) = \int_{-\infty}^{\infty} e^{i\lambda x} F(\lambda)\, d\lambda$$

if follows that

$$f'(x - ja) = \int_{-\infty}^{\infty} e^{i\lambda x} i\lambda F(\lambda) e^{-ij\lambda a}\, d\lambda$$

so that (10) can be written

$$\begin{aligned} \hat{g}(x) &= \int_{-\infty}^{\infty} d\lambda\, e^{i\lambda x} i\lambda F(\lambda) \sum_{j=0}^{p-1} e^{-ij\lambda a} \\ &= \int_{-\infty}^{\infty} d\lambda\, e^{i\lambda x} \lambda F(\lambda) \frac{\sin(\lambda pa/2)}{\sin(\lambda a/2)}\, i e^{-i(p-1)(\lambda a/2)} \end{aligned}$$

which shows that $\hat{g}[x + (p - 1)(a/2)]$ can be obtained from the extended blurred photograph $f$ by processing with a filter having transfer function

$$Y(\lambda) = \frac{i\lambda \sin(\lambda pa/2)}{\sin(\lambda a/2)}. \tag{11}$$

A different filter for restoration in the present case can be derived as follows. Recall our assumption that

$$g = 0 \quad \text{for} \quad x \leqq -L \quad \text{and} \quad x > L - a. \tag{12}$$

Then

$$\begin{aligned} f(x) &= \int_{x-a}^{x} g(y)\, dy \\ &= \int_{-\infty}^{\infty} h(x - y) g(y)\, dy \end{aligned} \tag{13}$$

holds true for all $x$. Here

$$h(x) = \begin{cases} 1, & -a \leqq x \leqq 0 \\ 0, & \text{otherwise.} \end{cases}$$

Taking the Fourier transform of (13) yields

$$G(\lambda) = \pi e^{-(ia\lambda/2)} \frac{\lambda}{\sin(\lambda a/2)} F(\lambda) \tag{14}$$

which shows that $g[x + (a/2)]$ can be obtained from the extended blurred photograph by processing with a filter having transfer function

$$Y_\infty = \pi \frac{\lambda}{\sin(\lambda a/2)} \tag{15}$$

as has been reported previously.[1]

The filter (15) has poles at the points $\lambda = 2n\pi/a$, $|n| = 1, 2, \cdots$ and hence cannot be realized in practice. Some ad hoc scheme for assigning a finite value at these pole positions must be made. Just what these modified filters do to picture quality is not easy to analyze. The filter (15), could it be instrumented, would yield $g$, that is, a picture with infinite white skirts. The filter (11), on the other hand, has no poles and hence can be realized.* It restores $g$ correctly in the interval $x_0 \leqq x \leqq x_0 + pa$ where this quantity is different from zero. It gives uninterpretable values for $x > x_0 + pa$ and the value zero for $x < x_0$. It would appear that the infinities in (15) with their attendant difficulties are due to insisting that the processed picture yield the value zero over an infinite region where from a priori knowledge one would accept no other value anyhow.

It is worth noting that if (12) is violated, then (13) does not hold for all $x$ and one cannot write (14). These edge effects have been overlooked in past treatments of the problem based on (14).[1]

## III. ESTIMATION OF MOTION PARAMETERS

The restoration technique of the preceding section presupposed knowledge of the direction and amount of the image displacement during exposure. We now consider how these quantities might be determined from the blurred photograph itself.

We suppose the blurred photograph density to be given by

$$f(x, y) = \int_0^T g(x - ut, y - vt)\, dt, \qquad |x| \leqq L_1, \quad |y| \leqq L_2, \tag{16}$$

where $g(x, y)$ is the image that would result if there were no motion. Again to avoid edge effects we suppose $g(x, y)$ defined everywhere

* Because of the growing factor $\lambda$, both (15) and (11) must ultimately be cut off at some point beyond the largest spatial frequency of interest in the photographs.

and different from zero only in the rectangle $-L_1 \leqq x \leqq L_1 - uT$, $-L_2 \leqq y \leqq L_2 - vT$, so that defining $f = 0$ for $|x| > L_1$, $|y| > L_2$ we can write

$$f(x, y) = \int_0^T g(x - ut, y - vt)\, dt, \qquad -\infty \leqq x, y \leqq \infty. \tag{17}$$

Into (17) now introduce the Fourier representation

$$g(x, y) = \int_{-\infty}^{\infty} d\xi \int_{-\infty}^{\infty} d\eta\, G(\xi, \eta) e^{i[\xi x + \eta y]}.$$

There results

$$\begin{aligned} f(x, y) &= \int_0^T dt \int_{-\infty}^{\infty} d\xi \int_{-\infty}^{\infty} d\eta\, G(\xi, \eta) e^{i[\xi(x-ut)+\eta(y-vt)]} \\ &= \int_{-\infty}^{\infty} d\xi \int_{-\infty}^{\infty} d\eta\, e^{i(\xi x+\eta y)} G(\xi, \eta) e^{-i[(\xi a+\eta b)/2]} \frac{\sin(\xi a + \eta b)/2}{(\xi a + \eta b)/2} \end{aligned} \tag{18}$$

on performing the $t$ integration. Here

$$a = uT, \qquad b = vT.$$

Since (18) holds for all $x$ and $y$, we see that the Fourier transform of $f$ is given by

$$F(\xi, \eta) = G(\xi, \eta) e^{-i[(\xi a+\eta b)/2]} \frac{\sin(\xi a + \eta b)/2}{(\xi a + \eta b)/2}. \tag{19}$$

As seen from (19) the transform of the blurred photograph is zero on the family of parallel lines

$$\xi a + \eta b = 2n\pi \qquad n = \pm 1, \pm 2, \cdots.$$

These lines of zero density in $F$ should provide a reasonable means of estimating the parameters $a$ and $b$. Due to noise, the curves of zeros of $F$ will not appear as straight lines. The job of fitting straight lines to these curves of zeros should be greatly simplified however by the knowledge that the lines are parallel and uniformly separated. Once the fitted lines are drawn, value of $a$ and $b$ are readily found.

## IV. MORE GENERAL MOTION

In the present model, the blurred photograph that results from the general nondistance-distorting motion of a small object is

$$f(x, y) = \int_0^T dt\, g[(x - u) \cos \varphi - (y - v) \sin \varphi, \cdot (x - u) \sin \varphi + (y - v) \cos \varphi]. \tag{20}$$

Here $g(x, y)$ is the illuminance that would result if the object were at rest with respect to the film during the exposure, $u$ and $v$ are functions of $t$ giving, respectively, the $x$ and $y$ coordinates of the origin of a coordinate system fixed with respect to the body, and $\varphi = \varphi(t)$ is the angle that this second coordinate frame makes with respect to the $x$–$y$ frame. In the case of most immediate interest

$$\begin{aligned} u &= x_0 + \bar{u}t \\ v &= y_0 + \bar{v}t \\ \varphi &= \omega t. \end{aligned} \tag{21}$$

One finds without difficulty that the Fourier transform of $f$ and $g$ are related by

$$F(\xi, \eta) = \int_0^T dt\, e^{-i[u\xi + v\eta]} G[\xi \cos \varphi - \eta \sin \varphi, \xi \sin \varphi + \eta \cos \varphi]. \tag{22}$$

This equation appears somewhat simpler in polar coordinates. We write

$$\begin{aligned} \xi &= \rho \cos \theta \qquad & \eta &= \rho \sin \theta \\ u &= V \cos \alpha \qquad & v &= V \sin \alpha \end{aligned}$$

and set

$$F(\xi, \eta) = \hat{F}(\rho, \theta) \qquad G(\xi, \eta) = \hat{G}(\rho, \theta).$$

Then (22) becomes

$$\hat{F}(\rho, \theta) = \int_0^T dt\, e^{-i\rho V \cos(\theta - \alpha)} \hat{G}(\rho, \theta + \varphi). \tag{23}$$

Here $V$, $\alpha$ and $\varphi$ are functions of $t$.

Under these general conditions, I have been unable to find a practical method for obtaining the undistorted scene $g$ from $f$, either in the space domain, or from the transform statements (22) and (23). Even in the case of combined uniform translation and uniform rotation given by (21) no method is as yet evident.

The case of pure uniform rotation, $\bar{u} = \bar{v} = 0$ can, however, be treated and complements the case of pure translation ($\omega = 0$) already discussed in Sections II and III. Working directly in the space domain,

(20) becomes

$$f(x, y) = \int_0^T dt\, g[(x - x_0) \cos \omega t - (y - y_0) \sin \omega t, \cdot (x - x_0) \sin \omega t + (y - y_0) \cos \omega t].$$

Introduce polar coordinates located at the center of rotation

$$x - x_0 = \rho \cos \theta$$

$$y - y_0 = \rho \sin \theta$$

$$\hat{f}(\rho, \theta) = f(x, y), \qquad \hat{g}(\rho, \theta) = g(\rho \cos \theta, \rho \sin \theta). \tag{24}$$

We now have

$$\hat{f}(\rho, \theta) = \int_0^T dt\, \hat{g}(\rho, \theta + \omega t) = \frac{1}{\omega} \int_\theta^{\theta + \omega T} d\theta'\, \hat{g}(\rho, \theta')$$

which is basically of the form (3) already treated. The basic restoration equation is

$$\hat{g}(\rho, \theta) = -\omega \frac{d}{d\theta} \hat{f}(\rho, \theta) + \hat{g}(\rho, \theta + \omega T), \tag{25}$$

where $\rho$ is to be regarded as a parameter, $\hat{g}$ and $\hat{f}$ are periodic in $\theta$ with period $2\pi$ and the equation holds for all values of $\theta$.

If $\hat{g}(\rho, \theta)$ is known *a priori* as a function of $\theta$ along an arc of angular extent $\omega T$ radians, (25) can be used successively to determine $\hat{g}$ for all $\theta$. It is not hard to show that *if $\hat{g}$ is not known a priori on a $\theta$ set of angular measure $\omega T$, unique restoration is impossible.* Indeed, there exists a scene with values assigned arbitrarily (except for an additive constant) in a wedge of angle $\omega T$ which, when rotated, will give rise to any preassigned blurred photograph.

In the case of a blurred photograph of a rotating unknown object, for example, if the center of rotation is within the body, unique restoration is impossible in the neighborhood of this center. If restoration is to be made, one must use some form of *a priori* knowledge to specify $\hat{g}$ or an estimate of $\hat{g}$ in some angular interval of amount $\omega T$.

Restoration by means of the difference equation (25) presupposes knowledge of $\omega$ and [from (24)] the center of rotation $x_0$, $y_0$. We have not found a simple way of estimating these parameters. Unlike the

case of pure translation, the Fourier transform of the blurred picture,

$$\hat{F}(\rho, \theta) = e^{-i\rho(x_0 \cos\theta + y_0 \sin\theta)} \int_0^T dt\, \hat{G}(\rho, \theta + \omega t),$$

does not seem to offer special clues. If the object has some straight line edges, their initial and final positions may show clearly enough in the blurred photograph to allow estimates of $x_0$, $y_0$ and $\omega T$ to be made. For example, if $l_1$ and $l_1'$ are the lines along the initial and final positions of some edge of the body, the angle between $l_1$ and $l_1'$ is clearly $\omega T$. Let $l_2$ and $l_2'$ be lines along the initial and final position of some other straight line feature of the object and let $P$ be the intersection of $l_1$ with $l_2$ and $P'$ be the intersection of $l_1'$ with $l_2'$. The center of rotation $O$ must lie on the perpendicular bisector of the segment $\overline{PP'}$, and its position is chosen so that $\angle POP' = \omega T$. It is likely that, in practice, restoration with several different trial values of the parameters will have to be made and the best result selected.

REFERENCES

1. O'Neill, E. L., *Introduction to Statistical Optics* Addison-Wesley Co., 1963, pp. 27–29. Shack, R. V., The Influence of Image Motion and Shutter Operation on the Photographic Transfer Function, Appl. Opt. *3*, October 1964, pp. 1171–1181, also considers this problem and lists a number of earlier references. For some recent experimental results on restoration see Harris, J. L., Image Evaluation and Restoration, J. Opt. Soc. Am., *56*, May, 1966, pp. 569–574.

# Cathode Activity Measurement: a Modification of the Dip Test

By D. W. MAURER

(Manuscript received August 17, 1965)

*A method of cathode activity measurement which yields fundamental cathode parameters has been developed. Basically, it is a modified dip test and consists of plotting cathode current vs cathode temperature. A simple geometric analysis of the data plot yields data that can be related from one tube to another and to the cathode work function. Thus, experience gained by this simple and rapid technique may be translated from one tube type to another.*

*This technique can be used to obtain the work function as a function of cathode temperature and a method is suggested for obtaining work function as a function of current density.*

## I. INTRODUCTION

The activity measurement technique to be described, was developed to fill the need for a standard technique to be used on a rather large diode program. The requirements of an activity measurement for this program which are common to any tube development, may be stated briefly as follows:

(*i*) The measurement must cause a minimum disturbance to the chemical equilibria existing in the tube, in other words not interrupt the life processes.

(*ii*) The measurement should be rapid, to permit regular study of a large number of tubes.

(*iii*) The parameter (*s*) measured should be related to some fundamental property of the cathode, independent of the tube.

(*iv*) The technique should not require complicated or specialized electronics which are subject to break down or drift.

A review was made of the currently available techniques. All of them suffer from one or more shortcomings when evaluated by the above

requirements. Child's law plots or perveance measurements are useful but tend to substantially upset the tube equilibrium especially when data are taken at higher cathode loading than the normal operating point of the tube. The higher power invariably leads to deactivation, especially in close spaced diodes. If data above the operating point are taken with short (1 to 2 $\mu$sec.) pulses this problem is eliminated but the process is very time consuming and involves complex electronics. Use of single high-voltage pulses to obtain the current at a fixed point in the Schottky region yields good information so long as equipment is stable and capable of precise calibration. However, it gives no information on uniformity of emission or possible changes in the shape of the Schottky line. The use of short pulses is also difficult without elaborate precautions in the life rack to eliminate stray capacitance and high voltage breakdown. Any of the above techniques are inappropriate in gun-type tubes because of high-voltage breakdown in the tubes and, in the case of traveling-wave tubes, because the beam current is limited by the magnetic field strength. Shot noise measurements are useful and give information on uniformity as well as activity, but require complicated equipment.

Dip testing as first described by Bodmer[1] would satisfy all the requirements previously stated if the data taken could be related to fundamental cathode parameters. That these techniques are effective given good cathodes has been demonstrated. However, for the proposed Bell Laboratories diode program, in which at least some of the cathodes would be of poor activity, and probably of nonuniform emission, this method did not appear suitable. The relationship to basic cathode parameters had also not been shown. Another concurrent and independent piece of work on the dip technique was described by Dominguez, Doolittle and Varadi.[2] They have explained the shape of the curve and used the data to follow the activation of production tubes.

This paper will describe a modification of the dip technique which is based on a method first used by A. J. Chick[3] in connection with the life study of the *Telstar*® TWT in 1962. Instead of measuring the usual dip in cathode current in a given time, he substituted a dynamic recording of cathode current and temperature to facilitate the study of the transition region between space charge and temperature limited emission, i.e., the knee. Plotting the knee temperature during life, he found it to be an accurate indication of cathode activity.

The technique has now been further improved and a simple and reliable method will be described to establish the knee even if the transi-

tion is poorly defined. An extensive diode program has been evaluated with this technique and its utility is shown by following tube activity on life. It will also be shown how data taken in this way can be used to determine basic cathode parameters and to obtain measurements of these under conditions not previously obtainable. Examples will also be shown of its use in analyzing the effects of cathode temperature on work function.

## II. THE TEST METHOD

In this section the experimental technique and the method of data analysis will be discussed followed by an example of its use. Then the details of several experimental problems will be discussed.

### 2.1 *The Measurement Technique and Data Analysis*

In the modification of the dip test developed here, an $X$-$Y$ recorder is used to plot cathode current vs cathode temperature when the heater power is turned off. The experimental apparatus is shown in Fig. 1. The cathode current of the tube on test is recorded on the $Y$-axis of the $X$-$Y$ recorder. The temperature, monitored by the infrared pyrometer, is recorded on the $X$-axis. A typical curve obtained by this technique is shown in Fig. 2. This consists of two regions: on the right is the current vs temperature in the space-charge limited region and on the left is the current vs temperature in the temperature limited region. These two regions are separated by a knee. The roundness of the knee is caused by nonuniformities of emission and the energy distribution of the electrons. The decrease in current with temperature in the space-charge limited region is caused by changes in spacing with cathode temperature and by a movement of the space-

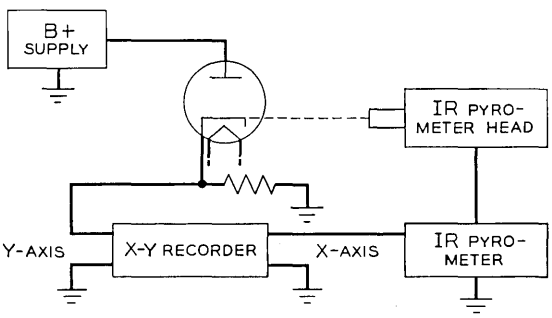


Fig. 1 — Apparatus for *IR* dip measurement.

charge minimum in front of the cathode towards the cathode as the temperature decreases. The decrease in current in the temperature limited region depends on the work function and is exponential in shape. Experimentally, the upper part of the exponential region can be approximated by a straight line over a short range, as shown in Fig. 2. This is extrapolated up to the initial current and is used to define the knee. The temperature at the knee which is characterized in this way ($T_{IR}$) corresponds roughly to the temperature at which the tube could be operated and just maintain space charge limited operation at the operating current density. Higher values of $T_{IR}$ derived from this plot imply lower activity and lower values, higher activity.

### 2.2 *A Life Plot*

An example of the use of this technique to make a life plot is shown in Fig. 3. This is a plot of data taken after activation on a set of six diodes with experimental cathodes. The curve is the average of data from six diodes. As the end of life approaches, (due in this case to coating depletion), the dip temperature rises to approach the operating temperature, i.e., there is no space-charge limited region at the operating temperature at the failure time.

### 2.3 *Experimental Problems*

A difficulty in the use of an infrared pyrometer to monitor temperatures in tubes containing borosilicate glass (Kovar sealing glass)

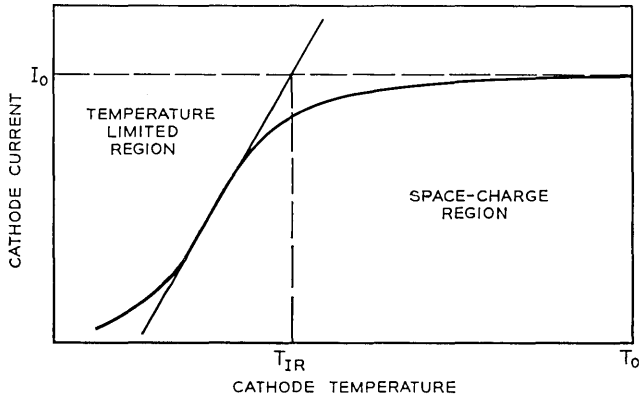


Fig. 2 — Typical data obtained by the *IR* dip technique.

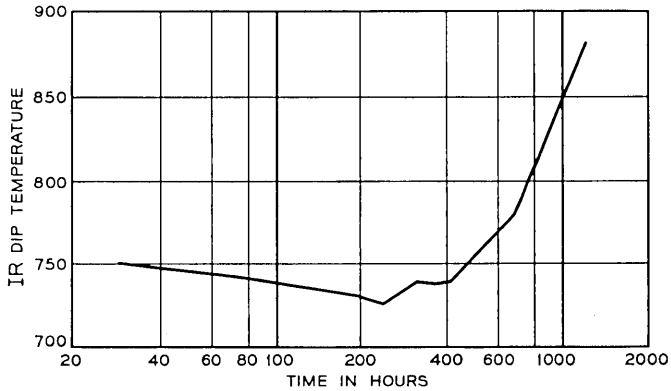


Fig. 3 — Life plot of the average of six diodes operating at 850°B.

envelopes is that the glass has a relatively high infrared absorption. Therefore, flaws and variations in thickness of the glass, etc., would have relatively large effects on the temperature measured. To circumvent this problem the temperature of the cathode is adjusted with an optical pyrometer. This technique allows the infrared pyrometer to be calibrated each time the tube is read. That is, glass flaws, variations in the thickness of the glass, etc., enter as correction terms to the emissivity. To demonstrate that these factors would have no effect on the dip temperature, this was measured with the infrared pyrometer in these various situations:

(*i*) The infrared pyrometer at various angles to the axis of the tube and at various distances from it.

(*ii*) The pyrometer sighted on the cathode base nickel or on the molybdenum cathode heater sleeve.

(*iii*) The pyrometer sighted on the image of the cathode nickel in a gold-backed mirror.

In all cases the dip temperatures were identical.

Another difficulty in the use of an infrared pyrometer is that the scale reading, and thus, the $X$ axis of the plot, is not a linear function of temperature and a conversion chart must be used to obtain the temperature. Since most of our diodes are operated at one of three temperatures we have alleviated this problem by making a plexiglass ruler which has the three temperature scales for the $X$ axis corresponding to each tube temperature. In this way, it is a simple process to measure the knee temperature directly from the plots.

Thermocouples may also be used to measure cathode temperature; however, these are often unreliable over long periods of time. In some cases thermocouples are not pratical and the cathode cannot be directly viewed with a pyrometer. This is usually the case for a traveling-wave tube in its magnetic circuit. In this case, we have obtained a temperature vs time curve for a dip outside the circuits; then a current vs time plot was taken in the circuit. The current-time curve is analyzed in the same manner as current-temperature curves to give a knee time. The temperature can then be obtained from the temperature-time calibration. This calibration must be checked periodically due to changes in cathode support welds, heater resistance, etc.

## III. OTHER APPLICATIONS OF THE TEST METHOD

In this section the analysis of the data will be extended to show how the information obtained from the dip plots is related to the work function $\varphi$. First, the method of obtaining $\varphi$ from the test data will be described. Then the description of the method of obtaining it as a function of temperature independently of the $A$ constant will be given. Finally, a method will be proposed for the determination of work function as a function of current density.

### 3.1 *Measurement of Work Function*

In the temperature limited region shown in Fig. 2, the current follows the well-known Richardson equation modified due to the Schottky effect caused by the field on the cathode.[4] The equation for the combination of the two effects is easily obtained by substitution:

$$\ln \frac{J}{T^2} = \ln A + \left(0.44(GV)^{\frac{1}{2}} - \frac{\epsilon\varphi}{k}\right)\frac{1}{T},$$

where

$J$ = current density,
$T$ = absolute temperature,
$A$ = the Richardson Constant,
$G$ = geometry factor,
$V$ = voltage,
$\epsilon$ = electronic charge,
$k$ = Boltzman constant,
$\varphi$ = work function.

According to this equation, in the temperature limited region at constant voltage, if the log of $J/T^2$ is plotted against $1/T$, a line should be obtained whose slope is a combination of the work function and the geometric factor. A calculation shows that the geometric term should be negligible for planar diodes with respect to the work function term at the voltages used.* Under these conditions this equation reduces to the Richardson equation. Originally, a series of dips were taken at various tube voltages and the knee temperatures ($T_{IR}$ on Fig. 2) were used to make a Richardson plot. These plots were always straight lines. This was taken as confirmation of the utility of the knee temperature as a significant measure of cathode activity.

Data have also been taken from a single dip curve below the knee and fed into a computer to determine a least squares fit, calculate the work function and plot the data. An example is shown in Fig. 4. There is a very good fit to a straight line. The slope corresponds to a work function of 1.2 eV.

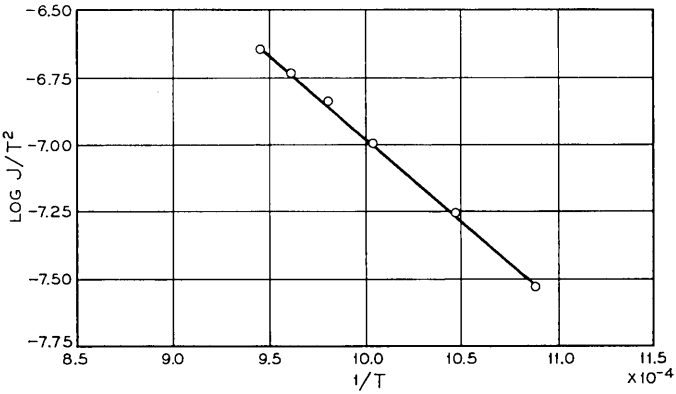


Fig. 4 — Richardson plot for tube 370.

### 3.2 *Work Function as a Function of Temperature*

As as basis for discussion in this section and the following one (Section 3.3) several points from the generally accepted hypothesis of cathode operation are pertinent:

(*i*) The cathode is a semiconductor with mobile donors which mi-

* The term $GV$ is the field at the cathode. For parallel plane geometry, $G = 1/D$ where $D$ is the separation distance. Other geometric configurations may be calculated appropriately, see Ref. 4, p. 30.

grate under the influence of fields. The time constant for donor redistribution is of the order of milliseconds.[5]

(*ii*) The lifetime of donors in the coating is much longer than their transit time across the coating. Usually the lifetimes are of the order of hours.[5, 6, 7]

(*iii*) The work function of the cathode is a slowly varying function of donor concentration at the surface down to a critical value, whereupon it rises rapidly with further decrease in concentration.

The fact that donors redistribute themselves within milliseconds under the influence of fields means that the work function measured by the dip technique will not contain the effect of current density. Therefore, measurements should be made at low current densities where these effects are small; otherwise an average of the donor distribution will be obtained and the effect will be difficult to analyze. On the other hand, the fact that donor loss is quite slow, means that the total donor concentration (not the concentration gradient) within the cathode will be essentially "frozen in" as the cathode cools and the effect measured will be that of a cathode *as it exists at the starting temperature.* Thus, with this technique, we can measure the work function and the $A$ constant *independently* at a given cathode temperature. This point is important. The usual technique of getting the temperature dependence of the work function is to measure $J$ and $T$, insert them into the Richardson equation and solve for $\varphi$ assuming $A = 120$. This assumption is not a good one for oxide cathodes. The $A$ constant contains a term which is the "effective" emitter area, i.e., that area which is actually emitting electrons. It has been widely demonstrated in the literature that oxide cathodes are composed of an aggregate of small areas of high and low work function. Furthermore, measured $A$ values for oxide cathodes determined by the conventional plotting techniques mentioned above vary widely ($10^{-3}$ to $2.8 \times 10^4$).[8]

The advantage of this technique in measuring work function is demonstrated from data taken on two similar diodes. The work function of one was measured by the usual technique of taking Schottky data at various cathode temperatures. A plot of these data is shown in Fig. 5. Data from these curves were then replotted according to the Richardson equation to give the plot shown in Fig. 6. This plot has a straight line section with a slope which corresponds to a work function of the order of 1.5 eV. The points deviating from this line at the higher temperatures are characteristic of what is observed on

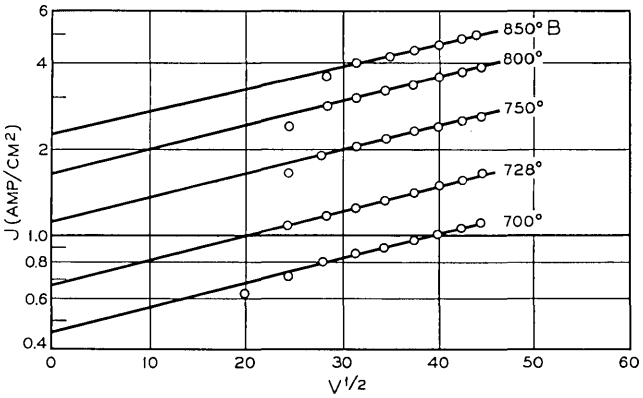


Fig. 5 — Schottky plot of tube 246.

many cathodes and represent a changing cathode system in these regions which results in an increasing work function and probably a changing $A$ value. The most likely explanation is that the donor depletion at the higher temperature increases faster than the donor production rate. This results in cathodes of higher work function at the higher temperature. This was confirmed on another tube where the work function was measured by the dip technique described above. The work function measured at an initial cathode temperature of 750° brightness was 1.5 eV in good agreement with the results of the Schottky plot. However, the work function measured at 850° brightness was 1.7 eV.

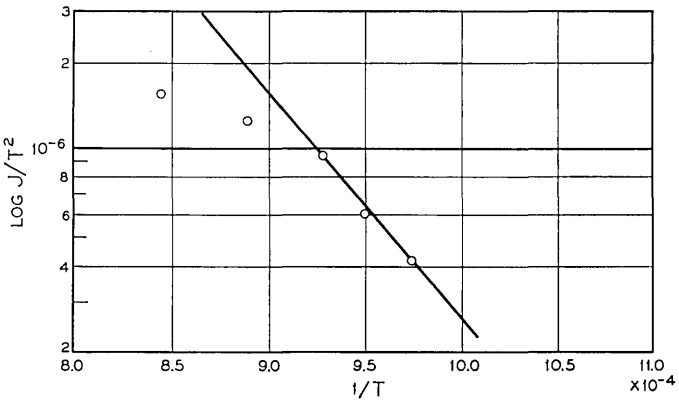


Fig. 6 — Richardson plot of data from Fig. 5.

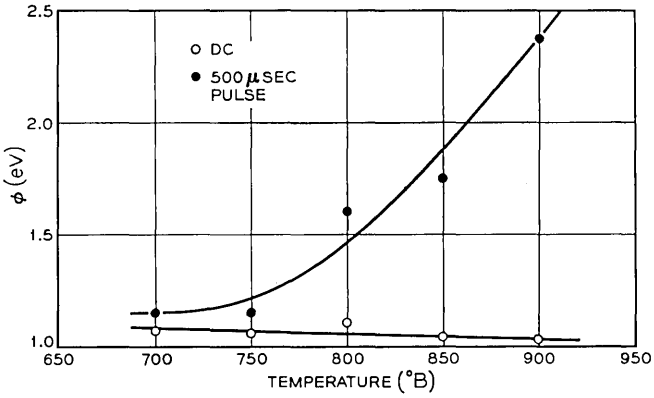


Fig. 7 — $\varphi$ $(T)$ for an experimental cathode.

This technique has been used to demonstrate electrolytic activation in an experimental cathode which is described elsewhere.[9] In this case the work function was measured for various cathode temperatures using both dc and 500 $\mu$sec pulses. The results are shown in Fig. 7. Notice that the values obtained by using dc follow what might be considered the normally expected pattern and are relatively constant. The pulse values, however, are constant only up to about 750°B where they increase rapidly with further increase in temperature. The explanation for the pulse results is the same as for the plots previously presented: The donor loss increases faster than donor production. The dc values remain constant because electrolysis is contributing to the donor production, and therefore, $\varphi$ remains low in

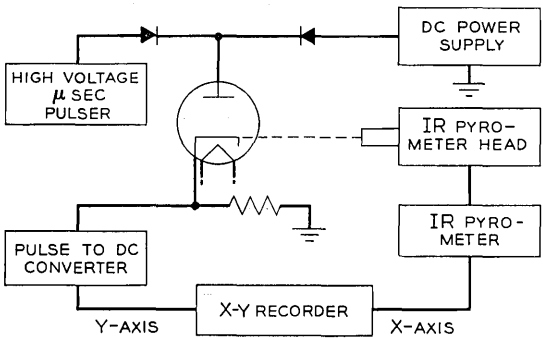


Fig. 8 — Apparatus for measurement of $\varphi$ vs $J$.

value. It may be expected that the dc values would increase if the temperature were taken higher.

The utility of this technique in measuring work function in an operating temperature range where the work function of the cathode is changing as a function of cathode operating temperature has been demonstrated. The possibility of measuring work function independently of $A$ at a set temperature in a region where $\varphi$ is changing as a function of temperature was not recognized before. Thus, it is a new tool for the investigation of the mechanism and operation of cathodes in this region.

### 3.3 *Proposed Measurement of Work Function as a function of Current Density*

If one wanted to observe the variation in work function with current density, the following technique could be used. The apparatus is shown in Fig. 8. Here, microsecond pulses are to be superimposed on a dc operating level. The pulse current is to be used to make dip measurements. In this way the temperature limited region well above the operating current density can be monitored to define the work function while the dc operating current density is still in the space-charge limited region. By this means, the point at which the work function begins to rise rapidly with current density, i.e., the dc current density at which donor depletion at the surface becomes appreciable, can be determined. This limiting current density is a measure of the minimum donor concentration required in the surface of the cathode under given dc conditions.

## IV. CONCLUSIONS

The modified dip test described here yields data which can be related to a fundamental cathode parameter, namely the work function. This permits quantitative studies of cathode activity throughout life. The technique can further be used to determine information about the concentration of the donors in the cathode. The method described is of general practical utility; the data can be obtained rapidly and be directly compared from one tube type to another.

## REFERENCES

1. Bodmer, M. G., Dip Testing, A New Method for Measuring Cathode Activity, IRE Transactions on Electron Devices, *ED-5*, #1, 1958, pp. 43–44; Bodmer, M. G., et al, Satellite Traveling-Wave Tube, B.S.T.J., *42*, No. 4, July 1963, pp. 1740–1743.

2. Dominguez, R., Doolittle, H. D., and Varadi, P. F., Oxide Cathode Evaluation by Dip Test Method, Rep. 24th Annual Conf. Phys. Elec., 1964, pp. 27–35.
3. Chick, A. J., private communication
4. Cf. Nottingham, W. B., Thermionic Emission, Handbuch der Physik, *21,* 1956, pp. 8 and 32.
5. Krusemeyer, H. J., and Pursley, M. V., Donor Concentration Changes in Oxide-Coated Cathodes Resulting from Changes in Electric Field, J. Appl. Phys., *27,* 1956, pp. 1537–1545.
6. Kawamura, H., Shinohara, A., and Takahashi, J., On the Active Centers of the Oxide-Coated Cathode, J. Phys. Soc. Japan, *3,* 1948, pp. 301–304.
7. Frost, H. B., Gas Content and Cathode Emission Changes in Cut-off Electron Tubes, Supplemento al Nuovo Cimento, Serie I, *1,* 1963, pp. 780–790.
8. Herrmann, G., and Wagener, S., The Oxide Coated Cathode, *2,* Chapman & Hall Ltd., London (1951), p. 181.
9. Maurer, D. W. and Pleass, C. M., The CPC: A Medium Current Density, High Reliability Cathode, B.S.T.J., this issue, pp. 2375–2404.

# The CPC: A Medium Current Density, High Reliability Cathode

By D. W. MAURER and C. M. PLEASS

(Manuscript received March 1, 1967)

*The coated powder cathode is an inexpensive, reproducible emitter which combines the virtues of various conventional cathode types, and is suited to use in modern high-power, high-reliability electron tubes. It is best considered as a modification of the classic oxide cathode in which each particle of the emissive coating is covered with a thin layer of nickel. Inherent advantages of this cathode over the oxide cathode include the ability to sustain current densities up to 1 amp/cm$^2$ over long, calculable lifetimes, increased flexibility in time and temperature during processing, and improved coating adhesion. This paper describes the concept, fabrication and mechanism of the cathode and presents data obtained from a diode evaluation program.*

## I. INTRODUCTION

Modern requirements for high-power microwave tubes having very high reliability have accentuated the demand for cathodes capable of dc or long pulse emission in the range 0.5 to 1.0 amps/cm$^2$ over lifetimes up to 50,000 hours. The best oxide cathodes available function only at the lower end of this range over relatively short lifetimes, and in consequence metal matrix types are normally used. The most widely used of these is the tungsten matrix, but this demands operating temperatures of the order of 1000°C,* and the reliability of the tube then begins to depend on factors such as the integrity of the cathode heater and its radiation shielding. Nickel matrix cathodes, prepared from powder compacts of nickel and active oxides, and

* Throughout the remainder of this paper, °C will be used to mean degrees Centigrade true temperature. The abbreviation °B will be used to mean degrees Centigrade brightness on nickel as measured by optical pyrometer on the side of the cathode button.

capable of operating at temperatures between the tungsten matrix and oxide cathodes, are limited in high-reliability applications by their shrinkage, residual gas context, and local inhomogeneities. The conventional oxide cathode, with its low operating temperature and "clean" structure, would normally be the best choice if it were possible to modify it in such a manner as to permit emission of the order of 1 amp/cm$^2$ over lifetimes in excess of 20,000 hours.

The coated powder cathode (CPC) can be regarded as a modified oxide cathode in which the active coating is prepared from particles of conventional electron tube grade carbonates, each lightly coated with nickel. The nickel normally constitutes only 1 to 3 percent by weight of the carbonate. Its primary effects are to change the electrical resistance, sintering behavior, and emissivity of the coating. The improved performance of the coated powder cathode can be interpreted in terms of these primary effects.

If an oxide cathode coating is permeated by metal forming electrical contacts between the base and the vacuum interface, the field lines along which electron donors drift during high current density operation are modified. The major component of the field will become transverse when the distance between metal "electrodes" in the coating becomes substantially less than the coating thickness. The donors will then remain in the surface layers of the cathode coating, keeping the work function low. This situation exists in metal matrix cathodes, where relatively small particles of oxide are embedded in nickel or tungsten, an analogy being one of metal tubes filled with oxide extending to the surface. The donors in such systems would be expected to move toward the metal-oxide boundary at the surface as current density is increased, giving an oxide-vacuum surface having a nonuniform but essentially constant concentration of donors. Despite the nonuniformity, the average or effective work function remains low.

The CPC is constructed with a novel distribution of nickel in the active coating, which achieves the surface donor retention mentioned above with only 0.5–3.0 wt percent of metal.* This should be compared to 70-80 wt percent metal normally required to provide a conducting path through a conventional matrix cathode. In reducing the amount of metal involved in the surface one approaches the lowest

* Normal oxide cathodes have resistances of the order of 1-10 $\Omega$/cm$^2$. Assuming the bulk resistivity of nickel, the nickel coating of a CPC particle could in theory be of the order of $10^{-13}$ cm thick to have a resistance comparable to the activated oxide. Therefore, films of the order used (0.01 $\mu$) should have substantial effects even if the resistivity of the film is substantially greater than the bulk resistivity.

practical work function—that of the classic oxide cathode. Thus, the operating temperature of the CPC (700-800°C) is comparable to that of the oxide cathode, and is essentially unaffected by the emission level in the region studied. Operating temperature is, however, influenced by the vehicle employed, in proportion to the rate of poisoning reactions. Thus, a close-spaced diode normally requires a cathode temperature of the order of 800°C, while a travelling-wave tube with a slow wave structure and remote collector will operate in the 700-750°C region.

The nickel film around each particle also inhibits the growth of relatively inactive, large single crystals of (Ba, Sr)O during high temperature outgassing. In this respect, note that Eisenstein[1] has shown (Ba, Sr)O crystallite growth in oxide cathodes to be relatively rapid above 900°C and many workers have observed the degraded high current density characteristics of oxide cathodes that experienced appreciable time at temperatures above 900°C. This is consistent with the suggestion[2] that donor movement in single crystal material is very fast, leading to deep donor depletion layers.

CP cathodes can be processed at temperatures as high as 1150°C without detectable degradation in subsequent emission. This has practical advantages in the reduction of time on the tube processing station, and in the thorough degassing afforded the heater-cathode assembly.

The inhibition of crystallite growth extends to the reprocessing of an activated CPC which has been exposed to room atmospheres. Although X-ray diffraction photographs taken before and after exposure show that water and carbon dioxide are indeed reabsorbed, the coating does not lift or "bloom," and if reprocessed by a conventional schedule will normally reactivate. This implies that the mixture of barium and strontium hydroxides and carbonates formed within each nickel shell is largely retained within the shell during reprocessing, reducing the tendency to form a glassy phase.

When sprayed onto a nickel base with a conventional nitrocellulose binder, the CPC coating shows excellent adhesion, resisting a Scotch Tape test. This appears to be related to the slight roughness of the particle surface. This is visible in Fig. 1, which shows representative photomicrographs of coated and uncoated powders. During breakdown of the carbonate to oxide, the nickel film is split to allow the escape of carbon dioxide, and at the same time, nickel-to-nickel sintering begins. The latter is effective in increasing the adhesion to the base and

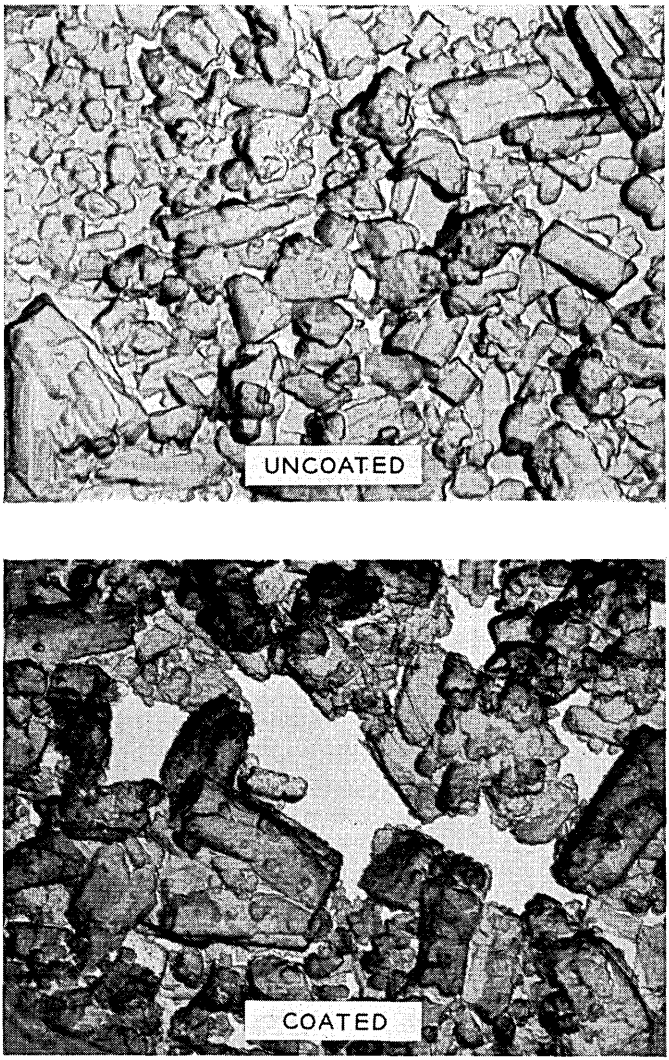


Fig. 1 — Electron micrographs of nickel coated and uncoated double carbonate particles.

the cohesion of the coating still further. The oxidation of the nickel shell during carbonate breakdown is found to be very slight. In tubes requiring ultra-smooth coatings (ultrafine powder), excessive cohesion between particles can give rise to surface cracking known as "mud-flatting" unless care is exercised during the processing. However, through the particle size range normally used in oxide cathode technology, the integrity and adhesion of the processed coating is excellent.

The nickel network responsible for the improved performance of the CPC is maintained during life by sublimation of nickel from the base alloy into the coating. An equilibrium is attained, wherein nickel is lost by evaporation from the surface of the coating, and replenished from the base. Thus, a CPC coating, applied to a low vapor pressure metal such as platinum, would slowly lose its metal network during life, and transform into a simple oxide cathode. This transformation has been observed, but has not been studied quantitatively. However, many of the advantages of the CPC are gained by establishing nickel-to-nickel contact between each particle prior to breakdown and activation, and use on substrates other than nickel to gain processing advantages is not unreasonable. Notice that the overall rate of nickel sublimation from a CPC is identical to that of an oxide cathode operating at the same temperature.

## II. PREPARATION OF THE NICKEL COATED POWDER

A useful technique for the preparation of metal coated powders involves the decomposition of a thermally unstable metal compound in a "fluid bed." In conventional nickel coating, the powder is normally maintained "fluidized" by the passage of hydrogen through a sintered disc at the foot of a vertical tube containing the powder. Nickel carbonyl, $Ni(CO)_4$, is introduced to the hydrogen stream and thermally decomposed to nickel on contact with the heated powder. This method is excellent for use with metal powders or insulating materials of particle size $>50\ \mu$. However, in the range $50\ \mu \rightarrow 5\ \mu$ the agglomeration of insulating particles as a result of the accumulation of static charge becomes increasingly serious, and it has previously been considered impractical to coat each individual particle of an insulating powder of particle size $<5\ \mu$.[3] Since most cathode powders are substantially $<5\ \mu$, and the coating of individual particles was most desirable, a new technique was required. This was found in a method we choose to call "wet" fluid-bed coating. The powder is maintained suspended in a suitable inert liquid and $Ni(CO)_4$ introduced through

a bubbler. This eliminates agglomeration, at the expense of an additional processing step—the removal of the liquid.

Since we are dealing with a cathode material where trace contamination may poison the emission and cause tube failure, extreme care in handling under ultraclean conditions is imperative. All vessels and handling devices must be cleaned according to normal oxide cathode preparation specifications, and all materials used must pass oxide cathode specifications for impurity content. Once cleaned, vessels must be protected from contamination prior to use.

The powders used in these experiments were coprecipitated from nitrate solutions with ammonium carbonate and have been extensively used for conventional cathode coatings. For the present study the "as received" powders were reduced in particle size by ball milling to give very smooth "high density" cathode coatings.* This procedure does not improve emission, and is, therefore, only required where electrode spacings require tight tolerances on coating uniformity and smoothness. Where the particle size of commercially available carbonate is appropriate for the tube requirement, "as received" powder may be nickel-coated without any preconditioning.

Fig. 2 is a schematic of the nickel coating apparatus. The apparatus is composed of a reaction vessel and a flow system. Hydrogen is the carrier gas used during the reaction. Nitrogen is used for flushing to keep the system free of contamination while on standby and to purge the hydrogen at the termination of the reaction.

A modified 500 cc gas wash bottle is used as the reaction vessel. It is modified to bring a gas entry tube down the wall inside the vessel to within 1 inch of the bottom. The center of the vessel is then free for a nickel stirring rod adapted to the vessel through a nickel taper fitting in the ground glass joint at the top. The nickel taper is, in turn, fitted to a rotary vacuum feed-through coupled to an electric motor. All of the joints are vacuum tight and only nickel faces the inside of the vessel, thus avoiding foreign contamination. The entire vessel is immersed to just below the gas inlet tube in an oil bath and the contents of the vessel brought to the reaction temperature of 110°C with a hotplate. A suspension of the carbonate in amyl acetate is added to the reaction vessel before sealing the system. A condenser is installed at the exhaust end of the reaction vessel to allow reflux of the amyl acetate that vaporizes at 110°C, thus keeping the solution level constant.

* Particle size: 90 percent $<1.6\ \mu$; coating density: approximately 2 g/cc.

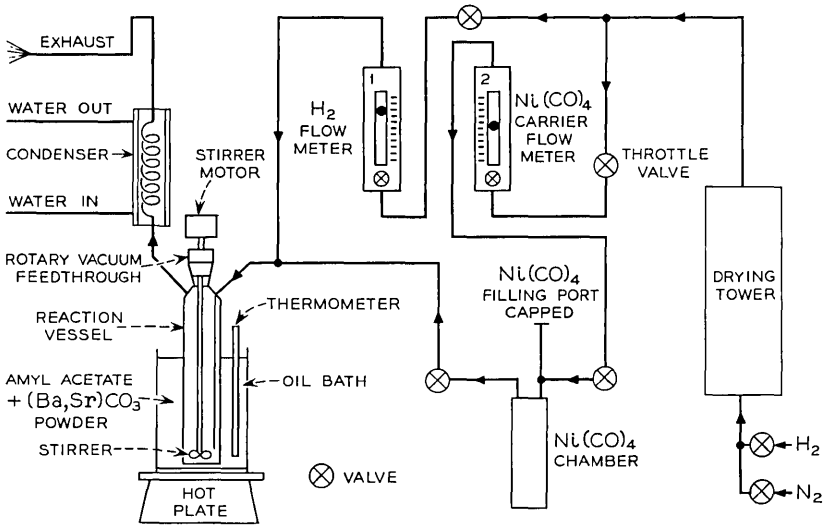


Fig. 2 — Nickel coating apparatus.

The $Ni(CO)_4$ chamber is made of metal, with a gas inlet tube running to within ½ inch of the bottom, and an inlet port that can be opened for filling and sealed during the reaction. A measured excess of carbonyl is added before every reaction and the chamber emptied and flushed with nitrogen at the completion of every run.

After the system is sealed and purged with nitrogen, a flow of hydrogen is established, bypassing the carbonyl chamber, such that vigorous bubbling occurs in the reaction chamber, and a hydrogen flame is established at the exhaust. Some hydrogen is then diverted through the carbonyl chamber and this proportion increased until the hydrogen flame at the exhaust become luminous with green fringes, indicating that excess carbonyl is being burned. Under these conditions of excess carbonyl and constant bath temperatures, with a given system and powder particle size distribution, the percent nickel deposited depends on the reaction time. For our system and particle size distribution, we achieved $2.5 \pm 0.3$ weight percent nickel in $3\frac{1}{2}$ hours, although this is not a linear function of time (the reaction is autocatalytic).

The thickness of nickel on each particle will be constant under the above conditions regardless of the particle size distribution. The percent nickel in the lot, however, will vary with the particle size. Thus, the operating parameters of a given system must be determined em-

pirically. Note that since the powder used in the study described here was very fine, values of approximately 1.0 wt percent Ni would correspond to comparable Ni thickness on coarser, conventional powder.

During the coating reaction there is essentially no agglomeration of the coated powder; however, pure nickel is deposited on some parts of the reaction vessel and flakes off into the mix. To remove these flakes the coated suspension is sieved, first through a 37 $\mu$ sieve and then through a 20 $\mu$ sieve. Concentrated nitrocellulose solution is then added to bring the suspension to a condition suitable for spraying. Spray mix prepared from nickel-coated powder has similar settling characteristics to conventional oxide cathode mixes. If long shelf-life precedes use, ultrasonic agitation should be used to resuspend prior to transferring to spray equipment.

Fig. 3 shows the effect of nickel coating on the particle size of the carbonate crystallites and indicates the change to be of the order of 10 to 15 percent of the initial size. This may be accounted for by slight agglomeration rather than particle size growth. This conclusion is supported by the many photomicrographic comparisons made between coated and uncoated double carbonates. (Fig. 1) It can be seen that the coated powder has a rougher surface than the uncoated powder. This roughness may account for the superior adhesion characteristic of the coated powder.

Data shown in Table I indicate an analysis representative of a CPC surface ready for activation compared with an analysis of the as-received powder. No pick-up of undesirable elements should occur

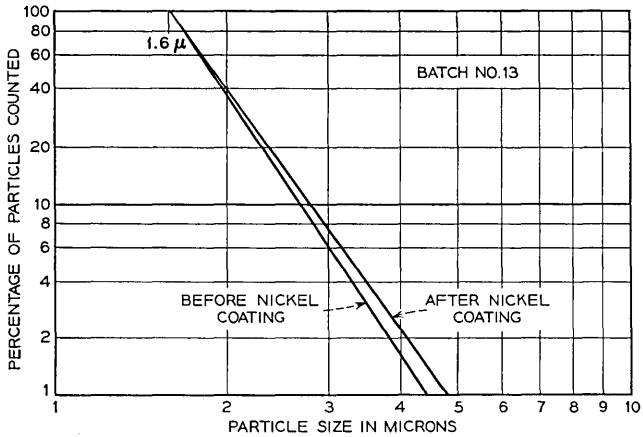


Fig. 3 — Effect of nickel coating on particle size.

TABLE I—SPECTROGRAPHIC ANALYSIS OF BARIUM-STRONTIUM CARBONATE BEFORE AND AFTER NICKEL COATING

| Element | Before (as received) | After (Ni coating) |
|---|---|---|
| Barium | Major | Major |
| Strontium | Major | Major |
| Nickel | 0.00X | Major low |
| Calcium | 0.X high | 0.X high |
| Sodium | 0.0X | 0.0X |
| Copper | 0.00X | 0.0X low |
| Silicon | Not found | Not found |
| Magnesium | 0.00X | 0.00X |
| Iron | 0.00X low | 0.00X |
| Lead | 0.00X low | 0.00X |
| Potassium | 0.00X low | 0.00X |
| Manganese | 0.000X | 0.000X |
| Silver | 0.000X low | 0.000X low |

Elements checked but not found: zinc, cadmium, indium, bismuth, antimony, arsenic, tin, thallium, gallium, germanium, zirconium, cobalt, chromium, molybdenum, vanadium, tungsten, lithium.

Note: Major = >5% Estimated

0.X, 0.0X, 0.00X, etc. = Concentration of Elements estimated to nearest decimal place, e.g., 0.0X = 0.01 − 0.09% estimated.

as a consequence of the coating operation. Infrared spectrographic analyses were made of the amyl acetate before and after the coating process. No contamination or change in the amyl acetate absorption spectrum was observed.

It is important to determine carbon introduced by the coating process, since carbon activation of the cathode would result in premature loss of oxide. Control analyses performed on nickel coated MgO of similar particle size shows that the carbon introduced (corrected for intrinsic carbon and absorbed amyl acetate) is of the order of 0.1–0.2 percent by weight of powder. This carbon appears to be completely removed during the breakdown of the carbonate to the oxide, probably through the high temperature oxidation-reduction reaction $C + CO_2 \rightleftarrows 2CO$ which favors the production of CO at temperatures above 800°C. This view is supported by the fact that there is no immediate activation in diodes, and that mass spectrometer analyses of platinum-based cathodes show no CO tail after breakdown.

## III. EMISSION AND LIFE TESTING

### 3.1 *Cathode Preparation, Vehicle, Processing and Testing*

The application of the coated powders to cathode bases used in the study described was carried out by conventional spray techniques.

Binder burnout[4] was used throughout diode testing. However, this has been found undesirable in processing large area cathodes coated with powder of a conventional particle size, since the coating coherence after binder burnout was minimal and did not allow good yields in assembly. Cathode bases were preconditioned by a rigorous method based on volatile acid cleaning[5] and including a liquid honing of the surface by calcium oxide. The base metal was high purity 0.1 weight percent zirconium/nickel alloy (see Table II) unless otherwise stated. This alloy is used to obtain long life, and is relatively inactive by comparison to standard alloys such as 220 grade nickel.

The test diode is illustrated in Fig. 4. It features a 0.085-inch cathode in a ceramic insulator, mounted on a massive anode heat sink, which includes a nickel button anode. The diode contained conventional tube materials including Kovar, steel, molybdenum, copper, nickel and ceramic. The final closure of the tube was done by heliarc welding. Pieceparts and subassemblies were cleaned by rigorous processing techniques and were atomizer clean.[5,6] Minimum grade: 3. These techniques were designed to eliminate activation or deactivation by extraneous variables and permit the study of deliberate changes in processing or material variables with a minimum of samples. The success of this can be estimated from the narrow spread in activity of "identical" diodes (Section 3.2.5) and the fact that the yield of tubes in the entire program was approximately 98 percent seal-in.

Tubes were processed in groups of six on individual getter-ion pump stations. Bakeout was for 16 hours at 425°C, at which point, the pressure was normally in the $10^{-9}$ torr range. All tubes then passed through

TABLE II—IMPURITY SPECIFICATION FOR HIGH PURITY ZIRCONIUM-NICKEL CATHODE ALLOY

| Element | Percent max. | Element | Percent max. |
|---|---|---|---|
| Copper | 0.005 | Iron | 0.005 |
| Manganese | 0.005 | Carbon | 0.003 |
| Silicon | 0.005 | Sulphur | 0.001 |
| Titanium | 0.005 | Magnesium | 0.005 |
| Tungsten | 0.005 | Oxygen | 0.001 |
| Hydrogen | 0.001 | Nitrogen | 0.001 |
| Cobalt | 0.005 | Each Other Metal | 0.005 |

All other impurities than those listed shall not exceed a total of 20 ppm and no individual impurity shall exceed 1 ppm.

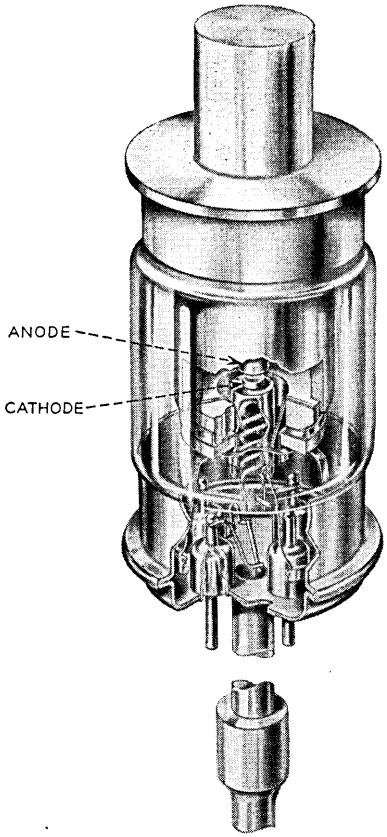


Fig. 4 — M-4059 diode.

a standard processing cycle which is described in Appendix A. They were then placed on aging racks with the cathodes at 900°C and with dc voltage applied. After 16 hours at this condition, the cathode temperature was lowered to 810°C and emission current adjusted to 0.3 amps/cm$^2$. This was the predominant current density throughout the diode program, and was based on past experience of adverse "diode effects" observed in the diode used at higher loadings. In addition, it represented a cathode design objective at the time.

The test method used for all of these tubes was the IR dip.[7] This is a modification of the dip test in which the cathode current-tempera-

ture transient is plotted on an $X-Y$ recorder when the heater power is turned off. Cathode activity is given by the temperature of the transition from space charge limited emission to temperature limited emission. Unless otherwise noted, all measurements were made at 125 mA/cm$^2$ rather than the operating level, to be assured of an activity measurement in extreme cases where the emission is not space charge limited at the operating level. With this analysis, high temperature indicates low activity, and low temperature high activity.

### 3.2 *Results of Diode Program*

Except where noted, each of the curves of diode activity shown in this section represent the average of six identical diodes. Since the significance of the difference between two such curves is difficult to assess without a knowledge of the spread in the data, the values of the probability that there is a difference between two curves are shown at significant points on the plots. The probability, $P$, is based on Student's $t$-test.

#### 3.2.1 *Reproducibility*

Fig. 5 shows the individual "IR dip" temperatures on a batch of six diodes processed according to the standard technique (Appendix A). The spread is rather wide early in life, and becomes much smaller after about 1000 hours as the tubes "age in." This allows an estimate of the spread inherent in the data to be illustrated in subsequent figures.

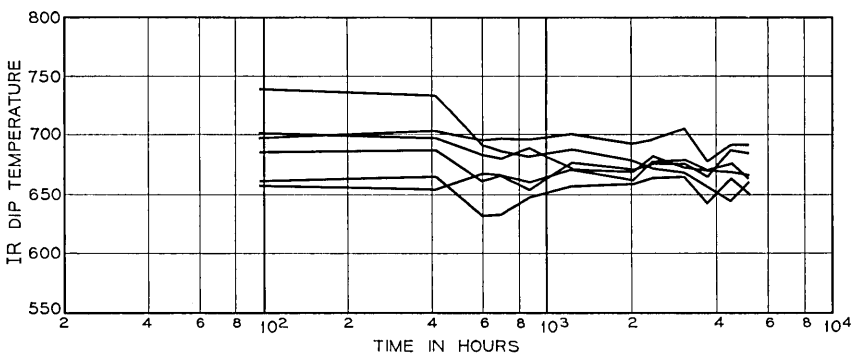


Fig. 5 — Typical spread in the data for six "identical" diodes.

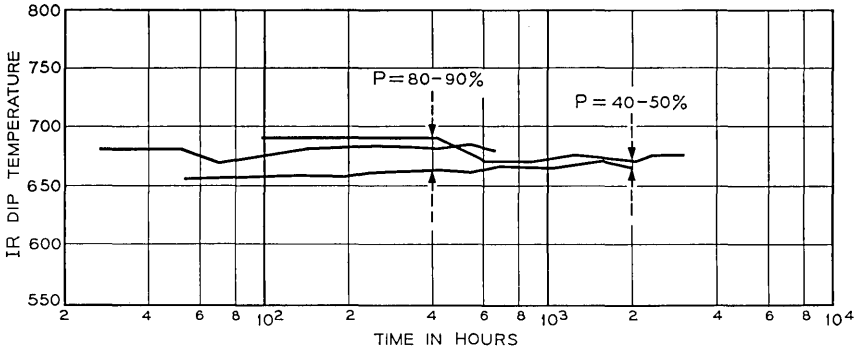


Fig. 6 — Reproducibility of the coating batches.

3.2.2 *Reproducibility of Coating Batches*

Fig. 6 shows the results of three groups each containing six diodes processed by standard technique, sprayed from three independent coating batches which were prepared in an "identical" manner. There is approximately 35°C spread in temperature initially, but by 1000 hours this spread is completely insignificant. This indicates that while there are some differences, perhaps in the small details of the processing cycle, or in the trace amounts of impurities within the system, these are lost after approximately 1000 hours.

3.2.3 *Percent Nickel in the Coating*

Fig. 7 shows the average dip temperatures for two groups of six diodes each made from the same coating batch which had been divided into two parts to permit different exposure times to nickel carbonyl. Batch 15b has 7.26 percent by weight of nickel,* and batch 15a 2.58 percent. As nickel content is reduced, we approach the oxide cathode which represents the lowest attainable work function in the system, useful as such when the required current density causes no appreciable donor depletion. Note that these measurements were carried out at a life condition of $0.3 A/cm^2$, where the detrimental effect of excessive nickel coating is accentuated. At higher current densities where donor depletion in the uncoated oxide is more significant, the beneficial effect of nickel coating tends to dominate even if nickel is applied in thicknesses substantially greater than the optimum.

* This cannot be considered a representative batch since it was deliberately created with an excessive nickel content to produce a pronounced effect.

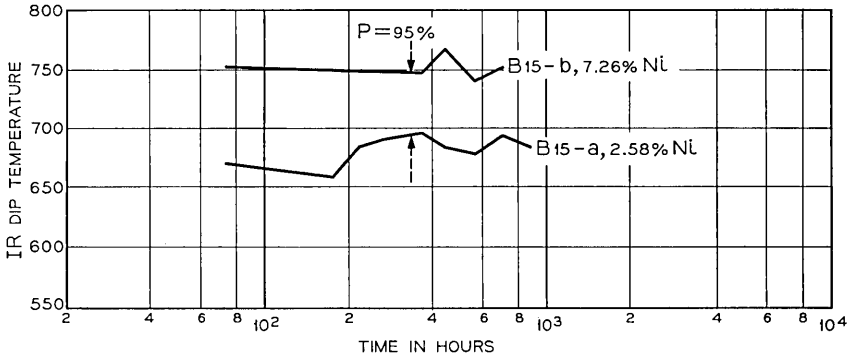


Fig. 7 — The effect of the percent nickel in the coating batch.

### 3.2.4 *The Effect of Cathode Coating Thickness*

This effect is shown in Fig. 8 in which we have plotted the data from cathodes coated with batch 15b which was discussed above. One group is sprayed 2-mils thick, the other 0.65-mils thick. The thicker spray coating yields a higher activity level. These effects may be explained as follows. The thin coating would be of the order of five particle diameters thick. The likelihood of a barium atom produced at the coating-base interface simply evaporating from a pore-end is relatively high. However, in the thicker coating there is a larger cross section for adsorption of the barium atom into the oxide lattice. Hence, the donor concentration in the surface of the thicker coating is likely to be higher than the concentration in the thinner

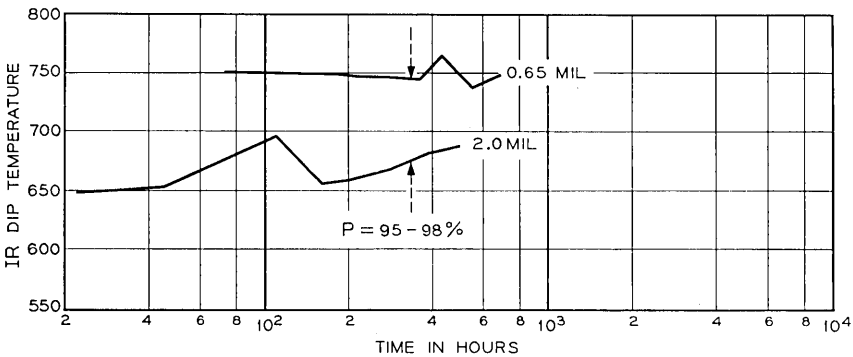


Fig. 8— The effect of the sprayed coating thickness.

coating, and the activity level higher in the former. One would expect this effect to be less pronounced with coatings which have a lower percentage nickel since there would be a higher probability of barium adsorption in the latter case.

### 3.2.5 *Coatings Applied by Electrophoresis*

A technique for applying the nickel-coated carbonate to cathode bases by electrophoresis was developed by M. Hanes[8] using a nickel nitrate activator. Diodes were made from six cathodes coated by this technique. These were processed by the standard technique and the results are shown in Fig. 9. These results are essentially the same as those obtained by other coating techniques and demonstrate that the nickel nitrate used as an activator in the electrophoresis process does not have an appreciable deleterious effect on the emission. This approach could prove useful in cases in which spray coating proved difficult, such as on very large radiused cathodes or filaments.

### 3.2.6 *Dependence on the Base Alloy*

Fig. 10 shows the results of two batches of six diodes based on two different cathode alloys. One group is on the alloy, used throughout the program, 0.1 percent zirconium/nickel the other is on a commercial alloy called "RM No. 8" which is essentially a magnesium/nickel alloy. The latter alloy is quite active. As expected, the "RM No. 8" activity is higher than the zirconium/nickel activity early in life since the former produces large initial amounts of reducing agent. Eventually, after approximately 1000 hours, the tubes are completely activated and give essentially the same result. Choice of base alloy

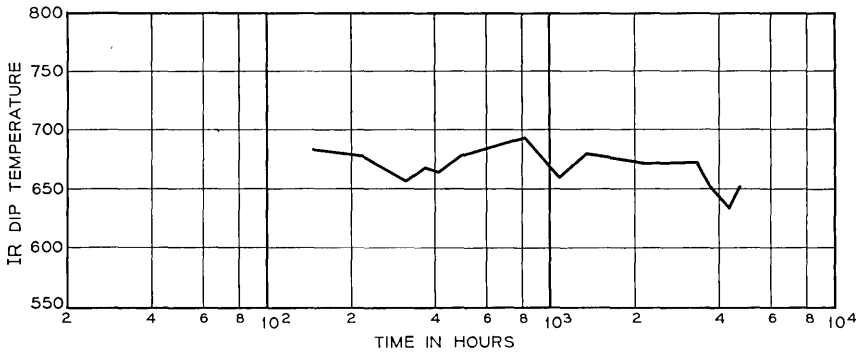


Fig. 9 — Cathode coatings applied by electrophoresis.

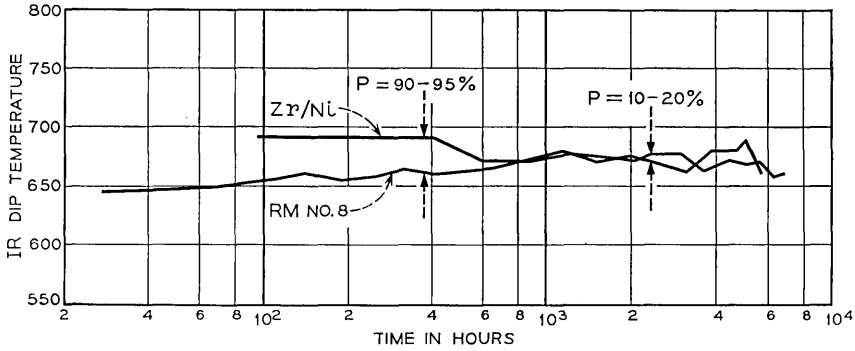


Fig. 10 — The effect of the base alloy.

would, therefore, normally be made on the basis of desired life, since high initial activity is reflected in shortened lifetimes.

### 3.2.7 *The Effect of Processing*

Fig. 11 shows the results of three groups of six diodes each, processed by different techniques. One set is processed by the standard technique already described. Another group marked "matrix," was processed according to a schedule originally developed for a nickel matrix cathode which features activation at 1050°B for 20 minutes. The detailed schedule is given in Appendix B. The third group marked "standard and bake" used the standard processing up to the point at which dc voltage had been applied. The dc voltage was turned off after about one hour and the cathode temperature reduced to approximately

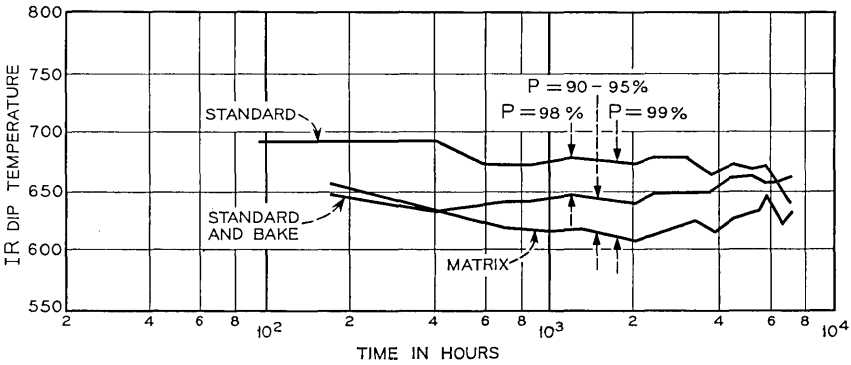


Fig. 11 — The effect of processing.

750°B. The tubes were then replaced in the oven and baked at 425°C for an additional 16 hours. The filaments were then turned off, the getters flashed, and the tubes pinched off.

The matrix processing results in tubes of much higher activity than either of the other processes; however, the rebake results in tubes of higher activity than the standard processing. In the case of standard plus bake, the substantial improvement in activity is attributed to reduction in "diode effects" such as gas on the anode. A rebake after the standard processing technique drives off a large amount of this gas and results in cathodes of higher activity, though this effect would not be so pronounced in an open structure. Matrix processing also achieves this by heating the anode to much higher temperatures than are encountered during the standard processing technique. Whether the cathodes processed by the matrix technique are inherently better than those processed by the standard technique other than because of diode effects is not clear. It is certainly evident that the matrix technique has no great detrimental effect on the cathode activity (as would be the case for an oxide cathode) and this confirms the function of the nickel network in inhibiting sintering. This property is of considerable practical importance. The fact that high temperatures are not detrimental means that temperature control during processing is no longer critical. More importantly, high temperature processing means more rapid outgassing of the cathode and its environment and more rapid activation. Together, these advantages can lead to greatly reduced processing and aging time.

### 3.2.8 *Anode Power and Current Density*

Fig. 12 shows the results of three groups of six diodes each at different anode powers and current densities. All diodes were processed by standard technique and placed on life at 800°B. One group was set at 0.3 amp/cm$^2$ with 0.9 watts anode dissipation. A second group was at 0.3 amp/cm$^2$ and 1.8 watts anode dissipation. A third group was set at 0.6 amp/cm$^2$ and three watts anode dissipation. These anode powers and current densities were achieved by varying the voltage and the cathode-anode spacing. In the two groups operating at 0.3 amp/cm$^2$, the higher the anode power, the lower the activity. This is due to outgassing of the anode and represents a "diode effect," as mentioned in the previous section. The third group, operating at twice the current density and at higher anode power has the highest activity level of all. This indicates that high current density per se is bene-

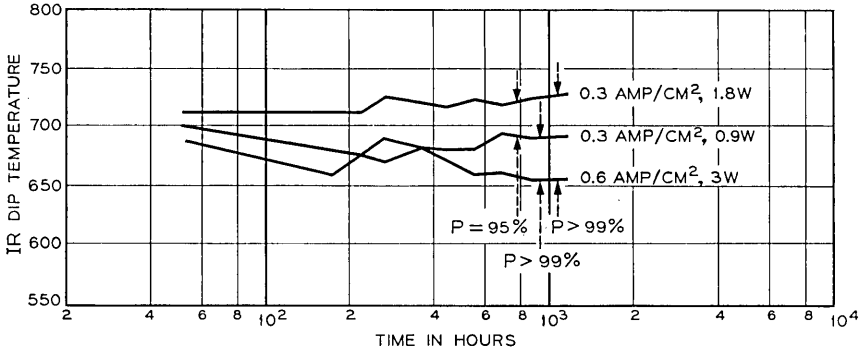


Fig. 12 — The effect of anode power and current density.

ficial to CPC activity and in this case was apparently sufficient to overcome even the effects of a higher power level on the anode. This activity enhancement by higher current density is probably a result of electrolytic activation. This effect will be discussed further in Section 4.3.

### 3.2.9 *The Effect of Breaking the Coated Carbonates*

As discussed above, we postulate that a large proportion of the barium atoms in the top layer of the cathode coating arrive there by a process of diffusion through the pores of the intervening coating. Upon arrival, they must contact an oxide particle to be useful as donor precursors. A continuous nickel film surrounding these particles would obstruct entry of the barium atoms into the oxide lattice and make the effective donor production rate low. It is reasonable to suppose that during the breakdown, ($BaCO_3 \rightarrow BaO + CO_2$) numerous fractures occur in the nickel film originally placed on the carbonate particles. These would be sites through which donor precursors could enter the surface particles.

If the coated particles are fractured by milling, the area of exposed oxide would be substantially larger and the number of Ba atoms absorbed might be expected to be higher. At low current densities, where donor depletion effects are insignificant, one would prefer the extreme configuration—the classic oxide cathode. At intermediate current densities, an optimum degree of fracture should be observed. We have shown this at 0.3 amp/cm² by ball milling the coated carbonate particles for 20 to 40 hours to fracture them and increase the exposed carbonate area. The results of these experiments are shown in

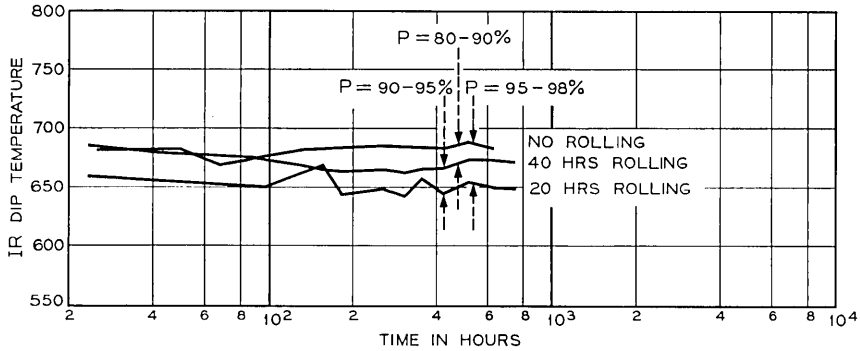


Fig. 13 — The effect of breaking the coated carbonates.

Fig. 13. The 20-hour rolling yields the highest activity level; the 40-hour rolling has caused some degradation. These rolled particles would not be expected to have as good high current density properties since the nickel network will be less complete.

### 3.2.10 *The Effect of Using Double or Triple Carbonates*

Fig. 14 shows the curves for two groups of six diodes prepared from nickel-coated double and nickel-coated triple carbonates, respectively, and processed by the standard technique. Both have the same amount of nickel in the coating. Obviously, the triple carbonates give much higher activity levels. Since one would expect the advantages due to the presence of nickel films to be common to any active oxide configuration, further experiments have been initiated.

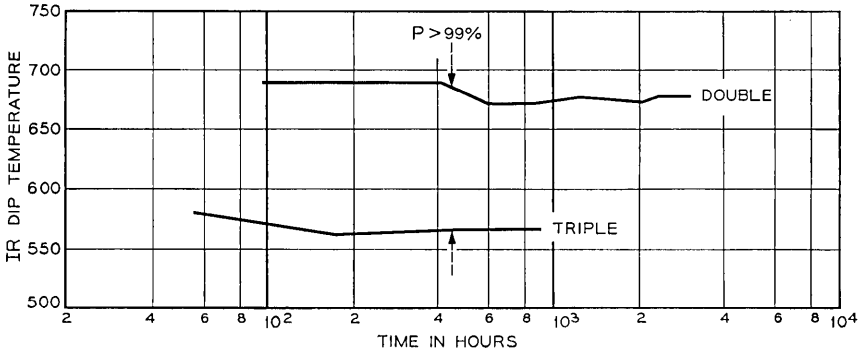


Fig. 14 — Comparison between double and triple carbonates.

3.2.11 *High Current Density Behavior*

The test diode used showed significant "diode effects" at current densities above approximately 0.5 amps/cm$^2$, and these were pronounced around 1 amp/cm$^2$. These effects are difficult to analyze and assign, and in proving the ability of the cathode to withstand current drain up to 1 amp/cm$^2$ it was necessary to rely on the IR dip characterization previously described.[7] The validity of this approach can be illustrated by the following example. When cathodes were operated at 810°C and 0.6 amps/cm$^2$ in the diode, classic $I^{2/3}$ vs $V$ activity plots entered the "knee" into temperature limited emission below the operating voltage. However, IR dip temperatures remained constant with time, and <700°C, implying that space-charge limited operation at 0.6 amps/cm$^2$ should be attained near 700°C in a "clean" structure. When the cathode was used in a traveling-wave tube operating at 0.6 amps/cm$^2$, the absence of anode effects allowed space-charge limited operation at temperatures as low as 700°C, and life is currently beyond 7000 hrs. with no sign of deterioration.

Fig. 15 illustrates the variation in IR dip temperature with time for a group of six diodes operated at 810°C, all at identical anode voltages, but with diode effects causing variations in available current between 0.7 and 1.0 amps/cm$^2$. Stability out to 25,000 hrs. is demonstrated, with a 100°C margin between the operating temperature and the maximum IR dip temperature observed.

## IV. LIFE EXPECTANCY

This section describes evidence that the mechanism of operation and the life limiting factors of the CPC are similar to those of an oxide

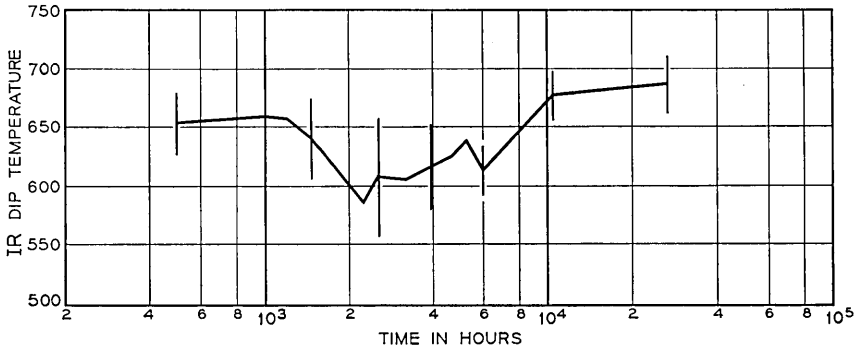


Fig. 15 — The effect of current densities up to 1 amp/cm$^2$.

cathode operated in a low current density regime where donor depletion effects are insignificant. Coating depletion and reducing agent arrival rate are demonstrated to be life determining processes. The theoretical basis for life prediction and its experimental verification are also included.

### 4.1 *Activation Mechanism*

In the studies described here, the zirconium/nickel base alloy was given an extensive wet hydrogen firing to reduce the initial zirconium arrival rate at the coating base interface and to reduce the total carbon content and hence its coating depletion effects (cf. Section 4.2). It is presumed that the cathode activation, defined as the increase in donors in the coating to a maximum level of cathode activity, involves an equilibrium between (*i*) the production of donors by zirconium at a relatively low and constant rate over the activation time, (*ii*) the production of donors by carbon at a relatively high initial rate which then falls off exponentially over a few hundred hours, and (*iii*) the loss of donors or reducing agent by oxidation in the initially poor environment which will improve with the arrival of reducing agents and the consequent irreversible consumption of oxidizing agents.

To demonstrate this and to show that zirconium is the ultimate activator during the life of the cathode, two cathodes were processed, one on 0.1 percent zirconium nickel and the other on a "pure" nickel similar in all impurity levels other than the omission of zirconium. These were set to operate at 850°B to accentuate the effect. Both alloys had 0.002 percent carbon. The results are shown in Fig. 16. The "pure" nickel alloy was quite active initially but declined very rapidly.

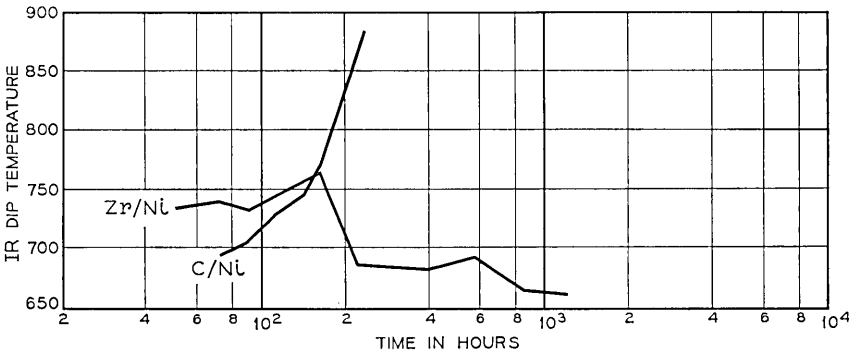


Fig. 16 — The activation profile on zirconium nickel and "pure" nickel.

It reached end-of-life at about the same point as the maximum in the zirconium nickel curve. It is reasonable to assume that the particular balance of the three factors mentioned above made carbon the dominant activator initially; as this was exhausted the cathode began to show signs of deactivation in both cases. During this period, oxidizing agents were scavenged to a sufficient degree to allow the relatively low zirconium arrival rate to build up the donor concentration beyond 200 hours—eventually completing the activation.

It should be emphasized that much faster activation can readily be obtained by such techniques as reducing or omitting the wet hydrogen prefiring of the cathode base. However, for maximum life in a system limited by eventual coating depletion, excessive initial donor production is undesirable. In such a case, the minimum donor production rate consistent with the tube meeting operating specifications as it leaves the processing station would normally be preferred.

### 4.2 *Coating Depletion*

If the arrival rate of reducing agent at the base remains above the emission cut off rate[9] for the operating current density for a sufficient time, the life of the cathode will be limited by coating depletion. Coating depletion is the result of several effects, some of which we can only estimate:

(*i*) Reaction of the coating with the reducing agent in the base. This can be calculated from the well-known diffusion equations. Included here must be the effect of prefiring on the zirconium and carbon profiles and the depletion during the activation cycle.

(*ii*) Evaporation of the coating at the operating temperature. BaO is the only major active component of the coating which evaporates at an appreciable rate. Since coprecipitated carbonates were used, the oxides form mixed crystals, and the vapor pressure of the BaO will be reduced. As an approximation we have assumed that the vapor pressure of BaO will be proportional to the mole fraction of BaO in the mixed crystal. Furthermore, to be conservative, we have not assumed that the vapor pressure decreases because of the decreasing net mole fraction of BaO as it evaporates. This is partially valid because many individual crystallites are involved (i.e., a large surface area) but the vapor pressure must decrease to some extent later in life. Therefore, the results of these calculations must be considered somewhat pessimistic as life considerations. Fig. 17 shows the results of a coating depletion calculation for cathodes given standard processing

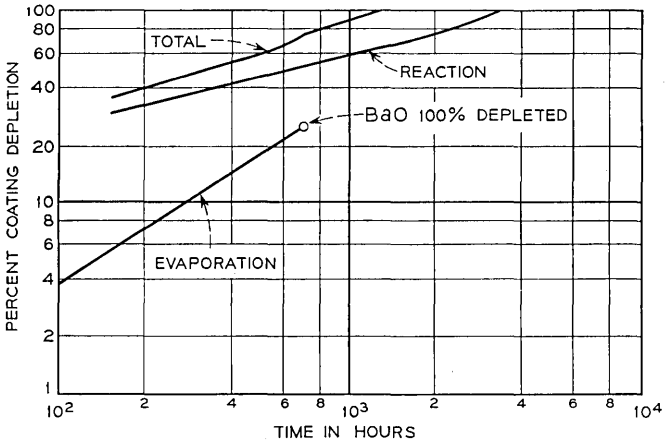


Fig. 17 — Calculation of coating depletion at 850°B on alloy CA703. Coating: 1.0g/cc, 0.6 mil thick.

and accelerated through life at 850°B. They were sprayed 1.0 g/cc, 0.6-mil thick on cathodes based on an alloy which had 0.1 percent Zr and 0.002 percent carbon. The curve marked "reaction" is the percent depletion due to carbon and zirconium. The curve marked "evaporation" is the corresponding percent depletion by evaporation. The latter curve has a point marked "100 percent BaO depletion." This assumes that the "reaction" proceeds at an equal rate for BaO and SrO and the "100 percent BaO depletion" point is reached when the sum of ½ the "reaction" curve plus the evaporation curve equals the total amount of BaO. From this point on, the cathode is assumed to be pure SrO. Fig. 18 shows the IR dip temperatures for these six diodes. It can be seen that the agreement between theory and experiment is good.

Fig. 19 shows similar results on a set of diodes lifed at 800°B. The uncertainty shown results from assuming the thickness to be 0.6 ± 0.1 mils. This gives some indication of the expected errors. As mentioned above, the calculation is somewhat pessimistic; therefore, the fact that the diodes run somewhat longer than the calculation predicts is not unexpected.

### 4.3 *Electrolytic Donor Production*

If the surface donor depletion under the influence of current induced emf is inhibited by a nickel network in the coating, the effect

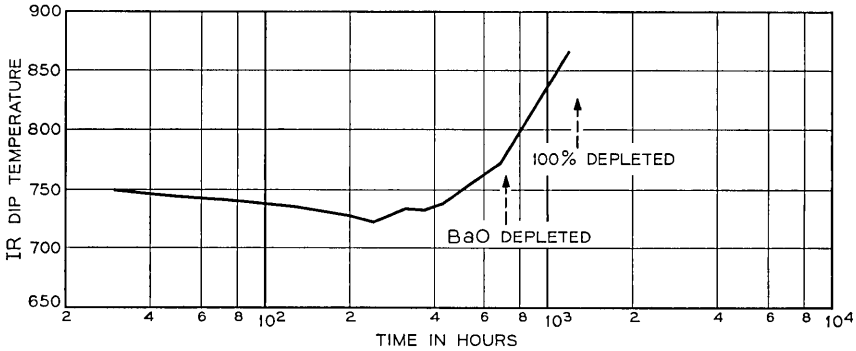


Fig. 18 — Coating depletion—comparison between theory and experiment at 850°B.

of electrolytic activation should be enhanced because donors will be trapped in the surface layers. We have observed the effect of electrolytic activation several ways:

(*i*) By activity measurement on a set of eight diodes using the IR dip technique with 5, 50, and 500 $\mu$sec pulses at 0.5 amp/cm$^2$. The duty cycle was maintained the same for each pulse length by varying the pulse frequency. In this way, the anode power level remained constant. The results are shown in Table III. The enhancement in activity with longer pulses is caused by the increasing concentration of donors induced in the coating by electrolysis.

(*ii*) With the IR dip technique, the work function, $\varphi$, may be deter-

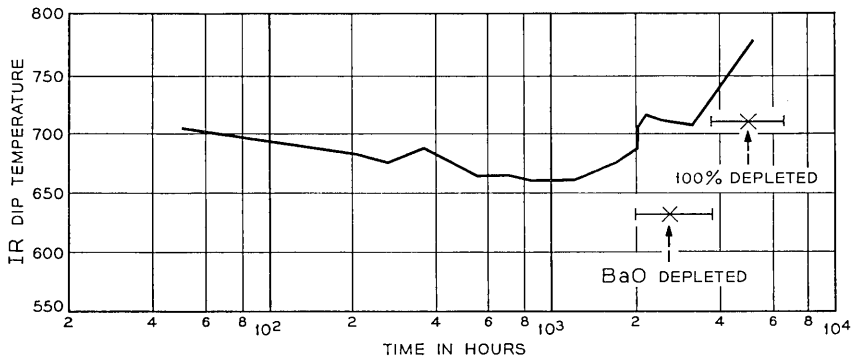


Fig. 19 — Coating depletion—comparison between theory and experiment at 800°B.

TABLE III—AVERAGE ACTIVITY MEASUREMENT ON EIGHT DIODES AS A FUNCTION OF PULSE LENGTH FOR CONSTANT DUTY CYCLE

| | | | |
|---|---|---|---|
| Pulse Length ($\mu$sec) | 5 | 50 | 500 |
| IR dip Temperature, °C | 725 | 681 | 672 |

mined as a function of temperature independent of the Richardson constant $A$.[7] When this is done for dc operation and for 500-microsecond pulse operation on a CPC cathode at 0.3 amp/cm$^2$, the result shown in Fig. 20 was obtained. As the temperature increases, the donor concentration decreases because evaporation loss increases faster than the production rate. Since electrolysis augments production more in dc operation than in pulse operation, $\varphi$ remains constant over this temperature range for dc operation whereas it increases for the pulse operation.

(*iii*) By the apparent lowering of the emission cut-off rate as will be discussed in the next section.

### 4.4 *Emission Cut-Off Rate, ECOR*

ECOR is defined as the minimum donor production rate from the reactions of reducing agents in the base which is necessary to sustain emission at a given level. This rate varies with current density because: (*i*) the number of donors required in the cathode surface is a function of current density and temperature, and (*ii*) at current densities above about 0.2 amp/cm$^2$, electrolysis of the coating adds to the donor concentration. Data shown by Kern[9] for the ECOR of

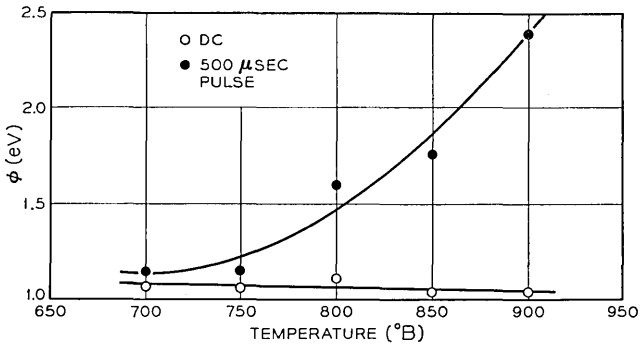


Fig. 20 — $\varphi$(T) for CPC.

oxide cathodes indicates that it varies rapidly with current density. His highest value is $1 \times 10^{-8}$ $\mu$moles/cm$^2$/sec at 200 ma/cm$^2$.

ECOR for the CPC at medium current densities would be expected to be lower than for the oxide cathode because electrolysis will contribute to the net concentration of donors in the surface. Experimental results to date have established an upper limit on ECOR for coated powder cathodes at current densities up to 1 amp/cm$^2$ as $1.5 \times 10^{-8}$ $\mu$moles/cm$^2$/sec confirming the stability of the CPC in this operating range.

### 4.5 *Typical Life Calculation*

In Fig. 21 we have plotted, for a typical cathode configuration, the barium production rate at 800°C as a result of zirconium diffusion in micromoles/cm$^2$/sec vs time in hours for a cathode alloy of 0.07 $\pm$ 0.01 percent zirconium, and for two different thicknesses of base metal. The higher percent zirconium results in a higher barium production rate. Thicker base metals yield the same barium production rates except that the "knee" occurs further out in time. For the 0.1-inch thick base the knee does not occur in the time interval shown. Since the ECOR is less than $1.5 \times 10^{-8}$ $\mu$moles/cm$^2$/sec a lower limit on the lifetime set by this mechanism is of the order 100,000 hours for the 0.06-inch thickness, and will increase with base thickness.

Coating depletion calculations have already been discussed. Fig. 22 shows the results of such a calculation on a typical cathode. The cathode considered is based on a 100 mil thick 0.08 percent zirconium,

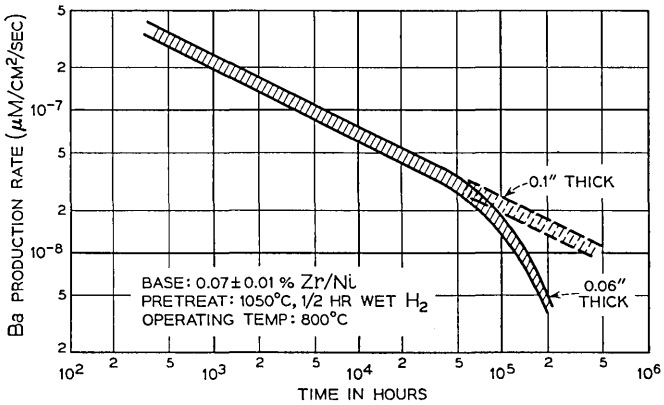


Fig. 21 — Ba production rate.

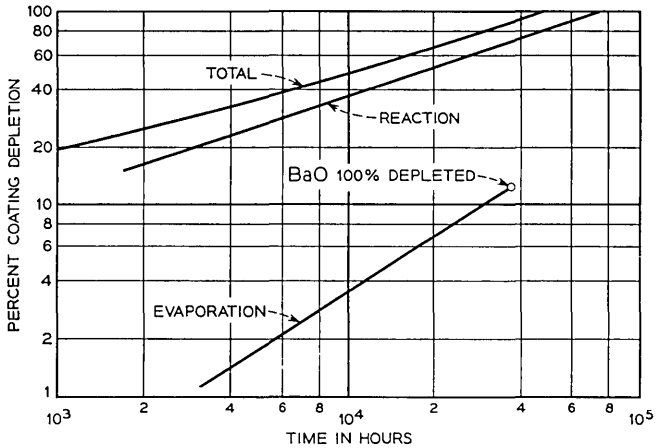


Fig. 22 — Calculation of coating depletion at 800°C on 0.08% Zr, 0.001% C/Ni 0.1 inch thick, coating: 1.1g/cc, 1.5 mil thick.

0.001 percent C alloy, sprayed with coated double carbonate at 1.1 g/cc, 1.5 mil thick. The base alloy has been pretreated in wet $H_2$ at 1050°C for ½ hour. The cathode is activated by the schedule; 800°B, 1 hour; 950°B, 6 minutes; 850°B, 17 hours, and operated at 800°C. Following the analysis described in Section 4.2, BaO is 100 percent depleted after 40,000 hours. It should be emphasized that while operation at 800°C is reasonable for diodes, tubes such as TWT's with more open structures can normally run at substantially lower temperatures, thus improving life expectancy still further.

### 4.6 *Life Prediction*

The lifetime of a typical CP cathode operating at less than 1 amp/cm$^2$ on a 0.10 inch thick 0.07 ± 0.01 percent zirconium/Ni at 800°C is therefore limited not by ECOR but by coating depletion, and in the typical examples described, BaO would be 100 percent depleted in >40,000 hours. The assumptions made in this prediction are supported by: (*i*) The failure of groups of diodes, on schedule, (Figs. 18 and 19) and (*ii*) 28 diodes currently on life, beyond 25,000 hours.

## V. SUMMARY

Examination of the theory of operation of the oxide cathode suggests that in order to improve the high current density properties of oxide cathodes, the movement of donors under the influence of cur-

rent-induced emf's should be inhibited. To do this a method of coating each individual particle of carbonate powder with a thin nickel film has been successfully developed. Carbonates coated in this manner have been used to prepare cathodes by conventional techniques.

Extensive diode experiments made mainly at 0.3 amps/cm$^2$ have outlined the general character of such cathodes and the major factors affecting their performance. Definitive comparisons of maximum performance with other cathode types were in general not attempted because diode effects were shown to obscure the interpretation of deliberate variations in cathode parameters at high current densities.

It has been shown that the new coating can be prepared reproducibly. The nickel film around each particle inhibits sintering of the oxide, enhances the beneficial effects of electrolytic activation, and allows operation of the cathode at temperatures in the range 700-800°C over lifetimes which are essentially independent of the current density up to 1 amp/cm$^2$. The cathode has been demonstrated to activate quickly and efficiently through high temperature processing schedules. Faster outgassing of the structure is therefore possible, and faster activation can be achieved. Direct substitution of CPC for oxide cathodes in production sequences is practical, since conventional activation schedules may also be used. In this case, the tolerance of the cathode to accidental overheating is helpful.

Activation and life determining mechanisms operative in the CPC have been defined as reducing agent diffusion and coating depletion, with the latter determining end-of-life in most practical configurations. Good agreement was obtained between theory and experiment for coating depletion, and a lower limit on reducing agent arrival rate of $1.5 \times 10^{-8}$ $\mu$moles/cm$^2$/sec has been established for current densities up to 1 amp/cm$^2$. On this basis lifetimes of 40,000 to 50,000 hours are entirely feasible for CPC operating up to 1 amp/cm$^2$.

The coated powder cathode, therefore, appears to combine many of the advantages of the standard oxide cathode with those of the matrix type. The system variables have been thoroughly explored, indicating its utility, particularly in the operating range 0.2 to 1.0 amps/cm$^2$, where diode life tests have presently reached 25,000 hours.

## VI. ACKNOWLEDGMENTS

The authors wish to acknowledge their debt to Mr. H. E. Kern, whose prior work on high-reliability oxide cathodes and high-purity cathode alloys formed a starting-point for this work; Mr. E. E.

Francois who was responsible for the production and physical characterization of the CPC powder; Messrs. A. G. Cannone and R. E. Straile who were responsible for fabrication, processing and life testing of the diodes; and to Mr. Hanes, who developed a technique for electrophoretic coating. The continued guidance and encouragement of Mr. D. E. Koontz is also gratefully acknowledged.

## APPENDIX A

*Standard Cathode Breakdown and Activation Schedule*

(°B Represents Optical Pyrometer Measurement on Cathode Base)

1. Bake out 16 hours at 425°C.
2. Outgas the getter.
3. Outgas the heater by slowly raising the cathode temperature to ca. 500°C keeping the pressure below $5 \times 10^{-5}$ torr on the getter ion pump.
4. Raise the cathode temperature as rapidly as possible to 800°B keeping the pressure $<5 \times 10^{-5}$ torr.
5. Hold until $P \leqq 10^{-7}$ torr.
6. Raise the cathode temperature rapidly to 950°B and hold for five minutes then lower the temperature to 850°B.
7. Apply 25 Vdc and age ca. one hour.
8. Turn off anode voltage and heater voltage and flash getter. Pinch off tube within 30 seconds after getter flash.

## APPENDIX B

*High Temperature Processing Schedule*

(°B Represents Optical Pyrometer Measurement on Cathode Base)

1. Follow the standard schedule (Appendix A) through step 3.
2. Raise the cathode temperature as rapidly as possible to 850°B keeping the pressure $<5 \times 10^{-5}$ torr on the getter ion pump.
3. Hold until $P \leqq 10^{-7}$ torr.
4. Rise the cathode temperature rapidly to 1050°B and hold for 20 minutes.
5. Apply dc voltage to the anode to draw 1 amp/cm$^2$ (40 mA).
6. When the activity reaches 1 amp/cm$^2$ (usually immediately) lower the cathode temperature in 50° steps holding at each step until 1 amp/cm$^2$ is attained. Continue until 850°B is reached.

7. Turn off anode and heater voltage and flash getters. Pinch off the tube within 30 seconds after the getter flash.

REFERENCES

1. Eisenstein, A., A Study of Oxide Cathodes by X-Ray Diffraction Methods, J. Appl. Phys., *17,* 1946, pp. 434–443.
2. Frost, H. B., Transient Changes in the Oxide Cathode, Thesis, M.I.T., 1954.
3. Goldberger, W. M. and Nack, H., Novel Uses of Fluidized Beds in Chemical Processing, Battelle Technical Rev, *13,* No. 11, 1964, pp. 3–9.
4. MacNair, D., A Method for Eliminating Binder Contamination from Oxide Coated Cathodes, Advances in Electron Tube Technology, *2,* 1962, pp. 173–178.
5. See Feder, D. O. and Koontz, D. E., Detection, Removal and Control of Organic Contaminants in the Production of Electron Devices, ASTM Symposium on Electron Device Components and Materials, STP 246, 1958, pp. 40–63.
6. Bodmer, M. G., et al, Satellite Traveling-Wave Tube, B.S.T.J., *42,* July 1963, pp. 1703–1748.
7. Maurer, D. W, Cathode Activity Measurement: A Modification of the Dip Test, B.S.T.J., this issue, pp. 2363–2374.
8. Hanes, M., private communication.
9. Kern, H. E, Emission and Life of Practical Oxide Cathodes as Limited by Diffusion and Chemical Reaction Phenomena, Rep. 23rd Annual Conf. Phys. Elec., 1963, pp. 106–113.

# Contraction Maps and Equivalent Linearization*

By J. M. HOLTZMAN

(Manuscript received July 26, 1967)

*This study is primarily concerned with the question: If the method of equivalent linearization indicates the existence of a periodic solution, is there actually a periodic solution near the approximation of equivalent linearization? To answer this question, we use a modification of the contraction mapping fixed point theorem. We discuss applications to differential equations and difference-differential equations (with forcing functions). Also, we show that our use of contraction maps is not applicable (without modification) to autonomous systems because the mapping evaluated in the neighborhood of a periodic solution to an autonomous system is not a contraction in a space of periodic functions.*

## I. INTRODUCTION

The method of equivalent linearization is a most valuable technique to investigate nonlinear phenomena, particularly nonlinear oscillations. It has its roots in the method of Krylov and Bogoliubov and is related to (or equivalent to, depending on the specific definitions) the method of harmonic balance, Galerkin's method, and the describing function method used by control engineers. The purpose of the present study is to develop a new technique for investigating the method of equivalent linearization.

We shall be primarily concerned with the following question: If the method of equivalent linearization indicates the existence of a periodic solution $x_0$, is there actually a periodic solution near $x_0$? To answer this question we first introduce a convenient modification of the contraction mapping fixed point theorem which is actually more general than just applicable to the question posed above.† We apply

* Taken from a dissertation submitted to the Faculty of the Polytechnic Institute of Brooklyn in partial fulfillment of the requirements for the degree of Doctor of Philosophy (System Science), 1967.

† Appendix A contains some reading suggestions for engineers interested in this work but who are not familiar with the mathematics used.

our approach to systems described by nonautonomous differential equations. Then we show that there is no essential difficulty in also handling difference-differential equations.

We shall try to clearly indicate what our method can and cannot do. The discussion of autonomous systems is particularly important in this regard. The relation of the present study to previous work is discussed in Section VIII.

## II. THE METHOD OF EQUIVALENT LINEARIZATION*

Consider the following vector differential equation

$$\dot{x}(t) = f(x(t), t) = A(t)x(t) + n(t, x(t)), \tag{1}$$

where

$$f(x, t) = f(x, t + T) \tag{2}$$

for all $(x, t)$ of interest. This, of course, includes the case of $f(x, t)$ independent of $t$, i.e.,

$$f(x, t) = f(x). \tag{3}$$

We shall be concerned with the situation that permits an equivalent representation of (1):

$$x = LN(x), \tag{4}$$

where $x$ now represents a vector function, $L$ is a linear operator, and $N$ is a nonlinear operator (these terms will be made more precise later). If it is assumed that $LN(x)$ has the following Fourier series,

$$LN(x)(t) \sim \frac{a_0}{2} + \sum_{k=1}^{\infty} \left( a_k \cos k \frac{2\pi}{T} t + b_k \sin k \frac{2\pi}{T} t \right). \tag{5}$$

Then we define $\tilde{L}N(x)$ as follows:

$$\tilde{L}N(x)(t) = a_1 \cos \frac{2\pi}{T} t + b_1 \sin \frac{2\pi}{T} t. \tag{6}$$

That is, $\tilde{L}$ extracts the fundamental component of the Fourier series.

The method of equivalent linearization seeks a solution of the equation

$$x = \tilde{L}N(x). \tag{7}$$

This study will be primarily concerned with the following problem:

* See Minorsky,[1] p. 350, for a discussion of the relationship of the method of equivalent linearization to the method of Krylov and Bogoliubov.

Given an $x_0$ satisfying (7), is there an $x^*$ satisfying (4) and if there is, how are $x_0$, and $x^*$ related?

Note that (4) is a functional relation more general than (1) and our method will be correspondingly applicable to a more general problem.

The above discussion is now related to the method of describing functions* as commonly used by control engineers. They are concerned with the feedback loop shown in Fig. 1. The linear operator $L$

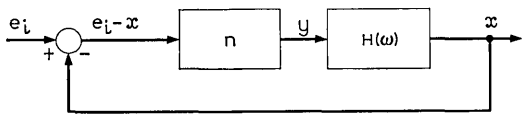


Fig. 1 — Feedback Loop.

is represented in this case by a transfer function $H(\omega)$ (see Kaplan[4] for a definition and discussion of transfer functions) and the nonlinear operator $N$ is represented by a nonlinear function,

$$y = n(e_i - x),$$

where $e_i$ is an input function. The engineer replaces the nonlinear function $n$ by its describing function which is defined loosely as the complex ratio of the fundamental component of the output to a sinusoidal input. That is, if†

$$n(A \sin \omega t) = \sum_{k=1}^{\infty} a_k \sin k\omega t + b_k \cos k\omega t \left(\omega = \frac{2\pi}{T_k}\right)$$

then the describing function of $n$ is

$$\frac{\sqrt{a_1^2 + b_1^2} \Big/ \tan^{-1} \dfrac{b_1}{a_1}}{A}.$$

Note that while the describing function may be dependent on both $A$ and $\omega$, it is still a relatively simple matter to replace $n$ by its describ-

* For further discussion of the use of describing functions by engineers see e.g., Truxal[2] or Graham and McRuer.[3] They give further references and historical background. The describing function method is associated with the names of Tustin, Goldfarb, Oppelt, Kochenberger, Dutilh, and Nichols and Kreezer. Also see Minorsky,[1] Chap. 17 for a discussion of the work of Theodorchik and Blaquière. The work of E. C. Johnson is discussed in Ref. 2.

† The constant term is assumed zero.

ing function, then to consider it as a "linear" (or quasi-linear) operator and then use standard techniques for linear systems. Of course, such a procedure should be mathematically justified and, in fact, that is the purpose of this study.

Before we embark on our investigation, it is well to review the arguments used by engineers in their justification of the method. These arguments seem to be plausible and they are suggestive of what may be expected of a more rigorous investigation. If it is assumed that the combination of $n$ and $H(\omega)$ operating on a sinusoidal function is primarily fundamental (i.e., the harmonics are "small" compared to the fundamental) then it would be expected that the describing function method might not be too inaccurate. The harmonics will be small if one or both of the following are satisfied:

(*i*) the nonlinearity $n$ is "not too nonlinear"

(*ii*) the transfer function $H(\omega)$ is low-pass, i.e., it attenuates harmonics much more than the fundamental. (It is assumed that no subharmonics arise).

We shall use Duffing's equation,

$$\ddot{y} + ay + by^3 = f \cos \omega t,$$

as a running example to illustrate the methods discussed. We show here how this differential equation corresponds to a feedback control problem and then make no further explicit reference to feedback systems. The appropriate feedback system is shown in Fig. 2.

The next section contains an approach to a problem much more general than the problem of equivalent linearization posed in this section. The remainder of the study will be primarily devoted to adapting the more general approach to the specific problem of equivalent linearization.

It may be noted that we are not getting more abstract in the next section just for the sake of abstraction. It should be clear to the reader

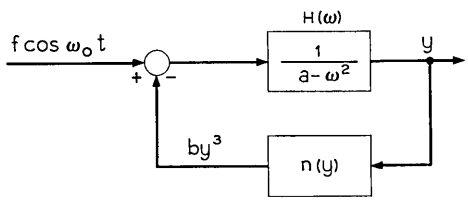


Fig. 2 — Feedback equivalent of Duffing's equation.

that the method of equivalent linearization leads to an integro-differential equation rather than an ordinary differential equation because Fourier coefficients are determined by integration (this is also pointed out in Bass[5], p. 898). We then cannot expect the theory of ordinary differential equations to answer our questions and we are led quite naturally to considering more general equations. In particular, the theory of operator equations in a Banach space is shown to provide the tools appropriate to the task. As an added bonus for the abstraction, we develop an approach which is applicable to problems unrelated to equivalent linearization.

## III. THE USE OF THE CONTRACTION MAPPING FIXED POINT THEOREM WITH DERIVATIVES IN A BANACH SPACE

Let $X$ be a complete metric space (with metric $d$) containing the the closed set $\Omega$ and let $P$ map $\Omega$ into itself. $P$ is a contraction mapping if

$$d(P(x), P(x')) \leqq \alpha d(x, x') \qquad (x, x' \varepsilon \Omega) \tag{8}$$

with $\alpha < 1$. The contraction mapping theorem† states that if $P$ is a contraction mapping then there is a unique $x^* \varepsilon \Omega$ such that $x^* = P(x^*)$, i.e., $x^*$ is a fixed point of the operation $P$. $x^*$ is the limit of a sequence $\{x_n\}$ where

$$x_{n+1} = P(x_n) \tag{9}$$

and $x_0$ is any element of $\Omega$. Furthermore,

$$d(x_n, x_0) \leqq \frac{d(x_1, x_0)}{1 - \alpha} = \frac{d(P(x_0), x_0)}{1 - \alpha} \qquad n = 1, 2, \cdots . \tag{10}$$

In order to use the contraction mapping fixed point theorem it has to be shown that some neighborhood of $x_0$ is mapped into itself and that in this neighborhood the operation is contracting. Our approach will be simultaneously to determine a set containing $x_0$ which is mapped into itself along with the contraction constant $\alpha$ for the operation on that set. This is possible because of relationship (10). The use of operator derivatives will be seen to be convenient. The method will result in a relation in $\alpha$ for which it is desired to find solutions with $\alpha \varepsilon [0, 1)$.

The following is proven in Kantorovich and Akilov[6] (p. 661).

---

† See Kantorovich and Akilov,[6] p. 627.

If $X$ is a Banach space and $P$ maps a convex closed subset $\Omega$ of $X$ into itself and if $P$ has a derivative* at every point of $\Omega$, then

$$\sup_{x \varepsilon \Omega} || P'(x) || = \alpha < 1 \tag{11}$$

implies that $P$ is a contraction on $\Omega$ (and thus, there is a unique fixed point of $P$ in $\Omega$).

The object then is to find a neighborhood of $x_0$ mapped into itself and in which the norm of the derivative is less than one. The following simple theorem is a help in this direction.

*Theorem: Let $B$ be a Banach space. $F$ maps $B$ into itself and $x_0 \varepsilon B$. It is assumed that*

(*i*) *$F$ has a derivative at all $x \varepsilon B$*

(*ii*) *There is a nondecreasing function $g$ such that if $x \varepsilon B$, then*

$$|| F'(x) || \leqq g(|| x - x_0 ||)$$

(*iii*) *There is an $\alpha \varepsilon [0, 1)$ such that*

$$g\left(\frac{k}{1 - \alpha}\right) \leqq \alpha,$$

*where*

$$k \geqq || F(x_0) - x_0 ||$$

*Then there is a unique $x^* \varepsilon \Omega$ such that*

$$x^* = F(x^*),$$

*where*

$$\Omega = \left\{x : x \varepsilon B, || x - x_0 || \leqq \frac{k}{1 - \alpha}\right\}$$

*Proof:* We will show that $|| F'(x) || \leqq \alpha$ for all $x \varepsilon \Omega$ and that $F$ maps $\Omega$ into itself and thus, there is a unique fixed point in $\Omega$. If $x \varepsilon \Omega$, we have from (*ii*)

$$\begin{aligned} || F'(x) || &\leqq g(|| x - x_0 ||) \\ &\leqq g\left(\frac{k}{1 - \alpha}\right) \\ &\leqq \alpha. \end{aligned}$$

* See Kantorovich and Akilov,[6] chap. XVII, for a general discussion of differentiation in Banach spaces. For convenience, Appendix B of this study repeats the definitions.

$F$ maps $\Omega$ into itself because if $x \in \Omega$, then

$$\begin{aligned} \| F(x) - x_0 \| &\leqq \| F(x) - F(x_0) \| + \| F(x_0) - x_0 \| \\ &\leqq \alpha \| x - x_0 \| + k \\ &\leqq \alpha \frac{k}{1-\alpha} + k \\ &= \frac{k}{1-\alpha}. \end{aligned}$$

We further discuss the use of the contraction mapping theorem in Ref. 7. This modification of the contraction map theorem is less general than some other modifications but is simpler to apply when applicable.

## IV. THE CHOICE OF BANACH SPACE

In order to use the result of the previous section, an appropriate Banach space must be chosen. For most of our investigation it will be found convenient to use the space of continuous periodic functions. Another space worth considering is the space of periodic functions square-integrable over a period. Before discussing the desirable characteristics of this space, a restrictive factor will be mentioned. The nonlinear operator of interest $y = N(x)$ is often defined by the ordinary function (satisfying the Carathéodory condition)

$$y(t) = n(t, x(t)). \tag{12}$$

A necessary condition that this operation map $L_2(0, T)$ into $L_2(0, T)$ is (see Krasnosel'skii,[8] p. 27) that for some $b > 0$ and some $a(t) \in L_2(0, T)$

$$| n(t, u) | \leqq a(t) + b | u | \qquad t \in [0, T]. \tag{13}$$

It is thus seen that the allowable nonlinearities are quite restricted. This is, in fact, the reason the present investigation will be carried out in a space of continuous functions where the requirement that a function map a continuous function into a continuous function is much more convenient. It should be noted, however, that in some cases one may focus attention on some subset of the Banach space and less restrictive requirements on the nonlinearities might be imposed. Also, for many control engineering problems the nonlinearities are Lipschitzian and the problems can be attacked in $L_2$.

The attractive feature of $L_2$ is that Fourier series results can be fully utilized (in particular, Parseval's relation). More generally, $L_2$

is a separable* Hilbert space with many useful properties and the trigonometric functions are a complete orthogonal system in $L_2$. The norms can often be conveniently evaluated in terms of quantities associated with the "transfer function" or "frequency response". For example, $L$ may be defined by the set of complex numbers $\{\ldots, L_2, L_{-1}, L_0, L_1, L_2, \ldots\}$ (i.e., the transfer function evaluated at the fundamental and harmonic frequencies).† A simple sufficient condition for $L$ to map $L_2$ into itself is that

$$\sup_n |L_n| < \infty.$$

The evaluation of $\| LN(x_0) - x_0 \|$ may be done as follows:

$$\begin{aligned} \| LN(x_0) - x_0 \| &= \| LN(x_0) - \tilde{L}N(x_0) \| \\ &\leqq \| L - \tilde{L} \| \cdot \| N(x_0) \| \\ \| L \| &= \sup_n |L_n|. \end{aligned}$$

The last relationship is proven in Appendix B of Sandberg.[10]

Despite the above mentioned attractive features of $L_2$, we chose to work in the space of continuous functions primarily because of the first-mentioned restriction placed on the nonlinearities in $L_2$. Also, the sup norm (uniform norm) in the space of continuous functions seems more appropriate in error analysis (the error between an approximation and an exact solution) than does the $L_2$ norm. The sup norm provides a bound on the magnitude of the error while the $L_2$ norm gives the integral of the square of the error.

Section V will give the details of working in the space of continuous periodic functions. First (in Section 5.1) an integral equation equivalent to the differential equation of interest will be derived. Then in Section 5.2, the derivatives will be determined and finally in Section 5.3, the quantity $\| F(x_0) - x_0 \|$ will be evaluated. Application of the results will then be seen to be rather straightforward.

## V. APPLICATION TO DIFFERENTIAL EQUATIONS

### 5.1 *The Equivalent Integral Equation*

Halanay[11] shows how to convert the quasi-linear differential equation

* It is, of course, assumed that the measure is Lebesgue. Then $L_2$ is separable; see Kolmogorov and Fomin,[9] Vol. II, p. 88.

† No confusion should arise because of the double use here of the symbol $L_2$.

$$\frac{dx(t)}{dt} = A(t)x(t) + n(t, x(t)) \tag{14}$$

into an integral equation which is convenient for examination of periodic solutions. First, consider

$$\frac{dx(t)}{dt} = A(t)x(t) + f(t), \tag{15}$$

where $A(t)$ and $f(t)$ are both continuous and periodic of period $T$. The following theorem is proven in Halanay,[11] p. 223.

*Theorem: A necessary and sufficient condition in order that, for any periodic function $f(t)$ of period $T$, system (15) admits periodic solutions of period $T$ is that the corresponding homogeneous system*

$$\frac{dy(t)}{dt} = A(t)y(t) \tag{16}$$

*does not admit a non-trivial periodic solution of period $T$.*

It is to be noted that if $Y(t)$ is the principal fundamental solution matrix for (16) then the existence of the inverse of $[I - Y(T)]$* is equivalent to the non-existence of a non-trivial periodic solution (of period $T$) to (16). Then the following proposition is proved in Halanay,[11] p. 225.

*Proposition:* If $[I - Y(T)]^{-1}$ exists, the unique periodic solution of the system (15) can be put in the form

$$x(t) = \int_0^T G(t, s)f(s)\, ds, \tag{17}$$

where

$$G(t, s) = \begin{cases} Y(t)[I - Y(T)]^{-1}Y^{-1}(s), & 0 \leqq s \leqq t \leqq T \\ Y(t + T)[I - Y(T)]^{-1}Y^{-1}(s), & 0 \leqq t < s \leqq T. \end{cases} \tag{18}$$

Since this reformulation into an integral equation is quite important, a sketch of the proof given in Halanay[11] will be given here. Solution of (15) is

$$x(t) = Y(t)x(0) + \int_0^t Y(t)Y^{-1}(s)f(s)\, ds. \tag{19}$$

---

* $I$ is the identity matrix.

For periodicity,

$$x(T) = x(0) = Y(T)x(0) + \int_0^T Y(T)Y^{-1}(s)f(s)\,ds \tag{20}$$

or

$$[I - Y(T)]x(0) = \int_0^T Y(T)Y^{-1}(s)f(s)\,ds. \tag{21}$$

Since $[I - Y(T)]$ is assumed invertible, we can solve for $x(0)$ and get

$$x(t) = Y(t)[I - Y(T)]^{-1} \int_0^T Y(T)Y^{-1}(s)f(s)\,ds + \int_0^t Y(t)Y^{-1}(s)f(s)\,ds. \tag{22}$$

The form of $G(t, s)$ given in the statement of the proposition results from algebraic manipulation of (22).

Now suppose that

$$\frac{dx(t)}{dt} = A(t)x(t) + n(t, x(t)) \tag{23}$$

with $A(t)$ and $n(t, u)$ both being periodic of period $T$ and $[I - Y(T)]$ invertible. It is assumed that $n(t, x(t))$ is continuous if $x(t)$ is continuous. Then, from the previous discussion, if we can find a continuous periodic $x$ of period $T$ satisfying

$$x(t) = \int_0^T G(t, s)n(s, x(s))\,ds, \tag{24*}$$

we have a periodic solution of (23). (It is easily shown that such an $x$ satisfies (23); see Halanay,[11] p. 237).

The problem is thus reduced to finding a continuous solution of a nonlinear integral equation. We need only consider the interval [0, T] because $G(t, s)$ was constructed so that $x(0) = x(T)$.

### 5.2 *Computation of Derivatives*

It is shown here how to evaluate the Fréchet derivative† of the

* The nonlinear integral operation represented by the right hand of (24) is of the form sometimes referred to as a Hammerstein operator which is a special case of Uryson's operator defined by $\int_0^T K(t, s, x(s))\,ds$ (see Krasnosel'skii,[8] pp. 32, 46).

† The Fréchet derivative is actually more than what is required. The Gateaux derivative (which does not require uniform convergence) would suffice for much of what follows. However, since the convergence is indeed uniform in most cases of interest and since the uniformity is easy to demonstrate, we shall derive the Fréchet derivative. Furthermore, Fréchet derivatives are needed in Section VI.

mapping $y = F(x)$ defined by

$$y(t) = \int_0^T G(t, s)n(s, x(s))\, ds \qquad t \in [0, T]. \tag{25}$$

This operation is assumed to map into itself the Banach space of real-valued $n$-vectors continuous on $[0, T]$ with norm

$$\| x \| = \max_{i=1,\cdots,n} \max_{t \in [0,T]} | x_i(t) |. \tag{26}$$

To determine the derivative of the operation $y = F(x)$ it is convenient to express it as $y = LN(x)$, where $N(x)$ is defined by the nonlinear function $n(t, x(t))$ and $L$ is the linear integral operator. Then $F'(x_0) = LN'(x_0)$ (see Kantorovich and Akilov,[6] p. 659). Thus, consider the mapping $y = N(x)$ defined by

$$\begin{aligned} y(t) &= n(t, x(t)) \\ &= \begin{bmatrix} n_1(t, x(t)) \\ \vdots \\ n_n(t, x(t)) \end{bmatrix}. \end{aligned} \tag{27}$$

It is assumed that $n(t, x(t))$ is continuous whenever $x(t)$ is continuous on $[0, T]$. For simplicity, the derivative will be determined for the case of

$$\begin{aligned} n_i(t, x(t)) &= 0 \qquad i = 1, 2, \cdots, n-1 \\ n_n(t, x(t)) &= p(t)h(x_1(t)) + r(t), \end{aligned} \tag{28}$$

where $p(t)$ and $r(t)$ are continuous functions of $t$ with period $T$ and $h(u)$ is a twice continuously differentiable function of $u$. This special case which covers our examples may arise, for example, when the matrix differential equation is actually derived from a scalar differential equation. The more general case offers no other difficulties than much more complicated notation (e.g., one must deal with matrices of partial derivatives).

The derivative operation $z = N'(x_0)x$ is defined by

$$z(t) = \begin{bmatrix} 0 \\ 0 \\ \vdots \\ 0 \\ p(t)h'(x_{01}(t))x_1(t) \end{bmatrix}, \tag{29}$$

where

$$x_0(t) = (x_{01}(t), \cdots, x_{0n}(t))^T, \qquad x(t) = (x_1(t), \cdots, x_n(t))^T,$$

(superscript $T$ denotes transpose) and

$$h'(x_{01}(t)) = \frac{dh(u)}{du}\bigg|_{u=x_{01}(t)}. \tag{30}$$

To prove this, it must be shown that

$$\lim_{\mu\to 0} \frac{N(x_0 + \mu x) - N(x_0)}{\mu} = P'(x_0)x, \tag{31}$$

that is,

$$\lim_{\mu\to 0} \max_{t\,\varepsilon\,[0,T]} \left| \frac{p(t)h(x_{01}(t) + \mu x_1(t)) - p(t)h(x_{01}(t))}{\mu} - p(t)h'(x_{01}(t))x_1(t) \right| = 0, \tag{32}$$

with that convergence being uniform with respect to all $x$ with $\| x \| = 1$. Since

$$\left| \frac{p(t)h(x_{01}(t) + \mu x_1(t)) - p(t)h(x_{01}(t))}{\mu} - p(t)h'(x_{01}(t))x_1(t) \right| = | p(t) |$$

$$\cdot \left| \frac{h(x_{01}(t)) + \mu x_1(t)h'(x_{01}(t)) + \frac{(\mu x_1(t))^2}{2} h''(x_{01}(t) + \theta(t)\mu x_1(t)) - h(x_{01}(t))}{\mu} - h'(x_{01}(t))x_1(t) \right| \qquad 0 < \theta(t) < 1$$

$$= | p(t) | \cdot \left| \frac{\mu}{2} \right| \cdot | x_1(t) |^2 \, | h''(x_{01}(t) + \theta(t)\mu x_1(t)) |$$

$$\leqq \left| \frac{\mu}{2} \right| \max_{t\,\varepsilon\,[0,T]} | p(t) | \max_{z\,\varepsilon\,Z} | h''(z) | \qquad (\text{for } | \mu | \leqq 1 \text{ and } \| x \| = 1), \tag{33}$$

where

$$Z = \{z : z = w + v;\, w = x_{01}(t),\, t\,\varepsilon\,[0, T];\, | v | \leqq 1\} \tag{34}$$

the uniform convergence relationship is seen to be satisfied.

To summarize the result, the first derivative operation $y = F'(x_0)x$

is defined by

$$y(t) = \int_0^T G(t, s) \begin{bmatrix} 0 \\ \vdots \\ p(s)h'(x_{01}(s))x_1(s) \end{bmatrix} ds. \tag{35}$$

Loosely speaking, the derivatives of the integral operators are obtained by differentiating under the integral.

5.3 *Evaluation of* $\| LN(x_0) - x_0 \|$

A bound on $\| LN(x_0) - x_0 \|$ is given here. The relationship

$$\| LN(x_0) - x_0 \| \leqq \| LN(x_0) \| + \| x_0 \| \tag{36}$$

is too gross an estimate. The evaluation is simplified if the following relation is used:

$$LN(x_0) - x_0 = (L - \tilde{L})N(x_0). \tag{37*}$$

Recall that the operation $\tilde{L}$ suppresses all frequency terms except the fundamental.

Consider the same system as in Section 5.2 and assume that

$$p(t)h(x_1(t)) + r(t) = \sum_{k=1}^{\infty} a_K \cos k \frac{2\pi}{T} t + b_K \sin k \frac{2\pi}{T} t. \tag{38}$$

and also, for simplicity, that $A$ is a constant matrix. Then,

$$\begin{aligned} &\| LN(x_0) - x_0 \| \\ &= \max_{i=1,\cdots,n} \max_{t \varepsilon [0,T]} \left| \int_0^T G_{in}(t, s) \sum_{k=2}^{\infty} \left( a_K \cos k \frac{2\pi}{T} s + b_K \sin k \frac{2\pi}{T} s \right) ds \right| \\ &\leqq \sum_{k=2}^{\infty} (| a_K | + | b_K |) \max_{i=1,\cdots,n} \max_{t \varepsilon [0,T]} \int_0^T | G_{in}(t, s) | \, ds. \end{aligned} \tag{39}$$

5.4 *Example*

Consider Duffing's equation†

$$\ddot{y} + ay + by^3 = f \cos \omega t \; (a > 0). \tag{40}$$

Equivalent linearization indicates that

$$y = A \cos \omega t \tag{41}$$

---

* From this expression, it is seen that $\| LN(x_0) - x_0 \|$ may be regarded as a quantitative measure of characteristics (*i*) and (*ii*) mentioned in section II.

† Duffing's equation is discussed in great detail in Stoker.[12] Also see Graham and McRuer[3] for a treatment of Duffing's equation as a feedback control problem.

with

$$\tfrac{3}{4}bA^3 + (a - \omega^2)A - f = 0 \tag{42}$$

is an approximate solution of the equation.

Letting

$$x = \begin{bmatrix} x_1 \\ x_2 \end{bmatrix} \tag{43}$$

$$x_1 = y \tag{44}$$

$$x_2 = \dot{x}_1 \tag{45}$$

the corresponding vector differential equation is

$$\dot{x} = \begin{bmatrix} 0 & 1 \\ -a & 0 \end{bmatrix} x + \begin{bmatrix} 0 \\ f \cos \omega t - bx_1^3 \end{bmatrix}. \tag{46}$$

The fundamental solution matrix for

$$\dot{y} = \begin{bmatrix} 0 & 1 \\ -a & 0 \end{bmatrix} y \tag{47}$$

is

$$Y(t) = \begin{bmatrix} \cos \sqrt{a}\, t & \dfrac{\sin \sqrt{a}\, t}{\sqrt{a}} \\ -\sqrt{a} \sin \sqrt{a}\, t & \cos \sqrt{a}\, t \end{bmatrix}. \tag{48}$$

$G(t, s)$ is given by

$$G(t, s) = \begin{cases} \dfrac{1}{2 \sin\left(\dfrac{\sqrt{a}\, T}{2}\right)} \begin{bmatrix} \sin \sqrt{a}\left(\dfrac{T}{2} - t + s\right) & \dfrac{1}{\sqrt{a}} \cos \sqrt{a}\left(\dfrac{T}{2} - t + s\right) \\ -\sqrt{a} \cos \sqrt{a}\left(\dfrac{T}{2} - t + s\right) & \sin \sqrt{a}\left(\dfrac{T}{2} - t + s\right) \end{bmatrix}, \\ \qquad\qquad 0 \leqq s \leqq t \leqq T \\ \dfrac{1}{2 \sin\left(\dfrac{\sqrt{a}\, T}{2}\right)} \begin{bmatrix} -\sin \sqrt{a}\left(\dfrac{T}{2} + t - s\right) & \dfrac{1}{\sqrt{a}} \cos \sqrt{a}\left(\dfrac{T}{2} + t - s\right) \\ -\sqrt{a} \cos \sqrt{a}\left(\dfrac{T}{2} + t - s\right) & -\sin \sqrt{a}\left(\dfrac{T}{2} + t - s\right) \end{bmatrix}, \\ \qquad\qquad 0 \leqq t < s \leqq T. \end{cases} \tag{49}$$

The integral operation of interest, $y = F(x)$, is defined by

$$y(t) = \int_0^T G(t, s) \begin{bmatrix} 0 \\ f \cos \omega s - bx_1^3(s) \end{bmatrix} ds. \tag{50}$$

The approximate solution (obtained from harmonic balance) is $x_0$, i.e.,

$$x_0(t) = \begin{bmatrix} x_{01}(t) \\ x_{02}(t) \end{bmatrix} = \begin{bmatrix} A \cos \omega t \\ -\omega A \sin \omega t \end{bmatrix} \tag{51}$$

with $\omega$ and $A$ being related by (42).

From Section 5.3 we have that

$$\begin{aligned} \| LN(x_0) - x_0 \| &\leqq T \max_{i=1,2} \max_{t,s \in [0,T]} | G_{i2}(t, s) | \frac{| bA^3 |}{4} \\ &\leqq TC \frac{| bA^3 |}{4}, \end{aligned} \tag{52}$$

where

$$C = \frac{1}{2 \left| \sin \left( \frac{\sqrt{a}\, T}{2} \right) \right|} \max \{1, 1/\sqrt{a}\}. \tag{53}$$

The derivative operation $z = F'(x_0)x$ is given by (see Section 5.2)

$$\begin{aligned} z(t) &= \int_0^T G(t, s) \begin{bmatrix} 0 \\ -3bx_{01}^2(s)x_1(s) \end{bmatrix} ds \\ &= \int_0^T \begin{bmatrix} -G_{12}(t, s)3bx_{01}^2(s) & 0 \\ -G_{22}(t, s)3bx_{01}^2(s) & 0 \end{bmatrix} \begin{bmatrix} x_1(s) \\ x_2(s) \end{bmatrix} ds. \end{aligned} \tag{54}$$

The norm of the derivative operation at an arbitrary point $x$ (not necessarily at $x_0$ as above) is evaluated as follows:

$$\begin{aligned} \| F'(x) \| &\leqq \max_{i=1,2} \max_{t \in [0,T]} \int_0^T | G_{i2}(t, s)3bx_1^2(s) | ds \\ &\leqq 3 | b | CT( \max_{t \in [0,T]} | x_1(t) | )^2 \\ &\leqq 3 | b | CT( \max_{t \in [0,T]} | x_{01}(t) | + \max_{t \in [0,T]} | x_1(t) - x_{01}(t) | )^2 \\ &\leqq 3 | b | CT(| A | + \| x - x_0 \|)^2. \end{aligned} \tag{55}$$

The above relation defines the nondecreasing function $g$ such that

$$\| F'(x) \| \leqq g(\| x - x_0 \|). \tag{56}$$

to use the theorem of Section II, let

$$\Omega = \left\{ x \colon \| x - x_0 \| \leqq \frac{k}{1 - \alpha} \right\} \tag{57}$$

where

$$k = CT \frac{|bA^3|}{4} \tag{58}$$

(see (52)).

If an $\alpha \in [0, 1)$ can be found satisfying

$$3 \mid b \mid CT \left[ \mid A \mid + \frac{CT \dfrac{\mid bA^3 \mid}{4}}{1 - \alpha} \right]^2 \leqq \alpha \tag{59}$$

then there is an $x^* \in \Omega$ such that $x^* = F(x^*)$, i.e., Duffing's equation has a periodic solution in the neighborhood of the approximation obtained by harmonic balance.

Rather than just solve the cubic relation (59) for particular numerical values of $a$, $b$, $f$, and $\omega$ (which is, of course, the thing to do if one is given a particular equation of interest) we shall obtain some general results. Consider $a$, $f$, and $\omega$ fixed and $f \neq 0$. Since† for any $\alpha \in [0, 1)$

$$\lim_{b \to 0} 3 \mid b \mid CT \left[ \mid A \mid + \frac{CT \dfrac{\mid bA^3 \mid}{4}}{1 - \alpha} \right]^2 = 0 \tag{60}$$

it is seen that for $b$ sufficiently small, there will be an $\alpha \in [0, 1)$ satisfying (59) (and thus a periodic solution neighboring the approximation). Note that while the result has been stated as an asymptotic result, it is possible to determine quantitatively what is meant by "sufficiently small". This is in contrast to most asymptotic analyses based on "small nonlinearities".

### 5.5 *Special Cases*

In many cases, it is not necessary to convert the differential equation into a vector integral equation. For example, let the system be

† See Appendix C for details.

described by the equation

$$a_0x^{(m)}(t) + a_1x^{(m-1)}(t) + \cdots + a_mx(t) = n(t, x(t)), \tag{61}$$

where the $a_0, \ldots, a_m$ are constants, $n(t, x)$ is continuous in $t$ when $x$ is continuous in $t$, and

$$n(t + T, u) = n(t, u). \tag{62}$$

A periodic solution to the differential equation will satisfy the following integral equation

$$x(t) = \int_0^T W_T(t - u)n(u, x(u))\, du, \tag{63}$$

where $W_T(t-u)$ is the appropriate convolution kernel (see Kaplan,[4] chap. 4 for details). All the manipulations of previous sections will be somewhat simplified as a result of not having to deal with matrices. In particular, the example of Section 5.4 could be repeated with some simplification. We omit the details because they exactly parallel the previous case. We felt it would be more useful to work out the details of the more complicated case. As the order of the differential equation increases it clearly becomes more advantageous to avoid the use of matrices.

It may be noted that there is a finite Fourier transform $Y(in\omega)$ (again see Kaplan,[4] chap. 4) associated with the differential equation (61)

$$Y(in\omega) = \frac{1}{a_0(in\omega)^m + \cdots + a_m}. \tag{64}$$

This $Y(p)$, considered as a function of a complex variable $p$, evidently can only have poles and cannot have finite zeros. In many electrical engineering applications (e.g., control systems, networks) the relevant transfer function has both poles and zeroes. In these cases, we would start with the transfer function, rather than a differential equation of the form (61), find the corresponding convolution integral and then apply our method. For other applications it must, of course, be verified that the appropriate conditions are satisfied.

### 5.6 *Autonomous Systems*†

The describing function method has been used by control engineers primarily for the prediction of self-oscillations (i.e., with no forcing

† Since the actual oscillation of an autonomous system may have a different period than that of the approximation, it is usually convenient to normalize the time variable and have the period be a parameter.

functions). It would seem at first glance that our approach should be appropriate for analysis of this problem. Suppose the describing function method indicates that there exists a non-trivial periodic solution, $x_0$, to the operator equation

$$x_0 = \tilde{L}N(x_0). \tag{65}$$

Usually, $N(0) = 0$, so that it is of interest to investigate whether there is any non-trivial solution to the exact equation near $x_0$. If our method is successful, then we can guarantee that $\Omega$ does not contain the trivial solution ($x = 0$) if

$$\frac{\| F(x_0) - x_0 \|}{1 - \alpha} < \| x_0 \| \tag{66}$$

since the fixed point x* satisfies

$$\| x^* - x_0 \| \leqq \frac{\| F(x_0) - x_0 \|}{1 - \alpha}. \tag{67}$$

Unfortunately, an attempt to use the approach in the autonomous case will be unsuccessful. The reason for the failure of our approach is due to the nature of the fixed point: the mapping is not a contraction in a neighborhood of the fixed point.† The discussion below will clarify this point.

Assume that the differential equation of interest is

$$\dot{x}(t) = Ax(t) + n(x(t)) \tag{68}$$

with $A$ a constant real valued matrix and $n(x)$ is a real-valued function having continuous partial derivatives with respect to all of the elements of the vector $x$. Suppose that there is a continuous periodic $x^*$ of period $T$ satisfying (68). Then $x^*$ satisfies the equivalent integral equation:

$$x^*(t) = \int_0^T G(t, s)n(x^*(s))\, ds. \tag{69}$$

The equation of first variation corresponding to (68) is

$$\dot{y}(t) = Ay(t) + \frac{\partial n}{\partial x^*}\, y(t), \tag{70}$$

where $\partial n/\partial x^*$ is a matrix with entries $\partial n_i/\partial x_j$ evaluated along the

† Actually, this should not be surprising since if $x(t)$ is a periodic solution, then so is $x(t + \epsilon)$.

trajectory defined by $x^*(t)$. As is easily shown (by differentiation; see, e.g., Hochstadt,[13] p. 251) the time derivative of $x^*(t)$ satisfies the equation of first variation and thus the equivalent integral equation

$$\dot{x}^*(t) = \int_0^T G(t, s) \frac{\partial n}{\partial x^*} \dot{x}^*(s)\, ds. \tag{71}$$

Now consider the derivative operation $y = LN'(x^*)x$ associated with the integral operation of (69). The derivative operation is defined by

$$y(t) = \int_0^T G(t, s) \frac{\partial n}{\partial x^*} x(s)\, ds. \tag{72}$$

We have shown above that $\dot{x}^*$ satisfies this last equation or

$$\dot{x}^* = LN'(x^*)\dot{x}^*. \tag{73}$$

Then

$$\| \dot{x}^* \| \leqq \| LN'(x^*) \| \cdot \| \dot{x}^* \|. \tag{74}$$

Since $\| \dot{x}^* \| > 0$, we must have that

$$\| LN'(x^*) \| \geqq 1 \tag{75}$$

or $LN$ cannot be a contraction in a neighborhood of $x^*$. We leave open, however, the possibility that the contraction mapping theorem might be applicable in a subspace.

The above reasoning also shows that there would be difficulty associated with using Newton's method for the problem. To seek a zero of $P(x)$, Newton's method uses the following iteration:

$$x_{n+1} = x_n - [P'(x_n)]^{-1}(P(x_n)) \qquad n = 0, 1, \cdots . \tag{76}$$

Letting

$$P(x) = x - F(x) \qquad (F(x) = LN(x)), \tag{77}$$

we are led to investigating the inveritibility of $I - F'(x)$ where $I$ is the identity operator. Consider the operation

$$y = P'(x^*)x = (I - F'(x^*))x. \tag{78}$$

If $x = 0$, then $y = 0$. But because $F'(x^*)$ is associated with the equation of first variation there is also a nonzero $x$ (the time derivative of $x^*(t)$) which results in $y = 0$. There is thus not a unique $x$ satisfying $y = 0$ and $P'(x^*)$ is not invertible (see Kantorovich and Akilov,[6] p. 168).

### 5.7 *Properties of the Fixed Point—Dependence on Parameters; Stability*

The method of this investigation is to obtain a relation for $\alpha$ in terms of parameters of the differential equations. If certain conditions are satisfied and $0 \leqq \alpha < 1$, then $\alpha$ represents a contraction constant. If $\alpha$ is a contraction constant and, also, $\alpha$ depends continuously on a parameter then for sufficiently small changes of that parameter $\alpha$ will still be a contraction constant and a periodic solution is still guaranteed. Once again note that "sufficiently small" can be quantitatively determined if one wishes to do that. As an illustration, in the Duffing equation example, $\alpha$ depends continuously on $b$.

If our method indicates the existence of a periodic solution of period $T$ then there is no neighboring solution of period $T$ (for a sufficiently small neighborhood). This condition does not imply stability of the periodic solution. With a perturbation of the initial conditions, stability is concerned with closeness to (asymptotic stability is concerned with the eventual approaching of) the original periodic solution. A perturbation of the initial conditions of the period solution of period $T$ may result in a solution not of period $T$ and thus, not even considered in the Banach space used.

A sufficient condition for the asymptotic stability of a periodic solution (of period $T$) to a nonautonomous system is the asymptotic stability of the null solution of the corresponding equation of first variation (Hochstadt,[13] p. 251). We are only able to show that the equation of first variation may not have a (nontrivial) periodic solution of period $T$ if the fixed point is a contraction. The nonexistence of a periodic solution to the equation of first variation is (along with a continuous differentiability requirement) a sufficient condition for the continuous dependence of the periodic solution on a parameter. This result is not identical to but is compatible with our initial comments on the continuity of the contraction constant with respect to a parameter.

### 5.8 *Perturbation Analysis*

A very common approach to nonlinear problems is to solve a linear problem ignoring the nonlinearity and then to use a series expansion or a perturbation about the linear solution (see, e.g., Hochstadt,[13] Sections 6.5, 7.4). As useful as these procedures are, they usually suffer from the defect of not providing adequate quantitative information about the nonlinear solution, i.e., it may not be possible to determine quantitatively what is meant by "sufficient small". Our use of

the contraction mapping theorem may prove useful in this regard.

As an illustration, again consider Duffing's equation and assume that $x_0$ was obtained by ignoring the nonlinear term $(by^3)$. In this case, $x_0 = F(x_0)$ is defined by

$$x_{01}(t) = \int_0^T G_{12}(t, s) f \cos \omega s \, ds. \tag{79}$$

Then arguments similar to (but simpler than) those of Section 5.4 show that if $b$ is "small enough" there is a continuous periodic solution to (40) which is "close" to the linear approximation

$$x_{01}(t) = \frac{f \cos \omega t}{a - \omega^2}. \tag{80}$$

Note that "small enough" and "close" may be quantitatively evaluated.

## VI. DIFFERENCE-DIFFERENTIAL EQUATIONS*

Our use of the contraction map fixed point therom is not limited to ordinary differential equations or integral equations. As a further example, consider the difference-differential equation represented by

$$x = LN(D_h x), \tag{81}$$

where $y = D_h x$ is defined by

$$y(t) = x(t - h). \tag{82}$$

If the Banach space $B$ of interest is the space of continuous periodic functions, then

$$\| D_h \| = 1. \tag{83}$$

This follows easily from

$$\begin{aligned} \| D_h \| &= \sup \{ \| D_h x \| : x \in B, \| x \| = 1 \} \\ &= \sup \{ \max_t | x(t - h) | : x \in B, \max_t | x(t) | = 1 \}. \end{aligned} \tag{84}$$

Assume that $N$ maps $B$ into itself. If $N$ is differentiable (i.e., has a Fréchet derivative) at $x_0$ then $N(D_h x)$ has a derivative at $x_0$ (Kantorovich and Akilov,[6] p. 658) given by $N'(D_h x_0) D_h$. Then $LN(D_h)$ has a derivative at $x_0$ given by $LN'(D_h x_0) D_h$. The norm is easily

* An interesting discussion of the problems of oscillations in difference-differential equations is given in Chap. 21 of Minorsky.[1] Halanay[11] contains much information (and references) on difference-differential equations.

evaluated:

$$\| LN'(D_h x_0) D_h \| \leqq \| L \| \cdot \| N'(D_h x_0) \|. \tag{85}$$

Conceptually, the introduction of the time delay offers no great difficulty as compared to the case without the time delay. However, it will generally complicate the arithmetic involved in examples, in particular, in obtaining the solution to $x_0 = \tilde{L}N(x_0)$. This relative lack of complication going from differential equations to difference-differential equations is not typical. In existence, uniqueness, and stability considerations one must consider initial function conditions in difference-differential equations while the initial conditions for differential equations are merely at one time (or perhaps boundary conditions at several times).

To illustrate the above remarks, consider the following difference-differential equation:

$$\ddot{y} + ay + by_h^3 = f \cos \omega t \tag{86}$$

$$y_h(t) = y(t - h) \tag{87}$$

This is Duffing's equation but with the argument of the cubic term retarded. The corresponding operator equation is

$$x = LN(x) = L[N_1(D_h x) + F], \tag{88}$$

where $y = N_1(x)$ is defined by the cubic nonlinearity, $L$ is the same linear operator as in Section V, and

$$F(t) = \begin{bmatrix} 0 \\ f \cos \omega t \end{bmatrix}. \tag{89}$$

It is clear that

$$\| LN'(x_0) \| \leqq \| L \| \, \| N_1'(x_0) \| \tag{90}$$

and that the analysis will be completely analogous to that of Section V, except that the approximate solution, $x_0$, will be different. Note that the Banach space is the space of continuous periodic functions, not the space of functions continuous on one period.

To obtain the equivalent linearization approximation let

$$\begin{aligned} y(t) &= A \cos \omega t + B \sin \omega t \\ &= C \sin (\omega t + \theta), \end{aligned} \tag{91}$$

where

$$C = \sqrt{A^2 + B^2}$$
$$\theta = \tan^{-1}\left(\frac{A}{B}\right). \tag{92}$$

Substitution of this function into (86) yields

$$-\omega^2 C \sin(\omega t + \theta) + aC \sin(\omega t + \theta) + \tfrac{3}{4}C^3 b\,[\cos \omega h \sin(\omega t + \theta)$$
$$- \sin \omega h \cos(\omega t + \theta) + \text{third harmonics}] = \text{f} \cos \omega t. \tag{93}$$

The approximation is obtained by neglecting the third harmonics and equating coefficients of $\cos \omega t$ and $\sin \omega t$. It is interesting to compare the equivalent linearization solution obtained for the difference-differential equation with that obtained for the following differential equation (Duffing's equation with a damping term):

$$\ddot{y} + k\dot{y} + ay + by^3 = f \cos \omega t. \tag{94}$$

Substituting (91) into (94) yields

$$-\omega^2 C \sin(\omega t + \theta) + k\omega C \cos(\omega t + \theta) + aC \sin(\omega t + \theta)$$
$$+ \tfrac{3}{4}bC^3 \sin(\omega t + \theta) + \text{third harmonics} = f \cos \omega t. \tag{95}$$

Comparing (93) and (95) it is seen that, as far as harmonic balance is concerned, the effect of the lag is to introduce a damping term with damping coefficient $k$,

$$k = -(\sin \omega h)\tfrac{3}{4}C^2 b/\omega \tag{96}$$

(Also, one other term is multiplied by $\cos \omega h$).

For some parameter values, the equivalent damping is negative. Because of the negative damping, it appears that the periodic solution is not asymptotically stable. We say "appears that" rather than making a more definite statement for the following reason. While it seems plausible that the stability properties of the solution of the equation of equivalent linearization should carry over to the actual solution, the mathematical proof does not seem so obvious.

## VII. RELATION TO PREVIOUS WORK*

As mentioned previously, the method of equivalent linearization has its roots in the method of Krylov and Boguliubov. For an ac-

* The literature on equivalent linearization is vast. We shall thus discuss only those references which seem most pertinent. Even in those cases, we shall discuss only those aspects which are directly related to the present study. The reader should consult these references for many other interesting ideas.

count of the very important work of Krylov, Boguliubov, and Mitropolsky in this area, see Minorsky.[1] Their work is primarily of the asymptotic type, i.e., leading to statements of the form, "for sufficiently small $\mu$, there exists . . . ." We may view our approach as using a fixed point theorem to be able to determine quantitatively what is meant by "sufficiently small" for a somewhat different but related problem.

Bass[5] considers the justification of the method of equivalent linearization in the autonomous case. In view of our comments on the inapplicability of the contraction map fixed point theorem, it is of interest to note that Bass uses a much more sophisticated fixed point theorem. Much of his analysis is interesting and important but his final results are unfortunately difficult to apply (as Bass himself points out).

Sandberg[10] considers the operator equation*,

$$x = LN(x + f) \tag{97}$$

and the equivalent linearization approximation

$$x_0 = \tilde{L}N(x_0 + f). \tag{98}$$

Sandberg's analysis is carried out in the space of periodic functions square integrable over a period. He presents conditions under which there exists a unique periodic response to an arbitrary periodic input with the same period as well as an upper bound on the mean square error in using equivalent linearization. He also gives conditions under which sub-harmonics and self-sustained oscillations cannot occur. Sandberg's method is to determine conditions that guarantee that $LN$† is a contraction mapping in the whole space. As mentioned previously, we do not try to obtain a contraction mapping in the whole space but only in a neighborhood of $x_0$. We thus free ourselves from Lipschitz type requirements. It may be noted that many nonlinearities encountered in engineering are non-differentiable and Lipschitzian (e.g., piecewise linear functions such as saturation-type nonlinearities). For these, Sandberg's analysis is applicable while ours is not because we have required differentiability. Thus, Sandberg's work and ours complement each other in this regard. Also, Sandberg very fruitfully uses Fourier transform results in his analysis of feedback systems.

* This is the same notation as in Section II except that in Section II we did not explicitly show the dependence on a forcing function. That is, $y = N(x)$ could be defined by $y(t) = n(x(t)+f(t))$ or by $y(t) = n(x(t)) + f(t)$.

† Actually, an operator related to $LN$.

Cesari[14] considers the real differential system

$$\begin{aligned} \dot{x} &= g(x, t) \\ x &= (x_1, \cdots, x_n) \\ \dot{x}_j &= g_j(x_1, \cdots, x_n, t) \qquad j = 1, \cdots, n. \end{aligned} \tag{99}$$

(For the specific conditions imposed on the above functions see Ref. 14). If

$$x_j(t) \sim a_{j0} + \sum_{s=1}^{\infty} (a_{js} \cos s\omega t + b_{js} \sin s\omega t) \tag{100}$$

and $m$ is a positive integer the vector function $Px = (P_1x_1 \ldots, P_nx_n)$ is defined by

$$P_jx_j(t) = a_{j0} + \sum_{s=1}^{m} (a_{js} \cos s\omega t + b_{js} \sin s\omega t) \qquad j = 1, \cdots, n. \tag{101}$$

The operation $H(x) = (X_1, \ldots, X_n)$ is defined by

$$X_j(t) = \sum_{s=m+1}^{\infty} \frac{1}{s\omega} (-b_j \cos s\omega t + a_{js} \sin s\omega t) \qquad j = 1, \cdots, n. \tag{102}$$

The operation $F(x)$ is defined by

$$F(x) = H(I - P)g(x), \tag{103}$$

where $I$ is the identity map and

$$\begin{aligned} g(x) &= (g_1x, \cdots, g_nx) \\ g_jx &= g_j[x(t), t] \qquad (j = 1, \cdots, n). \end{aligned} \tag{104}$$

Letting $T = P + F$, Cesari determines conditions for the existence of fixed points of $x = Tx$. He uses both Banach's fixed point theorem (contraction mapping theorem) and Schauder's fixed point theorem (which does not give uniqueness but requires weaker conditions). He then shows that if $y$ is a fixed point, it satisfies

$$\dot{y}_j = g_j(y(t), t) + P_j(\dot{y}_j - g_jy). \tag{105}$$

If

$$P_j(\dot{y}_j - g_jy) = 0, \qquad j = 1, \cdots, n \tag{106}$$

then

$$\dot{y}(t) = g(y(t), t) \tag{107}$$

Cesari discusses the solution of (106) which may be reduced to determining a Galerkin approximation. Cesari worked in the space of square integrable (periodic) functions and Knobloch[15] adapted his approach to the space of continuous functions.

While the above method has the use of truncations of Fourier series in common with our approach, there seems to be a closer relationship between Urabe's approach and ours.

Urabe[16] considers the real nonlinear periodic system

$$\frac{dx}{dt} = X(x, t),$$

where $X(x, t)$ is periodic in $t$ of period $2\pi$. If

$$x_m(t) = a_0 + \sqrt{2} \sum_{n=1}^{m} a_n \cos nt + b_n \cos nt, \tag{108}$$

a Galerkin approximation* of order $m$ is obtained if one can determine the $2m + 1$ coefficients $a_0, a_1, b_1, \ldots, a_m, b_m$ that satisfies the following equation:

$$\begin{aligned} \frac{dx_m}{dt} = \frac{1}{2\pi} \int_0^{2\pi} X[x_m(s), s]\, ds \\ + \frac{1}{\pi} \sum_{n=1}^{m} \left\{ \cos nt \int_0^{2\pi} X[x_m(s), s] \cos ns\, ds \right. \\ \left. + \sin nt \int_0^{2\pi} X[x_m(s), s] \sin ns\, ds \right\}. \end{aligned} \tag{109}$$

Urabe considers the problem of determining whether there is an exact periodic solution near an approximate (Galerkin) solution, $x_0$. He determines conditions under which an iteration starting at $x_0$ converges to an exact periodic solution. His proof, while not explicitly mentioning a fixed point theorem, is closely related to the contraction mapping fixed point theorem and uses the fact that a contracting iteration sequence must stay within a certain sphere centered about the initial point.† Our approach is in the same spirit but we take a more general viewpoint at the beginning. The basic theorem is derived in an arbi-

* The method of equivalent linearization is essentially a first-order Galerkin approximation.

† It may be shown that Urabe's result (Proposition 3, p. 125 of Ref. 16) is essentially equivalent to requiring that the operator derivative have norm less than one (a contraction) in the appropriate sphere.

trary Banach space where derivatives of operators are fruitfully used. The more general viewpoint is very simple conceptually and also permitted the easy extension to difference-differential equations. Urabe in Ref. 16, and also in Ref. 17 and 18, considers many aspects of Galerkin's method for differential equations not touched on in our study. Also, see his comments on Cesari's method on p. 121 of Ref. 16.

## VIII. CONCLUDING REMARKS

The development of analytical methods (other than asymptotic methods) for the equivalent linearization technique with autonomous systems remains a very important area for investigation.* Whether a modification of the contraction mapping theorem (perhaps using a subspace) might be applied to this problem remains to be seen. In connection with autonomous systems, a question perhaps more important than the one we have considered (if equivalent linearization indicates a periodic solution, does there actually exist one?) is the following: If a non-trivial periodic solution exists, will the method of equivalent linearization indicate it? A typical engineering use of the describing function is to determine conditions under which no self-sustained oscillations are predicted. The engineer would like these same conditions to also imply that there are no oscillations in the original (exact) system. Urabe[16] has shown that the existence of a periodic solution will (under certain conditions) imply the existence of a Galerkin approximation of sufficiently high order. The equivalent linearization technique is essentially a first-order Galerkin approximation and the first-order approximation may not be high enough to indicate the existence of a periodic solution according to a result of the type of Ref. 16. It would be very useful to determine conditions that would answer the question. This question is related to that rased by Aizerman's conjecture.

Leaving the problem of autonomous systems we find our adaptation of the contraction mapping theorem to be quite convenient in analyzing equivalent linearization in forced systems. The calculations are straightforward and require no difficult mathematical argument in the execution of the basic idea. It is hoped that the method may prove useful in justifying and refining approximations.

It should be clear that our approach is easily adapted to the dual-

---

* A theory of autonomous systems, due to Urabe, is outlined in Chap. 3 of Halanay.[11]

input describing function approximation (see, e.g., Gibson,[19] p. 402).* The remarks in Section VI concerning difference-differential equations apply in that case also. That is, the only essential difficulty is in obtaining the dual-input describing function solution (which has nothing to do with our method of investigating the accuracy of such a solution). It should be noted that the dual-input describing function method has been used primarily for two sinusoids with commensurate frequencies (one an integral multiple of the other) and is actually equivalent to a Galerkin approximation. When the ratio of the two frequencies is irrational, we are in the realm of almost-periodic functions where analysis can get much more complicated. Boyer has presented an interesting approximate method of analysis (an account of which is given in Gibson,[19] p. 408ff.) for an input consisting of two sinusoids with incommensurate frequencies but with one much larger than the other. Analysis of this method would be of interest.

## IX. ACKNOWLEDGMENTS

I wish to express my appreciation to Professor H. Hochstadt for his valuable suggestions and constructive criticism. I am grateful to Bell Telephone Laboratories for the financial support received as a participant in the Doctoral Support Plan.

## APPENDIX A

### *Guide to Some Mathematical Background Reading for Engineers*

The purpose of this appendix is to make reading suggestions to engineers interested in this work but who are not familiar with the mathematics used. The primary reference on functional analysis used for this work is Kantorovich and Akilov.[6] A more elementary introduction is given in Kolmogorov and Fomin.[9]† Lucid introductions to the theory of differential equations are given in Hochstadt[13] and Struble.[20] The theory of oscillations is extensively covered in Minor-

* The dual-input describing function was apparently first used by J. C. West, J. L. Douce, and R. K. Livesly. In Ref. 7 there is an example of the existence of a subharmonic solution to Duffing's equation. This is actually an example of the dual-input describing function.

† The reader should be cautioned that some of the terminology is not standardized among American and Russian writers. For example, Kantorovich and Akilov do not require a compact set to be closed while most American authors do. Also, a linear operator is necessarily bounded according to Kantorovich and Akilov but not necessarily bounded according to most American writers (Kolmogorov and Fomin's definition agrees with American writers on this point).

sky[1] which also has a discussion on difference-differential equations. Kaplan treats Fourier series and finite Fourier transforms on an elementary level.[4] Further information on Fourier series (but still on an elementary level) can be found in Tolstov.[21]

## APPENDIX B

### *Derivatives in a Banach Space*

The following material is abstracted from Chap. XVII of Kantorovich and Akilov.[6]

Let $P$ map an open subset $\Omega$ of a Banach space $X$ into a subset $\Delta$ of another Banach space $Y$. Let $x_0 \varepsilon \Omega$ and suppose that there exists a linear* operation $U$ mapping $X$ into $Y$ such that for every $x \varepsilon X$

$$\lim_{t \to 0} \frac{P(x_0 + tx) - P(x_0)}{t} = U(x). \tag{110}$$

The linear operation $U$ is said to be the derivative of the operation $P$ at the point $x_0$. We write this

$$U = P'(x_0). \tag{111}$$

The derivative thus defined is the Gateaux or weak derivative and $U(x)$ is the Gateaux differential.

If the convergence relationship of (110) is satisfied uniformly with respect to all $x \epsilon X$ with $\| x \| = 1$, then the operation $P$ is differentiable at the point $x_0$ and the derivative $P'(x_0)$ is called the Fréchet or strong derivative.

## APPENDIX C

To discuss the satisfaction of (59), let

$$Z = 3 \mid b \mid CT \left[ \mid A \mid + \frac{CT \dfrac{\mid bA^3 \mid}{4}}{1 - \alpha} \right]^2 .$$

Consider $a$, $f$, and $\omega$ fixed with $f \neq 0$ and let $\alpha \varepsilon [0, 1)$. To show that

$$\lim_{b \to 0} Z = 0$$

we must show that

$$\lim_{b \to 0} \mid bA^2 \mid = 0$$

* Kantorovich and Akilov[6] include boundedness in their definition of linear.

since

$$Z = 3CT\left\{ | bA^2 | + \frac{\frac{CT}{2} | bA^2 |^2}{1 - \alpha} + \left(\frac{CT}{1 - \alpha}\right)^2 \frac{| bA^2 |^3}{16} \right\}.$$

From (42) we have that

$$bA^2 = \frac{4}{3}\left(\frac{f}{A} + \omega^2 - a\right).$$

Also

$$\lim_{b \to 0} A = \frac{f}{a - \omega^2}$$

so that

$$\lim_{b \to 0} bA^2 = 0.$$

REFERENCES

Several of these works refer to still other works which contain helpful information. For example, see the first footnote on page 2407.


1. Minorsky, N., *Nonlinear Oscillations,* D. Van Nostrand Co., Inc., Princeton, New Jersey, 1962.
2. Truxal, J. G., *Automatic Feedback Control System Synthesis,* McGraw-Hill Book Co., Inc., New York, 1955.
3. Graham, D. and McRuer, D., *Analysis of Nonlinear Control Systems,* John Wiley and Sons, Inc., New York, 1961.
4. Kaplan, W., *Operational Methods in Linear Systems,* Addison-Wesley, Reading, Mass., 1962.
5. Bass, R. W., Mathematical Legitimacy of Equivalent Linearization by Describing Functions, in *Automatic and Remote Control,* ed. J. F. Coales, Butterworths, London, 1961.
6. Kantorovich, L. V. and Akilov, G. P., *Functional Analysis in Normed Spaces,* (translation), Pergamon Press Limited, Oxford, England, 1964.
7. Holtzman, J. M., The Use of the Contraction Mapping Theorem with Derivatives in a Banach Space, unpublished work.
8. Krasnosel'skii, M. A., *Topological Methods in the Theory of Nonlinear Integral Equations,* (translation), Pergamon Press Limited, Oxford, England, 1963.
9. Kolmogorov, A. N. and Fomin, S. V., *Elements of the Theory of Functions and Functional Analysis,* Vol. 1, Graylock Press, Rochester, N. Y., 1957 and Vol. 2, Graylock Press, Albany, N. Y., 1961.
10. Sandberg, I. W., On the Response of Nonlinear Control Systems to Periodic Input Signals, B.S.T.J., *43,* May, 1964, pp. 911–926.
11. Halanay, A., *Differential Equations: Stability, Oscillations, Time Lags,* (translation) Academic Press, New York, 1966.
12. Stoker, J. J., *Nonlinear Vibrations in Mechanical and Electrical Systems,* Interscience Publishers, New York, 1950.
13. Hochstadt, H., *Differential Equations,* Holt, Rhinehart and Winston, New York, 1964.
14. Cesari, L., Functional Analysis and Periodic Solutions of Nonlinear Differen-

tial Equations, *Contributions to Differential Equations,* Vol. 1, No. 2, J. Wiley and Sons, Inc., New York, 1963, pp. 149–167.
15. Knobloch, H. W., Remarks on a Paper of L. Cesari on Functional Analysis and Nonlinear Differential Equations, Michigan Math. J., *10,* 1963, pp. 417–430.
16. Urabe, M., Galerkin's Procedure for Nonlinear Periodic Systems, Arch. Rational Mech. Anal., *20,* 1965, pp. 120–152.
17. Urabe M. and Reiter, A., Numerical Computation of Nonlinear Forced Oscillations by Galerkin's Procedure, J. Math. Anal. Applic., *14,* 1966, pp. 107–140.
18. Urabe, M., Periodic Solutions of Differential Systems, Galerkin's Procedure and the Method of Averaging, J. Diff. Equat., *2,* 1966, pp. 265–280.
19. Gibson, J. E., *Nonlinear Automatic Control,* McGraw-Hill Book Co., Inc., New York, 1963.
20. Struble, R. A., Nonlinear Differential Equations, McGraw-Hill Book Co., Inc., New York, 1962.
21. Tolstov, G. P., *Fourier Series,* (translation), Prentice-Hall, Inc., Englewood Cliffs, New Jersey, 1962.

# Power Density Spectrum of the Sum of Two Correlated Intermodulation Noise Contributors in FM Systems

By T. G. CROSS

(Manuscript received August 15, 1967)

*In the recent literature, two noise contributors in FM systems have been analyzed:(i) intermodulation noise due to transmission deviations, and (ii) AM/PM intermodulation noise. Even though different, these two contributors have the same property of being functions of the baseband signal. Hence, one would expect them to be correlated to some degree.*

*In this paper, we derive the expression for the power density spectrum for the sum of these two noise contributors. The resulting expression has been programmed on a digital computer. It has been found that, under certain conditions, the correlation can be quite significant. In fact, an example using a representative FM radio relay system shows that the correlation can result in greater than 4 dB error if the two contributors are assumed to be uncorrelated.*

## I. INTRODUCTION

Two noise contributors in FM systems are: (*i*) intermodulation noise due to transmission deviations, and (*ii*) AM/PM intermodulation noise. The first noise contributor is generated when an FM signal is passed through a linear transmission medium which has transmission deviations. The second noise contributor is generated when an FM signal is passed through such a medium which is followed by an AM/PM conversion device. These two noise sources are different, in general, but have in common the property that they are a function of the baseband signal. Therefore, one would expect that they are correlated to some degree. This would mean that combining the two noise power density spectra together assuming random addition (uncorrelated random variables), i.e., power addition, might not be sufficient in general.

In this paper, we will derive the power density spectrum for the sum of these two noise contributors. We will then examine the results, with the help of a digital computer program, for the conditions under which the two noise contributors are correlated. We will also present an example using a representative FM radio relay system. However, before considering the correlation problem, we will first briefly consider the two noise contributors individually.

## II. INTERMODULATION NOISE DUE TO TRANSMISSION DEVIATIONS

Intermodulation noise is produced in FM systems whenever the FM signal is passed through a linear transmission medium which has transmission deviations.* This situation is depicted in Fig. 1 where

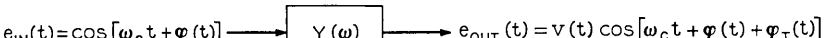


Fig. 1 — Generation of intermodulation noise due to transmission deviations.

the transmission medium, $Y(\omega)$, is represented by power series gain and phase transmission deviations up to fourth order, or

$$Y(\omega + \omega_c) = [1 + g_1\omega + g_2\omega^2 + g_3\omega^3 + g_4\omega^4] \cdot \exp i[b_2\omega^2 + b_3\omega^3 + b_4\omega^4]. \quad (1)$$

where $\omega_c$ = carrier frequency in radians per second. The output signal is phase modulated by the desired signal, $\varphi(t)$, as well as the phase modulating distortion function $\varphi_T(t)$. This distortion function consists of first- (linear), second-, third- and higher-order functions of the input phase modulating function $\varphi(t)$. Because of their significance in FM radio relay systems, we will concentrate on the second- and third-order terms which will generate second- and third-order intermodulation noise once the signal is demodulated. In other words, we will let

$$\varphi_T(t) = \varphi_2(t) + \varphi_3(t), \quad (2)$$

where $\varphi_2(t)$ and $\varphi_3(t)$ represent the second- and third-order intermodulation noise components produced by the transmission deviations in $Y(\omega)$. In Ref. 1, these components were derived and are given by

* Transmission deviations are defined as any deviation in the gain and phase characteristics from the ideal characteristics of constant gain and linear phase for all frequency components of the FM wave.

$$\varphi_2(t) = \left[-\tfrac{1}{2}\lambda_{2i} + \tfrac{1}{4}l_{2i}\frac{d}{dt} - \tfrac{1}{12}l_{3i}\frac{d^2}{dt^2}\right]\varphi'^2(t) + [\tfrac{1}{24}l_{4i}]\varphi''^2(t) \tag{3}$$

$$\varphi_3(t) = \left[\tfrac{1}{6}\lambda_{3r} - \tfrac{1}{12}l_{1r}\frac{d}{dt}\right]\varphi'^3(t) \tag{4}$$

with the prime (′) notation depicting the derivative with respect to time. The $\lambda$ and $l$ coefficients can be expressed in terms of the transmission deviation coefficients of the transmission medium by the appropriate equations in Ref. 1. Equations (2), (3), and (4) can be represented as shown in Fig. 2 where

$$H_1(\omega) = [\tfrac{1}{12}l_{3i}\omega^2 - \tfrac{1}{2}\lambda_{2i}] + i[\tfrac{1}{4}l_{2i}\omega] \tag{5}$$

$$H_2(\omega) = \tfrac{1}{24}l_{4i} \tag{6}$$

$$H_3(\omega) = [\tfrac{1}{6}\lambda_{3r}] + i[-\tfrac{1}{12}l_{1r}\omega]. \tag{7}$$

The autocorrelation function of $\varphi_T(t)$ is given by

$$\begin{aligned} R_{\varphi_T}(\tau) &= \overline{\varphi_T(t)\varphi_T(t+\tau)} \\ &= \overline{[\varphi_2(t) + \varphi_3(t)][\varphi_2(t+\tau) + \varphi_3(t+\tau)]} \\ &= \overline{\varphi_2(t)\varphi_2(t+\tau)} + \overline{\varphi_3(t)\varphi_3(t+\tau)} \\ &\quad + \overline{\varphi_3(t)\varphi_2(t+\tau)} + \overline{\varphi_2(t)\varphi_3(t+\tau)} \\ &= R_{\varphi_2}(\tau) + R_{\varphi_3}(\tau) + R_{\varphi_3\varphi_2}(\tau) + R_{\varphi_2\varphi_3}(\tau), \end{aligned} \tag{8}$$

where the bar notation depicts the time average of the function over an infinite interval, and e.g., $R_{\varphi_3\varphi_2}(\tau)$ is the crosscorrelation of $\varphi_3(t)$ and $\varphi_2(t)$. In the Appendix of Ref. 2, it was shown that

$$R_{\varphi_3\varphi_2}(\tau) = R_{\varphi_2\varphi_3}(\tau) = 0 \tag{9}$$

so

$$R_{\varphi_T}(\tau) = R_{\varphi_2}(\tau) + R_{\varphi_3}(\tau). \tag{10}$$

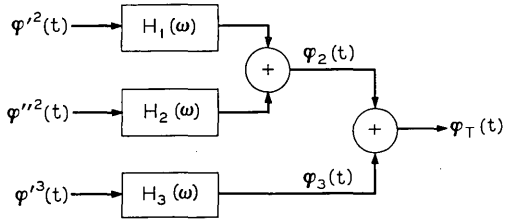


Fig. 2 — Block diagram of total intermodulation noise due to transmission deviations.

Taking the Fourier Transform of (10) gives

$$S_{\varphi_T}(\omega) = S_{\varphi_2}(\omega) + S_{\varphi_3}(\omega), \tag{11}$$

where $S_{\varphi_T}(\omega)$ is the intermodulation noise power density spectrum due to transmission deviations. We see from (11) that the second- and third-order noise contributions are additive on a power basis since they are not crosscorrelated. It can be shown that[1]

$$\begin{aligned} S_{\varphi_T}(\omega) = {} & 2 \mid H_1(\omega) \mid^2 \mathfrak{F}[R^2_{\varphi'}(\tau)] + 2 \mid H_2(\omega) \mid^2 \mathfrak{F}[R^2_{\varphi''}(\tau)] \\ & + 2[H_1(-\omega)H_2(\omega) + H_2(-\omega)H_1(\omega)]\mathfrak{F}[R^2_{\varphi'\varphi''}(\tau)] \\ & + 6 \mid H_3(\omega) \mid^2 \mathfrak{F}[R^3_{\varphi'}(\tau)], \end{aligned} \tag{12}$$

where $\mathfrak{F}$ denotes the Fourier Transform.

## III. AM/PM INTERMODULATION NOISE

We see in Fig. 1 that the output signal from the transmission medium is both envelope and phase modulated. If the transmission medium shown in Fig. 1 were followed by an AM/PM converter*, i.e., a device that converts envelope variations at its input to phase perturbations at its output, then the signal at the converter output will possess an added phase modulating distortion function along with that shown in Fig. 1. This situation is depicted in Fig. 3. The added

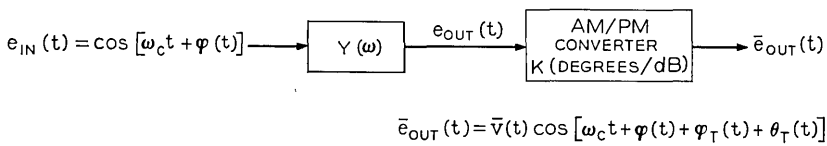


Fig. 3 — Generation of AM/PM intermodulation noise.

distortion term, $\theta_T(t)$, is similar in format to $\varphi_T(t)$ and analogously we will concentrate on the second- and third-order AM/PM intermodulation noise components. That is,

$$\theta_T(t) = \theta_2(t) + \theta_3(t), \tag{13}$$

where $\theta_2(t)$ and $\theta_3(t)$ are the second- and third-order AM/PM intermodulation noise components. These components were derived in Ref.

* The characterization of the AM/PM converter is discussed on pp. 1750-51 in Ref. 2.

2 and are given by

$$\theta_2(t) = k\left[-\frac{1}{2}\lambda_{2r} + \tfrac{1}{4}l_{2r}\frac{d}{dt} - \tfrac{1}{12}l_{3r}\frac{d^2}{dt^2}\right]\varphi'^2(t) + k[\tfrac{1}{24}l_{4r}]\varphi''^2(t) \tag{14}$$

$$\theta_3(t) = k\left[-\tfrac{1}{6}\lambda_{3i} + \tfrac{1}{12}l_{1i}\frac{d}{dt}\right]\varphi'^3(t), \tag{15}$$

where the $\lambda$ and $l$ coefficients can be determined from Ref. 2, and $k$ is the AM/PM conversion parameter which is defined as the phase modulation index in radians divided by the amplitude modulation index. Equations (13), (14), and (15) can be represented as shown in Fig. 4 where

$$G_1(\omega) = [k\tfrac{1}{12}l_{3r}\omega^2 - k\tfrac{1}{2}\lambda_{2r}] + i[k\tfrac{1}{4}l_{2r}\omega] \tag{16}$$

$$G_2(\omega) = k\tfrac{1}{24}l_{4r} \tag{17}$$

$$G_3(\omega) = [-k\tfrac{1}{6}\lambda_{3i}] + i[k\tfrac{1}{12}l_{1i}\omega]. \tag{18}$$

Since $\theta_2(t)$ and $\theta_3(t)$ are uncorrelated, we can write

$$R_{\theta_T}(\tau) = R_{\theta_2}(\tau) + R_{\theta_3}(\tau) \tag{19}$$

or

$$S_{\theta_T}(\omega) = S_{\theta_2}(\omega) + S_{\theta_3}(\omega), \tag{20}$$

where $S_{\theta_T}(\omega)$ is the AM/PM intermodulation noise power density spectrum. It can be shown that[2]

$$\begin{aligned} S_{\theta_T}(\omega) = {} & 2\,|\,G_1(\omega)\,|^2\,\mathfrak{F}[R^2_{\varphi'}(\tau)] + 2\,|\,G_2(\omega)\,|^2\,\mathfrak{F}[R^2_{\varphi''}(\tau)] \\ & + 2[G_1(-\omega)G_2(\omega) + G_2(-\omega)G_1(\omega)]\mathfrak{F}[R^2_{\varphi'\varphi''}(\tau)] \\ & + 6\,|\,G_3(\omega)\,|^2\,\mathfrak{F}[R^3_{\varphi'}(\tau)]. \end{aligned} \tag{21}$$

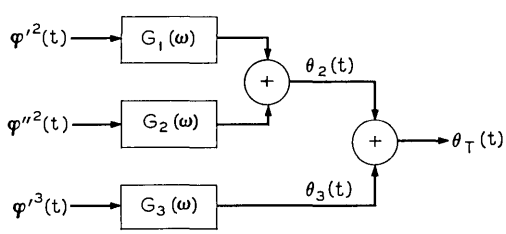


Fig. 4 — Block diagram of total AM/PM intermodulation noise.

## IV. POWER DENSITY SPECTRUM OF THE SUM OF TWO NOISE CONTRIBUTORS

The previous two sections presented basic system models which were used to describe the two noise sources under study. In this section, we will treat the more general case whereby the signal to be demodulated, after passing through a transmission system, will be given by

$$e(t) \propto \cos\,[\omega_c t + \varphi(t) + \underbrace{\varphi_T(t) + \theta_T(t)}_{\text{composite distortion}}].$$

The power density spectrum for each noise contributor has been derived in Refs. 1 and 2, as previously discussed. However, adding these two spectra together on a power basis, i.e., assuming that they are uncorrelated, may yield a result which is grossly in error. In order to determine the degree to which $\varphi_T(t)$ and $\theta_T(t)$ are correlated, we must derive the crosscorrelation function and examine its effect.

To examine the effects of crosscorrelation we combine Figs. 2 and 4 as shown in Fig. 5. The autocorrelation function of the sum of the two noise contributors, $\varphi_T(t)$ and $\theta_T(t)$, is

$$\begin{aligned} R_{\varphi+\theta}(\tau) &= \overline{[\varphi_T(t) + \theta_T(t)][\varphi_T(t+\tau) + \theta_T(t+\tau)]} \\ &= R_{\varphi_T}(\tau) + R_{\theta_T}(\tau) + \overline{\theta_T(t)\varphi_T(t+\tau)} + \overline{\varphi_T(t)\theta_T(t+\tau)}. \end{aligned} \tag{22}$$

The first two terms are given by (10) and (19), respectively. Sub-

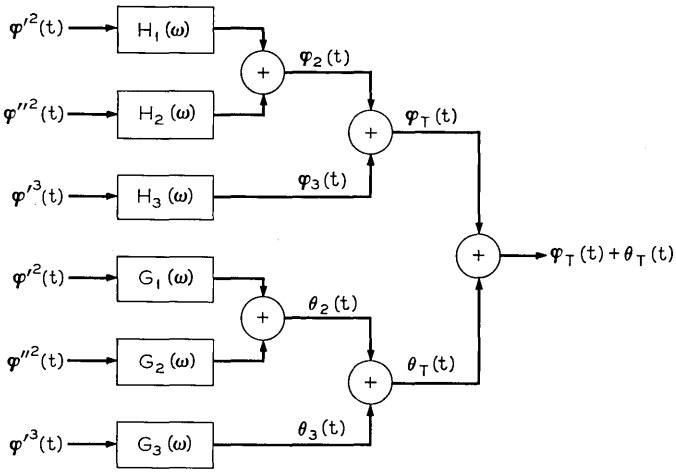


Fig. 5 — Block diagram of composite intermodulation noise.

stituting (2) and (13) into (22) gives

$$\begin{aligned} R_{\varphi+\theta}(\tau) = R_{\varphi_T}(\tau) + R_{\theta_T}(\tau) + \overline{\theta_2(t)\varphi_2(t+\tau)} + \overline{\theta_3(t)\varphi_3(t+\tau)} \\ + \overline{\theta_2(t)\varphi_3(t+\tau)} + \overline{\theta_3(t)\varphi_2(t+\tau)} + \overline{\varphi_2(t)\theta_2(t+\tau)} \\ + \overline{\varphi_3(t)\theta_3(t+\tau)} + \overline{\varphi_2(t)\theta_3(t+\tau)} + \overline{\varphi_3(t)\theta_2(t+\tau)} \end{aligned} \tag{23}$$

which can be written

$$\begin{aligned} R_{\varphi+\theta}(\tau) = R_{\varphi_T}(\tau) + R_{\theta_T}(\tau) + R_{\theta_2\varphi_2}(\tau) + R_{\theta_3\varphi_3}(\tau) + R_{\theta_2\varphi_3}(\tau) \\ + R_{\theta_3\varphi_2}(\tau) + R_{\varphi_2\theta_2}(\tau) + R_{\varphi_3\theta_3}(\tau) + R_{\varphi_2\theta_3}(\tau) + R_{\varphi_3\theta_2}(\tau). \end{aligned} \tag{24}$$

Using the same approach as in the Appendix of Ref. 2, it can be shown that

$$R_{\theta_2\varphi_3}(\tau) = R_{\theta_3\varphi_2}(\tau) = R_{\varphi_2\theta_3}(\tau) = R_{\varphi_3\theta_2}(\tau) = 0 \tag{25}$$

so

$$\begin{aligned} R_{\varphi+\theta}(\tau) = R_{\varphi_T}(\tau) + R_{\theta_T}(\tau) + R_{\theta_2\varphi_2}(\tau) \\ + R_{\theta_3\varphi_3}(\tau) + R_{\varphi_2\theta_2}(\tau) + R_{\varphi_3\theta_3}(\tau). \end{aligned} \tag{26}$$

Hence,

$$\begin{aligned} S_{\varphi+\theta}(\omega) = S_{\varphi_T}(\omega) + S_{\theta_T}(\omega) + S_{\theta_2\varphi_2}(\omega) \\ + S_{\theta_3\varphi_3}(\omega) + S_{\varphi_2\theta_2}(\omega) + S_{\varphi_3\theta_3}(\omega). \end{aligned} \tag{27}$$

### 4.1 *Consideration of $S_{\theta_3\varphi_3}(\omega)$ and $S_{\varphi_3\theta_3}(\omega)$*

To examine $S_{\theta_3\varphi_3}(\omega)$, the cross-power density spectrum of $\theta_3(t)$ and $\varphi_3(t)$, we reduce Fig. 5 to the block diagram shown in Fig. 6. Using the relationship for the crosscorrelation of linearly transformed random functions, we have

$$S_{\theta_3\varphi_3}(\omega) = G_3(-\omega)H_3(\omega)S_{\varphi'^3}(\omega). \tag{28}$$

It can be shown that[1]

$$R_{\varphi'^3}(\tau) = 6R^3_{\varphi'}(\tau) + 9R^2_{\varphi'}(0)R_{\varphi'}(\tau). \tag{29}$$

The term $9R^2_{\varphi'}(0)\ R_{\varphi'}(\tau)$ is merely a scaled power density spectrum of the input baseband signal and hence can be neglected since it does not contribute to the intermodulation noise distortion. Therefore,

$$S_{\theta_3\varphi_3}(\omega) = 6G_3(-\omega)H_3(\omega)\mathfrak{F}[R^3_{\varphi'}(\tau)]. \tag{30}$$

By inspection, we can write

$$S_{\varphi_3\theta_3}(\omega) = 6H_3(-\omega)G_3(\omega)\mathfrak{F}[R^3_{\varphi'}(\tau)]. \tag{31}$$

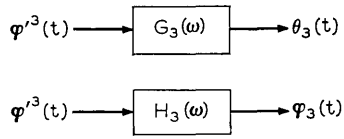


Fig. 6 — Third-order noise correlation.

4.2 *Consideration of* $S_{\theta_2\varphi_2}(\omega)$ *and* $S_{\varphi_2\theta_2}(\omega)$

To examine $S_{\theta_2\varphi_2}(\omega)$, we reduce Fig. 5 to the block diagram shown in Fig. 7. Now

$$\begin{aligned} R_{\theta_2\varphi_2}(\tau) &= \overline{\theta_2(t)\varphi_2(t+\tau)} \\ &= \overline{[x(t)+y(t)][u(t+\tau)+v(t+\tau)]} \\ &= R_{xu}(\tau)+R_{yv}(\tau)+R_{xv}(\tau)+R_{yu}(\tau). \end{aligned} \tag{32}$$

Taking the Fourier Transform of (32) and referring to Fig. 7, we can directly write

$$\begin{aligned} S_{\theta_2\varphi_2}(\omega) &= G_1(-\omega)H_1(\omega)S_{\varphi'^2}(\omega) + G_2(-\omega)H_2(\omega)S_{\varphi''^2}(\omega) \\ &\quad + G_1(-\omega)H_2(\omega)S_{\varphi'^2\varphi''^2}(\omega) + G_2(-\omega)H_1(\omega)S_{\varphi''^2\varphi'^2}(\omega). \end{aligned} \tag{33}$$

Now it can be shown that[1,2]

$$S_{\varphi'^2}(\omega) = 2\mathfrak{F}[R^2_{\varphi'}(\tau)] \tag{34}$$

$$S_{\varphi''^2}(\omega) = 2\mathfrak{F}[R^2_{\varphi''}(\tau)] \tag{35}$$

$$S_{\varphi'^2\varphi''^2}(\omega) = 2\mathfrak{F}[R^2_{\varphi'\varphi''}(\tau)] = S_{\varphi''^2\varphi'^2}(\omega) \tag{36}$$

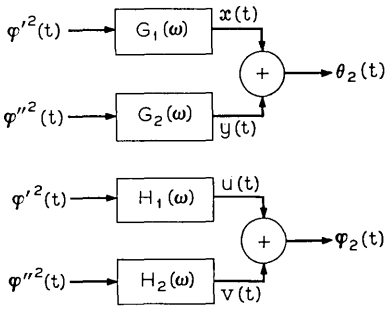


Fig. 7 — Second-order noise correlation.

neglecting the dc components. Hence,

$$S_{\theta_2\varphi_2}(\omega) = 2G_1(-\omega)H_1(\omega)\mathfrak{F}[R^2_{\varphi'}(\tau)] + 2G_2(-\omega)H_2(\omega)\mathfrak{F}[R^2_{\varphi''}(\tau)] + 2[G_1(-\omega)H_2(\omega) + G_2(-\omega)H_1(\omega)]\mathfrak{F}[R^2_{\varphi'\varphi''}(\tau)]. \quad (37)$$

Similarly,

$$S_{\varphi_2\theta_2}(\omega) = 2H_1(-\omega)G_1(\omega)\mathfrak{F}[R^2_{\varphi'}(\tau)] + 2H_2(-\omega)G_2(\omega)\mathfrak{F}[R^2_{\varphi''}(\tau)] + 2[H_2(-\omega)G_1(\omega) + H_1(-\omega)G_2(\omega)]\mathfrak{F}[R^2_{\varphi'\varphi''}(\tau)]. \quad (38)$$

Substituting (12), (21), (30), (31), (37), and (38) in (27) gives

$$\begin{aligned} S_{\varphi+\theta}(\omega) &= 2\{|H_1(\omega)|^2 + |G_1(\omega)|^2 \\ &+ G_1(-\omega)H_1(\omega) + H_1(-\omega)G_1(\omega)\}\mathfrak{F}[R^2_{\varphi'}(\tau)] \\ &+ 2\{|H_2(\omega)|^2 + |G_2(\omega)|^2 + G_2(-\omega)H_2(\omega) + H_2(-\omega)G_2(\omega)\}\mathfrak{F}[R^2_{\varphi''}(\tau)] \\ &+ 2\{H_1(-\omega)H_2(\omega) + H_2(-\omega)H_1(\omega) + G_1(-\omega)G_2(\omega) + G_2(-\omega)G_1(\omega) \\ &+ G_1(-\omega)H_2(\omega) + G_2(-\omega)H_1(\omega) + H_2(-\omega)G_1(\omega) \\ &+ H_1(-\omega)G_2(\omega)\}\mathfrak{F}[R^2_{\varphi'\varphi''}(\tau)] + 6\{|H_3(\omega)|^2 + |G_3(\omega)|^2 \\ &+ G_3(-\omega)H_3(\omega) + H_3(-\omega)G_3(\omega)\}\mathfrak{F}[R^3_{\varphi'}(\tau)]. \end{aligned} \quad (39)$$

This expression, (39), gives the baseband power density spectrum for the sum of two intermodulation noise sources: (*i*) intermodulation noise due to transmission deviations, and (*ii*) AM/PM intermodulation noise. The effect of the crosscorrelation relationship shows up as cross products of the defining transfer functions for each noise source as would be expected. The second and third order distortions of the summed noise spectra are additive as was the case for the two individual noise contributors.

### 4.3 *Signal-To-Noise Ratio*

The signal characterization is the same as in Refs. 1 and 2, or

$$S_{\varphi'}(\omega) = P_0[a_0 + a_2f^2 + a_4f^4 + a_6f^6], \qquad |f| \leqq f_b \quad (40)$$

= pre-emphasized multichannel baseband signal power density spectrum at the input to an FM modulator.

The constant $P_0$ is given by

$$P_0 = \frac{(2\pi\sigma)^2}{2f_b\left(a_0 + \frac{a_2f_b^2}{3} + \frac{a_4f_b^4}{5} + \frac{a_6f_b^6}{7}\right)} \text{ (rad/sec)}^2/\text{Hz}, \quad (41)$$

where $\sigma$ = rms frequency deviation, in Hertz, due to the multichannel baseband signal; the $a$'s are the pre-emphasis coefficients; and $f_b$ is the top baseband frequency, in Hertz. Hence, the signal-to-noise ratio is

$$10 \log \frac{S_{\varphi'}(\omega)}{\omega^2 S_{\varphi+\theta}(\omega)}, \tag{42}$$

where the signal and noise are defined by (40) and (39), respectively.

## V. SOME BASIC TRENDS

The power density spectrum for the correlated sum given by (39) does not readily lend itself to any generalized remarks as to the conditions under which correlation exists and to what degree. In order to derive some useful information on the subject, (39) was programmed on a digital computer. The computer input consisted of the fundamental system parameters, e.g., peak frequency deviation, number of message channels in the baseband, etc., as well as the transmission deviation values to be used for "AM/PM intermodulation noise" and those to be used for "intermodulation noise due to transmission deviations. Note that the transmission medium may be different for the two cases. For example, we could have the case where the "AM/PM intermodulation noise" is created by a quartic gain transmission deviation prior to an AM/PM converter, and the "intermodulation noise due to transmission deviations" is caused by a linear delay distortion. The transmission functions for the two cases would be

$$Y_I(\omega + \omega_c) = \exp ib_2\omega^2, \qquad Y_{\mathrm{AM/PM}}(\omega + \omega_c) = 1 + g_4\omega^4. \tag{43}$$

As a clarifying point, it should be remembered that the AM/PM theory of Ref. 2, and associated computer program, are set up so that we only obtain the "AM/PM intermodulation noise" due to quartic gain, and not the "intermodulation noise due to transmission deviations" caused by a quartic gain transmission deviation.

Both of the noise sources discussed in Sections II and III have transfer functions associated of the basic form given in (1). Each transfer function can have seven transmission deviations, so the problem of permuting all possible combinations to see which are correlated becomes unreasonably cumbersome. However, a potentially useful test is to evaluate the correlation between $\varphi_T(t)$ and $\theta_T(t)$ when $Y_I(\omega)$ and $Y_{\mathrm{AM/PM}}(\omega)$ each have only one transmission deviation for each computer run. There are 49 possible combinations, one of which is given

by (43). Any results one obtains will depend on the inputs used, and because of the format of (39), one cannot make one run using normalized results and then scale all future runs according to some predetermined rules. For that reason, the results to be given can only be used to indicate trends.

The 49 runs previously mentioned yielded eight significantly correlated combinations. The evaluation of the results was made by adding the individual power density spectra $S_{\varphi_T}(\omega)$ and $S_{\theta_T}(\omega)$ on a power basis and comparing the results with those obtained from $S_{\varphi+\theta}(\omega)$, i.e., the power density for the correlated sum. Only top channel noise was used in the comparison. A combination was considered to be significantly correlated when the power sum and correlated sum differed by more than a few tenths of a dB. The amount that they differed depended on the inputs, but for the values used,* some cases had the correlated sum up to 3 dB *above* the power sum, in the top channel, and some combinations caused the correlated sum to be as much as 15 dB *below* the power sum, in the top channel.

The eight significantly correlated combinations are shown in Table I.

TABLE I—CORRELATED COMBINATIONS

| | Transmission deviation in | | Conditions under which the correlated sum is higher than the power sum (assuming $k$ is positive) |
|---|---|---|---|
| | $Y_I(\omega)$ | $Y_{AM/PM}(\omega)$ | |
| 1. | $g_3$ | $b_3$ | $g_3$ or $b_3$ is negative |
| 2. | $b_2$ | $g_1$ | $b_2$ is negative |
| 3. | $b_2$ | $g_2$ | $b_2$ and $g_2$ positive *or* $b_2$ and $g_2$ negative |
| 4. | $b_2$ | $g_4$ | $b_2$ and $g_4$ positive *or* $b_2$ and $g_4$ negative |
| 5. | $b_3$ | $g_3$ | $b_3$ and $g_3$ positive *or* $b_3$ and $g_3$ negative |
| 6. | $b_4$ | $g_1$ | $b_4$ is negative |
| 7. | $b_4$ | $g_2$ | $b_4$ and $g_2$ positive *or* $b_4$ and $g_2$ negative |
| 8. | $b_4$ | $g_4$ | $b_4$ and $g_4$ positive *or* $b_4$ and $g_4$ negative |

We see from Table I that the sign of the transmission deviations determine if the correlation is positive or negative, i.e., whether the

* Same values as those used in Section 3.2.2 of Ref. 2: all gain transmission deviations have 1 dB distortion, relative to the carrier, at 10 MHz away from the carrier; all delay transmission deviations have 1 nanosecond distortion, relative to the carrier, a 10 MHz away from the carrier.

actual noise power is larger or smaller than the power one would obtain from power addition of the two individual contributors. Also, we see that all eight cases have the same format, i.e., if one transfer function has a delay transmission deviation, the other transfer function has a gain transmission deviation and vice versa.

Referring back to (39), we see that all of the correlation terms have the same format, i.e., a $G_i(\pm\omega)H_j(\pm\omega)$ product. Since these terms have $k$ as a component, the sign of $k$ will play a role in determining if we have positive or negative correlation.

The results of Table I give us an idea of when to expect significant correlation, that is, when power addition should not be used. These results should prove useful for the more complex problems which are confronted in practice.

## VI. SYSTEM EXAMPLE

In Section 3.3.4 of Ref. 2, a representative FM radio relay system's repeater characteristics were used in deriving the noise responses shown in Fig. 11 of Ref. 2 and reproduced here as Fig. 8. The radio system carried 1200 message channels, had a peak frequency deviation of 4 MHz and a top baseband frequency of 5.772 MHz, and had an rms frequency deviation of 0.771 MHz. The system was pre-emphasized by the function shown in Fig. 5 of Ref. 2. The basic repeater was

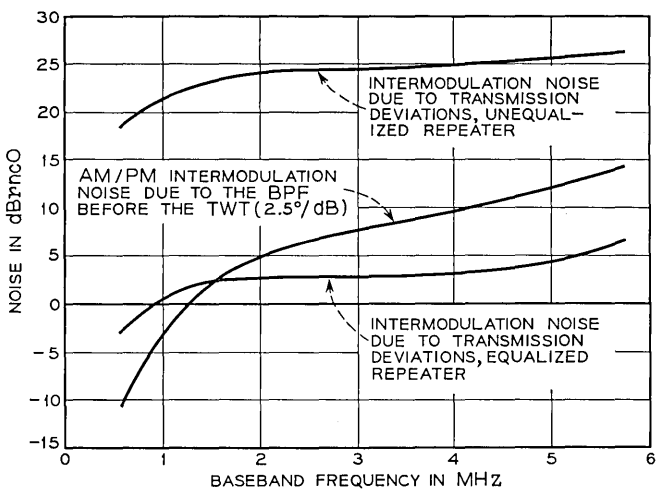


Fig. 8 — Representative radio system noise responses.

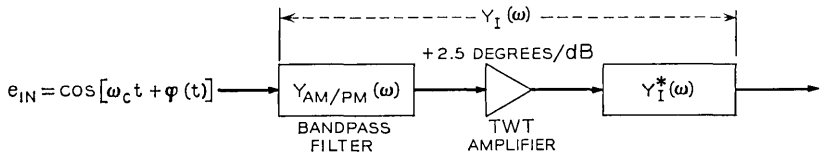


Fig. 9 — Repeater model.

gain and delay equalized and, from an analytical point of view, could be represented as shown in Fig. 9. The transmission characteristics for the equalized repeater, $Y_I(\omega)$, and for the bandpass filter, $Y_{AM/PM}(\omega)$, are shown in Fig. 10 of Ref. 2 and reproduced here as Fig. 10. The associated least squares fitted transmission deviations are as follows

| Transmission deviations | $Y_I(\omega + \omega_c)$ | $Y_{AM/PM}(\omega + \omega_c)$ |
|---|---|---|
| $g_1$ | $-9.67 \times 10^{-11}$ | $3.81 \times 10^{-11}$ |
| $g_2$ | $7.09 \times 10^{-18}$ | $9.17 \times 10^{-19}$ |
| $g_3$ | $1.17 \times 10^{-25}$ | $9.04 \times 10^{-27}$ |
| $g_4$ | $-2.57 \times 10^{-33}$ | $-1.97 \times 10^{-33}$ |
| $b_2$ | $6.50 \times 10^{-18}$ | $-4.82 \times 10^{-18}$ |
| $b_3$ | $5.58 \times 10^{-26}$ | $8.09 \times 10^{-25}$ |
| $b_4$ | $-3.16 \times 10^{-33}$ | $-3.35 \times 10^{-34}$ |

The power sum of the AM/PM intermodulation noise and the intermodulation noise due to the equalized repeater's transmission deviations (both are shown in Fig. 8) is shown in Fig. 11. Also shown is the power density spectrum which includes the effects of correlation between the two contributors. We see for this example that the actual noise is 4.5 dB *lower* in the top channel than that obtained from power addition alone.

Another interesting result is the curve shown in Fig. 12. This figure shows how the sign and magnitude of the AM/PM conversion factor can affect the noise response of a given system.

In Table I, eight correlated combinations were given. Of these eight possibilities, the first combination is probably responsible for the correlated sum being smaller than the power sum as shown in Fig. 11. There are three reasons for this observation: (*i*) the parabolic delay in $Y_{AM/PM}(\omega)$ is quite large, and the cubic gain in $Y_I(\omega)$ is a significant

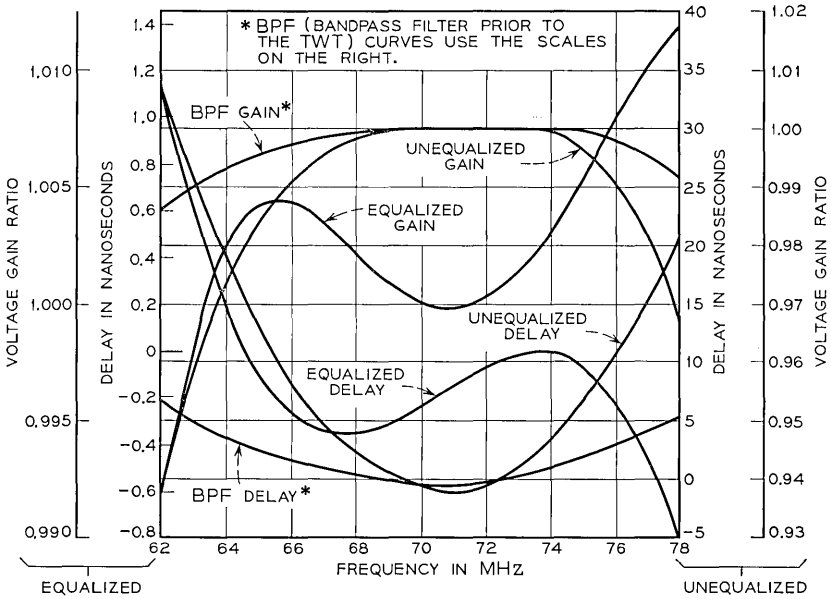


Fig. 10 — Gain and delay characteristics.

part of the equalized repeater gain shape; (*ii*) this combination causes negative correlation when the transmission deviations are both positive and the AM/PM conversion factor is positive; and (*iii*) a negative value for $K$ causes positive correlation,* for this combination, which is consistent with the results shown in Fig. 12. Hence, the trends given in Table I can be useful for more complicated problems and may serve as a tool for optimizing a system's noise performance.

## VII. CONCLUSIONS

In this paper, we have studied the correlation which exists between two noise contributors in FM systems: (*i*) intermodulation noise due to transmission deviations, and (*ii*) AM/PM intermodulation noise. The first contributor is generated when an FM signal is passed through a linear transmission medium which has transmission deviations. We denoted this medium by $Y_I(\omega)$. The second contributor is generated when an FM signal is passed through a similar medium, denoted by $Y_{\mathrm{AM/PM}}(\omega)$, which is followed by an AM/PM conversion device. These

* When the transmission deviations are both positive.

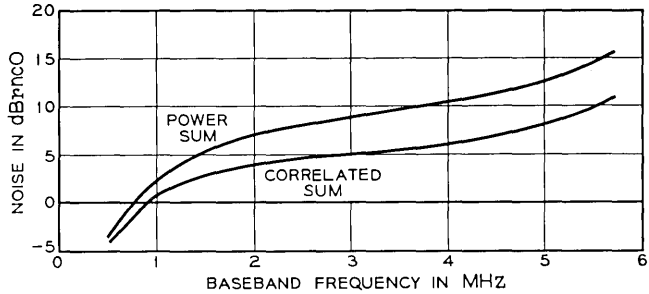


Fig. 11 — Comparison of power sum and correlated sum for a representative radio system.

two media may or may not possess the same transmission deviations in practice.

Even though these two contributors are different, they do possess the same property of being a function of the baseband signal. Therefore, one would expect that they would be correlated to some degree. This would mean that combining the two noise power density spectra assuming random addition (uncorrelated random variables), i.e., power addition, might not be sufficient in general.

To study the amount and character of this correlation, the power density spectrum was derived for the sum of the two noise contributors. The resulting equation was programmed on a digital computer and evaluated. Because of the format of the equation, no generalized results could be obtained. However, it was found that certain conditions exist under which the correlation can be significant. These conditions, even though not all engrossing, should prove useful in the complex problems which occur in practice.

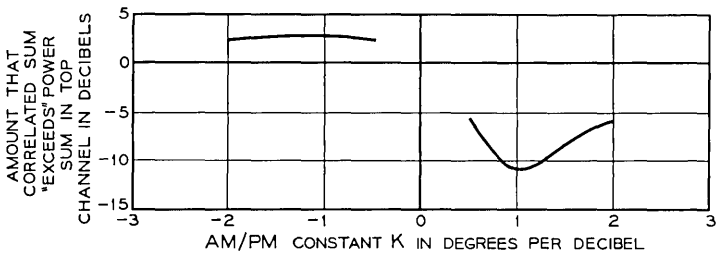


Fig. 12 — Affect of sign and magnitude of AM/PM constant on correlated sum for a representative radio system.

A representative FM radio relay system was examined, and it was found that the power density spectrum for the correlated sum of the two noise contributors was substantially different than the power addition of the individual noise spectra. In the top channel, the correlated noise power was about 4.5 dB lower than the noise resulting from a power sum.

It was also shown that a simple change in sign of the AM/PM conversion factor $k$, or certain transmission deviations, can cause the correlated noise to be substantially higher or lower than the power sum of the individual spectra.

## VIII. ACKNOWLEDGMENT

The author wishes to once again express his deep gratitude to Miss J. D. Witkowski, of Bell Telephone Laboratories, for programming the correlation noise equation on a digital computer, and also to thank those responsible for providing the motivation and priority for the work contained herein.

## REFERENCES

1. Liou, M. L., Noise in an FM System Due to an Imperfect Linear Transducer, B.S.T.J., *45,* November, 1966, pp. 1537–1561.
2. Cross, T. G., Intermodulation Noise in FM Systems Due to Transmission Deviations and AM/PM Conversion, B. S. T. J., *45,* December, 1966, pp. 1749–1773.

# Phase Progression in Conical Waveguides

By ELLIOTT R. NAGELBERG

(Manuscript received August 10, 1967)

*We studied the phase progression properties of normal modes in a conical waveguide in order to develop techniques for analysis of multimode microwave antennas. We found that the large-order asymptotic expansions of Bessel functions developed by F. W. J. Olver are most appropriate for such calculations by virtue of their simplicity and uniformity with respect to argument. These expansions are applied to analysis of the conical $TE_{11}$ and conical $TM_{11}$ modes and, in addition, to an examination of the "quasi-cylindrical approximation" in which the conical waveguide is regarded as a cylindrical waveguide with gradually changing cross section.*

## I. INTRODUCTION

For most applications to microwave communication systems, waveguides are designed in such a way that only the dominant mode can propagate. This has been the case principally for practical reasons, as evidenced for example by problems encountered in the development of millimeter-wave systems using the higher-order $TE_{01}^{\circ}$ mode.[1] Since the waveguide in this case must be oversized, small geometrical asymmetries due to errors in fabrication, bends, and other structural perturbations cause coupling to unwanted modes, which can result in a significant degradation in performance.

On the other hand, there has been considerable interest during the past several years in techniques which require the controlled excitation of higher-order modes combined with the dominant mode in, for example, a conical waveguide. Two such applications have been the $TE_{11}^{<} - TM_{01}^{<}$* precision autotrack system for the *Telstar*® satellite,[2] and the $TE_{11}^{<} - TM_{11}^{<}$ dual mode conical horn[3] which has been suggested as a primary feed configuration for low-noise satellite communication antennas.

* The notation $TE_{mn}^{<}$ or $TM_{mn}^{<}$ will be used to designate conical waveguide modes.

A common feature of these techniques is the necessity for maintaining a high degree of phase coherence among the various modes of propagation. It is therefore required, in order to design such systems and predict the effects of frequency, temperature and structural variations, to accurately determine the phase progression properties of the guided wave fields.

The paper's contents may be summarized as follows: We first describe the conical waveguide modes, which are vector eigenfunctions of Maxwell's equations in what is essentially spherical geometry. We note that although these solutions are well known in principle, the actual computation of their phase progression properties is not straightforward. It is, therefore, necessary to consider the problem of numerically evaluating both the eigenvalues and vector eigenfunctions so that we can apply these results to actual antenna problems. In order to do this we utilize certain uniform asymptotic expansions due to F. W. J. Olver[4] which are found to be well suited to such calculations. We thereby observe that a very common method of determining phase progression, which might be termed the quasi-cylindrical approximation, is not particularly accurate, and the errors associated with this method are evaluated.

Rationalized MKS units and the (suppressed) harmonic time dependence $e^{-i\omega t}$ will be used throughout.

## II. MODES IN A CONICAL WAVEGUIDE

The normal modes characteristic of a conical waveguide are derived in the usual manner by finding separable solutions to Maxwell's equations in spherical coordinates, subject to the boundary condition that the components of electric field tangent to the lateral surface must vanish. The solutions thus derived may be partitioned into two types, $\mathrm{TE}^<$ modes for which the electric field is transverse to the direction of propagation (the $r$-direction), and $\mathrm{TM}^<$ modes for which the magnetic field is transverse to the direction of propagation. In terms of the coordinate system shown in Fig. 1, the components of electric field, for example, are given by,[5]

$\mathrm{TM}^<$

$$E_r^{\mathrm{TM}} = A \frac{\mu(\mu+1)}{(kr)^{\frac{3}{2}}} H_{\mu+\frac{1}{2}}^{(1)}(kr) P_\mu^m(\cos\theta) e^{im\varphi}$$

$$E_\theta^{\mathrm{TM}} = \frac{A}{kr} \frac{d}{d(kr)} [\sqrt{kr}\, H_{\mu+\frac{1}{2}}^{(1)}(kr)] \frac{d}{d\theta} P_\mu^m(\cos\theta) e^{im\varphi} \tag{1}$$

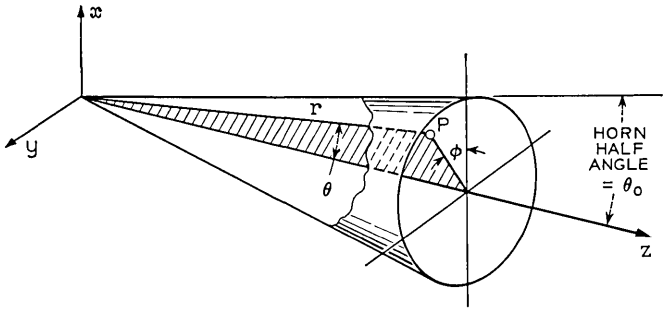


Fig. 1 — Conical horn geometry.

$$E_\varphi^{\mathrm{TM}} = \frac{imA}{kr \sin\theta} \frac{d}{d(kr)} [\sqrt{kr}\, H_{\mu+\frac{1}{2}}^{(1)}(kr)] P_\mu^m(\cos\theta) e^{im\varphi},$$

TE<

$$E_r^{\mathrm{TE}} = 0$$

$$E_\theta^{\mathrm{TE}} = \frac{mB}{\sin\theta\sqrt{kr}} H_{\nu+\frac{1}{2}}^{(1)}(kr) P_\nu^m(\cos\theta) e^{im\varphi} \tag{2}$$

$$E_\varphi^{\mathrm{TE}} = \frac{iB}{\sqrt{kr}} H_{\nu+\frac{1}{2}}^{(1)}(kr) \frac{d}{d\theta} [P_\nu^m(\cos\theta)] e^{im\varphi}.$$

In (1) and (2), $P_\nu^m$ $(\cos\theta)$ denotes the associated Legendre function ($m$ = integer) and $H_\nu^{(1)}(x)$ represents the Hankel function of the first kind, corresponding to outgoing waves under the assumed time dependence $e^{-i\omega t}$. The constant $k$ is the free-space wave number.

The eigenvalues $\nu$ and $\mu$ are found as solutions of the respective characteristic equations

$$\left[\frac{d}{d\theta} P_\nu^m(\cos\theta)\right]_{\theta=\theta_0} = 0 \tag{3}$$

$$P_\mu^m(\cos\theta_0) = 0 \tag{4}$$

for a specified horn half angle $\theta_0$.

These eigenvalues can be computed by a variety of numerical methods. For example, one can represent the associated Legendre function in terms of the hypergeometric function[6] as

$$P_\nu^m(\cos\theta) = C \sin^{m/2}\theta\, F\left(1 + m + \nu,\ m - \nu;\ m + 1;\ \frac{1 - \cos\theta}{2}\right), \tag{5}$$

where $C$ is a constant. The $\nu$- or $\mu$-zeros for a given $\theta_0$ can then be found by a variety of root finding techniques. It is, however, worth noting that a first-order approximation may be determined from the formula

$$P_\nu^m(\cos\theta) \approx J_m(\sqrt{\nu(\nu+1)}\,\theta) + \mathcal{O}(\theta^2), \tag{6}$$

where $J_m$ denotes a Bessel function. Since the roots of Bessel functions are well tabulated,[7] (6) can be conveniently used to provide either an estimate of the eigenvalue or a starting value for an iterative algorithm. The phase errors associated with this approximation will be discussed in a later section.

To indicate the behavior of the zeros and to provide helpful information for design of dual mode conical horns, a partial list of $\nu$ and $\mu$ values, computed using (5), has been prepared and is given in the Appendix.

## III. BEHAVIOR OF THE RADIAL FUNCTIONS. PRECISE CALCULATION OF PHASE PROGRESSION.

Having obtained the appropriate eigenvalues as defined by (3) and (4), we may then proceed to the more interesting calculation of the radial dependence. In principle, the phase shift between the two spherical surfaces $r = r_1$ and $r = r_2$ is given by

$$\delta\alpha^{\mathrm{TE}} = \arg\,[H_{\nu+\frac{1}{2}}^{(1)}(kr_2)] - \arg\,[H_{\nu+\frac{1}{2}}^{(1)}(kr_1)] \tag{7}$$

$$\delta\alpha^{\mathrm{TM}} = \arg\left\{\frac{d}{dx}\,[\sqrt{x}\,H_{\mu+\frac{1}{2}}^{(1)}(x)]\right\}_{x=kr_2} - \arg\left\{\frac{d}{dx}\,[\sqrt{x}\,H_{\mu+\frac{1}{2}}^{(1)}(x)]\right\}_{x=kr_1} \tag{8}$$

for the TE and TM modes, respectively, where arg ( ) denotes the phase angle associated with a complex number.

The difficulty which arises when one attempts to utilize these expressions is essentially one of computation, due to the particular regime of order and argument frequently encountered in analysis of conical horn waveguides. We are particularly concerned here with the so-called transition region where the argument and order of the Hankel functions are large and comparable. For example, when $\theta_0 = 5°$, $\nu = 20.6155$ and $\mu = 43.4109$ (see Appendix), which means that we must allow for a range of arguments increasing from these values.

Asymptotic formulas for Bessel functions have, of course, been

studied in great detail. Asymptotic *forms* in the transition region $kr \gtrsim \nu$ have been given, for example, by Watson and Langer.[8] Although of mathematical interest, these typically give only the limiting behavior of the function, with the remainder specified within some order. However, engineering design generally requires more precise results, which can be obtained only with the aid of complete asymptotic expansions.

Expansions particularly appropriate for our problem have been given by Olver.[4] These formulas represent the Bessel functions as asymptotic series in terms of reciprocal powers of the order, and are valid asymptotic expansions for all values of argument. Although their derivation is very complicated, and will not be discussed here, we shall state the general form of the result and indicate several simplifications which are valid for most problems involving phase progression in conical horns.

The complete asymptotic expansion for the Hankel function of the first kind, following Olver's notation, is given by

$$H_\nu^{(1)}(\nu x) \approx \left(\frac{4\zeta}{1-x^2}\right)^{\frac{1}{4}} \left\{ \frac{Ai(\nu^{\frac{2}{3}}\zeta) - iBi(\nu^{\frac{2}{3}}\zeta)}{\nu^{\frac{1}{3}}} \cdot \sum_{n=0}^{\infty} \frac{A_n(\zeta)}{\nu^{2n}} + \frac{Ai'(\nu^{\frac{2}{3}}\zeta) - iBi'(\nu^{\frac{2}{3}}\zeta)}{\nu^{5/3}} \sum_{n=0}^{\infty} \frac{B_n(\zeta)}{\nu^{2n}} \right\}. \tag{9}$$

In this expression, $Ai$, $Ai'$, $Bi$, and $Bi'$ represent Airy functions and their derivatives,[9] and $\zeta$ is a constant related to $x$ by the formula

$$\zeta = -\{\tfrac{3}{2}(x^2-1)^{\frac{1}{2}} - \tfrac{3}{2}\sec^{-1} x\}^{\frac{2}{3}}. \tag{10}$$

The coefficients $A_n(\zeta)$ and $B_n(\zeta)$ are determined through an auxiliary sequence $\{U_n(t)\}$ defined by the recursion formula

$$\begin{aligned} U_0(t) &= 1 \\ U_n(t) &= \frac{t^2(1-t^2)}{2} U'_{n-1}(t) + \frac{1}{8}\int_0^t (1-5t^2)U_{n-1}(t)\,dt, \end{aligned} \tag{11}$$

where the prime denotes differentation. The $A_n$ and $B_n$ can then be found using the relations

$$A_n(\zeta) = \sum_{m=0}^{2n} \frac{b_m U_{2n-m}(\tau)}{\zeta^{3m/2}} \tag{12}$$

$$B_n(\zeta) = -\sum_{m=0}^{2n+1} \frac{a_m U_{2n-m+1}(\tau)}{\zeta^{(3m+1)/2}}, \tag{13}$$

where $\tau = (1-x^2)^{-\frac{1}{2}}$ and $\{a_m\}$, $\{b_m\}$ are given by

$$a_0 = b_0 = 1 \tag{14}$$

$$a_m(m > 0) = \frac{(2m+1)(2m+3)\cdots(6m-1)}{m!\,(144)^m} \tag{15}$$

$$b_m(m > 0) = -\frac{6m+1}{6m-1}\,a_m\,. \tag{16}$$

Since for the range $x > 1$, which is of interest here, $\zeta$ is negative and $\tau$ is imaginary, it is also necessary to define the proper branches, which are as follows:

$$\tau = i(x^2 - 1)^{-\frac{1}{2}} \tag{17}$$

$$\frac{1}{\zeta^{\frac{1}{2}}} = \frac{i}{(-\zeta)^{\frac{1}{2}}} \tag{18}$$

$$\frac{1}{\zeta^{3m/2}} = \frac{i^{3m}}{(-\zeta)^{3m/2}}. \tag{19}$$

Using a table of Airy Integrals,[9] one can proceed to evaluate the required Hankel functions to whatever accuracy is needed. As an indication of the number of terms required in a typical calculation, it has been observed by J. A. Cochran and C. M. Nagel* that for $\nu \gtrsim 10$, four decimal place accuracy can be obtained simply by using terms including $B_0$ and $A_1$. The coefficients required for most horn calculations are thus given by

$$A_0 = 1 \tag{20}$$

$$A_1 = -\frac{81\tau_1^2 + 462\tau_1^4 + 385\tau_1^6}{1152} - \frac{7(3\tau_1 + 5\tau_1^3)}{1152\zeta_1^{\frac{3}{2}}} + \frac{455}{4608\zeta_1^3} \tag{21}$$

$$B_0 = \frac{3\tau_1 + 5\tau_1^3}{24\zeta_1^{\frac{1}{2}}} - \frac{5}{48\zeta_1^2}\,, \tag{22}$$

where $\tau_1 = (x^2 - 1)^{-\frac{1}{2}}$ and $\zeta_1 = -\zeta$.

## IV. APPLICATIONS

In this section we shall discuss several applications of the preceding results. After presenting examples of phase progression for different modes we consider the phase errors introduced by approximating the eigenvalues $\mu$ and $\nu$. Finally, we examine what might be called the

* Private communication.

"quasi-cylindrical approximation," in which phase progression is calculated by considering the horn to be a cylindrical waveguide with slowly varying cross section.

### 4.1 *Phase progression of the $TE_{11}^{<}$ and $TM_{11}^{<}$ modes. Effect of errors in $\nu$ and $\mu$.*

A qualitative understanding of the phase progression properties of conical waveguide modes can be achieved by regarding a horn as a cylindrical waveguide with gradually increasing cross section. Although such a model has limitations, which will be discussed later in Section 4.2, it correctly predicts the fact that the phase progression rates for both classes of modes begin at relatively low values and increase monotonically toward that corresponding to the far field of a spherical wave in free space. This limiting behavior is reached when the conditions $kr \gg \nu$ or $kr \gg \mu$ are satisfied, corresponding to conical TE or conical TM modes, respectively.

Fig. 2 shows, for example, a direct computation of the phase shift as a function of $kr_2 - kr_1$ for the conical $TE_{11}$ mode for half angles $\theta_0 = 3°, 10°$. The value $kr_1$ is in each case taken to be that corresponding to the cut-off cross section of a cylindrical waveguide, i.e.,

$$kr_1 = \frac{\zeta}{\sin \theta_0}, \tag{23}$$

where $\zeta \approx 1.84118$. Fig. 3 shows analogous results for the $TM_{11}^{<}$ mode,

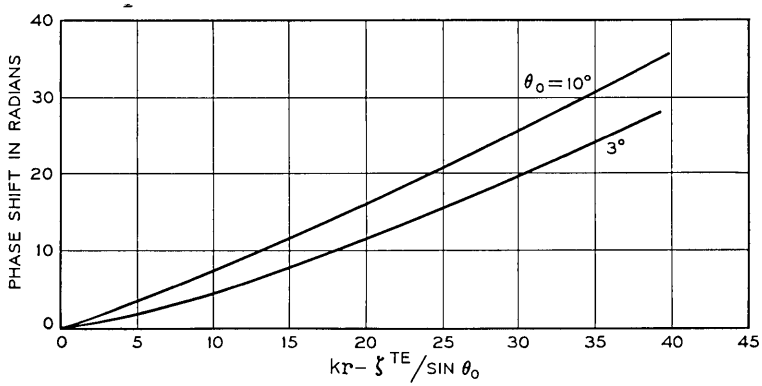


Fig. 2—Phase shift for the $TE_{11}^{<}$ mode relative to the cross section at which cut off would occur for a cylindrical waveguide. $\zeta_{TE} \approx 1.84118$.

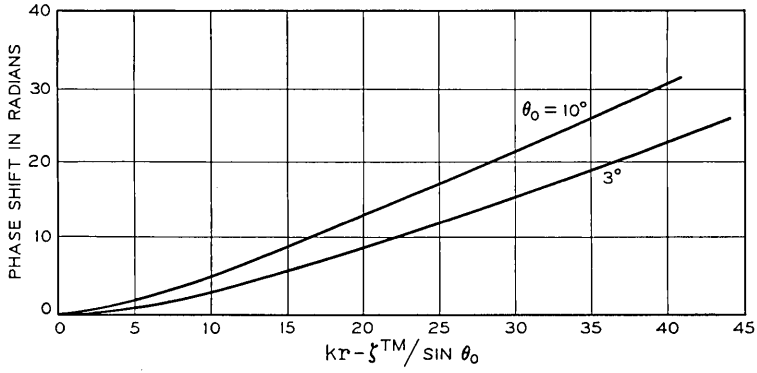


Fig. 3—Phase shift for the $TM_{11}^{<}$ mode relative to the cross section at which cut off would occur for a cylindrical waveguide. $\zeta_{TM} \approx 3.83171$.

the principal difference being in the more gradual increase in phase near $kr_1$.

In view of the difficulty in computing the $\nu$- and $\mu$-zeroes of the Legendre functions, as required by (3) and (4), it is of practical interest to determine how an error in the eigenvalue will effect the calculation of phase shift. If, for example, we denote by $\Delta^{TE}$ the *error in phase shift* due to a small error $\delta\nu$ in the eigenvalue, then from (7) we

TABLE I—MAXIMUM PHASE ERROR DUE TO 0.10 PERCENT MISCALCULATION OF $\nu$ OR $\mu$

$k(r_2 - r_1) = 100$

| | | $TE_{11}$ mode | |
|---|---|---|---|
| $\theta_0$ | $\delta\nu$ | $\Delta^{TE} = (\pi/2)\ \delta\nu$ | $\Delta^{TE}$ actual |
| 3° | 0.035 | 3.15° | 2.04° |
| 5° | 0.021 | 1.89° | 1.26° |
| 10° | 0.010 | 0.90° | 0.61° |

$TM_{11}$ mode

| $\theta_0$ | $\delta\mu$ | $\Delta^{TM} = (\pi/2)\ \delta\mu$ | $\Delta^{TM}$ actual |
|---|---|---|---|
| 3° | 0.073 | 6.87° | 4.68° |
| 5° | 0.043 | 3.87° | 3.14° |
| 10° | 0.021 | 1.89° | 1.16° |

have that

$$\Delta^{\mathrm{TE}} = \left\{\frac{\partial}{\partial\nu} \arg\,[H^{(1)}_{\nu+\frac{1}{2}}(kr_2)] - \frac{\partial}{\partial\nu} \arg\,[H^{(1)}_{\nu+\frac{1}{2}}(kr_1)]\right\}_{\nu=\nu_0} \cdot \delta\nu, \tag{24}$$

where $\nu_0$ denotes the correct eigenvalue. Although the calculation required by (24) is, in general, very difficult, it is relatively simple to obtain an upper bound to $\Delta^{\mathrm{TE}}$. First, it can be shown (see Ref. 7, p. 368), that at the cutoff radius $r_1$, the argument $kr_1$ is approximately equal to the eigenvalue $\nu$ (or $\mu$) and furthermore that the partial derivative at that value tends toward zero as $\nu$ or $\mu$ becomes very large. It follows that an upper bound on the error $\Delta^{\mathrm{TE}}$ can be obtained by neglecting the second term on the right side of (24) and letting $kr_2 \to \infty$. In this way we find, from the asymptotic behavior of the Hankel functions (see Ref. 6, p. 85), that

$$\max\,|\,\Delta^{\mathrm{TE}}\,| = |\,\delta\nu\,|\,\frac{\pi}{2} \tag{25}$$

and, in a similar way for $\Delta^{\mathrm{TM}}$,

$$\max\,|\,\Delta^{\mathrm{TM}}\,| = |\,\delta\mu\,|\,\frac{\pi}{2}. \tag{26}$$

In Table I we present a comparison between the actual computed error in differential phase shift, for an assumed relative 0.1 percent error in the eigenvalue, and the upper bound as determined by (25) and (26). The results indicate that the predicted estimates are quite reasonable. Note that the larger phase errors for smaller angles are due simply to the fact that the eigenvalue and hence the absolute error is greater.

The principal purpose of the previous exercise was to determine what error might be expected from using (6), which expresses the Legendre function in terms of a Bessel function. Results for the $\mathrm{TM}_{11}$ mode show that (6) is sufficiently accurate in predicting the $\mu$-zeroes that the maximum differential phase error for horns up to 30° in half angle should be less than 1°. As might be expected, however the same approximation applied to the $\nu$-zeroes of the derivative of the Legendre function is not as accurate. Nevertheless, as shown in Fig. 4, for a horn with half angle equal to 30° the maximum phase error is approximately 6°, which would ordinarily be acceptable.

### 4.2 *Evaluation of the Quasi-Cylindrical Approximation*

The difficulty of making precise calculations of phase progression in conical horns has led to the use of an approximate formula derived

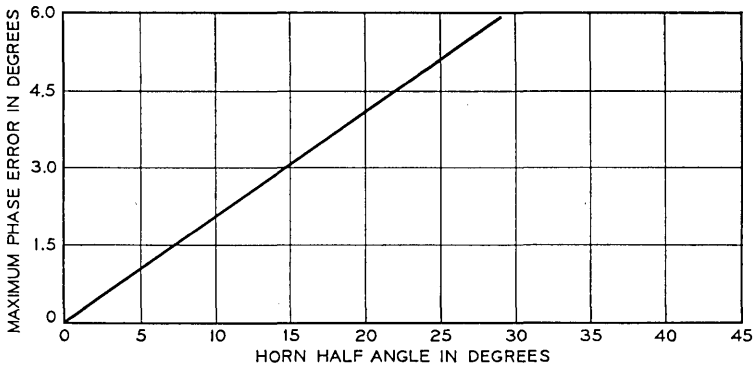


Fig. 4 — Maximum error in phase shift using Bessel approximation to the Legendre function.

by assuming that the horn behaves as a cylindrical waveguide with gradually increasing cross sectional radius. The phase shift is then determined simply by integrating the local waveguide propagation constant, with the result that

$$\delta\beta \approx \frac{1}{\tan\theta_0}\left[\sqrt{(kr\sin\theta_0)^2 - \zeta^2} - \zeta\cos^{-1}\frac{\zeta}{kr\sin\theta_0}\right]_{r_1}^{r_2}, \tag{26}$$

where $\zeta$ is the characteristic value for the particular mode (e.g., for the $TE_{11}^{\circ}$ mode $\zeta \approx 1.841$ and for the $TM_{11}^{\circ}$ mode $\zeta \approx 3.832$). This formula is, in fact, asymptotic to the true phase shift in certain limits. For example, let $(kr\sin\theta_0)$ be fixed and let $\theta_0 \to 0$. Then it can be shown that (26) becomes essentially equivalent to the simple Debye approximation. (See Ref. 7, p. 366.) However, this formula is known to be invalid in the range where order and argument are comparable. Nevertheless, it is useful to investigate the properties of (26) in order to determine what errors accompany its use.

Fig. 5 shows the resulting error in differential phase shift when the quasi-cylindrical approximation is applied to the $TE_{11}^{<}$ mode, with $kr_1 = \zeta/\sin\theta_0$ (corresponding to the cut-off diameter) and $\theta_0 = 5°$. The error is seen to grow very rapidly at first, showing that the quasi-uniform approximation predicts too slow an increase in propagation constant with increasing cross section. Eventually, the error curve approaches a linear variation. This asymptote can actually be predicted fairly well by using the large argument behavior of the Hankel function, combined with the fact that for large $\nu$ (see Ref. 7, p. 368),

$$\arg H_\nu^{(1)}(\nu) \approx -\pi/3. \tag{27}$$

By letting $kr \sin \theta_0 \to \infty$ in (26) and using (6), which relates $\zeta$ to $\nu$, we find that in the limit of large $kr$

$$\delta\alpha^{\mathrm{TE}} - \delta\beta^{\mathrm{TE}} \approx \frac{\pi}{12} - \zeta_{\mathrm{TE}}\left(\frac{1}{\theta_0} - \frac{1}{\tan \theta_0}\right)\frac{\pi}{2} + \left(1 - \frac{\sin \theta_0}{\tan \theta_0}\right)kr \tag{28}$$

which, for small $\theta_0$ reduces to

$$\delta\alpha^{\mathrm{TE}} - \delta\beta^{\mathrm{TE}} \approx \frac{\pi}{12} - \frac{\zeta_{\mathrm{TE}}\pi}{6}\,\theta_0 + \frac{\theta_0^2}{2}\,kr. \tag{29}$$

This result, shown in Fig. 5 as the dotted line, is seen to predict very accurately the asymptotic behavior of the error.

Fig. 6 shows the corresponding error for the $\mathrm{TM}_{11}^{<}$ mode. In contradistinction to the previous example, the quasi-cylindrical approximation at first predicts too high a phase progression rate, but eventually also conforms to the linear error predicted by the last term of (28). The formula analogous to (29) is given by

$$\delta\alpha^{\mathrm{TM}} - \delta\beta^{\mathrm{TM}} = -\frac{\pi}{12} - \frac{\zeta_{\mathrm{TM}}\pi}{6}\,\theta_0 + \frac{\theta_0^2}{2}\,kr. \tag{30}$$

This result, shown in Fig. 6 as the dotted line, is also seen to correctly describe the asymptote.

A salient feature of these results is that the linear portion of these curves is quite independent of the type and order of the mode being

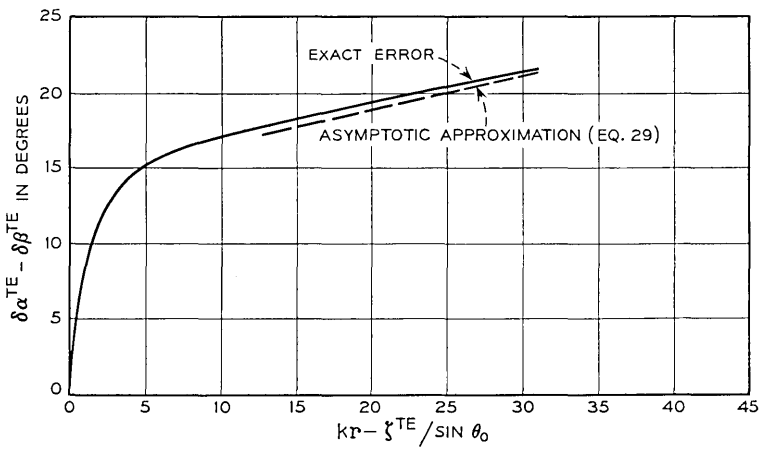


Fig. 5—Error in phase shift due to quasi-cylindrical approximation for the $\mathrm{TE}_{11}^{<}$ mode. $\zeta_{\mathrm{TE}} \approx 1.84118$.

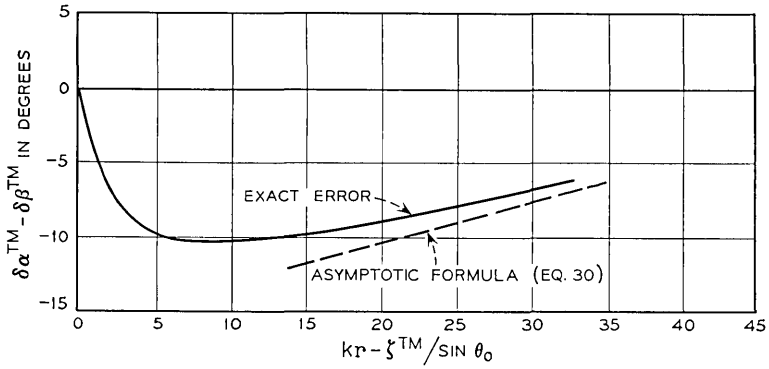


Fig. 6 — Error in phase shift due to quasi-cylindrical approximation for $TM_{11}^{<}$ mode. $\zeta_{TM} \approx 3.83171$.

considered. This immediately implies that the error in *differential phase shift between modes* resulting from the quasi-cylindrical approximation is *always bounded* at a value easily predicted by (29) and (30). This latter result is considered to be one of the more significant conclusions of this study.

## V. SUMMARY AND CONCLUSIONS

In this paper, we have considered the phase progression properties of conical waveguide modes. The principal difficulties have been in computing Bessel functions over their so-called transition region. It is suggested that, in view of the typically large orders involved, the asymptotic expansions due to Olver are the most applicable. An examination of the quasi-cylindrical approximation has shown that this latter formula, although not necessarily accurate for evaluating phase progression of a particular mode, can be used to determine differential phase shift between modes with an error which is bounded over the conical region.

## VI. ACNKOWLEDGMENTS

The author would like to thank Dr. J. Alan Cochran for helpful comments on the properties of Olver's expansions, and Miss Eileen Foley and Mr. C. M. Nagel, who were responsible for the computational aspects of this study.

APPENDIX

*Roots of* $P_\mu^1$ *(cos* $\theta$*)* $=$ 0 *and* $d/d\theta\ P_\nu^1$ *(cos* $\theta$*)* $=$ 0 *for a Given Value of* $\theta$

In order to assist in design of dual-mode conical horns, we have prepared an accurate table of the roots of the associated Legendre Function and its derivative for a given value of the horn half angle $\theta$. These values of $\nu$ and $\mu$ may then be used to evaluate the vector wave functions which characterize the propagation of the $TE_{11}^{<}$ and $TM_{11}^{<}$ modes in the horn section.

The computational program consisted of using the hypergeometric series representation for the Legendre function, and determining the zeroes by a standard root finding method. The program was terminated when the value of the function was less than $10^{-6}$ in amplitude.

TABLE II—ROOTS OF $P_\mu^1$ (COS $\theta$) = 0

| $\theta$ | $\mu$ | $\theta$ | $\mu$ |
|---|---|---|---|
| 3.00° | 72.6819 | 17.00° | 12.4239 |
| 3.50 | 62.3379 | 17.50 | 12.0552 |
| 4.00 | 54.3874 | 18.00 | 11.7070 |
| 4.50 | 48.2893 | 18.50 | 11.3777 |
| 5.00 | 43.4109 | 19.00 | 11.0657 |
| 5.50 | 39.4196 | 19.50 | 10.7697 |
| 6.00 | 36.0935 | 20.00 | 10.4885 |
| 6.50 | 33.2792 | 20.50 | 10.2211 |
| 7.00 | 30.8669 | 21.00 | 9.9664 |
| 7.50 | 28.7764 | 21.50 | 9.7235 |
| 8.00 | 26.9471 | 22.00 | 9.4918 |
| 8.50 | 25.3332 | 22.50 | 9.2703 |
| 9.00 | 23.8985 | 23.00 | 9.0585 |
| 9.50 | 22.6110 | 23.50 | 8.8557 |
| 10.00 | 21.4597 | 24.00 | 8.6613 |
| 10.50 | 20.4146 | 24.50 | 8.4749 |
| 11.00 | 19.4645 | 25.00 | 8.2960 |
| 11.50 | 18.5970 | 25.50 | 8.1241 |
| 12.00 | 17.8019 | 26.00 | 7.9589 |
| 12.50 | 17.0704 | 26.50 | 7.7998 |
| 13.00 | 16.3952 | 27.00 | 7.6467 |
| 13.50 | 15.7700 | 27.50 | 7.4992 |
| 14.00 | 15.1894 | 28.00 | 7.3570 |
| 14.50 | 14.6490 | 28.50 | 7.2197 |
| 15.00 | 14.1446 | 29.00 | 7.0871 |
| 15.50 | 13.6728 | 29.50 | 6.9591 |
| 16.00 | 13.2304 | 30.00 | 6.8354 |
| 16.50 | 12.8149 | | |

TABLE III—ROOTS OF $d/d\theta\ P_\nu^1\ (\cos\theta) = 0$

| $\theta$ | $\nu$ | $\theta$ | $\nu$ |
|---|---|---|---|
| 3.00 | 34.6743 | 17.00 | 5.7637 |
| 3.50 | 29.6526 | 17.50 | 5.5881 |
| 4.00 | 25.8867 | 18.00 | 5.4224 |
| 4.50 | 22.9581 | 18.50 | 5.2657 |
| 5.00 | 20.6155 | 19.00 | 5.1174 |
| 5.50 | 18.6992 | 19.50 | 4.9768 |
| 6.00 | 17.1026 | 20.00 | 4.8432 |
| 6.50 | 15.7518 | 20.50 | 4.7163 |
| 7.00 | 14.5943 | 21.00 | 4.5955 |
| 7.50 | 13.5913 | 21.50 | 4.4804 |
| 8.00 | 12.7139 | 22.00 | 4.3706 |
| 8.50 | 11.9400 | 22.50 | 4.2658 |
| 9.00 | 11.2522 | 23.00 | 4.1656 |
| 9.50 | 10.6370 | 23.50 | 4.0697 |
| 10.00 | 10.0835 | 24.00 | 3.9779 |
| 10.50 | 9.5828 | 24.50 | 3.8900 |
| 11.00 | 9.1279 | 25.00 | 3.8056 |
| 11.50 | 8.7126 | 25.50 | 3.7246 |
| 12.00 | 8.3321 | 26.00 | 3.6467 |
| 12.50 | 7.9822 | 26.50 | 3.5719 |
| 13.00 | 7.6593 | 27.00 | 3.4999 |
| 13.50 | 7.3605 | 27.50 | 3.4306 |
| 14.00 | 7.0831 | 28.00 | 3.3638 |
| 14.50 | 6.8250 | 28.50 | 3.2995 |
| 15.00 | 6.5842 | 29.00 | 3.2374 |
| 15.50 | 6.3591 | 29.50 | 3.1775 |
| 16.00 | 6.1481 | 30.00 | 3.1196 |
| 16.50 | 5.9500 | | |

REFERENCES


1. Morgan, S. P., Mode Conversion Losses in Transmission of Circular Electric Waves through Slightly Non-Cylindrical Guides, J. Appl. Phys., *21,* 1950, p. 329.
2. Cook, J. S. and Lowell, R., The Autotrack System, B.S.T.J., *42,* July 1963, pp. 1283–1307.
3. Potter, P. D., A New Horn Antenna with Suppressed Sidelobes and Equal Beamwidths, Microwave J. *6,* 1963, p. 71.
4. Olver, F. W. J., The Asymptotic Expansion of Bessel Functions of Large Order, Phil. Trans., A, *247,* 1954, p. 328. Also see Olver's Tables of Bessel Functions of Moderate or Large Orders, National Physical Laboratory Mathematical Tables, *6,* 1962, Her Majesty's Stationery Office, London.
5. Borgnis, F. and Papas, C. H., Electromagnetic Waveguides and Resonators, *Encyclopedia of Physics,* Volume XVI, Springer, Berlin, 1958, p. 356.
6. Erdelyi, A., et al., *Higher Transcendental Functions, Volume I,* McGraw-Hill Book Company, Inc., New York, 1953, p. 148.
7. Abramowitz, M. and Stegun, I. A., *Handbook of Mathematical Functions,* U. S. Government Printing Office, Washington, D. C., 1964, p. 409.
8. Erdelyi, A., et al., *Higher Transcendental Functions, Volume II,* McGraw-Hill Book Company, Inc. New York, 1953, p. 89.
9. Miller J. C. P., *The Airy Integral,* Cambridge University Press, Cambridge (G. B.), 1946.

# Mode Conversion in Lens Guides with Imperfect Lenses

By D. GLOGE

(Manuscript received August 16, 1967)

*A coherent Gaussian beam transmitted through many imperfect lenses suffers a distortion of its profile. Particularly smooth polishing errors generate parasitic modes which travel with a slightly different propagation constant and about the same low loss as the beam. While the two modes of lowest order essentially influence position and width of the beam, all higher-order modes deform the profile and may hamper position control and detection if they build up to sufficient power. The calculations show that this effect can be reduced to a negligible amount if the beam cross-section is of the order or smaller than the dimensions of the irregularities. This is in agreement with experiments. The perturbation of the beam in the air path between the lenses is also investigated and it is shown from experimental data that this effect is negligible in a properly shielded underground lens guide.*

## I. INTRODUCTION

There has been much uncertainty about the optical quality required for the components in an optical transmission link. Particularly for a lens guide with thousands of lenses, this is a major cost factor. It has been shown that systematic lens aberrations may lead to a severe degeneracy of a transmitted laser beam,[1] but hardly anything is known about random errors. Previous work in this field dealt with antenna or imaging problems,[2, 3, 4] but none of these theories can be applied to iterative structures.

The theory presented here was developed in parallel with experiments in a half-mile underground lens guide designed to gain data about the required component quality.[5] This guide employed antireflection-coated quartz lenses separated by about 140 m. A loss of roughly 1 percent per lens was measured, so that a transmission over 100 miles without amplification seems feasible. Systematic aber-

rations are negligible as compared with random surface irregularities.

These irregularities are of various nature and origin. There are minute scratches in the polished surface and tiny holes or craters in the antireflection coatings. Both cause a wide angle scattering and part of the measured overall loss without considerably changing the intensity profile or the phasefront of the transmitted light beam.

On the other hand, the polishing process achieves a spherical surface only to a certain degree, so there are always small smooth protuberances and recesses called "polishing errors." They show up in an interferometer check and their magnitude is usually given in fringes or wavelength of the light used in the interferometer. This magnitude defines the quality of the lens.

It is this imperfection which will be of interest here, for, without introducing immediate loss, it distorts the light beam in a way that may lead to complete deformation of the intensity profile when occurring repetitively. The consequence may eventually be an additional loss. Furthermore, it influences the choice of the receiving technique used at the end of a long lens guide because the efficiency of a heterodyne system will depend on how well the signal and local oscillator beams can be matched. Thirdly, it affects the applicability and design of beam position control systems which probably will have to be employed in some sections of the lens guide to provide for occasional realignment.[6, 7]

Refractive index variations in the atmosphere between the lenses are of course an additional source of beam distortion. Though weak in a shielded underground lens guide the influence might be comparable to that of imperfect optical components. The calculations in the last part of this work consider these index variations using the model of an imperfect waveguide.[8] Though not as general or accurate as previous work[9] this approach has the advantage that it yields simple formulae for the case of weak coupling. By inserting some experimental data the influence of the air paths and the optical components will be compared.

## II. THE STATISTICAL FEATURES OF IMPERFECT LENSES

Restricting the following calculations to smooth irregularities has two consequences. First, in the proximity of the lens surface the approximations of geometrical optics may be applied, which means that the wavefront emerging from the surface exhibits a phase deviation but no amplitude change.

If there is, for example, a protuberance of magnitude $\delta$ at a certain point of a lens surface, the phase retardation of a light ray passing this point will be

$$\varphi = k\,\Delta n\,\delta, \tag{1}$$

where $k$ is the propagation constant of the light outside the lens and $\Delta n$ is the refractive index change at the surface.

Second, the surface irregularities and consequently also the phase deviations may be described by a random function which is both well-behaved (with at least the first derivative being finite) and homogeneous over the whole surface, since the irregularities were generated everywhere by the same process.

To proceed in the mathematical description, some assumptions must be made which seem to be reasonable for the random function under consideration, but will not be proved as valid here. One may conceptually construct an ensemble of identical optical surfaces which exhibit different point-by-point deviations, but are statistically equivalent. It is assumed that averages over the surface are replaceable by ensemble averages, and that $\delta$ and therefore $\varphi$ are Gaussianly distributed, have zero mean, and variance $\Delta^2$ and $\Phi^2$, respectively. Obviously, the correct lens surface can always be defined in such a way that the mean value of $\delta$ is zero.

For simplicity, the two-dimensional model shown in Fig. 1 is used at the beginning. $\delta$ and $\varphi$ are now functions of the surface coordinate $x$ only. The covariance

$$F(x_1 - x_2) = \langle \varphi(x_1)\varphi(x_2)\rangle \tag{2}$$

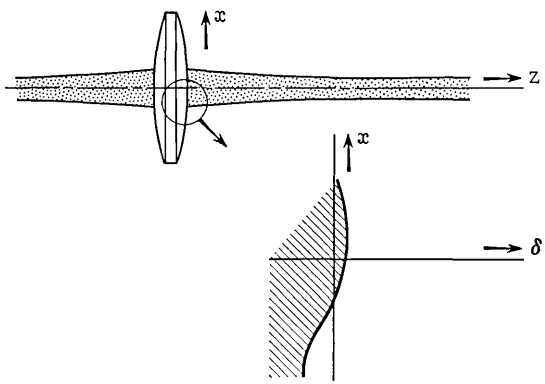


Fig. 1 — Two-dimensional model of an imperfect lens.

can be shown to exist and be a function of the distance $x_1 - x_2$ only because of the assumed features of $\varphi(x)$. For later calculations the identity

$$\langle \exp i[\varphi(x_1) - \varphi(x_2)] \rangle = \exp (F - \Phi^2) \tag{3}$$

is needed, which can be derived from those assumptions also.[3]

The fact that $\varphi$ is smooth and stationary suggests a Gaussian covariance

$$F = \Phi^2 \exp [-(x_1 - x_2)^2/v^2], \tag{4}$$

where $v$ is a correlation length determined by the dimension of those protuberances and recesses on the optical surface.

## III. COUPLING TO PARASITIC MODES

A coherent light beam with Gaussian field profile conserves itself from lens to lens in a lens guide if it enters with the right phasefront curvature and the right half-width $w$ of the field profile.[11] This "Gaussian beam" is the lowest order of an infinite set of modes which can propagate in such a lens guide. All these modes have the same phase fronts, slightly different propagation constants and a field profile that can be described by the orthogonal set of hyperbolic cylinder functions

$$D_n\left(2\,\frac{x}{w}\right) = e^{-x^2/w^2} He_n\left(2\,\frac{x}{w}\right), \tag{5}$$

where $He_n$ are the hermite polymonials.[10, 11] Note that $He_0 = 1$ and, therefore, $D_0$ describes the Gaussian beam profile.

The higher the mode number, the further the profile extends about the lens area. As will be shown, the smooth irregularities under consideration here generate mainly low order modes and those to an amount that the comparatively small losses at the lens apertures are negligible. It seems justified, therefore, to consider the lenses as unbounded.

Assume that a perfect Gaussian beam traverses the optical surface in Fig. 1. Then the emerging wave function is

$$u(x) = D_0 \exp [i\varphi(x)] \tag{6}$$

which, on the other hand, can be expanded into the infinite series

$$u(x) = \sum_{n=0}^{\infty} c_n D_n \,. \tag{7}$$

The expansion coefficient $c_n$ describes the coupling or scattering from the Gaussian beam to the $n^{\text{th}}$ mode. Using (6), (7), and the orthogonality relation given in Ref. 10, one finds

$$c_n = \frac{\sqrt{2/\pi}}{n!\, w} \int_{-\infty}^{+\infty} D_0 D_n \exp(i\varphi)\, dx. \tag{8}$$

Multiplying this by its conjugate complex and averaging over the ensemble yields the average power coupled to the $n^{\text{th}}$ mode from a Gaussian beam of unit power passing one distorted surface. The calculation is shown in the Appendix. The result is

$$p_n = \frac{\sqrt{2/\pi}}{n!\, 2^n w} \int_{-\infty}^{+\infty} D_0 D_{2n} \exp\left[F(\sqrt{2}\,\xi) - \Phi^2\right] d\xi. \tag{9}$$

For a Gaussian correlation function $F$ as defined in (4), the most useful representation is an expansion in powers of the variance $\Phi^2$

$$p_n = \frac{(2n)!}{2^{2n}(n!)^2} \exp(-\Phi^2) \sum_{q=0}^{\infty} \frac{\Phi^{2q}}{q!} \frac{(qw^2/v^2)^n}{(1 + qw^2/v^2)^{n+\frac{1}{2}}}. \tag{10}$$

This formula is valid for any value of $\Phi$ and $v$. In practice, the converted power is only a small part of the total beam power and therefore,

$$\Phi w/v \ll 1. \tag{11}$$

In the case of a lens guide, this is a necessary condition for reconversion from parasitic modes into the beam to be negligible.

Two cases are of interest: $\Phi$ is large, say, of the order of 1 rad or larger, but (11) is satisfied since $v$ is large at the same time. A series expansion in powers of $\Phi$, as in (10), is not very useful in this case. However, expanding $F$ in powers of $w/v$ and truncating after the quadratic term yields for (9)

$$p_n = \frac{(2n)!}{2^{2n}(n!)^2} \frac{(\Phi^2 w^2/v^2)^n}{(1 + \Phi^2 w^2/v^2)^{n+\frac{1}{2}}}. \tag{12}$$

Probably of more importance are optical surfaces which cause a small rms phase distortion $\Phi$ but have a correlation length $v$ of the order or even smaller than the beam width $w$. Then (10) may be used and terms with $q > 2$ in (10) may be neglected. Note that for both (10) and (12) a summation over all $n$ yields unity. No power is lost in the conversion process. $p_0$ is the power that is left in the Gaussian beam and $1 - p_0$, consequently, the conversion loss.

## IV. THE THREE-DIMENSIONAL REPETITIVE STRUCTURE

To investigate the three-dimensional model, the additional assumption is made that the irregularities are isotropic over the optical area. The correlation function (4) may then be extended to two dimensions by

$$F = \Phi^2 \exp\left[-\frac{(x_1 - x_2)^2 + (y_1 - y_2)^2}{v^2}\right]. \tag{13}$$

The modes of the new model are defined by two numbers $n$ and $m$. It can be shown that groups of modes with the same

$$r = n + m \tag{14}$$

are degenerate, that is, they travel with the same propagation constant.[11]

The coupling coefficients for the three-dimensional model must be evaluated from double integrals which are separable if higher orders of $\Phi^2$ may be neglected. One finds for the average power coupled from a unit power beam

$$p_{00} = 1 - \frac{\Phi^2}{1 + v^2/w^2}, \tag{15}$$

and

$$p_{nm} = \frac{(2n)!}{2^{2n}(n!)^2}\frac{(2m)!}{2^{2m}(m!)^2}\frac{\Phi^2 v^2/w^2}{(1 + v^2/w^2)^{n+m+1}} \quad \text{for} \quad n, m = 1, 2, \cdots .$$

Physically more meaningful is the computation of the average power that is coupled to a complete group of degenerate modes:

$$P_0 = 1 - \frac{\Phi^2}{1 + v^2/w^2},$$

and

$$P_r = \frac{\Phi^2 v^2/w^2}{(1 + v^2/w^2)^{r+1}} \qquad r = 1, 2, \cdots . \tag{16}$$

It has been shown in Ref. 1 that an optical surface can be adjusted in such a way that no power is coupled to the first group of parasitic modes. If this is done, the power loss is a minimum and the power kept in the beam may be found from (16) to be

$$\bar{P}_0 = 1 - \frac{\Phi^2}{(1 + v^2/w^2)^2}. \tag{17}$$

If, furthermore, one is free to adjust the width of the transmitted beam at the receiving end, say by a telescope arrangement or by adapting the local oscillator beam to the width of the signal beam, one can minimize the losses even further. In this case no power is coupled to the second mode group either.[1] The power kept in the beam may be found from (16) to be

$$\bar{P}_0 = 1 - \frac{\Phi^2}{(1 + v^2/w^2)^3}. \tag{18}$$

It seems reasonable to assume that the irregularities on both sides of a lens surface are uncorrelated, in which case the powers generated in both conversion processes simply add. Fig. 2 shows the conversion loss $1 - 2P_0$ and the powers in the three parasitic modes of lowest order versus $w/v$ for a lens quality of $\lambda/10$. For the first approximation, it is assumed that such a lens has an rms deviation of $\Delta = \lambda/10$ though actually the rms value should be somewhat smaller. $\Delta n$ in (1) is 0.5. The loss increases rapidly with decreasing correlation length. For $v < w$, the loss approaches the value $\Phi^2$. For a correlation length larger than the beam width, almost all the losses are found in the first parasitic mode.

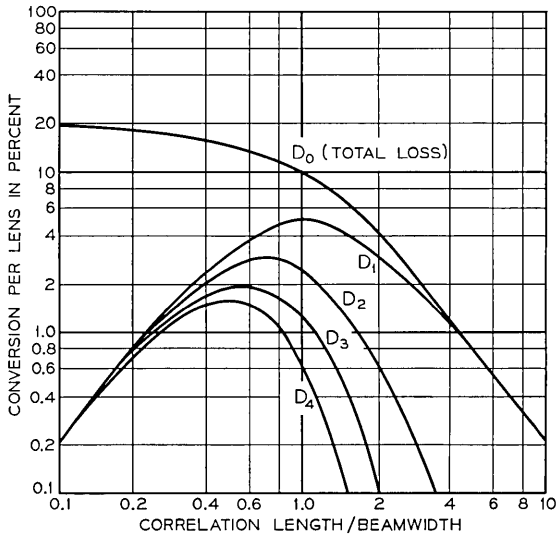


Fig. 2 — Average loss and power coupled to higher mode groups by a lens of quality $\lambda/10$.

Proper adjustment reduces the loss by this amount. This is shown in Fig. 3. For $v = 2w$, a factor of 4 is gained by adjustment. The loss decreases by more than an order of magnitude if the beam spread is neglected also. The lens quality in this example is $\lambda/10$. Fig. 4 compares the losses for lenses of various qualities. Fig. 5 gives the same quantities when proper adjustment of the lenses is taken into account. Fig. 6 in addition neglects spreading of the beam.

For hand-polished lenses, the correlation length can be expected to be of the order of cm. The beam width in a lens guide depends on the lens spacing and the wavelength of the transmitted light.[11] For lenses separated by 140 m and red light of 0.63 $\mu$, the beam width is $2w = 1$ cm. Fig. 6 shows that in this case the conversion loss is less than 0.1 percent and therefore, a negligible amount of the total loss. Nevertheless, poorly attenuated parasitic modes may build up and distort the beam profile.

Certainly there is no correlation from lens to lens. So the average mode power simply increases proportionally to the number of lenses. The modes under consideration have about the same overall attenuation as the Gaussian beam. Therefore, after $N$ lenses, the average

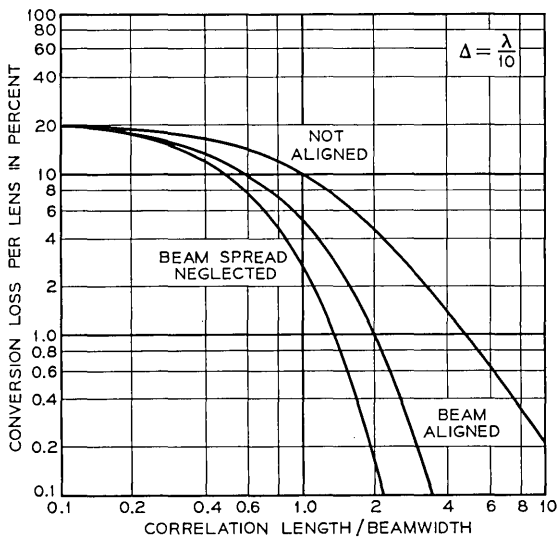


Fig. 3 — The conversion loss is reduced if the lens is adjusted and a beam spread tolerated (quality $\lambda/10$).

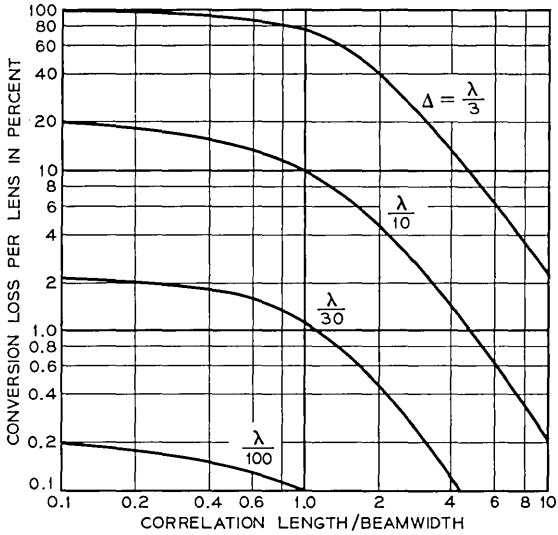


Fig. 4 — Average conversion loss for lenses of various qualities.

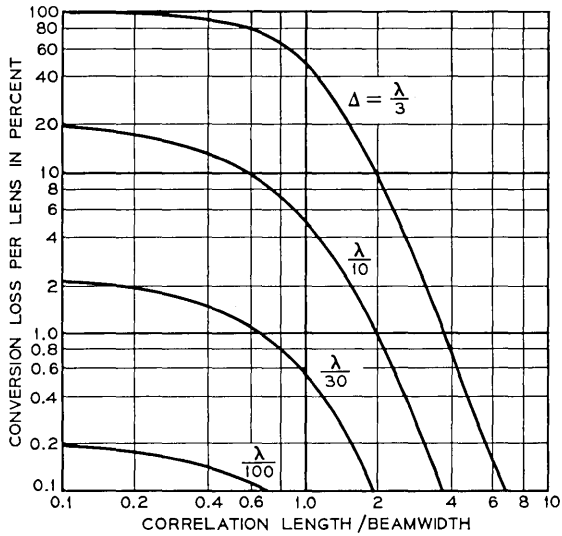


Fig. 5 — Average conversion loss for lenses of various qualities (beam aligned on axis).

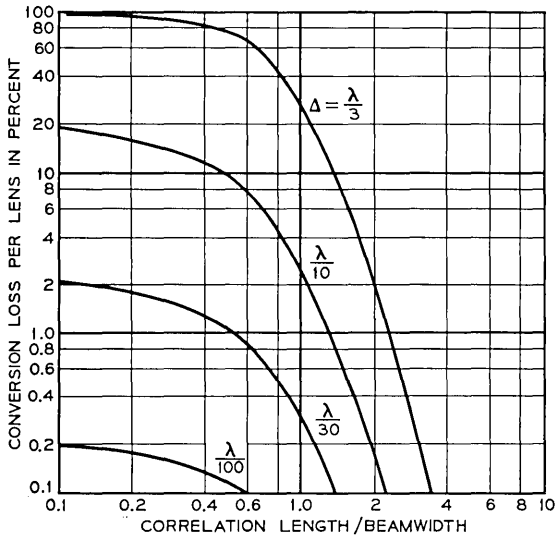


Fig. 6 — Average conversion loss for lenses of various qualities (beam spread tolerated).

power in the $r$th parasitic group of degenerate modes is

$$\frac{2NP_r}{1 - 2NP_0} \tag{19}$$

times the power in the Gaussian beam, provided that the conversion even after $N$ lenses is small enough to permit the negligence of reconversion and higher-order loss terms. The average amplitude ratio is

$$\frac{\sqrt{2NP_r}}{1 - NP_r}. \tag{20}$$

The respective phases even of modes in the same group are undetermined.

To gain a conception of the distortion a situation is assumed in Fig. 7 to 9 where all modes are in phase. Fig. 7 shows a possible intensity profile after passing a lens of quality $\lambda/10$ and correlation length $v = 2w$. The result is mainly a displacement. In Fig. 8 the beam passed 10 lenses but these now are adjusted so that the beam stays on the guide axis. The main effect is a spreading. Fig. 9 is a sketch of the profile after 100 lenses, all adjusted, and the profile is

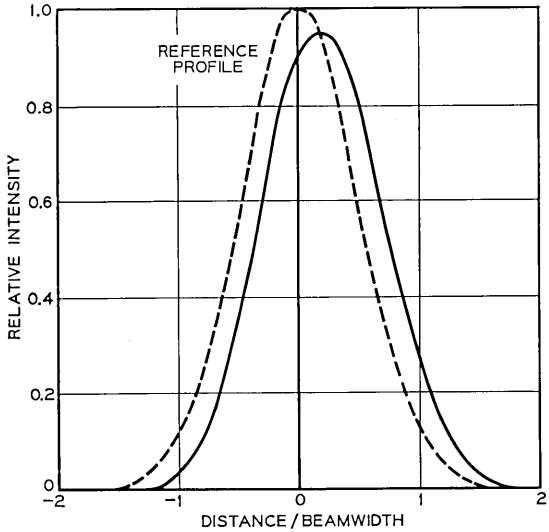


Fig. 7 — Possible profile distortion caused by a lens of quality λ/10.

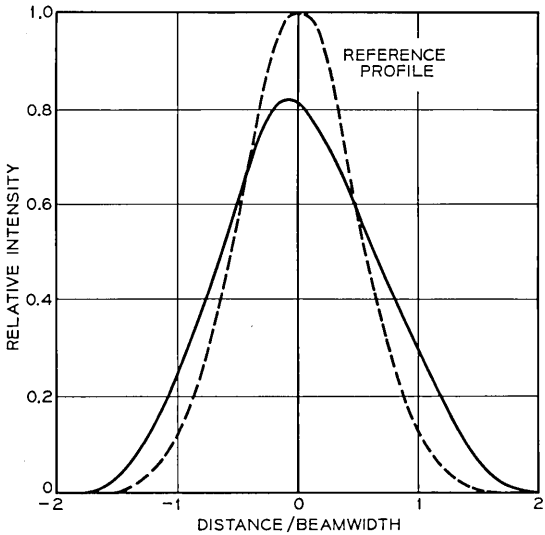


Fig. 8 — Possible profile distortion after 30 lenses of quality λ/10 (beam aligned on axis).

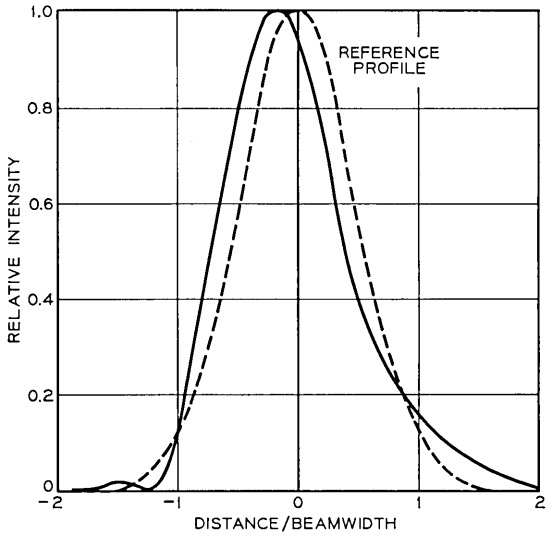


Fig. 9 — Possible profile distortion after 900 lenses of quality $\lambda/10$ (beam spread tolerated).

reduced to the nominal beam width. There is a slight tilt of the profile and a side lobe, but no basic destruction of the beam.

## V. CONVERSION IN THE ATMOSPHERE BETWEEN LENSES

Similar to the mode coupling at certain cross-sections of the lens guide there can be mode coupling all along the guide if there is a source of distortion. In the case of a gas between the lenses the source may be the random fluctuation of the refractive index of this gas.

For simplicity let us return to the two-dimensional model of Fig. 1. Here $\Delta n$, the deviation from the mean index $n_0$, is a function of $x$ and $z$. Consider slabs of thickness $\Delta z$ cut perpendicular to the guide axis. A light beam traversing a slab at $z$ suffers a distortion of its phase front

$$\varphi(x, z) = k \, \Delta z \, \Delta n(x, z). \tag{21}$$

This causes a conversion into parasitic modes which can be calculated from (8). The validity of this model has been investigated in Ref. 8. Its usefulness lies in its physical simplicity which allows controlled approximations.

Contrary to the lens irregularities $\delta$, the index variations $\Delta n$ are

only "locally homogeneous," which makes it necessary to use structure functions instead of covariance functions for the statistical description. In two dimensions the structure function of $\varphi$ is

$$S(x_1 - x_2, z_1 - z_2) = \langle[\varphi(x_1, z_1) - \varphi(x_2, z_2)]^2\rangle. \tag{22}$$

Instead of (3) the identity

$$\langle \exp i[\varphi(x_1, z_1) - \varphi(x_2, z_2)]\rangle = \exp[-\tfrac{1}{2}S]. \tag{23}$$

will be used later, which may be derived in the same way as (3).[3] From Kolmogoroff's theory for a locally isotropic turbulent flow one finds[12]

$$S = k^2(\Delta z)^2\sigma[(x_1 - x_2)^2 + (z_1 - z_2)^2]^{\frac{1}{3}}. \tag{24}$$

$\sigma$ is called the refractive index structure constant and measures the strength of the index fluctuations.

If $\Delta z$, the thickness of the slabs, is made very small the coupling per slab will be proportional to $\Delta z$, say $c_n\Delta z$ for the $n$th mode. Assume that a Gaussian beam of unit amplitude traverses the air path from one lens to the next. Then in every slab an amplitude $c_n\Delta z$ is generated in the $n$th mode. Assume that the coupling to all parasitic modes is so small that reconversion can be neglected. Then, at the end of the air path of length $L$, the amplitude in the $n$th mode is

$$a_n = \int_0^L c_n(z) \exp(-in\theta z/L)\, dz. \tag{25}$$

$n\theta/L$ describes the phase lag between the fundamental and the $n$th mode as they travel along the path.[1] For a confocal system $\theta = \pi/2$, i.e., the phase retardation of the first parasitic mode with respect to the fundamental is $\pi/2$ from one lens to the next. Considering that the patches of correlated index variations are much smaller than the lens distance, it can be expected that the phase between low-order modes changes only a negligible amount within the area of correlated coupling. In the following, therefore, the phase lag will be neglected.

For the evaluation of (25) it has to be considered also that $c_n$ is a function of the beam width $w$ which varies slowly along the transmission path. In a confocal lens guide the modes are $\sqrt{2}$ times wider at a lens than in the center between two lenses.[11] It is by a factor of this order that the results will deviate from the true values if for the following $w$ is kept constant and equal to the width at a lens.

With this in mind the expected power coupled to the $n$th mode can

be calculated by multiplying (25) by its conjugate complex and taking the average, which in this case will be an average over an infinite time. The evaluation agrees with the one outlined in the appendix. Since $S$ is proportional to the square of the small increment $\Delta z$ the exponential function in (23) may be expanded up to the linear term of the argument. The average power in the $n$th mode is finally

$$p_n = \frac{\sqrt{2/\pi}}{n!\,2^n w} \int_{-\infty}^{+\infty} D_0 D_{2n}[1 - \tfrac{1}{2} S_L(\sqrt{2}\,\xi)]\, d\xi \tag{26}$$

with

$$S_L(x_1 - x_2) = \int_0^L \int_0^L S(x_1 - x_2\,, z_1 - z_2)\, dz_1\, dz_2\,. \tag{27}$$

$S_L$ has been calculated elsewhere in connection with the investigation of a plane wave propagating in a turbulent flow.[13] It is called the phase structure function of a plane wave and describes the statistics of the phases in a phase front that has traversed a turbulent air path. Equation (26) states that under the employed approximations the parasitic power arriving at the path end can be calculated from the intensity profile of an undisturbed beam multiplied by the phase structure function of a plane wave at the path end. From Ref. 13 one finds

$$S_L(x_1 - x_2) = 2.91 k^2 L \sigma (x_1 - x_2)^{5/3}. \tag{28}$$

As long as the function $S_L$ is of the form $\xi^\alpha$ for $\alpha > -1$ the following general solution can be found for (26):

$$p_n = \delta_{0n} - S_L(\sqrt{2}\,w)\, \frac{\Gamma\left(\frac{1}{2} + \frac{\alpha}{2}\right)}{\Gamma(\frac{1}{2})} \binom{\alpha/2}{n} (-1)^n 2^{\alpha/2} \tag{29}$$

with

$$\delta_{0n} = \begin{cases} 1 & \text{for} \quad n = 0 \\ 0 & \text{for} \quad n = 1, 2, \cdots . \end{cases}$$

For the three-dimensional case again groups of modes with equal propagation constants are combined. The expected power in the $r$th group can be calculated from an expression similar to (26) but with double integrals for the $x$ and $y$ coordinates. It is

$$P_r = \delta_{0r} - S_L(\sqrt{2}\,w)\, \frac{\alpha}{2}\, \Gamma\left(\frac{\alpha}{2}\right) \binom{\alpha/2}{n} (-1)^n 2^{\alpha/2}. \tag{30}$$

In the case of the plane wave approximation $\alpha = 5/3$. $1 - P_r$ is the total average power loss for a Guassian beam. Note that the summation over all $P_r$ yields unity. No power is dissipated.

The application of the waveguide model is no longer useful if the refractive index variations are so large that reconversion from parasitic modes into the fundamental must be considered. The mode conversion at the path end, however, may then still be calculated from the undisturbed profile multiplied by the appropriate phase structure function. Only, the phase fluctuations at the path end will then be so large that an expansion of the exponential function in (26) is no longer valid. For a configuration close to confocal the phase structure function $S_L$ of the plane wave will be a good starting point to calculate the expected powers

$$p_n = \frac{\sqrt{2/\pi}}{n!\, 2^n w} \int_{-\infty}^{+\infty} D_0 D_{2n} \exp\left[-\tfrac{1}{2} S_L(\sqrt{2}\,\xi)\right] d\xi. \tag{31}$$

A better approximation would have to consider the amplitude variations at the path end in (34) as well. It has been shown elsewhere that its neglection results in an error of the order of two only.[14]

The results given in Fig. 10 for the three-dimensional case were calculated from an expression similar to (31). Fig. 10 shows the loss

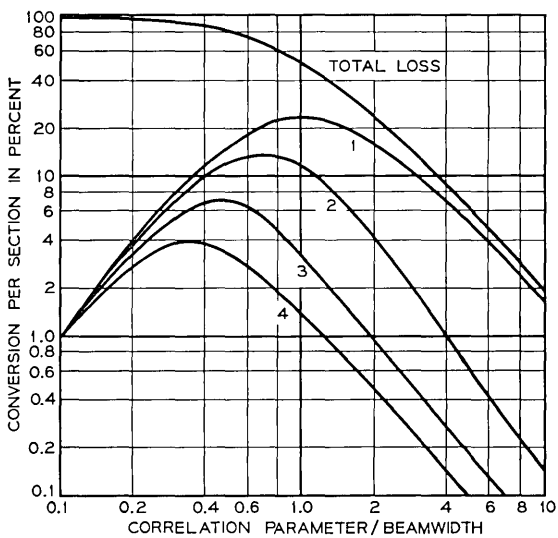


Fig. 10 — Average loss and power coupled to higher mode groups versus the phase correlation parameter $(2.91\ k^2 L\sigma)^{-3/5}$ for a turbulent medium.

in the beam and the powers in the first four parasitic mode groups versus the correlation parameter

$$v = (2.91k^2L\sigma)^{-3/5} \tag{32}$$

which is a measure for the correlation at the path end. This plot allows a comparison with Fig. 2.

For large $v$ the curves in Fig. 10 turn into straight lines indicating a functional dependence $w^{5/3}$ as given by the approximate formula (30). Also for large $v$ the ratio between $P_1$ and the total loss is a constant close to 1. By measuring $P_1$ the total power loss can be found.

This has been done in an experimental underground lens guide using a photoresistor bridge.[7] The first mode group consists of two modes of equal average power orientated in perpendicular planes. The photoresistor bridge described in Ref. 7 measures the instantaneous amplitude of one of these modes as compared to the amplitude in the fundamental. Actually if this ratio is of the order of some percent or smaller it is equal to the ratio of bridge signal $V$ to bridge battery voltage $V_0$ (see Ref. 7). The variance of this signal is the ratio of expected first mode power to beam power and twice that is the loss. Neglecting a seasonal slow beam drift a variance of $3\ 10^{-7}$ was measured in a 400-foot section of the underground lens guide. The loss is consequently of the order of $10^{-6}$ of the total power.

It cannot be asserted here that this loss is indeed due to atmospheric effects. Microseisms may cause fluctuations of the lens positions that lead to disturbances of the same order. The measurement must be understood merely as an upper limit for the conversion caused by a well-shielded air path. The conversion expected from the lenses is several orders of magnitude larger, but, being independent of time, it can only be measured in a large number of sections to represent a reasonable average. An experiment of this kind is described in Ref. 5.

## VI. CONCLUSIONS

In a lens guide with widely separated solid lenses, aberrations are negligible as compared to random surface irregularities. How much a Gaussian beam is distorted by the irregularities depends not only on the rms deviation $\Delta$, but also very strongly on the dimension of the irregularities as compared to the beam cross-section.

For a beam of width $2w$, which loses no power into the two parasitic modes of lowest order, the conversion loss is proportional to $(w/v)^6$

where $v$ is a correlation length defining the dimension of the irregularities. Consequently, $w$ should be made small enough to assure that the conversion loss is negligible compared to all other losses and that the beam profile distortion caused by the generated parasitic modes is tolerable.

A beam with nominal width of 1 cm seems to satisfy these conditions if lenses with a quality $\lambda/10$ are used. These calculations are based on a conservative estimate of 1 cm for the correlation length. In this case, the conversion losses are smaller than 0.1 percent per lens and 1/10 of all other losses. The profile after 100 lenses may, at best, exhibit small side lobes with a peak intensity of the order of 1 percent of the beam peak intensity.

Refractive index variations in the air path between the lenses also lead to a conversion loss. It grows with $w^{5/3}$ for weak distortions. In a 400-foot section of the underground lens guide described in Ref. 7 an upper bound for this loss was measured to be $10^{-6}$ of the total power.

## APPENDIX

A meaningful measure for the effect of surface imperfections is the power coupled from the Gaussian beam into parasitic modes, averaged over the ensemble of equivalent surfaces:

$$p_n = n!\,\langle c_n c_n^* \rangle. \tag{33}$$

The coupling coefficients $c_n$ are given by (8). After changing the order of integration and averaging process and by replacing the ensemble average by an average over the surface, one gets

$$p_n = \frac{2}{n!\,\pi w^2} \iint D_0(x_1) D_n(x_1) D_0(x_2) D_n(x_2) \langle e^{i[\varphi(x_1)-\varphi(x_2)]} \rangle \, dx_1 \, dx_2 \,, \tag{34}$$

where all integrals here and in the following extend from $-\infty$ to $+\infty$. To separate the double integral in (34), it is appropriate to change to new coordinates

$$\xi = \frac{x_1 - x_2}{\sqrt{2}} \quad \text{and} \quad \eta = \frac{x_1 + x_2}{\sqrt{2}} \tag{35}$$

in the plane of integration. From the properties of the hyperbolic cylinder functions, the identity

$$D_n(x_1) D_n(x_2) = \sum_{p=0}^{n} (-2)^{-n} \binom{n}{p} D_{2p}(\xi) D_{2n-2p}(\eta) \tag{36}$$

can be derived. The use of (35), (36), and (3) turns (34) into

$$p^n = \frac{2}{n!\,\pi w^2} \sum_{p=0}^{n} (-2)^{-n} \binom{n}{p} \int D_0 D_{2n-2p}\, d\eta \int D_0 D_{2p} e^{F(\sqrt{2}\xi)-\Phi^2}\, d\xi \quad (37)$$

and because of the orthogonality of the $D_n$, this can finally be simplified to

$$p_n = \sqrt{2/\pi}\, \frac{(-2)^{-n}}{n!\, w} \int D_0 D_{2n} e^{F(\sqrt{2}\xi)-\Phi^2}\, d\xi. \quad (38)$$

REFERENCES


1. Marcatili, E. A. J., Effect of Redirectors, Refocusers, and Mode Filters on Light Transmission Through Aberrated and Misaligned Lenses, to be published.
2. Ruze, I., Antenna Tolerance Theory—A Review, Proc. IEEE, *54,* April, 1966, pp. 633–640.
3. O'Neill, E. L., *Introduction to Statistical Optics,* Addison-Wesley Publishing Co., 1963.
4. Rowe, H. E., Lenses with Random Imperfections, unpublished work.
5. Gloge, D., Pulse Shuttling in a Half-Mile Underground Lens Guide, to be published.
6. Marcatili, E. A. J., Ray Propagation in Beam Waveguides with Redirectors, B.S.T.J., *45,* January, 1966, pp. 105–116.
7. Gloge, D., Experiments with an Underground Lens Waveguide, B.S.T.J., *46,* April, 1967, pp. 721–735.
8. Matveyev, R. F., Analysis of the Passage of Beamguide Waves Through an Inhomogeneous Medium, Radio. Eng. Electron. Phys., *11,* November, 1966, pp. 1721–1727.
9. Schmeltzer, R. A., Means, Variances, and Covariances for Laser Beam Propagation Through a Random Medium, Quant. Appl. Math. *24,* April, 1967, pp. 339–354.
10. Magnus, W., and Oberhettinger, I., *Formulas and Theorems for the Functions of Mathematical Physics,* Chelsea Publishing Co., New York, 1954, p. 93.
11. Boyd, G. D. and Kogelnik, H. W., Generalized Confocal Resonator Theory, B.S.T.J., *41,* April, 1962, pp. 1347–1369.
12. Kolmogoroff, A., in *Turbulence, Classic Papers on Statistical Theory,* edited by Friedlander, S. K. and Topper, L., Interscience Publishers, Inc., New York, 1961, p. 151.
13. Tatarski, V. I., *Wave Propagation in a Turbulent Medium,* McGraw Hill Book Co., Inc., New York, 1961, pp. 93–115.
14. Fried, D. L., Statistics of a Geometric Representation of Wavefront Distortion, J. Opt. Soc. Amer., *55,* November, 1965, pp. 1427–1435.

# Contributors to This Issue

VÁCLAV E. BENEŠ, A.B., 1950, Harvard College; M.A. and Ph.D., 1953, Princeton University; Bell Telephone Laboratories, 1953—. Mr. Beneš has been engaged in mathematical research on stochastic processes, traffic theory, and servomechanisms. In 1959–60 he was visiting lecturer in mathematics at Dartmouth College. He is the author of General Stochastic Process in the Theory of Queues (Addison-Wesley, 1963), and of Mathematical Theory of Connecting Networks and Telephone Traffic (Academic Press, 1965). Member, American Mathematical Society, Association for Symbolic Logic, Institute of Mathematical Statistics, SIAM, Mind Association, Phi Beta Kappa.

THOMAS G. CROSS, B.S.E.E., 1963, California State Polytechnic College; M.S.E.E., 1965, Northeastern University; Bell Telephone Laboratories, 1963—. Mr. Cross has been involved in a group responsible for the system analysis of the new TD-3 Long-Haul Radio System, and is currently involved in system planning for microwave radio relay systems.

DETLEF GLOGE, Dipl. Ing., 1961, D.E.E., 1964, Braunschweig Technische Hochschule (Germany); research staff, Braunschweig Technische Hochschule 1961–1965; Bell Telephone Laboratories, 1965—. In Braunschweig, Mr. Gloge was engaged in research on lasers and optical components. At Bell Telephone Laboratories, he has concentrated in the study of optical transmission techniques. Member, VDE, IEEE.

JACK M. HOLTZMAN, B.E.E., 1958, City College of New York; M.S., 1960, University of California (Los Angeles); Ph.D., 1967, Polytechnic Institute of Brooklyn; Hughes Aircraft Company, 1958–1963; Bell Telephone Laboratories, 1963—. Mr. Holtzman has worked in various aspects of systems and control theory. Member, SIAM, Sigma Xi.

GERALD KRONACHER, Diploma in Electrical Engineering, Federal Institute of Technology, Switzerland, 1937; professor of physics and chief of the Meteorological Observatory, University of Potosi, Bolivia (concurrently associated with the Unificada Mining Company),

1940–46; Bell Telephone Laboratories, 1953—. He was engaged at first in the development of analog-to-digital converters. He obtained several patents including one covering the multi-pole-pair resolver, a precise angle transducer, and published several technical papers. He is concerned with shielding electronic equipment from atmospheric electromagnetic pulses. Senior member, IEEE.

KANEYUKI KUROKAWA, B.S., 1951, Ph.D., (Engineering), 1958, both from the University of Tokyo; assistant professor, University of Tokyo, 1957–1963; Bell Telephone Laboratories, 1963—. Mr. Kurokawa has been engaged in designing and developing microwave transistor amplifiers. He supervises a group responsible for the exploratory development of solid state functional devices and circuits. Member, IEEE, Institute of Electronics and Communications Engineers of Japan.

MASON A. LOGAN, B.S., 1927, California Institute of Technology; M.A., 1933, Columbia University; Bell Telephone Laboratories, 1927–1967. His early work included transmission design problems of local manual and dial circuits and circuit research on alternating current methods of signaling. During and immediately after the war he worked on mine fire-control systems, proximity fuses, Nike-Ajax, and other military projects. Later he was engaged in development of electromagnets and relays, followed by development of instrumentation for semiconductor device process control and evaluation. The article in this issue is related to his interest in this field. Most recently he has been supervising the development and design of new four-phase data sets for world-wide government networks. He retired after more than 40 years of service and now lives in Sun City Center, Florida.

DEAN W. MAURER, B.S. (Chemistry), 1954, Carnegie-Mellon University; Ph.D. (Chemistry), 1959, University of Rochester; Bell Telephone Laboratories, 1959—. Since joining Bell Laboratories Mr. Maurer has been concerned with the chemistry of vacuum tube devices, thermionic emission and life factors, and the development of new and improved cathode types. In 1964 he became concerned with the development of new photosensitive materials for hologram recording media. In January 1967 he became supervisor of the Nickel Cadmium Battery Applications and Development Group. Member,

American Physical Society, American Association for the Advancement of Science, Sigma Xi.

ELLIOTT R. NAGELBERG, B.E.E., 1959, City College of New York; M.E.E., 1961, New York University; Ph.D., 1964, California Institute of Technology; Bell Telephone Laboratories, 1964—. Mr. Nagelberg has been concerned with problems involving microwave antennas and propagation. Member, IEEE, American Physical Society, Eta Kappa Nu, Sigma Xi.

C. M. PLEASS, B.Sc., 1953, Ph.D. (Chemistry), 1955, both from the University of Southampton, England. Scientific Officer, Atomic Weapons Research Establishment, England, 1955–1959; Fellow, National Research Council of Canada, 1959–1961; Bell Telephone Laboratories, 1961—. Mr. Pleass was engaged at first in the development of high reliability electron tube cathodes. Subsequent research involved photosensitive materials for use in hologram recording. He is responsible for *Picturephone** materials and processing at the Reading Laboratory of Bell Telephone Laboratories.

DAVID SLEPIAN, 1941–43, University of Michigan; M.A., 1947, Ph.D., 1949, Harvard University; Bell Telephone Laboratories, 1950—. He has been engaged in mathematical research in communication theory and the theory of noise, as well as in a variety of aspects of applied mathematics. Mr. Slepian has been mathematical consultant on a number of Bell Laboratories projects. During the academic year 1958–59, he was visiting Mackay Professor of Electrical Engineering at the University of California at Berkeley and during the Spring semester 1967 was a Visiting Professor of Electrical Engineering at the University of Hawaii. Member, AAAS, American Math. Society, Institute of Math. Statistics, IEEE, SIAM.

R. D. STANDLEY, B.S., 1957, University of Illinois; M.S., 1960, Rutgers University; Ph.D., 1966, Illinois Institute of Technology; U.S. Army Research and Development Laboratory, Fort Monmouth, N. J., 1957–1960; IIT Research Institute, Chicago, 1960–1966; Bell Telephone Laboratories, 1966—. At Fort Monmouth, Mr. Standley was project engineer on various microwave component development

* Registered trade mark of the Bell System.

programs. His work at IITRI included microwave and antenna research, and management of an electromagnetic compatibility group. At Bell Telephone Laboratories he has been concerned with millimeter-wave up-converters, local oscillator injection filters, and channel dropping filters. He is investigating millimeter-wave impact ionization avalanche transit time diode devices, integrated circuits, and time delay equalizers. Member, IEEE, Sigma Tau, Sigma Xi.